

University of New Mexico

UNM Digital Repository

Nanoscience and Microsystems ETDs

Engineering ETDs

Fall 11-10-2021

Explorations and Developments in Multifunctionality, 3D Printing, and Accelerated Aging for Thermoplastics and Thermosets

Zachary Brounstein
University of New Mexico

Follow this and additional works at: https://digitalrepository.unm.edu/nsms_etds



Part of the [Polymer and Organic Materials Commons](#)

Recommended Citation

Brounstein, Zachary. "Explorations and Developments in Multifunctionality, 3D Printing, and Accelerated Aging for Thermoplastics and Thermosets." (2021). https://digitalrepository.unm.edu/nsms_etds/63

This Thesis is brought to you for free and open access by the Engineering ETDs at UNM Digital Repository. It has been accepted for inclusion in Nanoscience and Microsystems ETDs by an authorized administrator of UNM Digital Repository. For more information, please contact disc@unm.edu.

Zachary Brounstein

Candidate

Nanoscience and Microsystems Engineering

Department

This dissertation is approved, and it is acceptable in quality and form for publication:

Approved by the Dissertation Committee:

Prof. Heather Canavan, Chairperson

Prof. Sang M. Han

Prof. Nathan Jackson

Dr. Andrea Labouriau

Dr. Carl Iverson

**EXPLORATIONS AND DEVELOPMENTS IN
MULTIFUNCTIONALITY, 3D PRINTING, AND
ACCELERATED AGING FOR THERMOPLASTICS AND
THERMOSETS**

BY

ZACHARY BROUNSTEIN

B.S. Mathematics, University of Nevada, Reno, 2016
B.S. Chemical Engineering, University of Nevada, Reno, 2016
M.S. Nanoscience and Microsystems Engineering, University of New
Mexico, 2019

DISSERTATION

Submitted in Partial Fulfillment of the
Requirements for the Degree of

Doctor of Philosophy
Nanoscience and Microsystems Engineering

The University of New Mexico
Albuquerque, New Mexico

December 2021

Dedication

To Samantha and Jakob

*“And you think you’ve figured out everything
I think I know my geography pretty damn well.”*

Acknowledgements

I would like to express my appreciation towards the members of this committee, Professors Heather Canavan, Sang M. Han, and Nathan Jackson, and Doctors Andrea Labouriau and Carl Iverson for participating in the evaluation of my Doctoral Defense. In addition, I am grateful for Professor Jackson's enriching academic drive as one of my graduate teachers, Professor Canavan's guidance and emotional support as my University of New Mexico advisor, and for Dr. Labouriau's motivation and encouragement as my Los Alamos National Laboratory mentor. I would also like to thank Linda Stewart for her auspicious student advocacy and for being a great introduction to the University of New Mexico.

I would like to thank Los Alamos National Laboratory (LANL) for supporting my work, which is under U.S. Department of Energy's National Nuclear Security Administration Contract No. DE-AC52-06NA25396. Specific agencies and drivers I would like to extend my gratitude towards include the Los Alamos Mission Foundation and Los Alamos Institute of Materials Science for sponsoring the research with which I have been engaged. I would also like to extend my thanks to the institutions that have provided instruments to conduct my research, specifically the Los Alamos Neutron Science Center (LANSCE), the Sandia National Laboratory Annular Core Research Reactor facility (ACRR), and the Argonne National Laboratory Advanced Photon Source (APS).

My deep gratitude goes towards my group members, Eamonn Murphy, Dr. Joseph H. Dumont, Dr. Samantha Talley, Jianchao Zhao, Jeff Wheat, Adam Pacheco, Dr. Kwan-Soo Lee, Dr. Chris Yeager, and Dr. Josemari Sansiñena for helping me learn various

experimental techniques, engaging in insightful discussions, and working with me to complete my projects at Los Alamos National Laboratory. Each of your presences made going to work immensely enjoyable and I have learned more from all of you than any textbook could hope to impart. I would also like to thank Peter Stark, my Group Leader in the Chemistry Division, Chemical and Engineering Diagnostics Group, for supporting me throughout my time in C-CDE. Additionally, the reason I was able to attend graduate school, and ultimately change the course of my life, is because of Karen McHugh, my former boss at Los Alamos National Laboratory who, upon being asked by me which graduate program she would consider sponsoring, responded with, “Whichever one interests you.” Thank you so much.

I would like to thank my parents, Jodi and Robert Brounstein, for their unconditional love, for being a stable support system, and for always pushing me towards my greatest potential. I would like to thank my brother, Jakob, and sister, Samantha, for sharing my enthusiasm for all of life’s quirks and for always being open to talking at any hour of the day, even if we are thousands of miles apart. Additionally, working through scientific endeavors would not have transpired as readily without the immense love from my extended family, which includes my grandmother and bubby, who cheered me on through highs and lows.

I would like to thank my partner, Lindsey Newman, who has ignited my passion to explore the world and is fervent to adventure with me. As long as our world keeps turning, I can imagine nothing better than traversing its wonders and eating whatever we find along the way. I am infinitely grateful for my friends, Cameron Elwardt, Alex Buettner, Brandon Weiler, Gregg “Old Gregg” Rosenberg, and Johnathan “Twigs” Pietz, and would like to

thank them for keeping me grounded and for helping me become the man I am today. Cameron, I am immensely glad that we have kept such a strong bond across time and space and that we have overcome our inability to play board games by reading the rules beforehand. Alex and Brandon, I hope this dissertation vociferously and unequivocally demonstrates that I can be street smart. I have an idea for our next trip – The Moon & Antarctica. Gregg and Twigs, ΕΣΠΙΟΝΔΑ. I am sure we will all meet in New Mexico someday.

Explorations and Developments in Multifunctionality, 3D Printing, and Accelerated Aging for Thermoplastics and Thermosets

by

Zachary Brounstein

B.S. Mathematics, University of Nevada, Reno, 2016

B.S. Chemical Engineering, University of Nevada, Reno, 2016

M.S. Nanoscience and Microsystems Engineering, University of New Mexico, 2019

Ph.D. Nanoscience and Microsystems Engineering, University of New Mexico, 2021

Abstract

If the world is to progress through the fourth industrial revolution, rapid advances in materials science must complement new technological feats in manufacturing, computation and device functionality, and a broader understanding of how materials behave as they age and degrade. To this effect, much effort has been directed towards polymeric materials to address and solve many problems in this new era. This includes developing polymer composites that incorporate fillers to imbue multifunctionality, fabricating novel formulations for additive manufacturing, and conducting aging studies to assess the performance of these materials over long time spans. Building and expanding on the latest research in these endeavors, this work explores developing novel thermoplastic and thermoset composites for fused filament fabrication and direct ink write 3D printing and evaluates the long-term aging behavior of polymer composite formulations.

Table of Contents

Abstract.....	vii
List of Figures.....	xii
List of Tables	xx
Chapter 1 Introduction.....	1
1.1 3D Printing.....	2
1.2 Radiation Shielding Polymer Composites	4
1.3 Antimicrobial Polymer Composites.....	5
1.4 Polymer Composites as Sensors	6
1.5 Accelerated Aging of Thermosets	7
1.6 Research Conducted in this Work which Expands Current Capabilities.....	11
References	12
Chapter 2 Methods	32
2.1 Instrumentation	32
2.1.1 FTIR.....	32
2.1.2 TGA	33
2.1.3 DSC.....	34
2.1.4 MXRF	35
2.1.5 Mass Spectrometry.....	36
2.1.6 GPC.....	37
2.1.7 Contact Angle	38
2.1.8 CTE.....	39
2.1.9 Thermal Conductivity	39
2.1.10 Mechanical Tests	40
2.1.11 Shore A Hardness	41
2.1.12 Rheology	41
2.2 Methodology.....	42
2.2.1 Filament Composites	42
2.2.2 3D Printing.....	43
2.2.3 Thermal Aging.....	44
2.2.4 Solvent Swelling	45
References	46

Chapter 3 Fused Filament Fabrication of Polymer Composites for Extreme Environments	49
3.1 Introduction.....	49
3.2 Materials and Methods.....	51
3.2.1 Materials	51
3.2.2 Feedstock and Filament Fabrication	52
3.2.3 Gamma Irradiation	53
3.2.4 Characterization Techniques.....	54
3.3 Results and Discussion	57
3.3.1 Chemical Characterization.....	57
3.3.2 Morphological Characterization	59
3.3.3 Thermal Characterization.....	63
3.3.4 Mechanical Properties.....	67
3.3.5 Properties of Multifunctionality.....	70
3.4 Conclusions.....	71
References.....	72
Chapter 4 Development of Antimicrobial PLA Composites for Fused Filament Fabrication.....	78
4.1 Introduction.....	78
4.2 Materials and Methods.....	80
4.2.1 Materials	80
4.2.2 Feedstock and Filament Fabrication	81
4.2.3 Characterization Techniques.....	82
4.2.3.1 Chemical Structure Characterization	82
4.2.3.2 Thermal Characterization.....	83
4.2.3.3 Mechanical Characterization	84
4.2.3.4 Antimicrobial Efficacy.....	85
4.3 Results and Discussion	86
4.3.1 Chemical Structure Characterization	88
4.3.1.1 FTIR.....	88
4.3.1.2 MXRF	90
4.3.2 Thermal Characterization.....	90
4.3.2.1 Thermal Phase Behavior	90

4.3.2.2 Thermal Stability	96
4.3.4 Mechanical Characterization	100
4.3.5 Antimicrobial Efficacy.....	104
4.4 Conclusions.....	106
References.....	107
Chapter 5 Tuning the Thermomechanical Properties of 3D Printed Radiation Shields	116
5.1 Introduction.....	116
5.2 Experimental.....	119
5.2.1 Materials	119
5.2.2 Formulation Development and 3D Printing.....	120
5.2.3 Material Characterization Techniques	122
5.3 Results and Discussion	125
5.3.1 Rheology	125
5.3.2 3D Printing.....	127
5.3.3 Relating Rheology to Printing	129
5.3.4 Thermomechanical Properties	135
5.3.5 Attenuation of Ionizing Radiation	141
5.4 Conclusions.....	143
References.....	145
Chapter 6 3D Printed Chromophoric Sensors	154
6.1 Introduction.....	154
6.2 Experimental.....	156
6.2.1 Materials	156
6.2.2 Formulation Development.....	157
6.2.3 Material Characterization Techniques	159
6.3 Results and Discussion	162
6.3.1 Sensor Performance	162
6.3.2 Sensor Material Characterization.....	168
6.3.3 3D Printing.....	172
6.4 Conclusions.....	174
References.....	176
Chapter 7 Long-Term Thermal Aging of Modified Sylgard 184 Formulations	186

7.1 Introduction.....	186
7.2 Materials and Methods.....	189
7.2.1 Materials	189
7.2.2 Sylgard 184 Formulations.....	189
7.2.3 Thermal Accelerated Aging.....	190
7.2.4 Chemical Characterization Techniques	191
7.2.5 Mechanical Characterization Techniques	195
7.2.6 Thermal Characterization Techniques	196
7.3 Results and Discussion	197
7.3.1 Material Properties of Pristine Samples.....	197
7.3.2 Mechanisms for Aging under Nitrogen	203
7.3.3 Material Properties of Aged Samples	212
7.4 Conclusions.....	217
References.....	219
Chapter 8 Conclusions and Future Work	229
Appendix.....	232

List of Figures

FIGURE 1.1: HYDROSILYLATION REACTION: (A) HOW A SILOXANE WITH A SI-H BOND REACTS WITH A VINYL GROUP IN THE PRESENCE OF A CATALYST AND (B) HOW CROSSLINKING OCCURS BETWEEN TWO POLYDIMETHYL SILOXANE (PDMS) CHAINS... 9	9
FIGURE 3.1: ABS/BI (A) FILAMENT AND (B) PRINTED PADS	53
FIGURE 3.2: (A) FTIR SPECTRA OF PRINTED SAMPLES AND (B) MXRF OF A BI COLOR MAPPING OF ABS/BI 34/66.	58
FIGURE 3.3: (A) FTIR AND MXRF OF (B) PRE- AND (C) POST-IRRADIATED SAMPLES SHOWING AN EVEN DISTRIBUTION OF BISMUTH AND THAT IT DOES NOT CHANGE AFTER IRRADIATION. BECAUSE THE SAMPLES ARE ORIENTED ALONG THE VIEWING AXIS, THE GREEN COLORATION CORRESPONDS TO THE TOP LAYER AND THE BLUER COLORATION CORRESPONDS TO THE DEEPER LAYERS.	59
FIGURE 3.4: USAXS/SAXS PROFILES OF ABS, PVDF, AND BI-FILLED COMPOSITE BLENDS. PROFILES ARE SHIFTED VERTICALLY FOR CLARITY.	60
FIGURE 3.5: DIGITAL MICROSCOPY IMAGES ON THE ORDER OF 100 μm SHOWING PRINTED SAMPLES OF (A) ABS, (B) ABS/BI 34/66, AND (C) ABS/BI/PVDF 25/50/25. EACH RED SCALE BAR IN THE BOTTOM RIGHT OF EACH IMAGE REPRESENTS 100 μm IN THE HORIZONTAL DIRECTION. TO EVALUATE THE ABILITY OF EACH MATERIAL BEING PRINTED AND OBSERVE DISTINCT LAYERS, THE 3D-PRINTED PARTS INCLUDED SOME GAPS AND POROSITY.	63
FIGURE 3.6: DSC OF SAMPLES WITH (A) BI AND (B) PVDF.....	65
FIGURE 3.7: TGA OF (A) PRINTED SAMPLES WITHOUT PVDF AND (B) WITH PVDF.	67

FIGURE 3.8: TENSILE STRESS AND STRAIN FOR (A) 1.75E FILAMENTS AND (B) 0.5P FILAMENTS.....	68
FIGURE 4.1: DIGITAL MICROSCOPY CROSS-SECTION IMAGES OF: (A) PLA/TiO ₂ 90/10; (B) PLA/ZNO 90/10; (C) PLA/TiO ₂ /PEG2K 80/10/10; AND (D) PLA/ZNO/PEG2K 80/10/10.	87
FIGURE 4.2: DIGITAL MICROSCOPY CROSS-SECTION IMAGES OF: (A) PLA/PEG1K 90/10; (B) PLA/PEG2K 90/10; AND (C) PLA/PEG10K 90/10.	88
FIGURE 4.3: FTIR SPECTRA OF PLA (A) WITH 10 WT% CERAMIC FILLERS AND (B) WITH 10 WT% PEG. THE ARROWS CORRESPOND TO PEAKS THAT ARE DETAILED IN TABLE 4.4 BELOW.	89
FIGURE 4.4: MXRF COLOR MAPPING OF: (A) TI IN PLA/TiO ₂ 90/10; (B) ZN IN PLA/ZNO 90/10; (C) TI IN PLA/TiO ₂ /PEG2K 80/10/10; AND (D) ZN IN PLA/ZNO/PEG2K 80/10/10. INCREASING AMOUNTS OF THE INDICATED ELEMENT ARE COLORED FROM BLUE TO GREEN TO RED.....	90
FIGURE 4.5: THERMOGRAMS OF SELECTED FILAMENTS: (A) TGA; (B) DERIVATIVE OF TGA; AND (C) DSC (EXOTHERM UP) OF THE FIRST HEATING CURVE.	93
FIGURE 4.6: CRYSTALLINITY OF FILAMENTS.	95
FIGURE 4.7: THE THERMAL PROPERTIES OF THE COMPOSITE FILAMENTS: (A) THE ONSET OF THERMAL DEGRADATION (T _{D5%}); (B) THE DECOMPOSITION TEMPERATURE (T _{DMAX}); AND (C) THE ACTIVATION ENERGY.	99
FIGURE 4.8: THE MECHANICAL PROPERTIES OF THE COMPOSITE FILAMENTS: (A) MAX STRESS; (B) MAX STRAIN; AND (C) YOUNG'S MODULUS.	103

FIGURE 4.9: MICROSCOPY IMAGES OF STAINED COMPOSITE FILAMENTS THAT WERE INCUBATED IN SOIL FOR A MONTH: (A) PLA; (B) PLA/TiO ₂ 90/10 WITH GELATIN; (C) PLA/ZnO 90/10; AND (D) PLA/ZnO 90/10 WITH GELATIN.	105
FIGURE 5.1: RHEOLOGICAL EXPERIMENTS SHOWING (A) THE STORAGE MODULUS OF THE LINEAR VISCOELASTIC REGION AND BEGINNING OF THE NONLINEAR VISCOELASTIC REGION OF A REPRESENTATIVE SAMPLE OF INK FORMULATIONS, AND (B) THE LOSS AND STORAGE MODULI OF THE W FORMULATION UNTIL THE FLOW POINT.	127
FIGURE 5.2: 3D-PRINTED CYLINDERS OF THE INK FORMULATIONS DETAILED IN THIS STUDY.	128
FIGURE 5.3: POROSITIES OF THE PRINTED FORMULATIONS AT VARYING SPACING RATIOS, WITH MICROSCOPY IMAGES OF WO ₃ AT (A) 500 μM OR H = 2; (B) 750 μM OR H = 3; (C) 1000 μM OR H = 4; AND (D) 1500 μM OR H = 6; AND (E) COMPARING THE POROSITIES OF THE PRINTED SAMPLES ALONG WITH THE THEORETICAL 3D-PRINTED POROSITIES....	129
FIGURE 5.4: SIDE VIEWS COMPARING DEVIATIONS IN PRINTED (A) SiO ₂ AND (B) WO ₃ SAMPLES.	130
FIGURE 5.5: DETERMINING HOW THE STRUCTURE PARAMETERS ARE RELATED TO SPACING RATIOS, WHERE (A) THE THICKNESS DEVIATION IS PLOTTED AGAINST <i>KinkΨlattice</i> , WITH A YELLOW LINE AT THE ONE STANDARD DEVIATION MARK DENOTING WHETHER A PRINT WAS ACCEPTABLE, AND (B) <i>KinkΨlattice</i> PLOTTED AGAINST THE SPACING RATIO ALONG WITH THE MODEL PRESENTING THE UPPER BOUND FOR THE STRUCTURE PARAMETERS.....	134
FIGURE 5.6: USING A 250 MM NOZZLE AND AN FCT GEOMETRY, RHEOLOGY-TESTED INK FORMULATIONS WERE ASSESSED BASED ON THEIR MATERIAL PROPERTIES AND	

THICKNESS DEVIATIONS TO DETERMINE EQUATION (7), WHICH PROVIDES A REGIME FOR PRINTABILITY. VALUES BELOW THE UPPER LIMIT IN EQUATION (7) ARE IN REGION I (GOOD PRINTABILITY), WHICH IS DEFINED AS MINIMAL SLUMPING AND WITHIN ONE STANDARD DEVIATION. VALUES ABOVE THE UPPER LIMIT ARE IN REGION II (POOR PRINTABILITY), WHICH IS DEFINED AS THICKNESS DEVIATIONS ABOVE ONE STANDARD DEVIATION. 134

FIGURE 5.7: MECHANICAL PROPERTIES FROM COMPRESSION TESTING AS FUNCTIONS OF SAMPLE POROSITY: (A) MAXIMUM COMPRESSIVE STRAIN, AND (B) YOUNG’S MODULUS. 136

FIGURE 5.8: THERMAL CONDUCTIVITY OF 50 WT% METAL- AND CERAMIC-FILLED PRINTED CYLINDERS PLOTTED AGAINST (A) POROSITY AND (B) MAXIMUM COMPRESSIVE STRAIN. 137

FIGURE 5.9: TGA CURVES FOR THE 3D-PRINTED CYLINDERS: (A) WEIGHT PERCENT FOR SAMPLES WITHOUT BORON; (B) DERIVATIVE WEIGHT PERCENT FOR SAMPLES WITHOUT BORON; (C) WEIGHT PERCENT FOR SAMPLES WITH BORON; AND (D) DERIVATIVE WEIGHT PERCENT FOR SAMPLES WITH BORON. 140

FIGURE 5.10: 2D RADIOGRAPHS, SUMMED OVER ALL NEUTRON ENERGIES FROM 0.001 TO 100 eV, OF PRINTED SAMPLES. FOR THE FORMULATIONS BESIDES SiO₂, THE TOTAL FILLER CONTENT WAS 50 WT%. LIGHTER IMAGES CORRESPOND TO MORE NEUTRONS PASSING INTO THE DETECTOR, WHILE DARKER IMAGES CORRESPOND TO A GREATER ATTENUATION OF INCOMING NEUTRONS: (A) 50 WT% B^N; (B) OPEN BEAM (NO SAMPLE); (C) 50 WT% Gd₂O₃; (D) 40/10 WT% B^N/Gd₂O₃; (E) 40/10 WT% B¹⁰/Gd₂O₃;

AND (F) 10 WT% SiO_2 . ALL NEUTRON-EXPOSED PADS WERE 3D PRINTED USING 500 UM SPACING.	142
FIGURE 5.11: 3D PRINTING WITH FORMULATIONS OF WO_3 AND Gd_2O_3 (A) IN ONE INK TO CREATE A HOMOGENEOUS PART AND (B) AS SEPARATE INKS TO PRODUCE A HETEROGENEOUS PART.	143
FIGURE 6.1: PRISTINE COMPOSITE PASSIVE ENVIRONMENTAL CHROMOPHORIC SENSORS SEPARATED BY INDICATOR WEIGHT PERCENT (0.5 WT% ON THE LEFT AND 10 WT% ON THE RIGHT OF EACH PHOTO) AND BY THE INITIAL INDICATOR FORM (PAINT-BASED ON THE LEFT AND POWDER-BASED ON THE RIGHT).	163
FIGURE 6.2: COMPARISON OF THE COLOR CHANGES BETWEEN PRISTINE AND EXPOSED COMPOSITE CHROMOPHORIC SENSORS (0.5 WT%).	165
FIGURE 6.3: THE TEMPORAL CHANGE OF BBS184 ONE DAY AFTER EXPOSURE.	165
FIGURE 6.4: UV-VIS SPECTROPHOTOMETRY DATA DEMONSTRATING THE CHROMOPHORIC BEHAVIOR OF THE SENSING DEVICES.	167
FIGURE 6.5: SURFACE SENSING PROPERTIES OF MRS184 AND PPS184. OBSERVE THAT THE SENSORS THEMSELVES DID NOT CHANGE COLOR BUT THE CLEAR LIQUID THAT WAS APPLIED DID.	168
FIGURE 6.6: A 3D PRINTED SENSOR WITH AN FCT STRUCTURE.	173
FIGURE 6.7: COMPARISON OF THE COLOR CHANGES IN SOME OF THE 3D PRINTED SENSORS – THE SENSORS TB184 AND BBS184 EXHIBITED A COLOR CHANGE WHEN CURED AT AN ELEVATED TEMPERATURE BUT IT DID NOT DISRUPT THEIR SENSING ABILITY. ADDITIONALLY, THE POROSITY IN THE 3D PRINTED SENSORS AIDED IN PROVIDING A	

BETTER VISUAL CUE FOR WHEN TBS184 AND MRS184 WERE EXPOSED TO BASIC OR ACIDIC CHEMICAL SPECIES, RESPECTIVELY.	174
FIGURE 7.1: RHEOLOGY OF THE FOUR FORMULATIONS – (A) STORAGE AND LOSS MODULI AND (B) GEL POINT.	198
FIGURE 7.2: SOLVENT SWELLING EXPERIMENTS OF THE PRISTINE SAMPLES IN TOLUENE – (A) SWELLING AND LOSS PERCENT FOR THE FORMULATIONS AND (B) SPECIFIC CROSSLINKING DENSITY ρ_x FOR THE FORMULATIONS	200
FIGURE 7.3: MECHANICAL PROPERTIES OF THE PRISTINE SAMPLES.	201
FIGURE 7.4: THERMAL STABILITY OF THE PRISTINE SAMPLES – (A) TGA CURVES AND (B) DTGA CURVES MAGNIFIED.....	202
FIGURE 7.5: SWELLING OF THE THERMALLY AGED SAMPLES – (A) CONTROL AND (B) OPT2.	204
FIGURE 7.6: MEASURING THE VOLATILE PRODUCTS THAT EVOLVED WHILE UNDERGOING THERMAL ACCELERATED AGING ON A PER MASS OF SYLGARD BASIS: (A) HYDROGEN GENERATION FROM THE CONTROL; (B) HYDROGEN GENERATION FROM OPT2; (C) METHANE GENERATION FROM THE CONTROL; AND (D) METHANE GENERATION FROM OPT2.....	206
FIGURE 7.7: SPECIFIC CROSSLINK DENSITY – (A) CROSSLINKS DUE TO HYDROSILYLATION FOR CONTROL; (B) CROSSLINKS DUE TO HYDROSILYLATION FOR OPT2; (C) WATER FRACTION FOR CONTROL; AND (D) WATER FRACTION FOR OPT2.	209
FIGURE 7.8: TIME-TEMPERATURE SUPERPOSITION MASTER CURVE MODELS OF THE THREE MAJOR EVOLVED GASEOUS PRODUCTS – (A) CONTROL AND (B) OPT2.....	211

FIGURE 7.9: DISCOLORATION OF THE FOUR FORMULATIONS AFTER 12 MONTHS OF THERMAL ACCELERATED AGING.....	213
FIGURE 7.10: TIME-TEMPERATURE SUPERPOSITION MASTER CURVE MODELS OF SHORE A HARDNESS FOR THE FOUR THERMAL ACCELERATED AGED SYLGARD 184 FORMULATIONS.....	216
FIGURE 7.11: LINEAR REGRESSION OF THE THERMALLY AGED SAMPLED – (A) AS A FUNCTION OF AGING TEMPERATURE AND (B) AS A FUNCTION OF AGING TIME.....	217
FIGURE A.1: USAXS AND SAXS PROFILES OF PURE ABS AND ABS/BI COMPOSITES.	232
FIGURE A.2: STORAGE AND LOSS MODULI OF THE RHEOLOGY-TESTED INK FORMULATIONS DURING THE STRESS SWEEPS.	233
FIGURE A.3: FTIR SPECTRA OF FORMULATIONS ALONG WITH THEIR PEAK ASSIGNMENTS.	235
FIGURE A.4: CUMULATIVE MOLAR MASS DISTRIBUTION OF THE EXTRACTS FROM PRISTINE SAMPLES.	236
FIGURE A.5: FTIR ABSORBANCE SPECTRA OF PRISTINE AND 50°C AGED SAMPLES SHOWING PEAKS AT 845 cm^{-1} AND 865 cm^{-1} WHICH CORRESPOND TO SILOXANOL GROUPS (Si-OH) – (A) CONTROL AND (B) 0PT2.....	236
FIGURE A.6: SPECIFIC CROSSLINK DENSITY OF THE THERMALLY AGED SAMPLES – (A) CONTROL; (B) 0PT2; (C) 1PT1; AND (D) 1PT2.....	237
FIGURE A.7: VALIDITY OF THE TTS MODEL FOR MASS SPECTROMETRY DATA, WHERE $\ln(a_T t)$ AND $1/T$ DISPLAY A LINEAR RELATIONSHIP FOR (A) ALL EVOLVED GASES AND (B) HYDROGEN.	237

FIGURE A.8: HYDROGEN GENERATION FOR THE CONTROL AND OPT2 FORMULATIONS.

INCLUDED IS THE SHIFTED DATA AND THE MODEL. FOR THE CONTROL, THE EQUATION IS $n(a_T t) = (4.22 \times 10^{-8})a_T t^{0.7257}$ AND FOR THE OPT2, THE EQUATION IS $n(a_T t) = (1.20 \times 10^{-7})a_T t^{0.5391}$ 238

FIGURE A.9: SHORE A HARDNESS OF THE THERMALLY AGED SAMPLES— (A) CONTROL; (B) OPT2; (C) 1PT1; AND (D) 1PT2..... 239

FIGURE A.10: VALIDITY OF THE TTS MODEL FOR SHORE A HARDNESS DATA, WHERE $\ln(a_T t)$ AND $1/T$ DISPLAY A LINEAR RELATIONSHIP FOR ALL THE MODIFICATIONS. 240

List of Tables

TABLE 3.1: UNIFIED FIT PARAMETERS EXTRACTED FROM SCATTERING PROFILES OF ABS/PVDF/BI COMPOSITE BLENDS.....	62
TABLE 3.2: MELTING AND CRYSTALLINITY OF SAMPLES WITH PVDF.....	65
TABLE 3.3: MECHANICAL PROPERTIES FOR THE 1.75E AND 0.5P FILAMENTS.	67
TABLE 4.1: LIST OF THE COMPOSITE FILAMENTS MADE IN THIS STUDY AND THEIR DESIGNATIONS.	82
TABLE 4.2: AVERAGE AND STANDARD DEVIATIONS OF D10, D50, AND D90 PARTICLE SIZE DISTRIBUTIONS FOR EACH PROCEDURE OF ZNO POWDER.	86
TABLE 4.3: AVERAGE AND STANDARD DEVIATIONS OF D10, D50, AND D90 PARTICLE SIZE DISTRIBUTIONS FOR EACH PROCEDURE OF TiO ₂ POWDER.	86
TABLE 4.4: FTIR PEAKS ASSOCIATED WITH THE SPECTRA OF PLA IN FIGURE 4.3.....	89
TABLE 4.5: THERMAL PHASE TRANSITIONS AND CRYSTALLINITY OF THE COMPOSITE FILAMENTS.....	95
TABLE 4.6: THERMAL STABILITY OF THE COMPOSITE FILAMENTS (DECOMPOSITION VALUES TAKE FROM 5°C/MIN AND THERMAL KINETIC PARAMETERS TAKEN FROM 15°C/MIN). 99	99
TABLE 4.7: MECHANICAL PROPERTIES OF THE COMPOSITE FILAMENTS.....	103
TABLE 5.1: THE FORMULATIONS DEVELOPED AND THEIR DENSITIES ALONG WITH THE WEIGHT AND VOLUME PERCENT OF EACH FILLER COMPONENT.	126
TABLE 5.2: RHEOLOGICAL PROPERTIES OF A REPRESENTATIVE SAMPLE OF INK FORMULATIONS.....	127
TABLE 5.3: INK PARAMETERS FOR THE RHEOLOGICAL-TESTED INK FORMULATIONS AND THEIR MAXIMUM SPACING RATIOS ACCORDING TO EQUATION 5.7.	135

TABLE 5.4: THERMAL STABILITY PROPERTIES OF THE 3D-PRINTED FORMULATIONS.....	140
TABLE 6.1: SOLUTION pH AND COLORS ASSOCIATED WITH THE POWDER INDICATORS IN THIS STUDY.....	157
TABLE 6.2: NOTATION OF THE PASSIVE ENVIRONMENTAL CHROMOPHORIC SENSORS USED IN THIS STUDY AND THEIR COMPONENTS.	158
TABLE 6.3: SOLVENT SWELLING PROPERTIES AND SHORE A HARDNESS OF THE 0.5 WT% COMPOSITE CHROMOPHORIC SENSORS COMPARED TO SYLGARD 184.	170
TABLE 6.4: THERMAL PROPERTIES OF THE 0.5 WT% COMPOSITE CHROMOPHORIC SENSORS COMPARED TO SYLGARD 184.....	172
TABLE 7.1: THE FORMULATIONS OF SYLGARD 184 USED IN THIS STUDY.....	190
TABLE 7.2: FINAL MECHANICAL PROPERTIES OF THE FOUR SYLGARD 184 FORMULATIONS.	215
TABLE A.1: TIME-TEMPERATURE SUPERPOSITION SHORE A HARDNESS MASTER CURVE MODEL PARAMETERS.....	239

Chapter 1 Introduction

Polymers are macromolecular structures built from smaller units that are chemically bonded together. Although humans have been unknowingly exploiting the properties of polymers since the dawn of civilization in the form of starches, proteins, wool, silk, and more, it was not until 1920 that the modern concept was developed and thus began the rapid expansion of theoretical and experimental work [1, 2]. Today, natural and synthetic polymers are ubiquitous and can be found as plastics [3, 4], sealants [5, 6], potting and encapsulating compounds [7, 8], conductive electronics and solar cells [9-14], and many high-tech and high-performance materials [15-20]. To better understand the materials science, physics, and general applications of different polymers, a variety of classification schemes have been developed, spanning types of polymerization, source material, structure of the monomer unit, and more.

In the broadest sense, all polymers can be divided into two categories: thermoplastics can undergo reversible phase transitions upon heating and cooling and thermosets undergo an irreversible curing, creating a crosslinked network formed through chemical bonds between individual polymer strands [21, 22]. This classification scheme is useful because the thermal behaviors of the two types are distinct; thermoplastics can be remolded at high temperatures whereas thermosets cannot. During the process of exploring new and existing materials for a particular application, focus is generally directed into only one of polymer classes.

1.1 3D Printing

As the world enters the fourth industrial revolution, new manufacturing methods and techniques are being developed and perfected [23, 24]. Referred to as advanced manufacturing, many nascent branches under this broad technology space are swiftly transforming commercially viable applications. One of the fastest growing classes of this technology is additive manufacturing, where parts are fabricated in a layer-by-layer fashion, and as such is commonly called 3D printing [25-29]. One 3D printing technique, referred to as Fused Filament Fabrication (FFF), heats thermoplastic filaments above their melting point (or glass transition temperature if a polymer is amorphous) and extrudes the softened material through a nozzle onto a bed, where the filament cools down slowly enough to adhere to the layers placed below and above it. There is a similar technique for thermosets called Direct Ink Write (DIW) that utilize non-Newtonian fluids to 3D print. Both of these 3D printing technologies, defined in the ISO/ASTM 52900:2015 standard as material extrusion techniques [30], are versatile, promising, and used by companies, researchers, and hobbyists across the globe.

Despite the intense demand and focus directed at these 3D printing technologies and additive manufacturing in a broader sense, there are still many limitations to overcome if the field of manufacturing is to undergo a revolution in progress. One of the most serious limitations is the narrowness of the materials library [25, 31]. For FFF, the thermoplastic filaments must possess a thermal phase transition in the temperature range of standard 3D printers or else modifications or an entirely new print setup will be required. Additionally, the filaments must possess a low coefficient of thermal expansion if the final 3D printed parts are to maintain their desired shape and not warp or deform as the successive layers

cool down. For DIW, the thermosetting ink must possess a large storage modulus so that lower layers can support themselves as more layers are printed above. If the storage modulus is too low, the print will flatten and spread out, deforming the part at best and making the making the entire part unprintable at worst. This phenomenon is tied to another requirement for DIW 3D printable inks – that the yield stress is within the range of the 3D printer. Similar to the temperature specifications for FFF filaments, a yield stress that is too high will necessitate a 3D printer to be retrofitted or built anew. Thus, one area of research into these technologies is to expand the materials library and ultimate applicability of additive manufacturing.

That is not to say that FFF filaments for general or specialty applications do not exist. Industry, research, and recreational usage commonly employs traditional single-component filaments such as acrylonitrile butadiene styrene (ABS), poly(lactic acid) (PLA), poly(ethylene terephthalate) (PET), and nylon due to their broadly favorable thermal and mechanical build properties [32-36]. Specialty and high-performance thermoplastic filaments include poly(ether sulfone) (PES), poly(ether ether ketone) (PEEK), bronze or metal-infused polymers, and carbon fiber-infused polymers *inter alia* [33, 37-42]. These and other thermoplastics are currently being researched and used in the development of more advanced filament compositions for high-tech applications. Examples include using poly(vinylidene difluoride) (PVDF) or ABS with barium titanate to make piezoelectric materials [43-45] and ABS with iron or copper to increase the thermal conductivity while reducing the coefficient of thermal expansion [36, 46, 47]. While these developments are being sought from space and civil construction projects to automotive and energy programs, FFF will become a more feasible manufacturing method

when a greater amount of complex compositions, which combine multiple functional components into a single filament, is available.

In a similar fashion, many researcher groups are investigating new materials for DIW 3D printing in order to expand its capability. An advantage of developments in this technique is that as long as a shear-thinning fluid can be cured or remain rigid, it is possible to use. Additionally, the rheological properties of an ink formulation can be tuned with various fillers so as to make a wider variety of materials capable of being 3D printed. Advancements in DIW ink formulations include using ceramics and carbonaceous materials to develop aerogels and foams [48-51] and metal and metal complexes for magneto-responsive parts[52-54], among many others. Thanks to Dow Corning's SE 1700 resin, a large set of DIW ink formulations use elastomeric siloxanes as the polymer network due to its ease of UV or heat-induced curing. Indeed, because curing siloxanes can be controlled via the hydrosilylation reaction and the inert nature of siloxanes allows for a range of filler particles to be incorporated and imbue additional material properties, an extensive body of work exists that explores this class of ink formulations.

1.2 Radiation Shielding Polymer Composites

Despite being well into the atomic age, radiation shielding materials and methods still necessitates progress in order to protect personnel, equipment, and/or instrumentation. While better protection of personnel is an obvious goal, equipment and instrumentation can also experience large amounts of bit flipping, embrittlement, or degradation when exposed to high levels of gamma or neutron radiation, and as such also require radiation shielding [55-62]. In the effort to lessen the effect of radiation damage to materials, extensive

research has been performed on known radiation attenuating elements and compounds to develop composites that can better be used for protection [63-68].

Applying these techniques to fabricating filaments or inks has also been investigated [69-71], however the weight percent loading of radiation shielding material has been low (less than 25% (w/w)). This is due to higher amounts causing poor print quality in the form of part warping or insufficient interlayer adhesion. For example, bismuth and tungsten have been used for gamma ray shielding, and boron nitride and boron carbide have been used for neutron radiation shielding, however the weight percent loading rarely exceeds 25% (w/w), resulting in 3D printed parts that can only provide sufficient attenuation at low radiation doses [70, 72-74]. In addition to research efforts currently focused on developing composite filaments possessing low amounts of radiation shielding filler material, there has not been much focus directed towards investigating multifunctionality. This includes being able to attenuate multiple types of radiation, possessing additional material properties such as chemical resistance, or using multiple materials to print heterogeneous parts. Thus, significant research and development is necessary to develop high-quality multifunctional filaments for FFF and DIW that will provide improved capability towards attenuating ionizing radiation.

1.3 Antimicrobial Polymer Composites

Spanning from the medical community in the form of medical implants and prostheses to the agricultural industry in the form of packaging and appliances, there are many polymers currently in use that are exposed to a wide variety of different microorganisms and as such represent a weak point in the supply chain from producer to consumer. One heavily relied upon polymer, PLA, is gaining popularity due to it being

biocompatible, compostable, having desirable mechanical and physical properties, and being able to be produced from renewable resources [34, 75-77]. PLA is used frequently in the medical and agriculture industries; however, one large bottleneck is that it decomposes when exposed to bacteria, fungi, viruses, and other microorganisms [78, 79]. Much work has been done on solving this problem by combining PLA with bactericides such as the ceramics ZnO and TiO₂, although composites of this form have not been thoroughly explored in the realm of FFF [80-88]. Indeed, other composites have been used to develop antimicrobial FFF filaments [89, 90], so this area remains to be investigated further. An additional problem that may have contributed to the dearth of research into PLA/ceramic composite filaments is the fact that the mechanical properties of PLA, which are necessary for its feasibility, become stiffer and more brittle when ceramics are incorporated. Thus, plasticizers and other compounds would need to be investigated for their ability to not only tune the mechanical properties of the composite, but to maintain or improve the biodegradability of PLA [91-93].

1.4 Polymer Composites as Sensors

In the past, human perception and action were required to detect if a change in the environment necessitated modifying behaviors, structures, or expectations. This includes observing weather patterns and events to plan short-term and long-term schedules, recognition of acute or chronic pain patterns in themselves and others to treat maladies, and evaluating stores of agricultural and livestock products in societal structure and well-being *inter alia*. With the current advances in materials science and technology, these active human perceptions and actions have been delegated with greater precision and accuracy to the realm of sensors and sensing devices. These comprise large sensors such

as satellites to track farming and migratory patterns as well as small sensors such as wearable monitors to measure glucose levels for people with diabetes. Increasingly, companies and research groups are developing more sophisticated technologies in the realm of small sensors to detect changes a wide variety of physical phenomenon ranging from electric current to relative humidity to local acceleration. These devices then proceed to measure and solely report data on the incredibly local environment or trigger a response in another device to act upon the measurements.

While there are many sensors and alarms setup in areas where hazardous operations take place, serious risks still exist with regards to long-term performance and conditions of equipment and instrumentations. This includes material wear in high-pressure pipes on oil rigs, air monitors in chemical manufacturing plants, and sealed drums used to store nuclear material. The last example is especially relevant due to the gap measured in years that could occur between individual inspections, where the intense rise in internal pressure and temperature or accumulation of harsh acidic or basic chemical species could pose a severe threat to personnel safety. To better prevent an accident occurring, work on developing devices that sense these conditions and alert personnel should be performed. Furthermore, for such a sensor to be successful, it would need to possess a long lifespan, function continuously and passively, and demonstrate a visual cue in order to protect people in situations with inherent risk.

1.5 Accelerated Aging of Thermosets

Thermosetting polymers provide manifold advantages over thermoplastics for many modern applications requiring materials that can withstand higher temperature ranges, are chemically inert, retain their shape upon mechanical deformations, and exhibit

tolerances against corrosive and electric environments [22, 94-98]. Indeed, common thermosetting resins such as epoxies, polyurethanes, polyimides, and silicones possess these desirable properties and are used as barriers in construction [99, 100], potting or encapsulants in microelectronics[101-104], and coatings in the automotive and aerospace realms [105-109]. Some thermosetting resins, such as epoxy and polysiloxanes, are separated into two parts, called prepolymers and hardeners, for ease of application and curing. These “potting” elastomers (referred to as such due to their hyperelasticity and use as encapsulating components to immobilize materials) are wide-spread throughout many different industries and often tailored to fit their application. Examples of applications that use potting materials include those mentioned above: sealants, adhesives, coatings, electrical insulators, flexible moldings, foam stabilizing agents, and water proofing *inter alia*. Methods for optimizing these potting materials include changing the ratio at which the prepolymer and hardener are combined and incorporating filler materials to enhance existing properties or provide entirely new characteristics [110-117].

One of the defining attributes separating thermosets from thermoplastics, the chemical curing of the polymer network, has been researched from this perspective of altering the prepolymer and hardener ratio as well as adding filler materials into the formulation. The reason for the copious amount of research into the curing behavior, especially of the Sylgard™ series (Sylgard™ 182, 184, and 186), which are commercial high-performance polysiloxane rubbers, is due to the working time of the polymeric material. The working time is defined as the time from application until the gel point, when the network has crosslinked across the entire substance and can no longer be readily molded into a different geometry. For systems where the potting material simply needs to

keep everything immobile and the components are not sensitive to heat, a common practice is to first apply the two-part thermoset and then subject the entire structure to high temperatures on the order between 50°C and 200°C [118-122]. A hydrosilylation reaction, where Si-H groups interact with vinyl moieties, occurs in the heating step and is responsible for crosslinking the polymer matrix [123]. This crosslinking reaction accelerates in the presence of a catalyst, causing the gel point to be reached on a much shorter time scale. An example of the hydrosilylation reaction is presented in Figure 1.1. While this is a feasible method to shorten the working time, a significant limitation is observed for heat-sensitive. In this regard, finding methods to accelerate room-temperature curing would provide vast improvements to current technology.

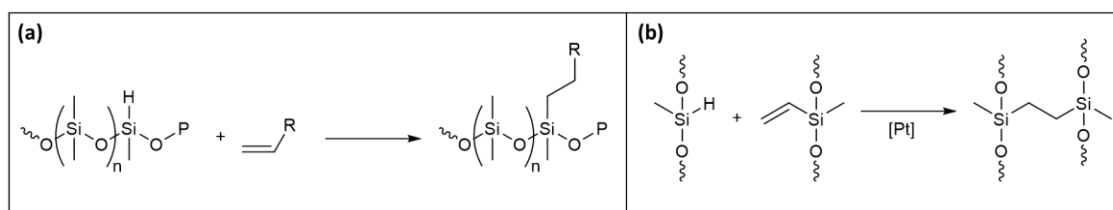


Figure 1.1: Hydrosilylation reaction: (a) how a siloxane with a Si-H bond reacts with a vinyl group in the presence of a catalyst and (b) how crosslinking occurs between two polydimethyl siloxane (PDMS) chains

In addition to curing, research has been performed on using fillers to imbue new attributes to thermosetting elastomers. One such polymer, poly(dimethyl siloxane) (PDMS), has been heavily explored because of the ease to further modify an already desirable polymeric system. Examples include incorporating graphene to make sensors [124-126], fumed silica to alter hydrophobicity for coatings and biomedical applications [127-129], and metal compounds to improve batteries and fuel cells [130-135]. Because of

its ease of application in a variety of scenarios, PDMS (commonly purchased as Sylgard™) could feasibly be used as a broad-based and benign environmental sensor. This is due to the chemically inert nature of Sylgard™, so a compound that reacts with an external stimuli, especially one that changes color, can be used to make a Sylgard™ composite. This composite material could act as a passive and inert indicator, alerting personnel if a hazard presents an immediate risk. Some work has been done in this realm, however an emphasis placed on easy-to-acquire compounds and simple formulation development would expand the applicability and ubiquity of Sylgard™ composite sensors, where the material could be fabricated as needed without advanced technical abilities and avoid logistical issues.

The final major concern with high-performance thermosetting elastomers, specifically Sylgard™, is their aging behavior. Understanding how a material will fail and predicting performance over a material's lifetime is still an active area of research [136-142]. Both short-term and long-term aging behaviors have been investigated on various types of Sylgard™, however experiments involving shorter time periods have been more thoroughly researched [118, 143-145].

One way to bridge this gap is by linking aging and material performance via assuming Arrhenius behavior. Marrying experimental and theoretical work, as this theory does, relies on performing accelerated aging. Accelerated aging is accomplished by exposing materials to environments with heightened levels of external degradation-causing stimuli. This includes environments with increased temperatures, acidic chemical species, UV or ionizing radiation, and other factors many levels above what would be present in normal operating conditions. Arrhenius behavior depends on the assumption that the

mechanism responsible for a material aging due to a specific factor is exponential with respect to that factor and can be described solely by it. Although it is empirical in theory and a rough approximation in practice, it is still of great use. Arrhenius behavior has allowed for the creation of the chemists' heuristic regarding reaction rates (the kinetics of reaction double for every temperature increase of ten degrees Celsius) [139, 146], synergistic modeling of multiple mechanistic effects such as gamma radiation and elevated temperature [140], and ultimately evaluating years of aging using much shorter time frames. To this end, the material performance of Sylgard™ and its composites after months and years can be studied in reduced time periods using thermal accelerated aging.

1.6 Research Conducted in this Work which Expands Current Capabilities

This body of work contains research exploring various methods to develop multifunctional thermoplastic and thermoset composites as well as investigating and modelling the aging behavior of some modified thermoset formulations. To expand the materials library for FFF 3D printing, multifunctional thermoplastic composites were developed using a solvent casting method, which demonstrated that a high loading of filler content is possible while still being able to make a filament that is 3D printable. Radiation shielding and antimicrobial filaments were created and their efficacies were tested via ionizing radiation exposure and aging in soil, respectively.

Sensing devices were explored by using a high-performance thermoset and incorporating various chromophoric indicators that changed color depending on whether the surrounding environment increased in temperature or experienced a change in pH. These sensors were created using a traditional manufacturing method, molding, as well as the additive manufacturing method of DIW 3D printing. Both methods led to promising

results that could ultimately protect workers, however the DIW 3D printed sensors exhibited an increased distinction between pristine and exposed samples, which is more desirable when developing engineered controls that prevent hazards from inflicting harm. Building off of the DIW work, ink formulations were developed that behave as radiation shields and their material properties were assessed. Finally, the same high-performance thermoset used in the sensors was modified to accelerate the room-temperature curing behavior and underwent thermal accelerated aging. Material properties were tested before, during, and after aging to develop models on how this polymer performed throughout its lifespan.

Taking this body of research as a whole into the broader context of polymer composites and materials science, the overall materials library for 3D printing has expanded and a roadmap can be derived to further increase the amount of compounds that can feasibly be used within the additive manufacturing domain. Additionally, aging models were explored to demonstrate how a ubiquitous thermoset, spanning industries from microelectronics and lab-on-chip devices to medical and monitoring appliances, performs over a long period of time and if any behaviors should be of concern.

References

1. Staudinger, H., Über polymerisation. *Berichte der deutschen chemischen Gesellschaft (A and B Series)* 1920, 53 (6), 1073-1085.
2. Feldman, D., Polymer history. *Designed monomers and polymers* 2008, 11 (1), 1-15.
3. Andrady, A. L., *Plastics and the Environment*. John Wiley & Sons: 2003.

4. Andrady, A. L.; Neal, M. A., Applications and societal benefits of plastics. *Philosophical Transactions of the Royal Society B: Biological Sciences* 2009, 364 (1526), 1977-1984.
5. Cole, R. C. In *Epoxy sealant for combating well corrosion*, SPE Oilfield and Geothermal Chemistry Symposium, Society of Petroleum Engineers: 1979.
6. Ding, H.; Xia, C.; Wang, J.; Wang, C.; Chu, F., Inherently flame-retardant flexible bio-based polyurethane sealant with phosphorus and nitrogen-containing polyurethane prepolymer. *Journal of Materials Science* 2016, 51 (10), 5008-5018.
7. Faheem, F. F.; Gupta, K. C.; Lee, Y.-C., Flip-chip assembly and liquid crystal polymer encapsulation for variable MEMS capacitors. *IEEE transactions on microwave theory and techniques* 2003, 51 (12), 2562-2567.
8. Davis, J.; Rees, D.; Riley, I., Silicone encapsulating and potting materials. *Proceedings of the IEE-Part B: Electronic and Communication Engineering* 1962, 109 (21S), 266-270.
9. Li, G.; Zhu, R.; Yang, Y., Polymer solar cells. *Nature photonics* 2012, 6 (3), 153-161.
10. Zhao, W.; Qian, D.; Zhang, S.; Li, S.; Inganäs, O.; Gao, F.; Hou, J., Fullerene-free polymer solar cells with over 11% efficiency and excellent thermal stability. *Advanced materials* 2016, 28 (23), 4734-4739.
11. Kumar, D.; Sharma, R., Advances in conductive polymers. *European polymer journal* 1998, 34 (8), 1053-1060.
12. Shi, Y.; Peng, L.; Ding, Y.; Zhao, Y.; Yu, G., Nanostructured conductive polymers for advanced energy storage. *Chemical Society Reviews* 2015, 44 (19), 6684-6696.

13. Bendikov, M.; Wudl, F.; Perepichka, D. F., Tetrathiafulvalenes, oligoacenes, and their buckminsterfullerene derivatives: the brick and mortar of organic electronics. *Chemical reviews* 2004, 104 (11), 4891-4946.
14. Margolis, J., *Conductive polymers and plastics*. Springer Science & Business Media: 2012.
15. Friedrich, K.; Sue, H.; Liu, P.; Almajid, A., Scratch resistance of high performance polymers. *Tribology International* 2011, 44 (9), 1032-1046.
16. Swager, T. M., Iptycenes in the design of high performance polymers. *Accounts of chemical research* 2008, 41 (9), 1181-1189.
17. Robeson, L.; Burgoyne, W.; Langsam, M.; Savoca, A.; Tien, C., High performance polymers for membrane separation. *Polymer* 1994, 35 (23), 4970-4978.
18. Hickner, M. A.; Ghassemi, H.; Kim, Y. S.; Einsla, B. R.; McGrath, J. E., Alternative polymer systems for proton exchange membranes (PEMs). *Chemical reviews* 2004, 104 (10), 4587-4612.
19. Kim, J. S.; Reneker, D. H., Polybenzimidazole nanofiber produced by electrospinning. *Polymer Engineering & Science* 1999, 39 (5), 849-854.
20. Meguid, S.; Sun, Y., On the tensile and shear strength of nano-reinforced composite interfaces. *Mater Design* 2004, 25 (4), 289-296.
21. Biron, M., *Thermoplastics and thermoplastic composites*. William Andrew: 2018.
22. Biron, M., *Thermosets and composites*. Elsevier: 2003.
23. Schwab, K., *The fourth industrial revolution*. Currency: 2017.

24. Yin, Y.; Stecke, K. E.; Li, D., The evolution of production systems from Industry 2.0 through Industry 4.0. *International Journal of Production Research* 2018, 56 (1-2), 848-861.
25. Thompson, M. K.; Moroni, G.; Vaneker, T.; Fadel, G.; Campbell, R. I.; Gibson, I.; Bernard, A.; Schulz, J.; Graf, P.; Ahuja, B.; Martina, F., Design for Additive Manufacturing: Trends, opportunities, considerations, and constraints. *Cirp Ann-Manuf Techn* 2016, 65 (2), 737-760.
26. Maiyar, L. M.; Singh, S.; Prabhu, V.; Tiwari, M. K., Part segregation based on particle swarm optimisation for assembly design in additive manufacturing. *Int J Comput Integ M* 2019, 32 (7), 705-722.
27. Dizon, J. R. C.; Espera, A. H.; Chen, Q. Y.; Advincula, R. C., Mechanical characterization of 3D-printed polymers. *Addit Manuf* 2018, 20, 44-67.
28. Szentmiklosi, L.; Maroti, B.; Kis, Z.; Janik, J.; Horvath, L. Z., Use of 3D mesh geometries and additive manufacturing in neutron beam experiments. *J Radioanal Nucl Ch* 2019, 320 (2), 451-457.
29. Attaran, M., The rise of 3-D printing: The advantages of additive manufacturing over traditional manufacturing. *Bus Horizons* 2017, 60 (5), 677-688.
30. Tamburrino, F.; Barone, S.; Paoli, A.; Razonale, A., Post-processing treatments to enhance additively manufactured polymeric parts: a review. *Virtual and Physical Prototyping* 2021, 16 (2), 221-254.
31. Levy, G. N.; Schindel, R.; Kruth, J.-P., Rapid manufacturing and rapid tooling with layer manufacturing (LM) technologies, state of the art and future perspectives. *CIRP annals* 2003, 52 (2), 589-609.

32. Abbott, A.; Tandon, G.; Bradford, R.; Koerner, H.; Baur, J., Process-structure-property effects on ABS bond strength in fused filament fabrication. *Addit Manuf* 2018, 19, 29-38.
33. Rohde, S.; Cantrell, J.; Jerez, A.; Kroese, C.; Damiani, D.; Gurnani, R.; DiSandro, L.; Anton, J.; Young, A.; Steinbach, D., Experimental characterization of the shear properties of 3D-printed ABS and polycarbonate parts. *Experimental Mechanics* 2018, 58 (6), 871-884.
34. Wang, L.; Gramlich, W. M.; Gardner, D. J., Improving the impact strength of Poly (lactic acid)(PLA) in fused layer modeling (FLM). *Polymer* 2017, 114, 242-248.
35. Wojtyła, S.; Klama, P.; Baran, T., Is 3D printing safe? Analysis of the thermal treatment of thermoplastics: ABS, PLA, PET, and nylon. *Journal of occupational and environmental hygiene* 2017, 14 (6), D80-D85.
36. Wang, X.; Jiang, M.; Zhou, Z.; Gou, J.; Hui, D., 3D printing of polymer matrix composites: A review and prospective. *Composites Part B: Engineering* 2017, 110, 442-458.
37. Yang, C.; Tian, X.; Li, D.; Cao, Y.; Zhao, F.; Shi, C., Influence of thermal processing conditions in 3D printing on the crystallinity and mechanical properties of PEEK material. *Journal of Materials Processing Technology* 2017, 248, 1-7.
38. Zaldivar, R.; Witkin, D.; McLouth, T.; Patel, D.; Schmitt, K.; Nokes, J., Influence of processing and orientation print effects on the mechanical and thermal behavior of 3D-Printed ULTEM® 9085 Material. *Addit Manuf* 2017, 13, 71-80.
39. Byberg, K. I.; Gebisa, A. W.; Lemu, H. G., Mechanical properties of ULTEM 9085 material processed by fused deposition modeling. *Polym Test* 2018, 72, 335-347.

40. Jahangir, M.; Billah, K.; Lin, Y.; Roberson, D.; Wicker, R.; Espalin, D., Reinforcement of material extrusion 3D printed polycarbonate using continuous carbon fiber. *Addit Manuf* 2019, 28, 354-364.
41. Stepashkin, A.; Chukov, D.; Senatov, F.; Salimon, A.; Korsunsky, A.; Kaloshkin, S., 3D-printed PEEK-carbon fiber (CF) composites: Structure and thermal properties. *Composites Science and Technology* 2018, 164, 319-326.
42. Zhansitov, A. A.; Khashirova, S. Y.; Slonov, A. L.; Kurdanova, Z. I.; Shabaev, A. S.; Khashirov, A. A.; Mikitaev, A. K., Development of technology of polysulfone production for 3D printing. *High Performance Polymers* 2017, 29 (6), 724-729.
43. Chen, C.; Wang, X.; Wang, Y.; Yang, D.; Yao, F.; Zhang, W.; Wang, B.; Sewvandi, G. A.; Yang, D.; Hu, D., Additive manufacturing of piezoelectric materials. *Advanced Functional Materials* 2020, 30 (52), 2005141.
44. Castles, F.; Isakov, D.; Lui, A.; Lei, Q.; Dancer, C.; Wang, Y.; Janurudin, J.; Speller, S.; Grovenor, C.; Grant, P. S., Microwave dielectric characterisation of 3D-printed BaTiO₃/ABS polymer composites. *Scientific reports* 2016, 6 (1), 1-8.
45. Kim, H.; Fernando, T.; Li, M.; Lin, Y.; Tseng, T.-L. B., Fabrication and characterization of 3D printed BaTiO₃/PVDF nanocomposites. *Journal of Composite Materials* 2018, 52 (2), 197-206.
46. Nikzad, M.; Masood, S. H.; Sbarski, I., Thermo-mechanical properties of a highly filled polymeric composites for fused deposition modeling. *Mater Design* 2011, 32 (6), 3448-3456.
47. Hwang, S.; Reyes, E. I.; Moon, K.-s.; Rumpf, R. C.; Kim, N. S., Thermo-mechanical characterization of metal/polymer composite filaments and printing parameter study

- for fused deposition modeling in the 3D printing process. *Journal of Electronic Materials* 2015, 44 (3), 771-777.
48. Liu, D.; Chen, C.; Zhou, Y.; Bao, Y.; Wang, R.; Liu, Y.; He, S.; Huang, H.; Zhang, C.; Foster, B.; Li, T.; Hu, L., 3D-Printed, High-Porosity, High-Strength Graphite Aerogel. *Small Methods* 2021, 5 (7), 2001188.
49. Chandrasekaran, S.; Yao, B.; Liu, T.; Xiao, W.; Song, Y.; Qian, F.; Zhu, C.; Duoss, E. B.; Spadaccini, C. M.; Li, Y.; Worsley, M. A., Direct ink writing of organic and carbon aerogels. *Materials Horizons* 2018, 5 (6), 1166-1175.
50. Li, V. C.-F.; Dunn, C. K.; Zhang, Z.; Deng, Y.; Qi, H. J., Direct Ink Write (DIW) 3D Printed Cellulose Nanocrystal Aerogel Structures. *Scientific Reports* 2017, 7 (1), 8018.
51. Minas, C.; Carnelli, D.; Tervoort, E.; Studart, A. R., 3D Printing of Emulsions and Foams into Hierarchical Porous Ceramics. *Advanced Materials* 2016, 28 (45), 9993-9999.
52. Compton, B. G.; Kemp, J. W.; Novikov, T. V.; Pack, R. C.; Nlebedim, C. I.; Duty, C. E.; Rios, O.; Paranthaman, M. P., Direct-write 3D printing of NdFeB bonded magnets. *Materials and Manufacturing Processes* 2018, 33 (1), 109-113.
53. Bastola, A. K.; Paudel, M.; Li, L., Development of hybrid magnetorheological elastomers by 3D printing. *Polymer* 2018, 149, 213-228.
54. Erkoc, P.; Odeh, Y. N.; Alrifai, N.; Zirhli, O.; Gunduz Akdogan, N.; Yildiz, B.; Misirlioglu, I. B.; Akdogan, O., Photocurable pentaerythritol triacrylate/lithium phenyl-2,4,6-trimethylbenzoylphosphinate-based ink for extrusion-based 3D printing

- of magneto-responsive materials. *Journal of Applied Polymer Science* 2020, 137 (35), 49043.
55. Tazi, F. Z.; Thibeault, C.; Savaria, Y.; Pichette, S.; Audet, Y., On extra delays affecting I/O blocks of an SRAM-Based FPGA due to ionizing radiation. *IEEE Transactions on Nuclear Science* 2014, 61 (6), 3138-3145.
56. Cellere, G.; Paccagnella, A., A review of ionizing radiation effects in floating gate memories. *IEEE Transactions on Device and Materials Reliability* 2004, 4 (3), 359-370.
57. Platonov, P.; Nikolaev, Y. A.; Shtrombakh, Y. I., Radiation embrittlement kinetics of the first generation of VVER-440 RVPs after post-irradiation annealing. *International journal of pressure vessels and piping* 2002, 79 (8-10), 643-648.
58. Fisher, W. K.; Corelli, J., Effect of ionizing radiation on the chemical composition, crystalline content and structure, and flow properties of polytetrafluoroethylene. *Journal of Polymer science: Polymer chemistry edition* 1981, 19 (10), 2465-2493.
59. Harries, D.; Barton, P.; Wright, S. In Effects of neutron spectrum and dose rate on radiation hardening and embrittlement in steels, *Symposium on Radiation Effects on Metals and Neutron Dosimetry*, ASTM International: 1963.
60. Clough, R.; Gillen, K., Polymer degradation under ionizing radiation: The role of ozone. *Journal of Polymer Science Part A: Polymer Chemistry* 1989, 27 (7), 2313-2324.
61. Golden, J.; Hazell, E., Degradation of a polycarbonate by ionizing radiation. *Journal of Polymer Science Part A: General Papers* 1963, 1 (5), 1671-1686.

62. Dumont, J. H.; Talley, S. J.; Geller, D.; Murphy, E. C.; Brounstein, Z. R.; Labouriau, A.; Lee, K.-S., Degradation of sPVC and Aromatic Polyether Urethane Bags Used in Nuclear Applications.
63. Cao, D.; Ge, Y.; Bourham, M.; Moneghan, D., Gamma radiation shielding properties of poly (methyl methacrylate)/Bi₂O₃ composites. *Nuclear Engineering and Technology* 2020.
64. Harrison, C.; Weaver, S.; Bertelsen, C.; Burgett, E.; Hertel, N.; Grulke, E., Polyethylene/boron nitride composites for space radiation shielding. *Journal of applied polymer science* 2008, 109 (4), 2529-2538.
65. Abdo, A. E.-S.; Ali, M.; Ismail, M., Natural fibre high-density polyethylene and lead oxide composites for radiation shielding. *Radiat Phys Chem* 2003, 66 (3), 185-195.
66. Zhong, W.; Sui, G.; Jana, S.; Miller, J., Cosmic radiation shielding tests for UHMWPE fiber/nano-epoxy composites. *Composites Science and Technology* 2009, 69 (13), 2093-2097.
67. Nambiar, S.; Yeow, J. T., Polymer-composite materials for radiation protection. *ACS applied materials & interfaces* 2012, 4 (11), 5717-5726.
68. Ambika, M.; Nagaiah, N.; Harish, V.; Lokanath, N.; Sridhar, M.; Renukappa, N.; Suman, S., Preparation and characterisation of Isophthalic-Bi₂O₃ polymer composite gamma radiation shields. *Radiat Phys Chem* 2017, 130, 351-358.
69. Fusco, M., *Multilayer Protective Coatings for High-Level Nuclear Waste Storage Containers*. 2016.
70. Ceh, J.; Youd, T.; Mastrovich, Z.; Peterson, C.; Khan, S.; Sasser, T. A.; Sander, I. M.; Doney, J.; Turner, C.; Leevy, W. M., Bismuth Infusion of ABS Enables Additive

- Manufacturing of Complex Radiological Phantoms and Shielding Equipment. Sensors-Basel 2017, 17 (3).
71. Brounstein, Z.; Talley, S.; Dumont, J. H.; Zhao, J.; Lee, K.-S.; Labouriau, A., Fused filament fabrication of polymer composites for extreme environments. *Journal of Materials Research* 2020, 35 (12), 1493-1503.
72. Woosley, S.; Galehdari, N. A.; Kelkar, A.; Aravamudhan, S., Fused deposition modeling 3D printing of boron nitride composites for neutron radiation shielding. *Journal of Materials Research* 2018, 33 (22), 3657-3664.
73. Rennie, A. R.; Engberg, A.; Eriksson, O.; Dalglish, R. M., Understanding neutron absorption and scattering in a polymer composite material. *Nuclear Instruments and Methods in Physics Research Section A: Accelerators, Spectrometers, Detectors and Associated Equipment* 2020, 164613.
74. Shemelya, C. M.; Rivera, A.; Perez, A. T.; Rocha, C.; Liang, M.; Yu, X.; Kief, C.; Alexander, D.; Stegeman, J.; Xin, H., Mechanical, electromagnetic, and X-ray shielding characterization of a 3D printable tungsten–polycarbonate polymer matrix composite for space-based applications. *Journal of Electronic Materials* 2015, 44 (8), 2598-2607.
75. Nofar, M.; Sacligil, D.; Carreau, P. J.; Kamal, M. R.; Heuzey, M.-C., Poly (lactic acid) blends: Processing, properties and applications. *International journal of biological macromolecules* 2019, 125, 307-360.
76. Scaffaro, R.; Lopresti, F.; Marino, A.; Nostro, A., Antimicrobial additives for poly (lactic acid) materials and their applications: current state and perspectives. *Applied microbiology and biotechnology* 2018, 102 (18), 7739-7756.

77. Edith, D.; Six, J.-L., Surface characteristics of PLA and PLGA films. *Applied Surface Science* 2006, 253 (5), 2758-2764.
78. Karamanlioglu, M.; Preziosi, R.; Robson, G. D., Abiotic and biotic environmental degradation of the bioplastic polymer poly (lactic acid): a review. *Polym Degrad Stabil* 2017, 137, 122-130.
79. Sedlarik, V.; Saha, N.; Sedlarikova, J.; Saha, P. In *Biodegradation of blown films based on poly (lactic acid) under natural conditions*, Macromolecular symposia, Wiley Online Library: 2008; pp 100-103.
80. Mallick, S.; Ahmad, Z.; Touati, F.; Bhadra, J.; Shakoor, R.; Al-Thani, N., PLA-TiO₂ nanocomposites: Thermal, morphological, structural, and humidity sensing properties. *Ceramics International* 2018, 44 (14), 16507-16513.
81. Man, C.; Zhang, C.; Liu, Y.; Wang, W.; Ren, W.; Jiang, L.; Reisdorffer, F.; Nguyen, T. P.; Dan, Y., Poly (lactic acid)/titanium dioxide composites: Preparation and performance under ultraviolet irradiation. *Polym Degrad Stabil* 2012, 97 (6), 856-862.
82. Segura González, E. A.; Olmos, D.; Lorente, M. Á.; Vélaz, I.; González-Benito, J., Preparation and characterization of polymer composite materials based on PLA/TiO₂ for antibacterial packaging. *Polymers* 2018, 10 (12), 1365.
83. Marra, A.; Silvestre, C.; Duraccio, D.; Cimmino, S., Polylactic acid/zinc oxide biocomposite films for food packaging application. *International journal of biological macromolecules* 2016, 88, 254-262.
84. Marra, A.; Cimmino, S.; Silvestre, C., Effect of TiO₂ and ZnO on PLA degradation in various media. *Adv. Mater. Sci* 2017, 2 (2), 1-8.

85. Doumbia, A. S.; Vezin, H.; Ferreira, M.; Campagne, C.; Devaux, E., Studies of polylactide/zinc oxide nanocomposites: influence of surface treatment on zinc oxide antibacterial activities in textile nanocomposites. *Journal of Applied Polymer Science* 2015, 132 (17).
86. Murariu, M.; Paint, Y.; Murariu, O.; Raquez, J. M.; Bonnaud, L.; Dubois, P., Current progress in the production of PLA–ZnO nanocomposites: Beneficial effects of chain extender addition on key properties. *Journal of Applied Polymer Science* 2015, 132 (48).
87. Nonato, R.; Mei, L.; Bonse, B.; Chinaglia, E.; Morales, A., Nanocomposites of PLA containing ZnO nanofibers made by solvent cast 3D printing: Production and characterization. *European Polymer Journal* 2019, 114, 271-278.
88. Jayaramudu, J.; Das, K.; Sonakshi, M.; Reddy, G. S. M.; Aderibigbe, B.; Sadiku, R.; Ray, S. S., Structure and properties of highly toughened biodegradable polylactide/ZnO biocomposite films. *International journal of biological macromolecules* 2014, 64, 428-434.
89. Gutierrez, E.; Burdiles, P. A.; Quero, F.; Palma, P.; Olate-Moya, F.; Palza, H., 3D Printing of Antimicrobial Alginate/Bacterial-Cellulose Composite Hydrogels by Incorporating Copper Nanostructures. *ACS Biomaterials Science & Engineering* 2019, 5 (11), 6290-6299.
90. Boyer, C. J.; Ballard, D. H.; Weisman, J. A.; Hurst, S.; McGee, D. J.; Mills, D. K.; Woerner, J. E.; Jammalamadaka, U.; Tappa, K.; Alexander, J. S., Three-dimensional printing antimicrobial and radiopaque constructs. *3D printing and additive manufacturing* 2018, 5 (1), 29-36.

91. Toncheva, A.; Mincheva, R.; Kancheva, M.; Manolova, N.; Rashkov, I.; Dubois, P.; Markova, N., Antibacterial PLA/PEG electrospun fibers: comparative study between grafting and blending PEG. *European Polymer Journal* 2016, 75, 223-233.
92. Fei, Y.; Chen, Y.; Wang, H.; Gao, W.; Yang, R.; Wan, Y., Preparation, characterization of antibacterial PLA/TP nanofibers. *Fibers and Polymers* 2011, 12 (3), 340-344.
93. Liu, J.; Sun, L.; Xu, W.; Wang, Q.; Yu, S.; Sun, J., Current advances and future perspectives of 3D printing natural-derived biopolymers. *Carbohydrate polymers* 2019, 207, 297-316.
94. Chatterjee, A., Thermal degradation analysis of thermoset resins. *Journal of applied polymer science* 2009, 114 (3), 1417-1425.
95. Ortiz, C.; Kim, R.; Rodighiero, E.; Ober, C.; Kramer, E., Deformation of a polydomain, liquid crystalline epoxy-based thermoset. *Macromolecules* 1998, 31 (13), 4074-4088.
96. Kosonen, H.; Ruokolainen, J.; Nyholm, P.; Ikkala, O., Self-organized cross-linked phenolic thermosets: Thermal and dynamic mechanical properties of novolac/block copolymer blends. *Polymer* 2001, 42 (23), 9481-9486.
97. Majumdar, P.; Ekin, A.; Webster, D. C., *Thermoset Siloxane—Urethane Fouling Release Coatings*. ACS Publications: 2007.
98. Conference, S. o. P. E. R. T.; Section, S. o. P. E. C.; Division, S. o. P. E. T., *Thermosets, the True Engineering Polymers: Regional Technical Conference*. Society of Plastic Engineers: 1996.

99. Song, D.; Gupta, R., The use of thermosets in the building and construction industry. In *Thermosets*, Elsevier: 2012; pp 165-188.
100. Wu, Q.; Wang, C.; Liang, R.; Liu, Y.; Cheng, J.; Kang, Y., Fractional linear viscoelastic constitutive relations of anhydride-cured thermosetting rubber-like epoxy asphalt binders. *Construction and Building Materials* 2018, 170, 582-590.
101. Schneider, F.; Draheim, J.; Kamberger, R.; Wallrabe, U., Process and material properties of polydimethylsiloxane (PDMS) for Optical MEMS. *Sensors and Actuators A: Physical* 2009, 151 (2), 95-99.
102. Henrey, M.; Tellez, J.; Wormnes, K.; Pambaguian, L.; Menon, C. In *Sticking in space: manufacturing dry adhesives and testing their performance in space environments*, 12th Symp. on Adv. Space Technologies in Robotics and Automation, 2013; pp 15-17.
103. Hergenrother, P.; Smith Jr, J., Chemistry and properties of imide oligomers end-capped with phenylethynylphthalic anhydrides. *Polymer* 1994, 35 (22), 4857-4864.
104. Brounstein, Z.; Armistead, E.; Duggina, M.; Sharma, P.; Jackson, N., *Microfabrication of MEMS Electro-Thermal Actuators for Problem-Based Learning*.
105. Kosolapov, A.; Plastinin, E.; Semjonov, S.; Bayminov, B.; Sapozhnikov, D.; Alekseeva, D.; Vygodskii, Y. S., Advanced polyimide varnish for optical fiber coating fabrication. *Bulletin of the Lebedev Physics Institute* 2017, 44 (6), 159-162.
106. Thomas, P. J.; Hellevang, J. O., A high response polyimide fiber optic sensor for distributed humidity measurements. *Sensors and Actuators B: Chemical* 2018, 270, 417-423.

107. Knowles, B. R.; Wagner, P.; Maclaughlin, S.; Higgins, M. J.; Molino, P. J., Silica nanoparticles functionalized with zwitterionic sulfobetaine siloxane for application as a versatile antifouling coating system. *ACS applied materials & interfaces* 2017, 9 (22), 18584-18594.
108. Wu, Y.-l.; She, W.; Shi, D.; Jiang, T.; Hao, T.-h.; Liu, J.; Zhang, Q.-c.; You, J.; Li, R. Y., An extremely chemical and mechanically durable siloxane bearing copolymer coating with self-crosslinkable and anti-icing properties. *Composites Part B: Engineering* 2020, 108031.
109. Nguyen, T. V.; Nguyen-Tri, P.; Azizi, S.; Dang, T. C.; Hoang, D. M.; Hoang, T. H.; Nguyen, T. L.; Le Bui, T. T.; Dang, V. H.; Nguyen, N. L., The role of organic and inorganic UV-absorbents on photopolymerization and mechanical properties of acrylate-urethane coating. *Materials Today Communications* 2020, 22, 100780.
110. Murphy, E. C.; Dumont, J. H.; Park, C. H.; Kestell, G.; Lee, K. S.; Labouriau, A., Tailoring properties and processing of Sylgard 184: Curing time, adhesion, and water affinity. *Journal of Applied Polymer Science* 2020, 137 (14), 48530.
111. Hopf, R.; Bernardi, L.; Menze, J.; Zündel, M.; Mazza, E.; Ehret, A. E., Experimental and theoretical analyses of the age-dependent large-strain behavior of Sylgard 184 (10: 1) silicone elastomer. *Journal of the mechanical behavior of biomedical materials* 2016, 60, 425-437.
112. Li, Z.; Li, K.; Liu, J.; Hu, S.; Wen, S.; Liu, L.; Zhang, L., Tailoring the thermal conductivity of Poly (dimethylsiloxane)/Hexagonal boron nitride composite. *Polymer* 2019, 177, 262-273.

113. Said, M. M.; Yunas, J.; Pawinanto, R. E.; Majlis, B. Y.; Bais, B., PDMS based electromagnetic actuator membrane with embedded magnetic particles in polymer composite. *Sensors and Actuators A: Physical* 2016, 245, 85-96.
114. Zhang, Y.; Zhao, M.; Zhang, J.; Shao, Q.; Li, J.; Li, H.; Lin, B.; Yu, M.; Chen, S.; Guo, Z., Excellent corrosion protection performance of epoxy composite coatings filled with silane functionalized silicon nitride. *Journal of Polymer Research* 2018, 25 (5), 130.
115. Ravandi, M.; Teo, W.; Tran, L.; Yong, M.; Tay, T., Low velocity impact performance of stitched flax/epoxy composite laminates. *Composites Part B: Engineering* 2017, 117, 89-100.
116. Gao, J.; Guo, D.; Santhanam, S.; Fedder, G. K., Material characterization and transfer of large-area ultra-thin polydimethylsiloxane membranes. *Journal of Microelectromechanical Systems* 2015, 24 (6), 2170-2177.
117. Ma, L.; Zhu, Y.; Wang, M.; Yang, X.; Song, G.; Huang, Y., Enhancing interfacial strength of epoxy resin composites via evolving hyperbranched amino-terminated POSS on carbon fiber surface. *Composites Science and Technology* 2019, 170, 148-156.
118. Tansel, D. Z.; Brenneman, J.; Fedder, G. K.; Panat, R., Mechanical characterization of polydimethylsiloxane (PDMS) exposed to thermal histories up to 300° C in a vacuum environment. *Journal of Micromechanics and Microengineering* 2020, 30 (6), 067001.

119. Liu, M.; Sun, J.; Chen, Q., Influences of heating temperature on mechanical properties of polydimethylsiloxane. *Sensors and Actuators A: Physical* 2009, 151 (1), 42-45.
120. Erickson, D.; Sinton, D.; Li, D., Joule heating and heat transfer in poly (dimethylsiloxane) microfluidic systems. *Lab on a Chip* 2003, 3 (3), 141-149.
121. Bayerl, T.; Duhovic, M.; Mitschang, P.; Bhattacharyya, D., The heating of polymer composites by electromagnetic induction—A review. *Composites Part A: Applied Science and Manufacturing* 2014, 57, 27-40.
122. Chung, D., Self-heating structural materials. *Smart materials and structures* 2004, 13 (3), 562.
123. Marciniak, B., *Hydrosilylation: a comprehensive review on recent advances*. Springer Science & Business Media: 2008; Vol. 1.
124. Wu, S.; Ladani, R. B.; Zhang, J.; Ghorbani, K.; Zhang, X.; Mouritz, A. P.; Kinloch, A. J.; Wang, C. H., Strain sensors with adjustable sensitivity by tailoring the microstructure of graphene aerogel/PDMS nanocomposites. *ACS applied materials & interfaces* 2016, 8 (37), 24853-24861.
125. Rinaldi, A.; Tamburrano, A.; Fortunato, M.; Sarto, M. S., A flexible and highly sensitive pressure sensor based on a PDMS foam coated with graphene nanoplatelets. *Sensors-Basel* 2016, 16 (12), 2148.
126. Wang, M.; Li, D.; Wang, R.; Zhu, J.; Ren, Z., PDMS-assisted graphene microfiber ring resonator for temperature sensor. *Optical and Quantum Electronics* 2018, 50 (3), 132.

127. Simovic, S.; Prestidge, C. A., Hydrophilic silica nanoparticles at the PDMS droplet– water interface. *Langmuir* 2003, 19 (9), 3785-3792.
128. Kim, H.; Kim, H.-G.; Kim, S.; Kim, S. S., PDMS–silica composite membranes with silane coupling for propylene separation. *J Membrane Sci* 2009, 344 (1-2), 211-218.
129. Paquien, J.-N.; Galy, J.; Gérard, J.-F.; Pouchelon, A., Rheological studies of fumed silica–polydimethylsiloxane suspensions. *Colloids and Surfaces A: Physicochemical and Engineering Aspects* 2005, 260 (1-3), 165-172.
130. Li, H.; Chen, Y.-M.; Ma, X.-T.; Shi, J.-L.; Zhu, B.-K.; Zhu, L.-P., Gel polymer electrolytes based on active PVDF separator for lithium ion battery. I: Preparation and property of PVDF/poly (dimethylsiloxane) blending membrane. *J Membrane Sci* 2011, 379 (1-2), 397-402.
131. Li, Q.; Zeng, F.-L.; Guan, Y.-P.; Jin, Z.-Q.; Huang, Y.-Q.; Yao, M.; Wang, W.-K.; Wang, A.-B., Poly (dimethylsiloxane) modified lithium anode for enhanced performance of lithium-sulfur batteries. *Energy Storage Materials* 2018, 13, 151-159.
132. Zhang, Y.; Pu, Y.; Yang, P.; Yang, H.; Xuan, S.; Long, J.; Wang, Y.; Zhang, H., Branched sulfonated polyimide/functionalized silicon carbide composite membranes with improved chemical stabilities and proton selectivities for vanadium redox flow battery application. *Journal of Materials Science* 2018, 53 (20), 14506-14524.
133. Bouridah, A.; Dalard, F.; Deroo, D.; Cheradame, H.; Le Nest, J., Poly (dimethylsiloxane)-poly (ethylene oxide) based polyurethane networks used as electrolytes in lithium electrochemical solid state batteries. *Solid State Ionics* 1985, 15 (3), 233-240.

134. Öztürk, A.; Fıçıcılar, B.; Eroğlu, İ.; Yurtcan, A. B., Facilitation of water management in low Pt loaded PEM fuel cell by creating hydrophobic microporous layer with PTFE, FEP and PDMS polymers: Effect of polymer and carbon amounts. *International Journal of Hydrogen Energy* 2017, 42 (33), 21226-21249.
135. Wolfson, A.; Janssens, S.; Vankelecom, I.; Geresh, S.; Gottlieb, M.; Herskowitz, M., Aqueous enantioselective hydrogenation of methyl 2-acetamidoacrylate with Rh-MeDuPHOS occluded in PDMS. *Chemical communications* 2002, (4), 388-389.
136. Namrata S, T.; Florence, D.-J.; Lawrence, F.; Jacques, L., Oxidation, chain scission and cross-linking studies of polysiloxanes upon ageings. *Open Journal of Organic Polymer Materials* 2012, 2012.
137. Chen, K.; Schweizer, K. S., Molecular theory of physical aging in polymer glasses. *Physical review letters* 2007, 98 (16), 167802.
138. Stone, G., The statistics of aging models and practical reality. *IEEE Transactions on Electrical Insulation* 1993, 28 (5), 716-728.
139. Hukins, D.; Mahomed, A.; Kukureka, S., Accelerated aging for testing polymeric biomaterials and medical devices. *Medical engineering & physics* 2008, 30 (10), 1270-1274.
140. Celina, M.; Gillen, K. T.; Assink, R., Accelerated aging and lifetime prediction: review of non-Arrhenius behaviour due to two competing processes. *Polym Degrad Stabil* 2005, 90 (3), 395-404.
141. Celina, M. C., Review of polymer oxidation and its relationship with materials performance and lifetime prediction. *Polym Degrad Stabil* 2013, 98 (12), 2419-2429.

142. Laycock, B.; Nikolić, M.; Colwell, J. M.; Gauthier, E.; Halley, P.; Bottle, S.; George, G., Lifetime prediction of biodegradable polymers. *Progress in Polymer Science* 2017, 71, 144-189.
143. Placet, V.; Delobelle, P., Mechanical properties of bulk polydimethylsiloxane for microfluidics over a large range of frequencies and aging times. *Journal of Micromechanics and Microengineering* 2015, 25 (3), 035009.
144. Xiang, K.; Huang, G.; Zheng, J.; Wang, X.; xian Li, G.; Huang, J., Accelerated thermal ageing studies of polydimethylsiloxane (PDMS) rubber. *Journal of Polymer Research* 2012, 19 (5), 9869.
145. Labouriau, A.; Robison, T.; Meincke, L.; Wroblewski, D.; Taylor, D.; Gill, J., Aging mechanisms in RTV polysiloxane foams. *Polym Degrad Stabil* 2015, 121, 60-68.
146. Fortenbaugh, R. J.; Lear, B. J., On-demand curing of polydimethylsiloxane (PDMS) using the photothermal effect of gold nanoparticles. *Nanoscale* 2017, 9 (25), 8555-8559.

Chapter 2 Methods

2.1 Instrumentation

2.1.1 FTIR

Molecules, due to their specific functional groups and bonds, possess many vibrational modes that absorb infrared radiation at particular wavelengths. This phenomenon is used in Fourier Transform infrared (FTIR) spectroscopy to characterize the chemical structure of a compound [1, 2]. For this technique, a laser passes through a beam splitter, where a stationary and moving mirror reflect the resulting beams back to the splitter and ultimately at the sample. The different mirrors are at different distances from the beam splitter, which causes the recombination of the transmitted beams to create an interference pattern. A detector behind the sample measures the amplitude of the transmitted wavelengths as a function of time. Instrument software then performs a Fourier Transform, which is a mathematical linear operator that deconvolutes the data into values of intensity as a function of frequency.

In this work, FTIR spectroscopy was used to characterize the chemical structure and composition by evaluating the peaks in the IR spectrum for each component and to assess whether aging produced any changes to the chemical structure of materials. FTIR spectroscopy was performed with a ThermoScientific Nicolet iS50 FT-IR instrument in Attenuated Total Reflection (ATR) mode with a diamond crystal reference. This instrument has a range from 525 cm^{-1} to 4000 cm^{-1} and a resolution of 4 cm^{-1} . Background

data were collected before each run and 32 scan increments were performed for each sample.

2.1.2 TGA

Thermal stability of a material can be assessed using thermogravimetric analysis (TGA), which heats a sample on a hanging pan within an enclosed environment to a specific temperature at a particular heating rate. Additionally, the surrounding environment can consist of a variety of gases, which can explore how inert or oxygen-rich atmospheres affect thermal degradation [3, 4]. Three measures are generally used to categorize thermal stability: the onset of thermal degradation, the decomposition temperature, and residual mass. The onset of thermal degradation $T_{d5\%}$ was taken as the temperature at which a sample lost 5% of its mass (or possessing 95% of its mass remaining). The decomposition temperatures T_{dMax} are those temperatures at which the derivative TGA curves (DTGA) are at a local extrema. The residual mass m_f is the mass of the sample after the temperature protocol has been executed.

Theoretical research has been conducted to correlate TGA data to thermal degradation kinetics. Using a variety of reaction mechanisms and models, one oft-used equation was derived by Coats and Redfern, which is shown as Equation 2.1 [5-8]. This model assumes that a single thermal reaction mechanism is responsible for the thermal degradation in a specific temperature range. The Coats-Redfern Equation, as it is referred to in literature, requires many samples taken from the same specimen all run at different heating rates β . Various reaction models $g(\alpha)$ are described for the percent conversion α (the mass loss percent of the sample), where one $g(\alpha)$ is chosen that creates a linear relationship between the quantity $\ln(g(\alpha)/T^2)$ and $1/T$. Thus, the mass loss, heating rate,

and temperature T can be used with the universal gas constant R to find the apparent thermal activation energy E and frequency factor A .

$$\ln\left(\frac{g(\alpha)}{T^2}\right) = \ln\left(\frac{AR}{\beta E}\right) - \frac{E}{RT} \quad \text{Equation 2.1}$$

In this work, TGA experiments were conducted on TA Q50 Series and TA 550 Discovery Series instruments. All the experiments in a study were performed using similar protocols and used specimen of similar masses. To solely assess the thermal stability of the materials instead of probing oxidative degradation, ultra-high purity nitrogen gas was used as the atmosphere to surround each sample. Specific TGA protocols are given in each chapter.

2.1.3 DSC

Thermal phase transitions can be investigated by differential scanning calorimetry (DSC), which measures the heat flow across a sample through a range of temperature and heating rates. Indeed, by understanding the shapes of the curves produced during a DSC experiment, the glass transition temperature, melting point, and crystallization temperature can be determined for polymers, metals, and other materials. Additionally, enthalpies of fusion and melting can be obtained by integrating the endothermic or exothermic peak, respectively. For polymers and composites, this allows for the evaluation of percent crystallinity $\%X_c$ by using Equation 2.2 by relating the enthalpy of melting ΔH_m , the enthalpy of formation ΔH_m^0 , and the weight fraction W_p of the polymer component of interest.

$$\%X_c = \frac{\Delta H_m}{\Delta H_m^0 W_p} \quad \text{Equation 2.2}$$

In this work, DSC experiments probed polymer networks to provide a better understanding of where certain thermal phase transitions exist, how crystallinity was affected by various plasticizers and fillers, and whether aging had an effect on a material's glass transition temperature or crystallinity. DSC was performed on TA Q20a and TA 2000 Discovery Series instruments. All the experiments in a study were performed using similar protocols and used specimen of similar masses. Specific DSC protocols are given in each chapter.

2.1.4 MXRF

Elemental analysis of materials can be performed using x-ray fluorescence (XRF), where incident x-rays possessing high enough energy to ionize electrons in the inner orbitals of atoms. This ionization results in the hole being filled with electrons in higher energy orbitals dropping down to lower energy states, which yields a photon [9]. The energy of this photon is dependent on the atom and the orbital in which the electron is ejected from. A detector measures the amount of photons at various energy levels and compares the resulting peaks to known values for elements in the periodic table. Thus, XRF is a highly sensitive technique for performing elemental analyses on samples.

In this work, XRF is performed to assess whether materials are homogeneous with respect to the filler distribution, which verifies if a process method produces uniform composites. Micro x-ray fluorescence (MXRF) measurements were performed using a Bruker M4 Tornado MXRF with acquisition parameters being an x-ray tube operating at 50 kV and 200 μ A, a spectrometer operating at 40 keV and 130 kcps, vacuum (20 mbar), 20 μ m spot size, 20 ms per pixel dwell time, and 10 μ m (cross section) to 20 μ m (top down) step size.

2.1.5 Mass Spectrometry

To analyze the chemical composition of a sample, mass spectrometry can be used on a variety of specimen types and phases with high precision and accuracy. On a foundational level, a mass spectrometer will bombard a sample with an electron beam to break up the specimen into smaller, ionically-charged fragments [10]. These fragments are then accelerated and passed through a series of electric and magnetic fields, which cause the charged fragments to deflect from the axial direction. The amount of deflection is based on the mass and charge of the fragments. A detector then measures the incoming fragments and produces a spectrum of intensity against mass-to-charge ratio, where the specific mass-to-charge ratio can be correlated to particular molecules.

In this work, gas samples that contain volatile products as a result of silicone aging are run through a mass spectrometer. Mass spectrometry was performed using a Finnigan MAT 271 magnetic-sector mass spectrometer. In addition to the standard Faraday-cup detector, this closed-source, electron-ionization (EI) gas mass spectrometer was equipped with a secondary electron multiplier for detection of trace species. The two detectors were calibrated against standards for several permanent gases. For other gases and vapors, estimates were made from the sensitivities based on the electric dipole polarizabilities of the molecules relative to those of the calibration gases [11]. Species were identified by comparison of the measured spectra against the National Institute of Standards and Technology (NIST) electron ionization catalog and the EI fragmentation patterns are used to subtract the contributions by ions of higher-mass molecules from lower-mass peaks. Raw data was in the form of parts per million (ppm) and was converted to moles using the ideal gas law and the measured pressure of the canisters.

2.1.6 GPC

To probe the size and dispersity of polymer samples, gel permeation chromatography (GPC) is often used as one of many size-exclusion chromatography instruments as long as the polymer in question can be dissolved in an organic solvent. The idea behind this empirical technique is to run a solution with a dissolved material through a column of packed beads with specific porosity and morphology. Smaller molecular weight compounds are impeded by these beads while larger molecules cannot fit into the obstacles and pass through the column much more quickly. A polymer solution of known molecular weight and polydispersity is used as a standard so that comparisons can be made, where the residence time in the GPC instrument is correlated with molecular weight.

In this work, GPC experiments were used to evaluate the molecular weight of the non-bound extracts. GPC was performed using chloroform on PDMS. The chloroform swells cured PDMS, where any molecules not bonded to the network would be extracted to the solvent. After swelling, the excess solvent that was not absorbed by the polymer was filtered using a 0.22 μm PTFE filter and then analyzed using an Agilent Infinity II instrument, with a Shodex (K-805L) column, and Wyatt Technology detectors: Dawn multi-angle light scattering (MALS, 25°C) and Optilab refractive index (RI, 30°C). The instrument used 75 μL of each sample per experiment and ran the material through the column at a rate of 1.0 mL/min. Data was analyzed using Astra Software. Values for the number average molar mass, M_n , weight average molar mass, M_w , and polydispersity, \mathcal{D} , were obtained using the Debye model for light scattering and a refractive index increment $dn/dc = -0.0646$.

2.1.7 Contact Angle

By performing contact angle measurements, the surface of a material's attraction or repulsion to water and other liquids can be determined. This is due to the interfacial energy between the various phases results in a droplet of a specific shape, where the angle between the phases is measured and the overall wettability can be evaluated. In these experiments, a well-defined volume of liquid is placed on the surface. If there is repulsion between the surface of a material and the liquid used, the droplet forms a spherical shape and the contact angle between the liquid and solid phases is greater than 90° . If there is attraction, however, the droplet forms a more flattened shape and the contact angle between the liquid and solid phases is less than 90° . These measurements have been explored theoretically and there are many equations and relations between contact angle and thermodynamic quantities.

In this work, contact angle measurements were used in Sylgard aging studies to determine how the hydrophobicity of PDMS changed over time. The hydrophobicity of various PDMS compounds can shift, especially when surface modifications are performed [12]. This is especially the case when considering low molecular weight PDMS chains, which migrate to the surface, and has quickly rendered an altered hydrophilic surface into a hydrophobic one. Static contact angle measurements were performed using a Drop Shape Analyzer (DSA30) from Krüss. An automated drop dispenser and deposition system was used to perform the measurements. A drop of $2\ \mu\text{L}$ deionized (DI) water was dropped on the material surface and the static contact angle was then determined by the computer software. Four trials were run on each specimen, with multiple specimen composing a sample, so that a large dataset existed in which to perform statistical analyses.

2.1.8 CTE

A dilatometer is used to measure the linear coefficient of thermal expansion (CTE), which is a metric that relates how much a material expands or contracts as it is heated or cooled. The instrument measures how much a sample expands or contracts and plots the relative change in length against temperature. An interesting feature of dilatometry is that glass transition temperatures can be determined in addition to CTE values. This is because the glass transition temperature is a second-order thermal phase transition that will produce a discontinuity in the plot of the derivative of the relative length change against temperature [13].

In this work, CTE experiments were conducted using the dilatometer TA Instrument DIL 802. Cylindrical samples were placed next to a fused silica standard and heated while nitrogen gas flowed across the specimen. Triplicates were run for each specimen so as to perform adequate statistical analyses.

2.1.9 Thermal Conductivity

Thermal conductivity assesses how well heat is transferred across a material and is one of many transport properties in a material that is dependent on composition and structure. In steady-state thermal conductivity test methods, the sample is sandwiched between two plates of known temperature and a heat flux is applied. Because the sample's cross-sectional area and thickness was known, the Fourier's Law can be used to determine the thermal conductivity of the sample. By changing the temperature of the plates, the thermal conductivity values for a sample can be obtained for a range of temperatures.

In this work, thermal conductivity experiments are performed with a TA Fox 50 Heat Flow Meter conforming to ASTM C518/ISO 8301. The protocol included nine temperature regimes where the upper and lower plates had a temperature difference of 10°C, starting with the plates equilibrating to 20°C and 10°C and ending with the plates equilibrating to 100°C and 90°C. Compressed air flowed to the instrument at 60 psi in order to pneumatically compress the samples, which had the added effect of relating the thermal conductivity to strain profiles.

2.1.10 Mechanical Tests

Tensile and compressive mechanical tests allow for the determination of the physical properties of a material under various stress and strain conditions. Specifically, the stress and strain responses under an applied load can help distinguish when a material transitions from its linear elastic regime to its nonlinear plastic regime. With this insight also comes the knowledge of a material's yield stress, mechanical hysteresis, stiffness by way of Young's Modulus, and if pushed to its limits, the maximum stress and strain before fracturing or breaking.

In this work, tension and compression tests were performed on ADMET eXpert 7601 and Instron 4340B testing systems. These mechanical tests evaluated how process conditions, filler and plasticizer content, and aging affected the investigated thermoplastics and thermosets. Tension tests were conducted on filaments of varying thicknesses as well as dogbones shaped using a type-A specimen die following ASTM D412 standards while compression tests were conducted on cylinders. The strain rates for each series of tests was held constant so accurate comparisons could be made. In each case, multiple specimen from each sample underwent mechanical testing to create a dataset for statistical analyses.

2.1.11 Shore A Hardness

Using a durometer, the resistance to indentation, or hardness, can be measured for a wide variety of thermosets and thermoplastics. There are numerous hardness scales that can be employed for different classes of materials, however Shore A Hardness is the scale of choice for flexible mold rubbers, which encompasses Sylgard 184 and other silicones. The Shore A Hardness gauge consists of a needle attached to a spring, where contact with a surface will cause the needle to retract. Based on the resistance to indentation of a material, the needle will only retract so far, which can be output as a value for hardness.

In this work, Shore A Hardness tests were conducted on a benchtop HPE II Zwick Roell Shore A Hardness durometer. Hardness was used to evaluate various formulation and assess how a material's performance and behavior changed as it aged. In each case, multiple specimen from each sample underwent mechanical testing to create a dataset for statistical analyses.

2.1.12 Rheology

Investigating the flow of Newtonian and non-Newtonian fluids and viscoelastic materials can be performed with a rheometer. Using this instrument can elucidate the elastic deformations and plastic flow of liquids, solids, gels, and many types of polymers. The basic methodology involves placing a sample between two plates, applying a rotational force or momentum, and measuring the response. Many operational modes can probe a material's flow characteristics, where the most common include performing strain or stress sweeps at constant strain rates and frequencies. Performing rheological measurements allows for the determination of a material's storage and loss moduli, viscosity, regions of

linear viscoelastic behavior and nonlinear viscoelastic behavior, and other important fluid properties.

In this work, rheological measurements were conducted to assess when some formulations cured as a function of time and to evaluate whether certain ink formulations were suitable for DIW 3D printing. Rheological tests were performed with TA Instruments Discovery Hybrid DHR-2 and DHR-3 Rheometers. The gel point, or working time, of the formulations was determined as the time elapsed from the beginning of the experiment until a crossover of the moduli was observed, where the loss modulus fell below the storage modulus. For suitable DIW 3D printing ink formulations, stress and strain sweeps allowed for the determination of the linear and non-linear viscoelastic regions. Additionally, these sweeps assessed whether the equilibrium storage modulus, yield stress, and flow point were adequate for 3D printing. The equilibrium storage moduli G'_{eq} for the samples were determined from the plateau of the stress sweeps in the linear viscoelastic region. The yield stress σ_y was determined from the intersection of lines formed from the storage moduli of the linear viscoelastic region and the beginning of the nonlinear viscoelastic region. The flow point of the ink formulations is the stress at which the storage and loss moduli cross or intersect.

2.2 Methodology

2.2.1 Filament Composites

Fabricating FFF filament composites was conducted using a solvent casting method. On a foundational level, the desired polymer network (ABS or PLA) and any fillers or plasticizers of interest were combined according to a specific weight percent

proportion. A suitable solvent was then introduced to this dry mixture (acetone for ABS composites and chloroform for PLA composites) and occasionally stirred. Once the base polymers were fully dissolved, the solution was placed in a planetary mixer for two minutes at 2,000 rpm at a vacuum of 17.6 kPa. The resulting slurry was poured into a high surface area to volume ratio mold and remained in a fume hood for 24 hours to evaporate any surface-level solvent. This allowed excess solvent to evaporate from the casted composite, while retaining enough malleability in the composite to cut it into 1 cm × 1 cm squares.

The composite squares were placed in a vacuum oven at 65 °C and 80 kPa negative pressure for at least 24 h, to fully evaporate the remaining solvent. The dried samples were then fed into a Filabot EX2 extruder. A container of room temperature DI water was placed a meter below the extruder. Thus, gravity pulled the filaments into the water, which cooled and hardened the samples and produced naturally coiled filaments.

2.2.2 3D Printing

FFF 3D printing was performed on a Hyrel MK-1 250 modular printing head with a 500 μm nozzle diameter was attached to a Hyrel System 30M. Using Repetrel software (Hyrel 3D), composite filaments were fed into the modular printing head and extruded onto the heating bed at a rate of 1,800.00 mm/min and according to designs made on Solidworks software. The final parts were square blocks measuring 3 cm on a side and 1.2 cm thick.

Once the resins were formulated and mixed for DIW printing, they were transferred into a metal syringe (EMO-XT printer head, Hyrel 3D) and then centrifuged at 2000 rpm for 1-2 minutes to remove any air bubbles. A MATLAB script was created to generate

Gcode with varying amounts of spacing and geometries. Repetrel software (Hyrel 3D) was used to control the printer and ran at a travel rate at 2250 mm/min with the material flow rate at 150 pulses/ μ L onto a glass substrate from the build stage. The geometry of the 3D parts were disks possessing a diameter of 5 cm and consisted of eight layers with each layer organized in faced-centered tetragonal (FCT) structure. Four different spacing between the printed struts (500 μ m, 750 μ m, 1000 μ m, and 1500 μ m) were used for tuning the thermomechanical properties and were cured in an oven at 150°C for 2 hours.

2.2.3 Thermal Aging

Determining long-term material performance and behavior of silicone polymers has been investigated using the concept and methodology of thermal accelerated aging. After samples had reached their gel point and fully cured, which was determined by rheology and the technical data sheet, respectively, in a 25°C oven, they were grouped to be thermally aged. Six ovens were kept isothermal at 25°C, 50°C, 60°C, 70°C, 80°C, and 90°C. Samples that did not have TDS added (Control and Opt2 formulations) were placed in sealed canisters. Each non-TDS formulation was placed in an individual canister per oven above 25°C, which made up ten canisters. Samples were placed such that they did not have contact with the metal canisters. After they were securely sealed and fastened, the canisters had their air evacuated, creating a vacuum around 10^{-3} torr, and filled with ultra-high purity nitrogen to around 600 torr. An additional Control canister and Opt2 canister went through the same process as described above with the exception that these two canisters were kept in air at atmospheric pressure and placed in the 90°C oven. Enough specimens were placed in the ovens that could be removed after aging for two, five, and twelve months.

2.2.4 Solvent Swelling

Solvent swelling experiments were used to evaluate the crosslinking of the polymer network in each sample. The cured polymer networks were swollen to equilibrium in toluene for 24 hours at 25°C. After being swollen, the samples were gently patted dry to remove residual toluene before recording the swollen mass. The samples were subsequently dried at 25°C for 24 hours and then at 70°C for 48 hours under vacuum. Percent loss from the solvent is reported as the difference between the initial mass and the vacuum dried mass. The network swelling is reported as the difference between the fully swollen mass and vacuum dried mass. Densities were evaluated by measuring the initial masses and volumes. Each sample was run in triplicate and standard deviation is reported as the error.

The polymer volume fraction φ_p was determined using the respective partial volumes of the polymer V_p and solvent V_s . Because these values are not easily measured, the densities of the polymer ρ_p and solvent ρ_s were used along with the network swelling, S , to obtain the volume fraction, which is shown as Equation 2.3. This was used to evaluate the Flory-Huggins polymer-solvent interaction parameter χ between PDMS and toluene, where many equations have been developed to describe the interaction parameter from theory and experimental methods [14-16]. Searching through literature regarding swelling PDMS with toluene, the equation that best describes the systems in this study is a finite Taylor series as a function of the polymer volume fraction with values shown in Equation 2.4 [17].

$$\varphi_p = \frac{V_p}{V_p + V_s} = \left(1 + S \frac{\rho_p}{\rho_s}\right)^{-1} \quad \text{Equation 2.3}$$

$$\chi = \chi_0 + \chi_1\varphi_p + \chi_2\varphi_p^2 = 0.459 + 0.134\varphi_p + 0.590\varphi_p^2 \text{ Equation 2.4}$$

Using the interaction parameter along with the polymer volume fraction and molar volume of the solvent $v_{m,s}$ the average molecular weight of the polymer between crosslinks M_c can be evaluated using a modified version of the Flory-Rehner equation. The standard Flory-Rehner equation is derived from thermodynamic interactions and treats the swollen polymer as a perfect network, where the numerator and denominator correspond to the elastic and mixing contributions, respectively. Groups working with both theoretical and experimental methods regarding polymer swelling behavior have shown that a phantom network models a swollen polymer with better precision and as such is used in this study as Equation 2.5 [18]. The same Flory-Rehner equation can also relate the effective number of chains in the network ν_e to the average molecular weight of the polymer between crosslinks and Avogadro's number N_A shown as Equation 2.6. Rearranging the terms in Equation 2.6 produces the specific crosslink density ρ_x of the polymer, shown as Equation 2.7, which describes the moles of crosslinks per mass of polymer.

$$M_c = \frac{\frac{1}{2}v_{m,s}\rho_p\varphi_p^{1/3}}{\ln(1-\varphi_p)+\varphi_p+\chi\varphi_p^2} \text{ Equation 2.5}$$

$$\nu_e = \frac{\rho_p N_A}{M_c} \text{ Equation 2.6}$$

$$\frac{\nu_e}{\rho_p N_A} = \frac{1}{M_c} = \rho_x \text{ Equation 2.7}$$

References

1. Griffiths, P. R.; De Haseth, J. A., Fourier transform infrared spectrometry. John Wiley & Sons: 2007; Vol. 171.
2. Amand, L.-E.; Tullin, C. J., The theory behind FTIR analysis. Dep. Of Energy Conversion, Chalmers University of Technology, Sweden 1999.

3. Thomas, T. H.; Kendrick, T., Thermal analysis of polydimethylsiloxanes. I. Thermal degradation in controlled atmospheres. *Journal of Polymer Science Part A-2: Polymer Physics* 1969, 7 (3), 537-549.
4. Grassie, N.; Macfarlane, I., The thermal degradation of polysiloxanes—I. Poly (dimethylsiloxane). *European polymer journal* 1978, 14 (11), 875-884.
5. K.M. Lu, W.J. Lee, W.H. Chen, T.C. Lin, Thermogravimetric analysis and kinetics of co-pyrolysis of raw/torrefied wood and coal blends, *Appl Energ* 105 (2013) 57-65.
6. Coats, A.W.; Redfern, J.P. Kinetic Parameters from Thermogravimetric Data. *Nat. Cell Biol.* 1964, 201, 68–69.
7. Ebrahimi-Kahrizsangi, R.; Abbasi, M. Evaluation of reliability of Coats-Redfern method for kinetic analysis of non-isothermal TGA. *Trans. Nonferrous Met. Soc. China* 2008, 18, 217–221.
8. Brems, A.; Baeyens, J.; Beerlandt, J.; Dewil, R. Thermogravimetric pyrolysis of waste polyethylene-terephthalate and polystyrene: A critical assessment of kinetics modelling. *Resour. Conserv. Recycl.* 2011, 55, 772–781.
9. Brouwer, P., *Theory of XRF*. Almelo, Netherlands: PANalytical BV 2006.
10. Gross, Jürgen H. *Mass spectrometry: a textbook*. Springer Science & Business Media, 2006.
11. Lampe, F., J. Franklin, and F. Field, Cross sections for ionization by electrons. *Journal of the American Chemical Society*, 1957. 79(23): p. 6129-6132.
12. Efimenko, K., W.E. Wallace, and J. Genzer, Surface modification of Sylgard-184 poly (dimethyl siloxane) networks by ultraviolet and ultraviolet/ozone treatment. *Journal of colloid and interface science*, 2002. 254(2): p. 306-315.

13. Dannis, Mark L. Thermal expansion measurements and transition temperatures, first and second order. *Journal of Applied Polymer Science* 1959. 1(1): p. 121-126.
14. Chasse, W., et al., Cross-link density estimation of PDMS networks with precise consideration of networks defects. *Macromolecules*, 2012. 45(2): p. 899-912.
15. Valentín, J., et al., Uncertainties in the determination of cross-link density by equilibrium swelling experiments in natural rubber. *Macromolecules*, 2008. 41(13): p. 4717-4729.
16. Muramoto, A., Studies on the Interaction Parameter in Polysiloxane Solutions. *Polymer Journal*, 1970. 1(4): p. 450-456.
17. Chassé, W., et al., Correction to cross-link density estimation of PDMS networks with precise consideration of networks defects. *Macromolecules*, 2015. 48(4): p. 1267-1268.
18. Dimitriyev, M.S., et al., Swelling thermodynamics and phase transitions of polymer gels. *Nano Futures*, 2019. 3(4): p. 042001.

Chapter 3 Fused Filament Fabrication of Polymer Composites for Extreme Environments

3.1 Introduction

With the aim of increasing performance, quality, and profitability while decreasing the amount of waste, development time, and cost, advanced manufacturing (AM) is making rapid gains in materials research, product design, and commercialization[1-5]. Advanced materials research ranges from ways to reduce anisotropy[6-8] for 3D printing and other techniques to imbuing common AM feedstocks with additional functionality, such as sensors[9], antimicrobial agents[10], or drug delivery[11, 12]. The AM technique most associated with 3Dprinting, known as fused filament fabrication (FFF), heats a thermoplastic polymer past its glass transition temperature (T_g) or melting point (T_m) and deposits the material into layered cross-sections via a printing nozzle. The deposited material subsequently cools down and undergoes interfacial adhesion between each layer, which forms a three-dimensional part. FFF printed parts are modeled first in computer software and as a consequence can possess complex geometries while allowing for agile requirement changes and fabrication. When deciding on which polymer materials to use for FFF, acrylonitrile butadiene styrene (ABS) is traditionally chosen if the final product needs mechanical strength and impact resistance, which has made it the second-most common 3D-printing polymer, after poly(lactic acid). Applications requiring these mechanical properties and many other capabilities have a variety of materials to choose from for FFF and more generally AM, however there are relatively few state-of-the-art printing feedstocks that deal directly with being used in extreme environments where

ionizing radiation, harsh chemical species such as solvents, or elevated temperatures and mechanical stresses are existent.

In a recent published study, commercial ABS filaments containing various concentrations of elemental bismuth (up to 18 wt%) were evaluated as phantom devices to mimic the radiopacity of native tissues during X-ray CT imaging and as safety labware[13]. The authors demonstrated that the 2.0 mm ABS filament with the highest Bi concentration attenuated half of the ^{99m}Tc gamma emission. Needless to say that filaments containing higher weight-percent of Bi loadings would provide even better shielding at comparable thickness, but unfortunately these are not commercially available. More recently, Woosley and co-workers demonstrated the feasibility of creating ABS filaments containing up to 20wt% boron nitride (BN) for potential aerospace applications[14]. Neutron attenuation of the 3D-printed pads increased from 50% for the neat ABS polymer to 72% for the 20 wt% BN composite. Greater attenuation values were not feasible since BN loadings higher than 20 wt% produced poor-quality filaments. Both studies illustrate well the potential of using FFF to create unique objects, but the application of the technology remains restricted due to the availability of functional filaments: either these are not available or are limited to relatively low loadings of additives that exhibit the desired functional characteristics. Furthermore, ionizing radiation is frequently present in environments that combine other harsh conditions as well, like those encountered in the storage of radioactive waste (solvents), nuclear power plants (high humidity, high temperatures), etc. Thus, it is important to consider approaches for filament fabrication that allow for easy material customization to address a range of functionalities.

In this work, we describe the preparation of highly filled FFF filaments containing three different components: ABS, Bi and polyvinylidene fluoride (PVDF). PVDF is an attractive hydrophobic polymer to be incorporated in the fabrication of filaments since it exhibits high chemical resistance[15, 16], and is widely used in numerous applications from electrical storage[17] to membrane filtration, distillation, and ion exchange[18, 19]. Our filaments were created to be used by the FFF technology to 3D-print objects that would experience combined extreme environments, such as exposure to ionizing radiation and solvent species. As such, homogenous ABS-composite filaments were made of increasing concentrations up to 66 wt% loading of bismuth for attenuating gamma radiation and up to 25 wt% loading of PVDF to increase chemical resistance. The filaments were printed into blocks via FFF technique, characterized to understand their chemistry and thermal and mechanical properties, and subjected to gamma radiation from a Cs-137 source to evaluate their shielding ability and tolerance to radiolysis.

3.2 Materials and Methods

3.2.1 Materials

ABS was supplied from Filabot. Extruder Purges E and NF were supplied from Asaclean. Acetone was supplied from Sigma Aldrich. Bismuth powder was supplied by Alfa Aesar and is from a sieve designation of No. 325, which correlates to particles sizes of 44 μm . PVDF powder was supplied from Aldrich Chemistry. Chloroform, xylene, and toluene were supplied by Thermo Fisher Scientific. Proton Nuclear Magnetic Resonance ($^1\text{H-NMR}$) was performed on the received ABS dissolved in deuterated acetone to estimate ABS chemical composition. It was found to be nominally comprised of 17% acrylonitrile, 20% butadiene, and 63% styrene.

3.2.2 Feedstock and Filament Fabrication

A ratio of 1:4 w/w ABS to acetone was combined and manually stirred before being placed in a temperature-controlled oven at 50°C for six hours to ensure the complete dissolution of ABS. The Bi metal filler and PVDF polymer were then added to the ABS solution. ABS composites with Bi and PVDF were made in ratios up to 66 weight-percent added content (Bi and/or PVDF added). All composite ratios herein are reported on a total wt% basis. To prevent the solution from becoming too viscous for adequate mixing, acetone was added in 5 mL increments while manually stirring. After stirring, the solution was placed in a planetary mixer for two minutes at 2,000 rpm at a vacuum of 17.6 kPa. The resulting slurry was poured into a high surface area to volume ratio mold and remained in a fume hood for 24 hours to evaporate any surface-level solvent. This allowed the sample to harden enough to be cut into approximate 1 cm x 1 cm pieces. The small fragments were stored in a vacuum oven at 50°C for another 24 hours to remove residual sub-surface solvent. Following solvent removal, a Filabot EX2 extruder equipped with a 1.75 mm-diameter extruder nozzle was heated to 215°C. A room-temperature DI-water bath was placed below the extruder nozzle such that the resulting filament was gravity-fed into the cooling bath to facilitate solidification. Extruder Purges E and NF were used to flush out the extruder system before and after each feedstock material was fed into the hopper. The screw speed was set to its maximum setting, producing 2 lbs/hr.

A Hyrel MK-1 250 modular printing head with a 500 μm nozzle diameter was attached to a Hyrel System 30M and heated up to 240°C while the heating bed within the system was heated up to 90°C. Composite filaments were fed into the modular printing head and extruded onto the heating bed at a rate of 1,800.00 mm/min and according to designs made

on Solidworks software. Composite feedstock materials were successfully fabricated and used for printing. An ABS/Bi composite extruded into a filament and printed into blocks is shown in Figure 3.1.

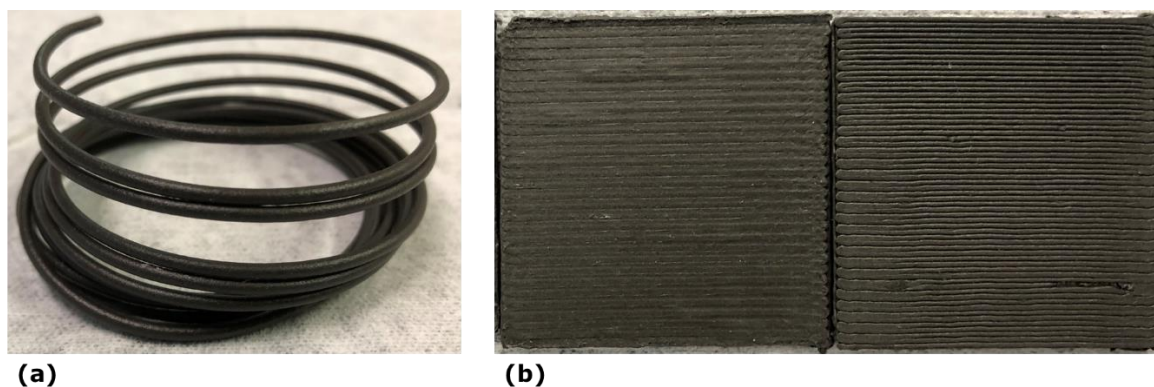


Figure 3.1: ABS/Bi (a) filament and (b) printed pads

3.2.3 Gamma Irradiation

A 3D-printed pad consisting of 34 wt% ABS and 66 wt% Bi was exposed to gamma irradiation from a Cs-137 source located at Sandia National Laboratories. The accumulated gamma dose was determined from TLDs-700 that were placed on the back of the 3D-printed pad. The final gamma dose was 75 Gy at 0.28 Gy/h. The experimental attenuation value was compared with the estimated one provided by the Beer-Lambert Law (Equation 3.1)[35-38].

$$I \approx I_0 e^{-\mu \rho t} \quad \text{Equation 3.1}$$

Where I is the outgoing intensity of radiation, I_0 is the incident radiation, μ the attenuation coefficient, ρ the density of the material, and t the thickness of the material.

3.2.4 Characterization Techniques

Fourier Transform-Infrared Spectroscopy (FTIR) was performed on an OMNIC FTIR instrument with a range from 525 cm^{-1} to 4000 cm^{-1} . Background data were collected before each sample and 32 runs were performed per sample pre- and post-irradiation. Digital microscopy utilized a VHX-6000, where high-resolution microscopic images were taken of the samples pre- and post-irradiation. Micro x-ray fluorescence (MXRF) measurements were performed using a Bruker M4 Tornado MXRF with acquisition parameters being an x-ray tube operating at 50 kV and 200 μA , a spectrometer operating at 40 keV and 130 kcps, vacuum (20 mbar), 20 μm spot size, 20 ms per pixel dwell time, and 10 μm (cross section) to 20 μm (top down) step size. Spectra and mapping were compiled for printed specimen before and after being irradiated. USAXS/SAXS measurements were collected at beam line 9-ID-C at the Advanced Photon Source (APS) at Argonne National Laboratory (Lemont, Illinois)[39]. SAXS profiles were reduced using the Indra and Nika programs for Igor Pro.[40] The Irena program for Igor Pro was used to merge same-specimen USAXS and SAXS as well as analyze the data.[41]

Thermal properties were investigated via differential scanning calorimetry (DSC) (TA Instruments DSC Q20 series) and thermogravimetric analysis (TGA) (TA Instruments TGA Q2000 series). DSC allows for the determination of phase transformations and percent crystallinity. This is important because the feasibility and usefulness of a printed part heavily relies on its mechanical properties, which are in turn influenced by its thermal properties. Specifically, a material's crystal domains affect the overall brittleness and elongation[42], thus determining the composite materials' crystallinity will assist in understanding their mechanical properties. To ensure the samples have identical thermal

history, only the second heating cycle from DSC were analyzed. All of the samples were from printed parts and had a mass ranging from 10 to 20 mg. The samples were run under nitrogen at a flowrate of 5 mL/min and were heated from room temperature (25°C) to 300°C at a rate of 10°C/min, held at 300°C for one minute, cooled to 25°C at a rate of 10°C/min, held at 25°C for one minute, and the entire process was repeated once more. Calculating percent crystallinity $\%X_c$ of a polymer composite uses Equation 3.2[43, 44]. It relates the percent crystallinity to the enthalpy of melting ΔH_m , the enthalpy of formation ΔH_m^0 , and the weight fraction W_p of the polymer component of interest. The enthalpy of melting was obtained by integrating the endothermic melting peak of a DSC curve.

$$\%X_c = \frac{\Delta H_m}{\Delta H_m^0 W_p} \quad \text{Equation 3.2}$$

TGA allows for the determination of thermal stability of a material. For TGA, all of the samples were from printed parts and had a mass of 15 ± 1 mg. The samples were run under nitrogen at a flowrate of 10 mL/min and were heated from room temperature (25°C) to 600°C at heating rates of 5, 8, 10, 13, and 15°C/min. TGA experiments were run three times for each sample at the heating rate of 10°C/min. The composite materials' degradation onset and decomposition temperatures are able to be determined by measuring the mass percent of each sample at the same percent conversion ($X = 95\%$) and the respective maximums of their derivative curves. The activation energy E_a of thermal decomposition for the printed samples was calculated from the rate-dependent thermal stability using the Coats-Redfern equation[45], shown in Equation 3.3.

$$\ln\left(\frac{-\ln(1-X)}{T^2}\right) = \ln\left(\frac{AR}{\beta E_a}\right) - \frac{E_a}{RT} \quad \text{Equation 3.3}$$

It is in the form of a linear equation relating the percent conversion X and temperature T in Kelvin against the inverse temperature. The resulting slope includes the activation energy and the universal gas constant R and the resulting y-intercept includes a frequency factor A , the universal gas constant, the activation energy, and the heating rate β .

Chemical resistance to solvents was tested on ABS-composites filaments with and without PVDF. The chosen specimens were ABS, ABS/Bi 56/44, and ABS/Bi/PVDF 50/25/25. Filament samples were placed in vials containing a solvent. The solvents included xylene, toluene, and chloroform. Upon placing the filaments in the vials with a solvent, the time was recorded to determine how long it took for dissolution to occur.

Mechanical testing was performed on an Instron 4340B, where 10 cm filaments of each composite were placed in the instrument for tensile testing. Two types of filaments from each composite were tested: those obtained from the extruder with a nozzle diameter of 1.75 mm (referred to as 1.75E) and those obtained from the 3D printer with a nozzle diameter of 500 μm (referred to as 0.5P). To make 0.5P filaments, 1.75E filaments were put through the 3D printer, but no design was specified thus providing default thin cylindrical wires. The 0.5P filaments had an average diameter of 600 μm . Every type of filament was placed in a configuration where the grippers of the tensile tester were separated by 3.5 cm and pulled apart at a rate of 0.5 mm/min. Before the tensile test, the diameter of each filament was measured with calipers at each end and the middle, where the resulting average was input into the mechanical testing software. The printed and extruded filaments for each listed composition were tested with at least four samples each and the reported values are derived from the calculated average and standard deviation.

3.3 Results and Discussion

3.3.1 Chemical Characterization

FTIR was performed to confirm that the feedstock material successfully incorporated all of the constituent polymers. The spectra of five typical samples are shown in Figure 3.2(a). Relevant IR information for the polymer composites includes peaks corresponding to: C-H alkane bonds between 3000-2850 cm^{-1} ; C-H alkene bonds between 3100-3010 cm^{-1} ; C=C aliphatic bonds between 1680-1620 cm^{-1} ; C=C aromatic bonds between 1700-1500 cm^{-1} ; C \equiv N nitrile bonds between 2260-2200 cm^{-1} ; C-F alkane bonds between 1400-1000 cm^{-1} ; and C-H aromatic bonds between 3100-3000 cm^{-1} . All five spectra in Figure 3.2(a) have the characteristic peak of a nitrile group around 2250 cm^{-1} , which is associated with ABS [20]. The 3D-printed pads containing PVDF show additional peaks from 1000-1400 cm^{-1} , which correspond to carbon-fluorine bonds. The IR data confirms that both polymers were successfully incorporated in the diverse 3D-printed pads thus validating our approach for filament fabrication.

MXRF experiments were performed to detect and evaluate the distribution of bismuth in the filament. A typical color mapping of a 34 wt% ABS and 66 wt% Bi filament is shown in Figure 3.2(b). The filament is at an angle so that a top view and a side view can be seen. Bismuth particles are scattered throughout the filament bulk and surface, confirming that the feedstock material has successfully incorporated the filler.

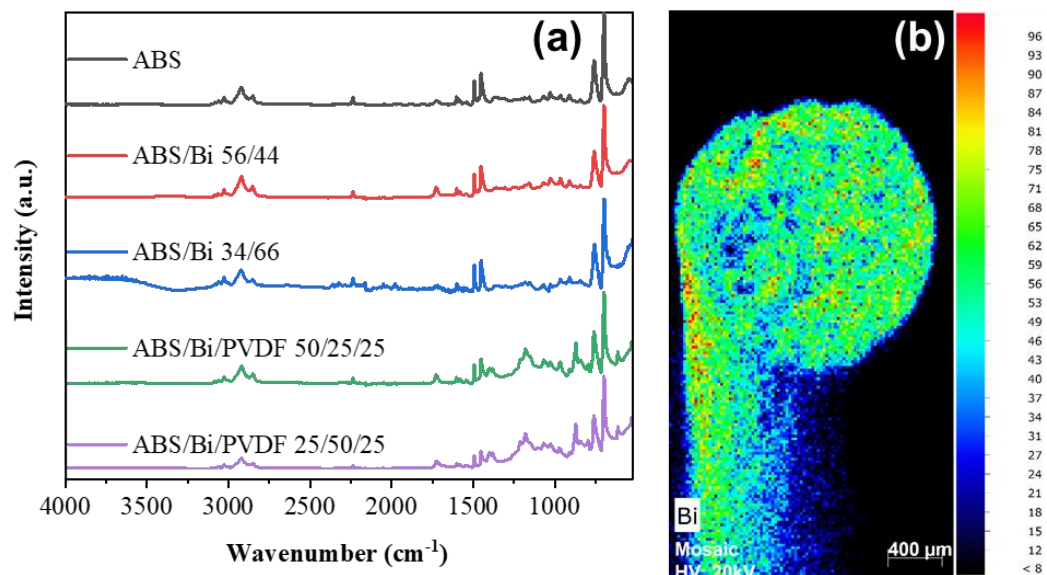


Figure 3.2: (a) FTIR spectra of printed samples and (b) MXRF of a Bi color mapping of ABS/Bi 34/66.

Both techniques were also employed to determine whether 3D-printed pads show evidence of degradation after being subjected to gamma irradiation. Formation of peroxide radicals on the polymer backbone evidenced by detection of OH groups at 3500 cm^{-1} in the IR spectrum would indicate changes in the chemical structure due to radiolysis and oxidation. The FTIR spectrum for the irradiated ABS/Bi/PVDF 25/50/25 sample is similar to the control sample as shown in Figure 3.3(a) indicating good tolerance to ionizing radiation. MXRF characterization of the same samples is shown in Figures 3.3 (b) and 3.3 (c). MXRF images are a top view of the cross-section of two different printed samples from the same batch of printing: one that was not irradiated and one that was irradiated. They both display information about the interior and exterior of the specimen. The color mapping shown in the figure is for Bi in printed ABS/Bi/PVDF 50/25/25 samples, which is fairly uniform throughout before and after irradiation. Thus, the fabrication procedure results in a homogenous printed material which is retained after irradiation.

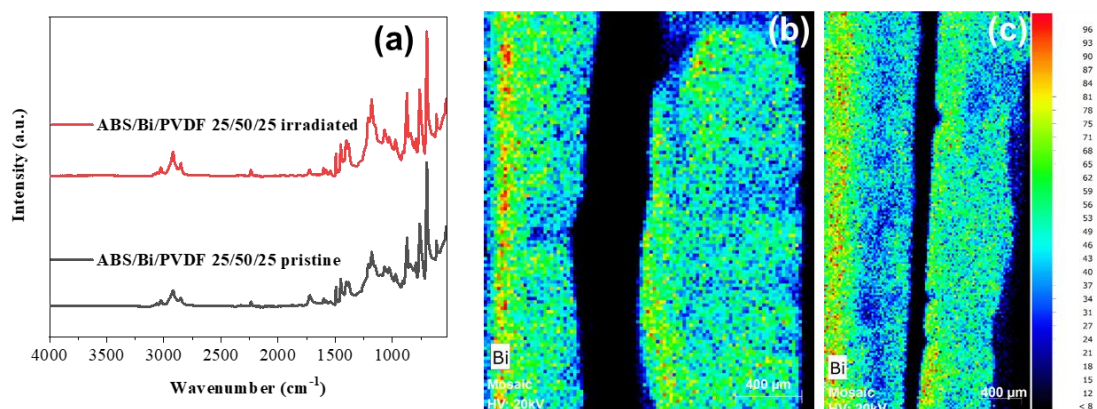


Figure 3.3: (a) FTIR and MXRF of (b) pre- and (c) post-irradiated samples showing an even distribution of bismuth and that it does not change after irradiation. Because the samples are oriented along the viewing axis, the green coloration corresponds to the top layer and the bluer coloration corresponds to the deeper layers.

3.3.2 Morphological Characterization

The complex morphology of the composite filaments was probed using ultra-small-angle X-ray scattering (USAXS) and small-angle X-ray scattering (SAXS) techniques. X-rays are scattered by fluctuations in electron density in 3 dimensions, such that the scattering pattern of materials gives significant insight into the spatial arrangement of scattering objects. In the case of complex composite materials, scattering objects can be inorganic particles, amorphous polymer domains, crystallites, or crystallographic faces depending upon the angle of scattered X-rays. Using a combination of USAXS and SAXS techniques, we are able to probe fluctuations in electron density across real space dimensions of approximately 3 Å up to 3 μm. Pure ABS and pure PVDF used for the composites each display distinct scattering patterns as shown in Figure 3.4. Pure ABS and ABS/Bi composites were also investigated and are shown in the Appendix as Figure A3.1. The inter-lamellar spacing (Long Period, L_p) of pure PVDF appears prominently around $q = 0.06 \text{ \AA}^{-1}$, corresponding to 10.4 nm. The determined L_p of pure PVDF filaments is in

agreement with previous synchrotron SAXS data obtained for PVDF[21, 22]. Pure ABS polymer displays distinct micro-phase separation in the USAXS region with scattering features around $q = 0.0013, 0.005, \text{ and } 0.014 \text{ \AA}^{-1}$. Interestingly, the micro-phase separated morphology of pure ABS is not present in the composite blends, likely due to scattering from Bi particles dominating the scattering profile at these scattering angles.

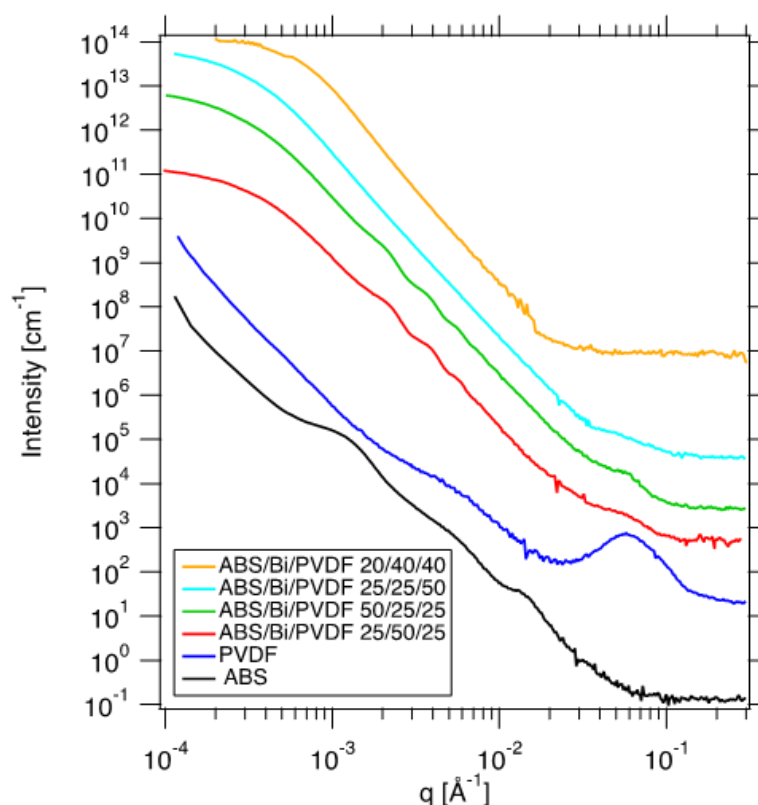


Figure 3.4: USAXS/SAXS profiles of ABS, PVDF, and Bi-filled composite blends. Profiles are shifted vertically for clarity.

The unified fit model was used to determine information about particle size and surface.[23, 24] The unified fit combines scattering contributions from the size (radius) of the scattering object referred to as the Radius of Gyration R_g and scattering from local, interfacial features. Interfacial scattering gives rise to power law scattering in which the exponent, P , is referred to as the Porod exponent. When P is greater than 3 and less than 4,

the scattering is indicative of surface fractal scattering. For the case when P is equal to 4, scattering is attributed to a sharp, smooth interface between regions of different electron density. For P less than 3, scattering is the result of mass fractals, such as polymers in solution or polymer gels.

As shown in Figure 3.4, all Bi-filled samples display a prominent Guinier “knee” scattering feature around $q = 0.0004 \text{ \AA}^{-1}$, which corresponds to R_g equal to 600-800 nm using the unified fit. This scattering feature is therefore attributed to the radius of the primary particle of Bi powder used in this study. The Porod exponents determined for the composite filaments in Table 3.1 approach a value of 4, such that the bismuth particles exhibit surface fractal characteristics. The variability across fit values in Table 3.1 is attributed to two parameters in the filament fabrication process that were not constrained, despite constant temperature and screw speed in the extruder: namely, lead time in the barrel of the hopper while at extrusion temperature and rate of cooling immediately following extrusion. The composite blends behaved differently in the extruder even under identical temperature and screw speeds, such that some blends took significantly longer to gravity-extrude from the barrel, and once the filament exited the nozzle, some compositions proceeded toward the water (quench) bath more rapidly than others. This variability during the fabrication process is likely due to the polymer composition, and could affect bismuth crystallization and incorporation processes. Future studies will probe the origin of variation in fabrication parameters and what effect, if any, they have on metallic fillers such as bismuth. It is clear from the scattering profiles that bismuth is incorporated into the bulk material during extrusion, and that the Bi particle size reported

by the manufacturer must refer to larger aggregates and agglomerates of the small, micron-sized primary particles of Bi reported in Table 3.1.

Table 3.1: Unified fit parameters extracted from scattering profiles of ABS/PVDF/Bi composite blends.

Feedstock Composition	R_g (nm)	P
ABS/Bi/PVDF 20/40/40	450 ± 50	3.90 ± 0.20
ABS/Bi/PVDF 25/25/50	870 ± 10	4.00 ± 0.01
ABS/Bi/PVDF 50/25/25	890 ± 30	3.90 ± 0.10
ABS/Bi/PVDF 25/50/25	620 ± 80	3.75 ± 0.20

The morphology of the composites on the macroscopic scale comprises smooth and homogenous filaments. When the scale is taken down to hundreds of microns, some filler particles become observable on the surface. Digital microscopy images at the hundreds of microns scale were taken of the printed blocks and shown in Figure 3.5. In order to evaluate each material on its ability to be printed and observe distinct layers, the 3D-printed blocks have some gaps between parallel components in the same layer and porosity between layers, which is seen in Figure 3.5. Figures 3.5(a) and 3.5(b) are top views of ABS and ABS/Bi 34/66 printed blocks, respectively, and Figure 3.5(c) is a side view of an ABS/Bi/PVDF 25/50/25 printed block.



Figure 3.5: Digital microscopy images on the order of 100 μm showing printed samples of (a) ABS, (b) ABS/Bi 34/66, and (c) ABS/Bi/PVDF 25/50/25. Each red scale bar in the bottom right of each image represents 100 μm in the horizontal direction. To evaluate the ability of each material being printed and observe distinct layers, the 3D-printed parts included some gaps and porosity.

3.3.3 Thermal Characterization

DSC experiments were performed to evaluate heat-treatment and compatibility effects on crystallization and melting behaviors of the 3D-printed samples. ABS does not exhibit a true melting point since it is an amorphous polymer. Its glass transition temperature (T_g) is at around 105°C and remains unchanged when the polymer is incorporated into the composite (not shown in the DSC curves). Composites comprised of ABS and PVDF are known to phase-separate[15, 16], so this implies that while the filament can be fabricated and 3D-printed, it is not a true blend. On the other hand, Bi and PVDF exhibit endotherm and exotherm peaks as shown in Figures 3.6(a) and 3.6(b). It is interesting to compare the thermal behavior of Bi in the 3D-printed pads with the neat Bi powder. As a reference, the onset melting point, peak melting point, and enthalpy of melting for elemental Bi are 269°C, 272°C, and 53 J/g, respectively[25]. DSC of the neat Bi powder shows two exotherm peaks, a sharp one at 241°C, and a broader one at around 180°C. Furthermore, a series of very small exothermic events are also observed as shown in Figure 3.6(a). The multiple exotherm peaks are likely related to crystal particle size distribution; larger particles melt and nucleate at higher temperatures than smaller metal

particles[26, 27]. Interestingly, the sharp crystallization peak at 241°C or the very small ones are not detected when Bi is incorporated into the ABS polymer matrix. This result indicates that the thermo-treatments used in the fabrication of filaments as well as in the printing of the pads altered the metal particle size distribution. Likely, the Bi powder used to fabricate our filaments contains a broad size distribution of aggregates which break up when treated to be incorporated into the polymer matrix during the feedstock fabrication process. The crystallization peak observed at around 180°C for the neat powder is also observed at a slightly lower temperature of 176°C for the 3D-printed ABS/Bi 34/66 composite material, which indicates that the polymer network may hinder Bi particle mobility towards agglomeration. The DSC thermograms also show a sharp melting peak at 273°C for the neat powder as well as for the composites. Thus irrespective of the amount of incorporated bismuth in a specimen, there are no significant changes regarding to Bi melting point.

The thermal behavior of PVDF-containing composites is shown in Figure 36(b). Broad crystallization and melting peaks are observed for neat PVDF and for PVDF in the composites. The enthalpy of melting, and thus the crystallinity of PVDF in the composites shows changes with respect to neat PVDF powder, as listed in Table 3.2. Using Equation 3, where the enthalpy of formation for PVDF is assumed to be $\Delta H_m^0=104.7$ J/g[28], allows for the crystallinity of the samples to be estimated. There is an increase in the percent crystallinity of the PVDF in the composite samples, which when taken with the narrowing of the melting peaks in Figure 3.6(b) indicate that more uniformly-sized crystals are formed when the polymer is incorporated in the polymer matrix. This change in the level of PVDF crystallinity does not affect its melting point.

Table 3.2: Melting and crystallinity of samples with PVDF.

Property	ABS/Bi/PVDF	ABS/Bi/PVDF	Neat PVDF
	50/25/25	25/50/25	powder
Peak melting point (PVDF) (°C)	160.0	160.2	160.4
Enthalpy of melting (PVDF) (J/g)	1.8	3.6	4.5
Crystallinity (PVDF) (%)	6.9	13.8	4.3

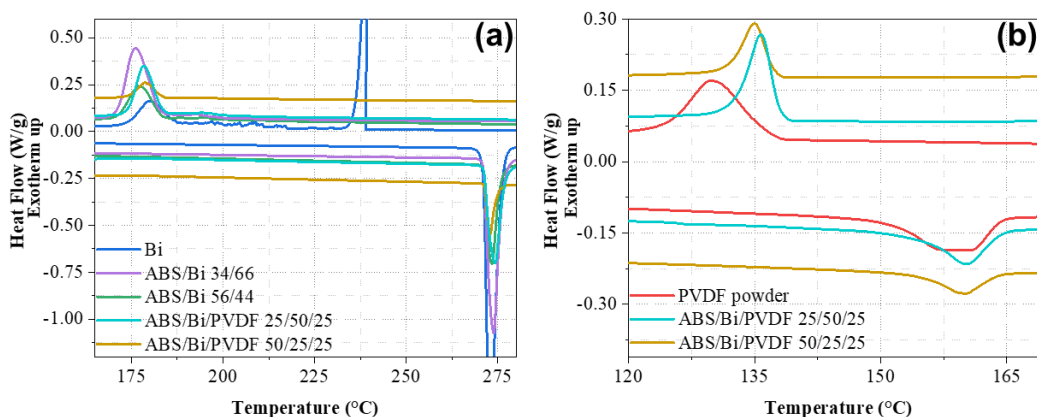


Figure 3.6: DSC of samples with (a) Bi and (b) PVDF.

TGA experiments were performed to evaluate the thermal stability of the 3D-printed pads. Figure 3.7(a) compares the weight loss of pads containing Bi and the ABS matrix with neat ABS as the temperature increases to 600°C. As it can be seen, the rate of decomposition is the same for the neat polymer and the composites, indicating similar thermal degradation mechanism. In addition, the residual masses at 600°C provide validation for the composites possessing the correct ratios of ABS and filler material. This is because ABS will not leave any char residue even at temperatures well above the decomposition temperature (440°C)[29], thus any remaining mass would be solely due to neat Bi. The degradation onset temperature and decomposition temperature of the neat ABS are 410°C and 431°C, respectively. Incorporation of bismuth slightly decreases the

ABS degradation temperature by about 20°C. For instance, the ABS/Bi 34/66 composite decomposes at 418°C, instead of 431°C. It has been observed that incorporation of metal nanoparticles such Ni, and Pd, tends to increase the thermal stability of polymers, whereas in other instances the opposite has also been reported.[30, 31] We infer that bismuth particles may help catalyze the thermal degradation of ABS.

TGA experiments were performed for the composites containing PVDF as well as for neat PVDF powder. The polymer backbone of PVDF starts to degrade at 416°C and fully decomposes at 464°C as shown in Figure 3.7(b). On the other hand, filaments containing both polymers, ABS and PVDF, show two distinct degradation mechanisms as readily observed in Figure 3.7(b). In addition, the residual mass of thermally decomposed filaments containing PVDF includes not only bismuth but also about 15 wt% char residue[32, 33] from PVDF; therefore, this needs to be taken into account if TGA is used to confirm composition of such filaments. Similar to the thermal stability observed in the ABS/Bi composites, increasing the bismuth content results in a slight decrease in the degradation onset temperature. For the composite with the highest Bi amount, ABS/Bi/PVDF 25/50/25, the material starts to degrade at 394°C, which represents an approximate decrease of 15°C from the ABS filament.

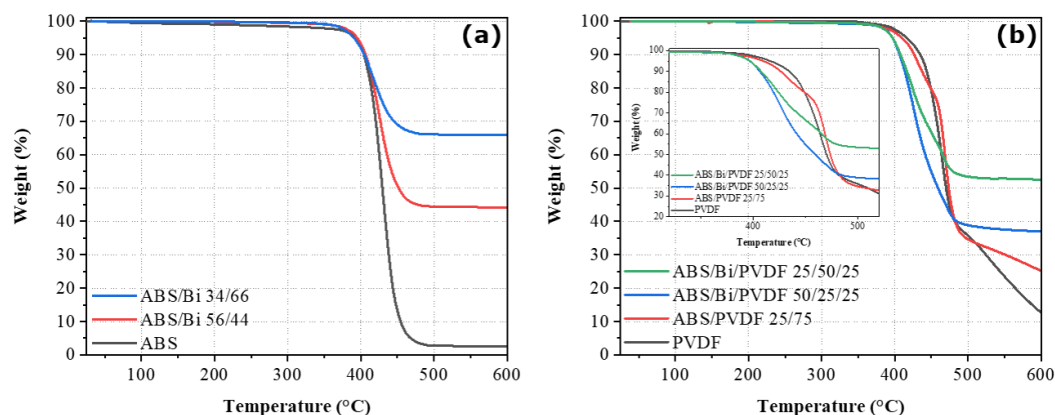


Figure 3.7: TGA of (a) printed samples without PVDF and (b) with PVDF.

In addition to the analysis presented above, TGA experiments were performed at different heating rates to estimate activation energy for the thermal decomposition of the composites. As expected, when the heating rate increases, the samples degrade at higher temperatures, thus the measured thermal stability increases. Using Equation 3, the thermal activation energy slightly decreases from 11.0 kJ/mol for the filaments without Bi to 10.6 kJ/mol for the ones having the highest Bi concentration.

3.3.4 Mechanical Properties

The results of the tensile testing for the 1.75E filaments and 0.5P, including the maximum stress and strain and Young's modulus, are listed in Table 3.3, and shown in Figure 3.8.

Table 3.3: Mechanical properties for the 1.75E and 0.5P filaments.

Sample	Maximum Strain (%)	Maximum Stress (MPa)	Young's Modulus (GPa)
	1.75E/0.5P	1.75E/0.5P	1.75E/0.5P
ABS	5.3±1.9 / 2.8±0.2	33.8±3.0 / 31.9±2.1	1.6±0.2 / 2.2±0.1
ABS/Bi 56/44	3.8±0.5 / 2.6±0.9	37.1±2.7 / 14.8±1.9	2.1±0.1 / 1.4±0.4
ABS/Bi 34/66	4.7±0.9 / 1.8±0.7	31.5±0.3 / 14.9±2.0	2.5±0.4 / 1.9±0.2
ABS/Bi/PVDF 50/25/25	2.6±0.1 / 1.2±0.4	29.5±3.2 / 10.9±2.4	1.9±0.3 / 1.2±0.1
ABS/Bi/PVDF 25/50/25	2.9±0.1 / 1.4±0.2	33.8±2.2 / 14.0±1.7	2.1±0.1 / 1.6±0.2

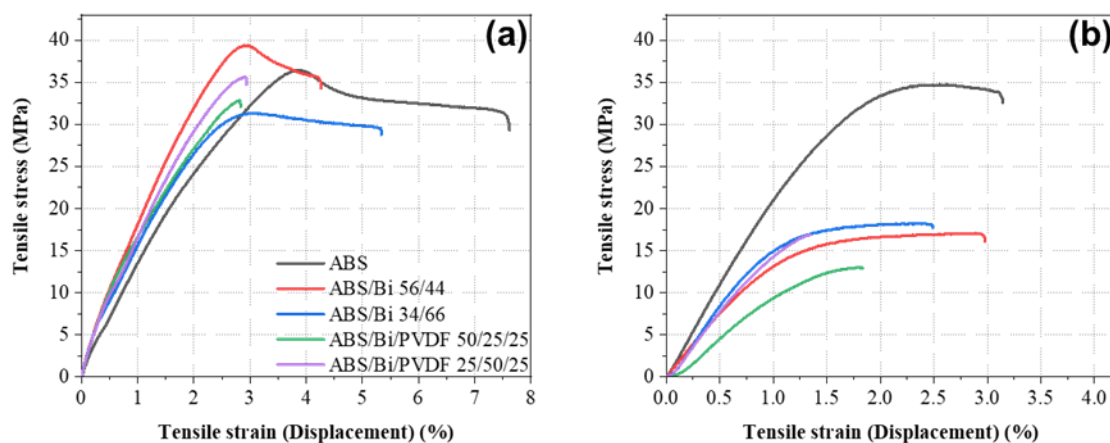


Figure 3.8: Tensile stress and strain for (a) 1.75E filaments and (b) 0.5P filaments.

All the 1.75E filaments have similar maximum stress (averaging 33.2 ± 2.5 MPa) and corresponding strain at maximum stress (averaging 3.09 ± 0.37 %). In addition, all the samples possess a similar Young's modulus (averaging 2.0 ± 0.3 GPa) as well. It is interesting to notice that samples with PVDF show a significant reduction in elongation. This result is in agreement with a previous work showing that the weaker mechanical properties of PVDF reduce elongation of a PVDF/ABS composite material[16]. We infer that all of the 1.75E filaments experience a necking phenomenon, where the filament gets thinner as it extends[34], which is expected in thicker materials, while none of the 0.5P filaments exhibit this behavior.

The maximum stress of the neat ABS sample remains unchanged when the diameter of the filament decreases from 1.75 to 0.5 mm. However, 0.5P filament samples containing bismuth or PVDF can only withstand half as much maximum stress when compared to the

corresponding 1.75E samples. This phenomena has been observed before, where thin ABS filaments exhibit greater maximum stress and strain at break than blended or composite filaments[14]. The difference in mechanical response from filaments having the chemical composition but different diameters is likely due to the filament fabrication process. Because the 0.5P filaments average 600 μm in diameter, enough Bi particles at the site of the printing nozzle may impede polymer flow, causing the polymer matrix to have regions of higher or lower filler concentrations. This in turn weakens the overall network, which causes a decrease in the mechanical strength of filaments with filler material. The 1.75E filaments possess a large enough diameter to make this phenomena negligible. When considering how fillers affect the maximum stress of the 0.5P filaments when compared against neat ABS, Table 3.3 shows that different concentrations of Bi and PVDF reduce the maximum stress by similar amounts (averaging a 54% and 61% change in MPa, respectively). However, there is no significant difference in the maximum stress between all the composite filaments (averaging 13.6 ± 2.0 MPa). In addition, the tensile strain at break of the 0.5P filaments are similar to each other. The samples containing PVDF do not elongate as much, which is similar to the 1.75E filament specimen. Based on these data, adding Bi significantly changes the maximum stress at break, although different concentrations do not have a considerable influence on the resulting mechanical properties. In addition, PVDF reduces the maximum elongation, which could be due to the crystallinity of the polymer making the overall composite more brittle and increasing phase separation between ABS and PVDF.

3.3.5 Properties of Multifunctionality

A 1.2 cm thick 3D-printed pad containing 34 wt% ABS and 66 wt% Bi with a density of 1.0 g/cm³ was exposed to gamma radiation from a Cs-137 source and its shielding ability was determined by TLD measurements. Considering the attenuation coefficient for Bi at 0.6617 MeV to be 0.11618 cm²/g, the estimated attenuation is 13%, compared to 15% measured experimentally. A 50% attenuation of the Cs-137 gamma rays would require the 3D-printed pad to have a thickness of 6 cm. For comparison purposes, a pure lead block, having a density of 11.34 g/cm³ and x-ray mass attenuation coefficient of 0.11366 cm²/g, would need to be 0.54 cm thick to shield 50% of the Cs-137 gamma rays. Although a pure lead block would be a more effective radiation shield, it poses serious and deleterious health effects. When higher-order terms in Equation 1 are negligible and the density of a composite material is a linear combination of its constituents, Equation 1 can readily predict radiation attenuation. However, casting composite materials and more importantly printing composite materials can lead to gaps and porosity, which results in a decreased bulk density and thus a deviation from the estimated values.

Because all the filaments contained ABS, which is soluble in the organic solvents chosen, the three samples, ABS, ABS/Bi 56/44, and ABS/Bi/PVDF 50/25/25, readily dissolved in their vials. It should be noted that for every solvent, which includes xylene, toluene, and chloroform, the filament containing PVDF took longer to show initial signs of dissolution, such as swelling and partial disintegration. Specifically, in chloroform, the ABS and ABS/Bi 56/44 samples exhibited many pieces peeling off the filaments after ten minutes, while it took twenty minutes for the ABS/Bi/PVDF 50/25/25 samples to exhibit the same phenomenon. Furthermore, after twenty minutes, the ABS was completely

dissolved, whereas the solution containing the ABS/Bi 56/44 was opaque and black while the solution containing the ABS/Bi/PVDF 50/25/25 was much clearer. With regards to using these multifunctional filaments in extreme environments where harsh solvents would be present, the ABS/Bi/PVDF 50/25/25 filament was observed to possess a greater chemical resistance because it showed signs of partial dissolution after twice as much time had elapsed.

3.4 Conclusions

In this work, multifunctional ABS-composite filaments were successfully fabricated using a solvent treatment, where the Bi filler and PVDF polymer were incorporated homogeneously as confirmed by FTIR and MXRF. Thermal properties of the filaments were investigated to evaluate the phase transformations, percent crystallinity, and thermal stability. The thermal analyses showed that the glass transition of 105°C for ABS did not change for the composites, increasing the filler amount increased the PVDF crystallinity, and the thermal stability decreased for the samples with the most Bi concentration, where composites with and without PVDF showed a reduction of 20°C and 15°C, respectively. Mechanical testing showed that adding Bi filler reduces the maximum engineered stress of the filaments, but that increasing the Bi concentration did not further significantly modify the mechanical strength. Radiation attenuation data proved that these composites can shield against incident gamma rays and that the polymer did not degrade. Printing with fewer gaps, thereby reducing the porosity, will effectively increase the bulk density of the printed parts and shield radiation to a greater extent. Testing the chemical resistance against organic solvents showed that filaments containing PVDF exhibited signs

of partial dissolution after twice as much time had elapsed when compared to filaments without PVDF.

References

1. M.K. Thompson, G. Moroni, T. Vaneker, G. Fadel, R.I. Campbell, I. Gibson, A. Bernard, J. Schulz, P. Graf, B. Ahuja, F. Martina, Design for Additive Manufacturing: Trends, opportunities, considerations, and constraints, *Cirp Ann-Manuf Techn* 65(2) (2016) 737-760.
2. L.M. Maiyar, S. Singh, V. Prabhu, M.K. Tiwari, Part segregation based on particle swarm optimisation for assembly design in additive manufacturing, *Int J Comput Integ M* 32(7) (2019) 705-722.
3. J.R.C. Dizon, A.H. Espera, Q.Y. Chen, R.C. Advincula, O Mechanical characterization of 3D-printed polymers, *Addit Manuf* 20 (2018) 44-67.
4. L. Szentmiklosi, B. Maroti, Z. Kis, J. Janik, L.Z. Horvath, Use of 3D mesh geometries and additive manufacturing in neutron beam experiments, *J Radioanal Nucl Ch* 320(2) (2019) 451-457.
5. M. Attaran, The rise of 3-D printing: The advantages of additive manufacturing over traditional manufacturing, *Bus Horizons* 60(5) (2017) 677-688.
6. N.P. Levenhagen, M.D. Dadmun, Interlayer diffusion of surface segregating additives to improve the isotropy of fused deposition modeling products, *Polymer* 152 (2018) 35-41.
7. B. Mooney, K.I. Kourousis, R. Raghavendra, Plastic anisotropy of additively manufactured maraging steel: Influence of the build orientation and heat treatments, *Addit Manuf* 25 (2019) 19-31.

8. N.P. Levenhagen, M.D. Dadmun, Bimodal molecular weight samples improve the isotropy of 3D printed polymeric samples, *Polymer* 122 (2017) 232-241.
9. J.F. Christ, N. Aliheidari, A. Ameli, P. Potschke, 3D printed highly elastic strain sensors of multiwalled carbon nanotube/thermoplastic polyurethane nanocomposites, *Mater Design* 131 (2017) 394-401.
10. E.Y. Teo, S.Y. Ong, M.S.K. Chong, Z.Y. Zhang, J. Lu, S. Moochhala, B. Ho, S.H. Teoh, Polycaprolactone-based fused deposition modeled mesh for delivery of antibacterial agents to infected wounds, *Biomaterials* 32(1) (2011) 279-287.
11. M. Alhijjaj, P. Belton, S. Qi, An investigation into the use of polymer blends to improve the printability of and regulate drug release from pharmaceutical solid dispersions prepared via fused deposition modeling (FDM) 3D printing, *Eur J Pharm Biopharm* 108 (2016) 111-125.
12. G. Kollamaram, D.M. Croker, G.M. Walker, A. Goyanes, A.W. Basit, S. Gaisford, Low temperature fused deposition modeling (FDM) 3D printing of thermolabile drugs, *Int J Pharmaceut* 545(1-2) (2018) 144-152.
13. J. Ceh, T. Youd, Z. Mastrovich, C. Peterson, S. Khan, T.A. Sasser, I.M. Sander, J. Doney, C. Turner, W.M. Leevy, Bismuth Infusion of ABS Enables Additive Manufacturing of Complex Radiological Phantoms and Shielding Equipment, *Sensors-Basel* 17(3) (2017).
14. S. Woosley, N.A. Galehdari, A. Kelkar, S. Aravamudhan, Fused deposition modeling 3D printing of boron nitride composites for neutron radiation shielding, *Journal of Materials Research* 33(22) (2018) 3657-3664.

15. G.P. Kar, S. Biswas, S. Bose, X-ray micro computed tomography, segmental relaxation and crystallization kinetics in interfacial stabilized co-continuous immiscible PVDF/ABS blends, *Polymer* 101 (2016) 291-304.
16. G.P. Kar, S. Biswas, S. Bose, Simultaneous enhancement in mechanical strength, electrical conductivity, and electromagnetic shielding properties in PVDF-ABS blends containing PMMA wrapped multiwall carbon nanotubes, *Phys Chem Chem Phys* 17(22) (2015) 14856-14865.
17. S. Abdalla, A. Obaid, F.M. Al-Marzouki, Preparation and characterization of poly(vinylidene fluoride): A high dielectric performance nano-composite for electrical storage, *Results Phys* 6 (2016) 617-626.
18. J. Liu, X. Shen, Y.P. Zhao, L. Chen, Acryloylmorpholine-Grafted PVDF Membrane with Improved Protein Fouling Resistance, *Ind Eng Chem Res* 52(51) (2013) 18392-18400.
19. F. Liu, N.A. Hashim, Y.T. Liu, M.R.M. Abed, K. Li, Progress in the production and modification of PVDF membranes, *J Membrane Sci* 375(1-2) (2011) 1-27.
20. D. Lin-Vien, N.B. Colthup, W.G. Fateley, J.G. Grasselli, CHAPTER 3 - Halocompounds, in: D. Lin-Vien, N.B. Colthup, W.G. Fateley, J.G. Grasselli (Eds.), *The Handbook of Infrared and Raman Characteristic Frequencies of Organic Molecules*, Academic Press, San Diego, 1991, pp. 29-44.
21. H. Guo, Y. Zhang, F. Xue, Z. Cai, Y. Shang, J. Li, Y. Chen, Z. Wu, S. Jiang, In-situ synchrotron SAXS and WAXS investigations on deformation and α - β transformation of uniaxial stretched poly (vinylidene fluoride), *CrystEngComm* 15(8) (2013) 1597-1606.

22. Y. Wang, M. Cakmak, Spatial variation of structural hierarchy in injection molded PVDF and blends of PVDF with PMMA. Part II. Application of microbeam WAXS pole figure and SAXS techniques, *Polymer* 42(9) (2001) 4233-4251.
23. G. Beaucage, Approximations leading to a unified exponential/power-law approach to small-angle scattering, *Journal of Applied Crystallography* 28(6) (1995) 717-728.
24. C. Beaucage, D.W. Schaefer, Structural studies of complex systems using small-angle scattering: a unified Guinier/power-law approach, *Journal of Non Crystalline Solids* 172 (1994) 797-805.
25. D.G. Archer, Enthalpy of fusion of bismuth: A certified reference material for differential scanning calorimetry, *J Chem Eng Data* 49(5) (2004) 1364-1367.
26. C.D. Zou, Y.L. Gao, B. Yang, Q.J. Zhai, Melting and undercooling of bismuth nanocrystals by solvothermal synthesis, *Physica B* 404(21) (2009) 4045-4050.
27. D. Turnbull, Formation of Crystal Nuclei in Liquid Metals, *J Appl Phys* 21(10) (1950) 1022-1028.
28. C. Marega, A. Marigo, Influence of annealing and chain defects on the melting behaviour of poly (vinylidene fluoride), *European Polymer Journal* 39(8) (2003) 1713-1720.
29. J. Feng, C. Carpanese, A. Fina, Thermal decomposition investigation of ABS containing Lewis-acid type metal salts, *Polym Degrad Stabil* 129 (2016) 319-327.
30. J.Y. Lee, Y.G. Liao, R. Nagahata, S. Horiuchi, Effect of metal nanoparticles on thermal stabilization of polymer/metal nanocomposites prepared by a one-step dry process, *Polymer* 47(23) (2006) 7970-7979.

31. S.M. Lebedev, O.S. Gefle, S.N. Tkachenko, Metal-polymer PVDF/nickel composites and evaluation of their dielectric and thermal properties, *J Electrostat* 68(2) (2010) 122-127.
32. Z.W. Ouyang, E.C. Chen, T.M. Wu, Thermal Stability and Magnetic Properties of Polyvinylidene Fluoride/Magnetite Nanocomposites, *Materials* 8(7) (2015) 4553-4564.
33. X. Jiang, C. Xu, Y. Wang, Y. Chen, Polyvinylidene Fluoride/Acrylonitrile Butadiene Rubber Blends Prepared Via Dynamic Vulcanization, *Journal of Macromolecular Science, Part B* 54(1) (2015) 58-70.
34. W.F. Hosford, *Mechanical behavior of materials*, Cambridge university press 2010.
35. A.H. El-Kateb, R.A.M. Rizk, A.M. Abdul-Kader, Determination of atomic cross-sections and effective atomic numbers for some alloys, *Ann Nucl Energy* 27(14) (2000) 1333-1343.
36. A. Canel, H. Korkut, T. Korkut, Improving neutron and gamma flexible shielding by adding medium-heavy metal powder to epoxy based composite materials, *Radiat Phys Chem* 158 (2019) 13-16.
37. I.I. Bashter, Calculation of radiation attenuation coefficients for shielding concretes, *Ann Nucl Energy* 24(17) (1997) 1389-1401.
38. S.J. Zinkle, G.S. Was, Materials challenges in nuclear energy, *Acta Mater* 61(3) (2013) 735-758.
39. J. Ilavsky, P.R. Jemian, A.J. Allen, F. Zhang, L.E. Levine, G.G. Long, Ultra-small-angle X-ray scattering at the Advanced Photon Source, *Journal of Applied Crystallography* 42(3) (2009) 469-479.

40. J. Ilavsky, Nika: software for two-dimensional data reduction, *Journal of Applied Crystallography* 45(2) (2012) 324-328.
41. J. Ilavsky, P.R. Jemian, Irena: tool suite for modeling and analysis of small-angle scattering, *Journal of Applied Crystallography* 42(2) (2009) 347-353.
42. J.S. Temenoff, A.G. Mikos, *Biomaterials : the intersection of biology and materials science*, Upper Saddle River 2008.
43. M.R. Kessler, *Advanced topics in characterization of composites*, Trafford Publishing 2004.
44. A.P. Gray, Polymer Crystallinity Determinations by Dsc - Anal, *Abstr Pap Am Chem S* (Feb) (1970) 82-&.
45. K.M. Lu, W.J. Lee, W.H. Chen, T.C. Lin, Thermogravimetric analysis and kinetics of co-pyrolysis of raw/torrefied wood and coal blends, *Appl Energ* 105 (2013) 57-65.

Chapter 4 Development of Antimicrobial PLA Composites for Fused Filament Fabrication

4.1 Introduction

The increasing awareness that traditional plastics derived from petrochemicals can accumulate in the environment and elicit long-lasting deleterious effects have galvanized efforts to develop and bring to market replacement polymers that are more amenable to recycling and upcycling. One such polymer, poly (lactic acid) (PLA), has garnered much interest due to its lifecycle and material properties. PLA can be synthesized from renewable resources and is biodegradable when composted at high temperatures and humidity [1–3]. Its chemical, thermal, and mechanical properties also lend itself numerous advantages: it is biocompatible, easily processable, and has a high strength and Young's modulus, even matching or exceeding that of polystyrene and poly (ethylene terephthalate), two of the world's most common plastics made from petrochemicals [4–8]. Because of this, PLA is used within industries spanning medicine, food and agriculture, and packaging.

Due to these beneficial characteristics, neat PLA is also one of the most popular polymers used in additive manufacturing (AM), especially within the domain of fused filament fabrication (FFF), a 3D printing technology [6,9]. FFF works by heating thermoplastic filaments past their glass transition temperature or melting point and extruding the softened material through a nozzle onto a bed, where the filament cools down slow enough to adhere to the layers placed below and above it. Despite past advances in FFF technology, a barrier towards future growth and expanded applications is the relatively small amount of feedstock polymers currently available for use [10,11].

To enhance the existing materials properties of PLA, and introduce new characteristics, many groups have investigated making composites, such as incorporating graphene-based components to increase the thermomechanical stability or imbue electrical conductivity [12–14] or blending PLA with other polymers to make a more mechanically and thermally stable material [15–20]. Although PLA is generally more resistant to biodegradation than other natural polymers [8,21], some applications such as transporting agricultural products or medical equipment demand more extensive antimicrobial properties. To meet this demand, previous work has demonstrated that PLA can be combined with bactericides, such as the ceramics ZnO and TiO₂. However, composites of this form have not been thoroughly explored in the realm of FFF technology [22–28]. Another issue to take note of is that while PLA/ceramic composites have been investigated for some time, much of the current research is focused on utilizing nanoparticles. Beyond the potential toxicity attributed to ZnO and TiO₂ nanoparticles [29–32], many of these studies present varied results with regards to material properties [22,24,33,34]. Breaking with this current trend, we contend that PLA composites incorporating micron-sized or agglomerated nanoparticle forms of either ZnO, TiO₂, or both, could address some of these issues.

Another challenge encountered during the development of PLA/ceramic composites for FFF technology is the stiffness and brittleness imparted on the material when ceramics are incorporated [35]. To remediate this, further material advances can be made in PLA composites through inclusion of poly-(ethylene glycol) (PEG), another biocompatible and biodegradable polymer, which acts as a miscible plasticizer in PLA and can be added in quantities up to 20 wt% without causing phase separation [15,36,37]. As

an added benefit, PEG can be conjugated to target molecules (e.g., drugs) or easily modified to produce specific attributes [37–41]. Due to these properties, incorporating PEG into filaments for 3D printing can lead to the development of a wide range of extremely useful multifunctional composite filaments with tunable material properties.

In this work, tunable, multifunctional antimicrobial composite PLA filaments were developed and characterized for FFF technology. Antimicrobial functionalities were successfully added to PLA feedstock by uniformly dispersing varying amounts of ceramic ZnO and TiO₂ fillers in a PLA/chloroform solution. Additional chemical, thermal, and mechanical functionalities were imbued with the addition of different molecular weight PEG at 10 wt% to the PLA/chloroform solution. Each specimen was thoroughly combined and the resulting mixture was cast and subsequently pelletized. Smooth and homogenous printable filaments were created by extruding the composite pellets. The chemical structure of the filaments was investigated to ensure homogeneity, thermal stability was determined to characterize degradation and range of feasibility, phase transitions were reviewed to ensure allowable use in FFF, mechanical limits were determined to understand structure-property relationships, and antimicrobial efficacy was tested.

4.2 Materials and Methods

4.2.1 Materials

PLA 4043D pellets were supplied by Filabot. TiO₂ powder was supplied by Alfa-Aesar. Chloroform, ZnO powder, and PEG (1k, 2k, and 10k) were purchased through Thermo Fisher Scientific.

4.2.2 Feedstock and Filament Fabrication

The overall process for fabricating filament feedstocks was similar to the work previously described for acrylonitrile butadiene styrene (ABS) [42]. PLA pellets were combined with the antimicrobial agents (TiO_2 , ZnO) and PEG to achieve the desired weight ratios. Chloroform was added to PLA to achieve a 1:5 *w/w* solution. The chloroform-PLA mixture was manually stirred for 30 s before being placed in an oven at 25 °C for 16 h to fully dissolve the PLA. If added, fillers were then suspended in the solution. To decrease the viscosity and allow for more homogenous stirring, an additional 15 mL of chloroform was added and the resulting slurry was thoroughly combined using a planetary mixer at 2000 rpm for two minutes. The mixture was then cast onto a clean Teflon-coated plate and left to dry in a fume hood for at least 12 h. This allowed excess chloroform to evaporate from the casted composite, while retaining enough malleability in the composite to cut it into 1 cm × 1 cm squares.

The composite squares were placed in a vacuum oven at 65 °C and 80 kPa negative pressure for at least 24 h, to fully evaporate the remaining chloroform. The dried samples were then fed into a Filabot EX2 extruder heated to 175 °C and set to its maximum extrusion rate (2 lb/h). A container of room temperature DI water was placed a meter below the extruder. Thus, gravity pulled the filaments into the water, which cooled and hardened the samples and produced naturally coiled filaments. The filament samples created using this method and their compositions are listed in Table 4.1.

Table 4.1: List of the composite filaments made in this study and their designations.

Sample	Material
PLA	100 wt% PLA
PLA/PEG1k 90/10	90 wt% PLA, 10 wt% PEG (MW, 1 kDa)
PLA/PEG2k 90/10	90 wt% PLA, 10 wt% PEG (MW, 2 kDa)
PLA/PEG10k 90/10	90 wt% PLA, 10 wt% PEG (MW, 10 kDa)
PLA/ZnO 90/10	90 wt% PLA, 10 wt% ZnO
PLA/ZnO 80/20	80 wt% PLA, 20 wt% ZnO
PLA/ZnO 70/30	70 wt% PLA, 30 wt% ZnO
PLA/ZnO/PEG2k 80/10/10	80 wt% PLA, 10 wt% ZnO, 10 wt% PEG (MW, 2 kDa)
PLA/ZnO/PEG2k 70/20/10	70 wt% PLA, 20 wt% ZnO, 10 wt% PEG (MW, 2 kDa)
PLA/ZnO/PEG2k 60/30/10	60 wt% PLA, 30 wt% ZnO, 10 wt% PEG (MW, 2 kDa)
PLA/TiO ₂ 90/10	90 wt% PLA, 10 wt% TiO ₂
PLA/TiO ₂ 80/20	80 wt% PLA, 20 wt% TiO ₂
PLA/TiO ₂ 70/30	70 wt% PLA, 30 wt% TiO ₂
PLA/TiO ₂ /PEG2k 80/10/10	80 wt% PLA, 10 wt% TiO ₂ , 10 wt% PEG (MW, 2 kDa)
PLA/TiO ₂ /PEG2k 70/20/10	70 wt% PLA, 20 wt% TiO ₂ , 10 wt% PEG (MW, 2 kDa)
PLA/TiO ₂ /PEG2k 60/30/10	60 wt% PLA, 30 wt% TiO ₂ , 10 wt% PEG (MW, 2 kDa)

4.2.3 Characterization Techniques

4.2.3.1 Chemical Structure Characterization

Chemical structural characterization of the PLA filaments was carried out using Fourier transform-infrared spectroscopy (FTIR) and micro X-ray fluorescence (MXRF). A Nicolet iS50 FTIR instrument was used to assess polymer functional groups by measuring absorbance from 525 to 4000 cm^{-1} (32 scan increments) and subtracting the background values. A Bruker M4 Tornado MXRF instrument was used to generate elemental color maps of filament cross sections to examine ceramic distribution. The acquisition parameters included an X-ray tube operating at 50 kV and 200 μA , a spectrometer operating at 40 keV and 130 kcps, a spot size of 20 μm , a dwell time of 5 ms per pixel, and a step size of 10 μm (cross section) by 20 μm (top down).

Particle size distribution of the ZnO and TiO₂ ceramic fillers was assessed using a Horiba particle size analyzer LA-960. Three different procedures were used in this determination: (1) mixing the individual fillers in a vial of water and circulating the slurry

in the reservoir of the instrument; (2) mixing the individual fillers in a vial of water and pipetting the slurry in the reservoir without circulation; and (3) placing the individual fillers in the reservoir with circulation and 30 s of ultrasonication employed. All three procedures were performed in triplicate. During the analysis using the software with instrument, refractive indices of 2.00 and 2.75 were used for ZnO and TiO₂, respectively.

4.2.3.2 Thermal Characterization

To investigate thermal properties of the PLA filaments, differential scanning calorimetry (DSC) and thermogravimetric analysis (TGA) were performed. DSC was performed using a TA Instruments DSC Q20 series instrument where each sample had a mass between 5 and 10 mg and the protocol ran under nitrogen with a flowrate of 5 mL/min. The protocol started by heating from room temperature to 200°C at a rate of 5°C/min, then cooling to 120°C at a rate of 10°C/min, a slower cooling to 80°C at a rate of 1°C/min, a cooling to 25°C at a rate of 10°C/min, and ending with heating to 200°C at a rate of 5°C/min. The first heating step in the procedure (to 200°C) was performed to measure the melting point temperature, T_m , and latent heat of fusion, ΔH_f , of the different PLA composites. To simulate the thermal environment of a realistic 3D printed part, which includes heating in the nozzle, cooling on a bed, and then used, the glass transition temperature, T_g , was obtained upon the second heating. In addition to determining material properties, slowing the cooling rate at 120°C to 1°C/min was done to help induce crystallization, although it was to no avail. Using the latent heat of fusion, the PLA weight percent of the sample, w , and the theoretical enthalpy of formation $\Delta H_f'$, taken as 93.0 J/g [43], the percent crystallinity, X_c , of each sample was determined using Equation 4.1. Based on previous experiments and comparative measurements, the error associated with

this instrument is under 3%.

$$X_c = \frac{\Delta H_f}{w\Delta H'_f} \times 100\% \quad \text{Equation 4.1}$$

TGA was performed using a TA Q50 Series instrument, where each sample had a mass of 10 ± 1 mg and was heated from room temperature to 600 C at heating rates of 5, 8, 10, 13, and 15 °C/min under a nitrogen flowrate of 40 mL/min. The mass percent and mass derivative curves were measured to evaluate thermal stability, where the degradation temperature, $T_{d5\%}$, was taken when the sample had lost 5% of its initial mass, and the decomposition temperature, T_{dMax} , was taken as the maximum of the mass derivative curve. Pyrolysis kinetic parameters were also assessed using Equation 4.2, known as the Coats–Redfern equation [44–47]. Using the mass-loss percent, α , taken from the TGA experiments, the absolute temperature, T , along with the heating rate, β , it is possible to estimate the thermal activation energy, E , and pre-exponential factor, A . This is done by assuming a reaction model, $g(\alpha)$, and plotting $\ln(g(\alpha)/T^2)$ against $1/T$, which in theory produces a linear relationship with slope $-E/R$ and intercept $\ln(AR/\beta E)$. This method assumes that a single mechanism is responsible for the thermal decomposition. As such, pyrolysis kinetic parameters were calculated using different heating rates, reaction models, and temperature intervals. Based on comparative measurements and calibration testing from the manufacturer, the error associated with this instrument is under 1%.

$$\ln\left(\frac{g(\alpha)}{T^2}\right) = \ln\left(\frac{AR}{\beta E}\right) - \frac{E}{RT} \quad \text{Equation 4.2}$$

4.2.3.3 Mechanical Characterization

Mechanical characterization was performed using tensile testing. Each sample was cut to 10-cm length and placed in an Instron 4340B instrument, where filament ends (3 cm)

were clasped, leaving a 4 cm section in the middle of the filament. At a constant rate of 8.333×10^{-3} mm/min, the filaments were stretched until breaking. At least 3 replicates of each filament material were tested. Engineering stress versus strain curves were generated, and the Young's modulus, as well as the maximum stress and strain values, were determined. Based on comparative measurements and calibration testing from the manufacturer, the error associated with this instrument is under 1%.

4.2.3.4 Antimicrobial Efficacy

Antimicrobial efficacy of the different PLA composites was assessed by incubating filaments (0.5–2 g) in soil at 30°C for 1 month. Soils were moistened to saturation every 2–3 days. Two trials were run. The first trial used one of every type of filament produced and the second trial used PLA and PLA/ceramic 90/10 composite filaments with or without the addition of 10 wt% gelatin to the soil. Gelatin was added as a possible means to stimulate growth of microorganisms capable of degrading PLA[48]. Following the incubation period, samples were removed from the soil and partially cleaned and inspected in a series of steps. First, small dirt particles were partially dislodged from dry filaments using a vortex mixer. Second, each specimen was submerged individually in sterile water and vortex mixed. After this washing, a crystal violet solution was used to stain the samples. Following this, a 30% acetic acid solution was used to partially de-stain the filaments. At each step, filaments were visually inspected by stereo microscopy using a Leica EZ4E to assess the extent of pitting/degradation and microbial colonization.

4.3 Results and Discussion

The particle size distribution analysis produced three parameters of interest for each ceramic filler: D10, D50, and D90, where 10%, 50%, and 90% of the population fall below this value, respectively. These parameters, shown as Tables 4.2 and 4.3, revealed that 80% of the broken up ZnO and TiO₂ particles were approximately between 1 and 7 microns. It should be noted that the ceramic fillers were not broken up via ultrasonication or any other method prior to their incorporation in the PLA/chloroform solution. This means that the particle sizes used in the composite filaments were agglomerated into sizes larger than the nanoscale.

Table 4.2: Average and standard deviations of D10, D50, and D90 particle size distributions for each procedure of ZnO powder.

	Procedure 1		Procedure 2		Procedure 3	
	Average (µm)	Standard Deviation	Average (µm)	Standard Deviation	Average (µm)	Standard Deviation
<i>D10</i>	3.54	0.16	1.38	0.18	1.60	0.26
<i>D50</i>	6.05	0.07	3.12	0.52	3.53	0.24
<i>D90</i>	10.04	0.08	5.55	1.04	6.44	0.11

Table 4.3: Average and standard deviations of D10, D50, and D90 particle size distributions for each procedure of TiO₂ powder.

	Procedure 1		Procedure 2		Procedure 3	
	Average (µm)	Standard Deviation	Average (µm)	Standard Deviation	Average (µm)	Standard Deviation
<i>D10</i>	1.71	0.05	1.40	0.22	2.18	0.53
<i>D50</i>	4.15	0.33	3.37	0.33	4.52	0.85
<i>D90</i>	7.85	1.02	6.39	0.59	7.86	1.20

Examination of the cross-sections of the filaments using a VHX 6000 digital microscope revealed several interesting features (Figures 4.1 and 4.2). The first row of

Figure 4.1 ((a),(b)) shows PLA/ceramic filaments, and while they appear homogenous in the core, a thin shell or crust can be seen. This becomes more apparent in the second row of Figure 4.1 ((c),(d)) which shows PLA/ceramic/PEG2k filaments. A similar core/shell structure is seen but a much thicker crust is observed. Cross sections of PLA/PEG filaments are shown in Figure 4.2, which does not show any observable crust. As discussed later on, the ceramic composite filaments exhibit a greater crystallinity with PEG than without PEG. Based on this data and from the microscopy images in Figures 4.1 and 4.2, it appears that the crust is different from the interior of the filaments. Additionally, because DSC data demonstrates that the filaments are semi-crystalline, it can be inferred that there are amorphous-rich and crystalline-rich regions.

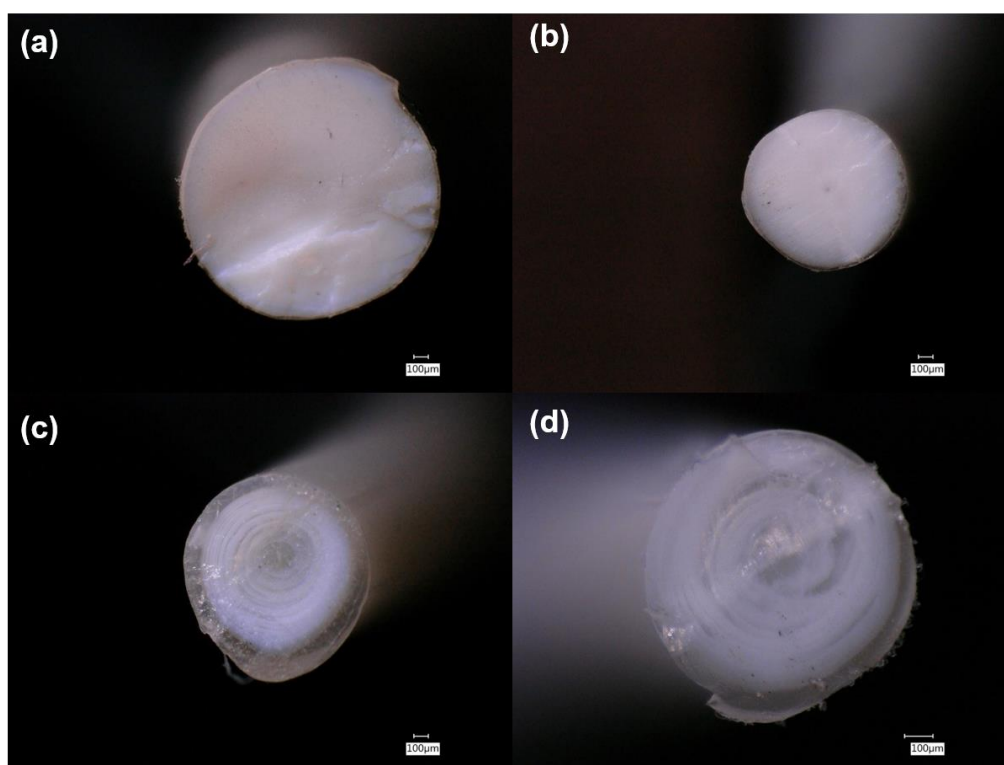


Figure 4.1: Digital microscopy cross-section images of: (a) PLA/TiO₂ 90/10; (b) PLA/ZnO 90/10; (c) PLA/TiO₂/PEG2k 80/10/10; and (d) PLA/ZnO/PEG2k 80/10/10.

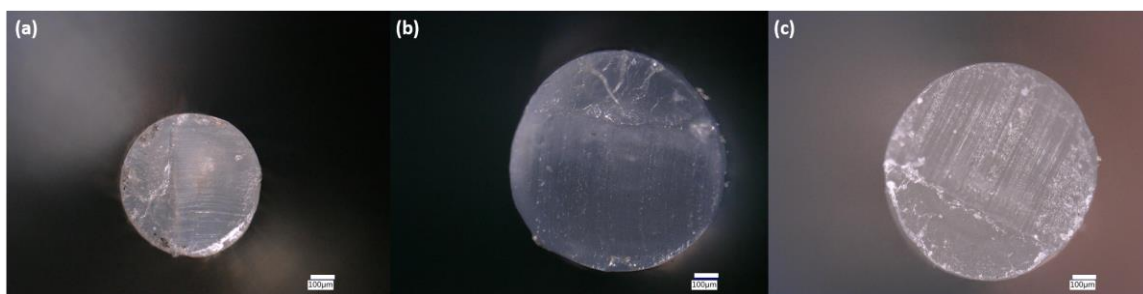


Figure 4.2: Digital microscopy cross-section images of: (a) PLA/PEG1k 90/10; (b) PLA/PEG2k 90/10; and (c) PLA/PEG10k 90/10.

4.3.1 Chemical Structure Characterization

4.3.1.1 FTIR

The chemical structure of the different PLA composite filaments (Table 4.1) was assessed using FTIR. Figure 4.3 shows the FTIR absorbance spectra of a 100% PLA filament compared to PLA composites with 10 wt% ceramic fillers, 10 wt% PEG, or a combination of both. There is a distinctive band at 1757 cm^{-1} indicating a carbonyl group from PLA and one at 2882 indicating $-\text{CH}_2$ stretching from PEG [49–51]. Other notable peaks in Figure 4.3 include $-\text{CH}-$ symmetric and asymmetric bending from 1130 to 1270 cm^{-1} [52]. Because PEG only makes up 10 wt% of the filaments, its typical peaks are not strongly exhibited. This has been observed in previous research, where composites up to 10 wt% PEG resemble neat PLA [50,53]. The major FTIR peaks associated with the functional groups of PLA are detailed in Table 4.4. Overall, the FTIR spectra do not show evidence for the formation of new bonds or moieties, thus demonstrating that no chemical reactions occurred between PLA, PEG, or ceramics and that the filament is a true composite.

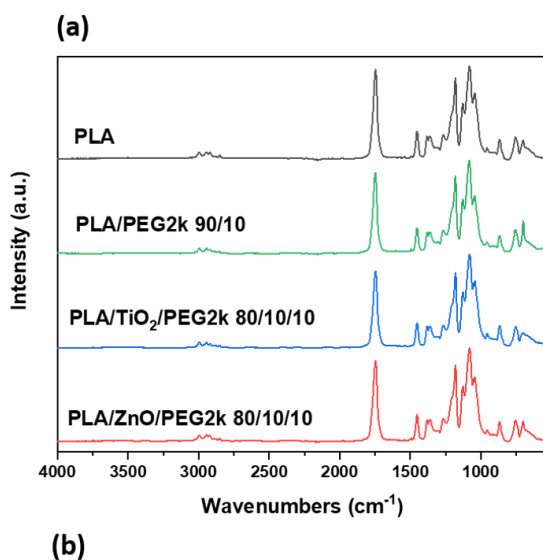
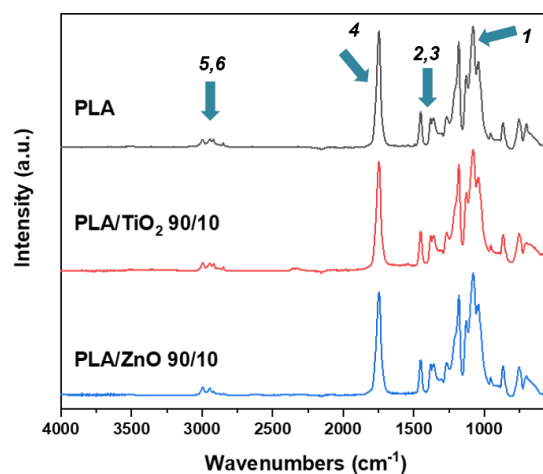


Figure 4.3: FTIR spectra of PLA (a) with 10 wt% ceramic fillers and (b) with 10 wt% PEG. The arrows correspond to peaks that are detailed in Table 4.4 below.

Table 4.4: FTIR peaks associated with the spectra of PLA in Figure 4.3.

Peak Number	Wavenumber (cm^{-1})	Vibrational Mode
1	1080, 1187	C–O stretching
2	1361	Symmetric $-\text{CH}_3$ bending
3	1452	Asymmetric $-\text{CH}_3$ bending
4	1746	C = O stretching
5	2946	Asymmetric $-\text{CH}_3$ stretching
6	2995	Symmetric $-\text{CH}_3$ stretching

4.3.1.2 MXRF

To ensure that the ceramics were successfully incorporated, MXRF data was used to generate an elemental color map representing the amount of metal present, which is a proxy for the Ti and Zn ceramic fillers. The results demonstrate that the ceramic fillers were uniformly distributed (Figure 4.4).

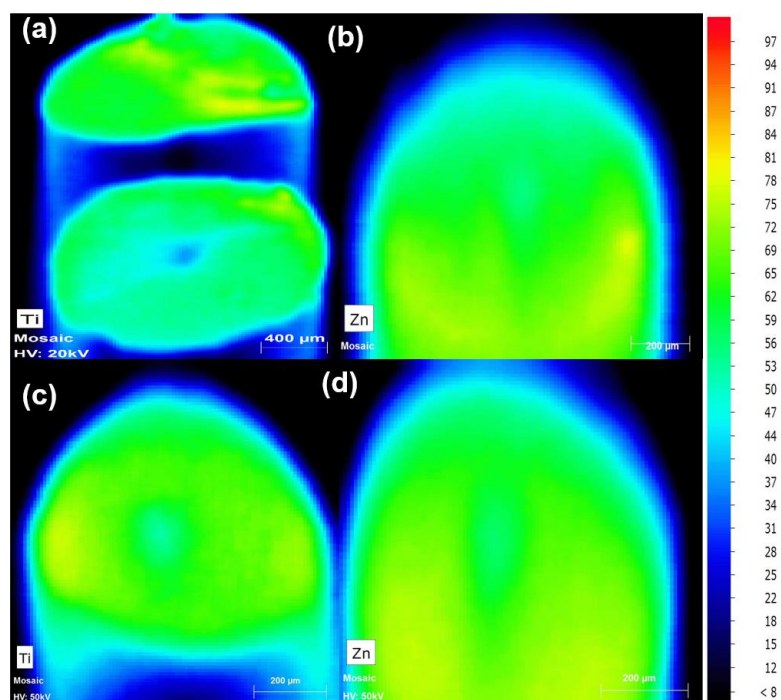


Figure 4.4: MXRF color mapping of: (a) Ti in PLA/TiO₂ 90/10; (b) Zn in PLA/ZnO 90/10; (c) Ti in PLA/TiO₂/PEG2k 80/10/10; and (d) Zn in PLA/ZnO/PEG2k 80/10/10. Increasing amounts of the indicated element are colored from blue to green to red.

4.3.2 Thermal Characterization

4.3.2.1 Thermal Phase Behavior

Thermal characterization provides insight into the phase transitions and stability of a material. This is especially useful when the filaments are going to be used for FFF, which requires heating past the material's glass transition temperature or melting point in a nozzle in order to have a suitable flow and then sufficiently cool on a heating bed so a rigid and

final product can be obtained. While the binding material, in this case PLA, can be used for 3D-printing, if the resulting composite changes the phase transitions enough or lowers the thermal stability by an appreciable amount, then it is no longer a feasible material for FFF applications.

PLA is reported to have a glass transition temperature (T_g) between 55 and 65 °C and a maximum melting point (T_m) of 175–180 °C in the purely l-isomer form, with a 5 °C decrease in T_m for every 1% increase of d-lactate in the polymer [40,54]. Indeed, the manufacturer reports that the neat PLA pellets have a glass transition temperature between 55 and 60 °C as well as a heat distortion temperature of 55 °C. The PLA filaments generated in this study exhibited a T_g of 62 °C and a T_m of 150 °C, suggesting that there is approximately 5% d-lactide within the PLA polymer. Calculating the percent crystallinity can be performed by integrating the heat flow through a sample during the melting transition, which provides information about the microstructure and can be related to explain macroscopic properties such as mechanical strength. It should be noted that some forms of PLA do not readily crystallize and while some research groups report the cold crystallization temperature of PLA and PLA composites, others report that no phase transition was observed at all. That is the case with all the filaments produced in this study; none of the filaments were found to possess a crystallization temperature for the experimental conditions employed in this work, even with the cooling rate of 1 °C/min.

Some researchers have added various fillers to PLA and altered the temperatures at which thermal phase transitions occur [22,33,39,40]. The composite filaments fabricated in this study did exhibit a slight increase in the T_m (between 5 and 7°C), however significant changes in the T_m value were not observed as a function of the amount of the

Ti or Zn ceramic filler incorporated into the material. The thermal phase transitions and percent crystallinity of the filaments fabricated in this study are listed in Table S3. Additionally, the thermograms of a selected representative sample of filaments are shown in Figure 4.5. Incorporation of the ceramic fillers did not alter the T_g of the filaments. Previous studies examining the thermal properties of PLA imbued with ceramic nanocomposites report conflicting results. For example, multiple research groups have shown that ZnO and TiO₂ nanoparticles have no effect on the thermal phase behavior of PLA in the composite form [24,55–57]; however Buzarovska found that the T_g values increased slightly upon the incorporation of TiO₂ nanoparticles [33], while Mallick et al. found that they could no longer detect the T_g or T_c [22], and Carrion et al. observed that increasing amounts of ZnO nanocomposites in polycarbonate/ZnO decreased the T_g [58]. The fact that the T_m and T_g of these ceramic composite materials vary across many laboratory conditions provides ever increasing evidence that additional research is required to assess the underlying micro and macroscopic effects and perform systematic batch testing on the composites as they are fabricated.

Unlike the effect of ceramics on the thermal phase behavior of PLA filaments, the incorporation of PEG significantly lowered the T_g . This phenomenon has been observed before [15,36], which is bolstered by the fact that the T_g of PEG, depending on the molecular weight, can vary between -20 and -60°C . Indeed, incorporating higher molecular weight PEG to PLA had a dramatic effect, where the composite filaments with PEG2k and PEG10k had no observable T_g in the temperature range tested (25 – 200°C). Furthermore, all the ceramic composite filaments containing PEG, except for PLA/ZnO/PEG2k 80/10/10 (which had a T_g of 59°C), did not exhibit an observable T_g in

the temperature range tested. This indicates that chain mobility in the composites is higher than that in the neat filaments and that PEG behaves as a plasticizer in the system. Thus, the processability, or material fabrication, is enhanced by PEG and can support greater amounts of ceramic or other filler, as well as ensuring that fillers and plasticizers are well-dispersed throughout the PLA matrix [39].

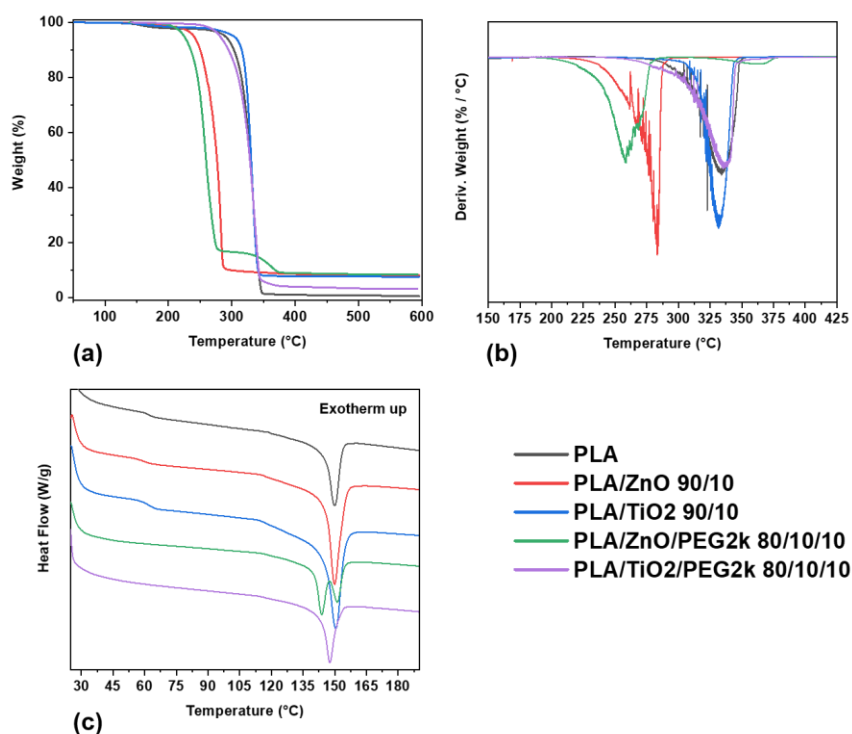


Figure 4.5: Thermograms of selected filaments: (a) TGA; (b) derivative of TGA; and (c) DSC (exotherm up) of the first heating curve.

Although our results revealed little difference between the T_m of the composites and pure PLA filaments, integration of the DSC thermograms revealed that significant changes in PLA crystallinity had occurred (Figure 4.6; Table 4.5). Compared to the PLA filament, which was 25% crystalline, incorporating the polymer plasticizer PEG into PLA led to an increase in crystallinity. Inclusion of 10 wt% PEG1k, PEG2k, or PEG10k yielded filaments with 30%, 32%, and 31% crystalline PLA, respectively. Additionally, the ternary

composite filaments comprising PLA, ceramics, and PEG exhibited double melting peaks (see Figure 4.5 (c)). This behavior was observed for all the ZnO ternary composite filaments and only at higher TiO₂ concentrations (20 wt% and 30wt%), where the two peaks were at most 10 °C apart.

The addition of ZnO increased the crystalline portion of PLA. Increasing the amount of ZnO in the composite from 10 to 30 wt% did not have a major effect on crystallinity, where addition of 10, 20, and 30 wt% ZnO produced filaments that were each ~30% crystalline. This indicates that ZnO acts as a nucleating agent for the PLA chains. A similar phenomenon has been reported in literature evaluating the crystallinity of PLA/ZnO composites [55,57,59]. TiO₂ had the opposite effect on crystallinity. Addition of 10 wt% TiO₂ yielded a 14% crystalline PLA filament. Increasing the TiO₂ content to 20 and 30 wt% resulted in filaments that were ~18% crystalline. Again, these results are inconsistent with those reported for nanocomposites, where it was found that the crystallinity of PLA/TiO₂ composites dramatically increases compared to neat PLA [33]. Inclusion of 10% PEG2k increased the PLA crystallinity from 3 to 5% in each of the ZnO-PLA composite (10–30 wt% ZnO). A similar trend is observed for the inclusion of PEG2k in the PLA/TiO₂ composites, however the increase in crystallinity was much more dramatic. That stated, while the composite filaments that incorporated PEG, ZnO, or TiO₂ displayed either an increase or decrease in the degree of crystallinity as compared to that of the PLA filaments, morphological analysis was not performed and thus it is not certain that PEG, ZnO, or TiO₂ is actually promoting crystal growth or changing the crystalline lamellar size.

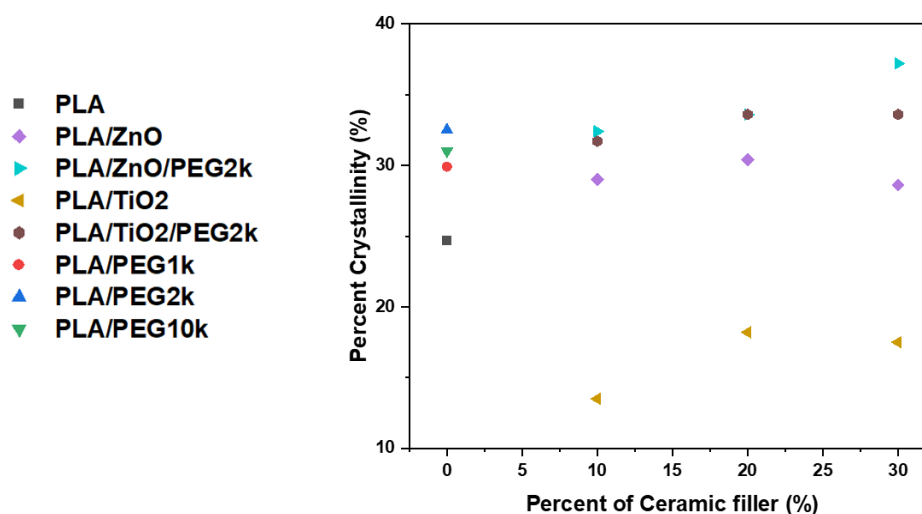


Figure 4.6: Crystallinity of filaments.

Table 4.5: Thermal phase transitions and crystallinity of the composite filaments.

Sample	T_g (°C)	T_m (°C)	ΔH_m (J/g)	X_c (%)
PLA	60	145	23.04	25
PLA/ZnO 90/10	59	152	24.32	29
PLA/ZnO 80/20	59	152	22.62	30
PLA/ZnO 70/30	59	152	18.63	29
PLA/TiO2 90/10	60	149	11.35	14
PLA/TiO2 80/20	61	150	13.58	18
PLA/TiO2 70/30	61	149	11.39	17
PLA/PEG1k 90/10	52	153	25.02	30
PLA/PEG2k 90/10	-	151	27.22	32
PLA/PEG10k 90/10	-	151	25.98	31
PLA/ZnO/PEG2k 80/10/10	59	152	24.13	32
PLA/ZnO/PEG2k 70/20/10	-	152	21.92	34
PLA/ZnO/PEG2k 60/30/10	-	152	20.76	37
PLA/TiO2/PEG2k 80/10/10	-	151	23.59	32
PLA/TiO2/PEG2k 70/20/10	-	152	21.88	34
PLA/TiO2/PEG2k 60/30/10	-	151	18.78	34

4.3.2.2 Thermal Stability

Measures of thermal stability, $T_{d5\%}$ and T_{dMax} , characterize the temperatures at which a material will degrade and decompose. It should be noted that these temperatures can be dependent on the heating rate of the TGA experiment; higher heating rates will result in higher values for the thermal stability. This is mainly thought to be due to the delay in the temperature a material experiences compared to the temperature of the surrounding environment. Five different heating rates were used during testing (5, 8, 10, 13, and 15°C/min) and a shift towards higher degradation and decomposition temperatures was observed for faster heating rates. A similar trend was found for all the filaments that the $T_{d5\%}$ of 15°C/min was approximately 20 °C higher than the $T_{d5\%}$ at 5 °C/min. To err on the side of caution and provide data that can be used for future work by others, the values for $T_{d5\%}$ and T_{dMax} presented in Figures 4.7 (a) and (b) and Table 4.6 are taken from experiments using a heating rate of 5°C/min.

With regard to the pyrolysis kinetic parameters, previous researchers have noted that the activation energy and pre-exponential factor can also be dependent on the heating rate in a similar manner to the thermal stability. Additionally, it has been observed that at higher heating rates (e.g., $\beta > 30$ °C/min for polyethylene terephthalate and $\beta > 80$ °C/min for polystyrene [46,60]), the activation energy becomes nearly constant. Because of this, the pyrolysis kinetic parameters were determined from the highest heating rate tested ($\beta = 15$ °C/min). When using Equation (1), it is important to test for which reaction model produces the best fit to the data. Eight different models were evaluated on the PLA filament, spanning mechanisms that cover chemical reactions, diffusion-controlled reactions, and phase boundary reactions [45–47]. The models were plotted from near the

beginning of the TGA experiment until the T_{dMax} , upon which almost every single model showed a sharp break, which can be assumed to follow a different pyrolysis mechanism. For the PLA filament, the best fitting models were the first-order chemical reaction ($g(\alpha) = -\ln(1 - \alpha)$) and one-dimensional diffusion parabolic law ($g(\alpha) = \alpha^2$), with the diffusion model fitting slightly better. Because of this, it was assumed that the pyrolysis mechanism follows a one-dimensional diffusion parabolic law reaction until decomposition and all the other filaments were evaluated in this manner. Thus, unlike the thermal stability values, which were taken using a heating rate of $\beta = 5$ °C/min, the pyrolysis kinetic parameters were determined using a heating rate of $\beta = 15$ °C/min. The calculated thermal activation energies for the filaments are presented in Figure 4.7 (c) and Table 4.6.

For the thermal stability of the filaments, the trends as observed in Figure 4.7 are that the addition of PEG results in a composite material that degrades and decomposes earlier. This can be observed comparing PLA to PLA/PEG as well as comparing PLA/ceramics to PLA/ceramics/PEG2k in Figure 4.7. This behavior has been exhibited in PLA/PEG mixtures in previous studies [36,61], with explanations spanning from neat PEG, which exhibits a lower thermal stability affecting the overall composite, to PEG lowering the crystallinity and thus making the polymer blend easier to degrade. However, as seen in Figure 6, the PLA/PEG filaments possess a higher crystallinity than PLA filaments, therefore the former explanation may provide a more plausible insight into the physical phenomenon. Interestingly, the polymer blends with PEG1k and PEG10k demonstrated better thermal stability than PEG2k, which could indicate how plasticizer size affects the PLA matrix. It appears that increasing from small to medium-sized PEG molecules contribute towards breaking up the composite at lower thermal energies, however the trend

is reversed when larger PEG molecules are incorporated. This can be inferred to mean that greater miscibility occurs with PEG at greater molecular weights.

The thermal stability of composite filaments with ceramic fillers, shown in Figures 4.5 and 4.7 (a) and (b) indicate that TiO₂ provides better thermal stability than ZnO of similar composition by about 60°C. Indeed, while TiO₂ composite filaments had thermal stabilities near that or slightly better than PLA, the incorporation of ZnO significantly reduced the onset thermal degradation and decompositions. This phenomenon has been observed before, where incorporating TiO₂ into PLA has led to slightly better thermal stability [24]. The opposite effect has been demonstrated by incorporating ZnO, which has decreased the $T_{d5\%}$ and T_{dMax} of PLA composites [26,52,55]. This effect can be explained by the catalytic role zinc compounds play in the transesterification reaction of lactide oligomers [62], which is further supported with Figure 4.7 (c), discussed below. It should be noted that Wang et al. and Mallick et al. found that PLA/TiO₂ nanocomposites exhibited lower thermal stability than neat PLA, however the varied results could be due to the use of amorphous PLA and the presence of solvent, respectively [22,34].

It was found that the calculated activation energies and pre-exponential factors followed trends similar to each other. The data supports the observed thermal stabilities, where filaments with lower activation energy, which is a measure of the energy barrier for the pyrolysis reaction, degraded at lower temperatures than those with higher activation energies. Differences to this observation can be found in the ZnO composites, which can be explained with the pre-exponential factors found in Table 4.6. Although the activation energy for these filaments is larger than the others, the pre-exponential factor, which is a measure of collisions and reactions per unit time, are also significantly higher, with

PLA/ZnO 90/10 and PLA/ZnO/PEG2k 80/10/10 having around 2 and 23 orders of magnitude above PLA, respectively.

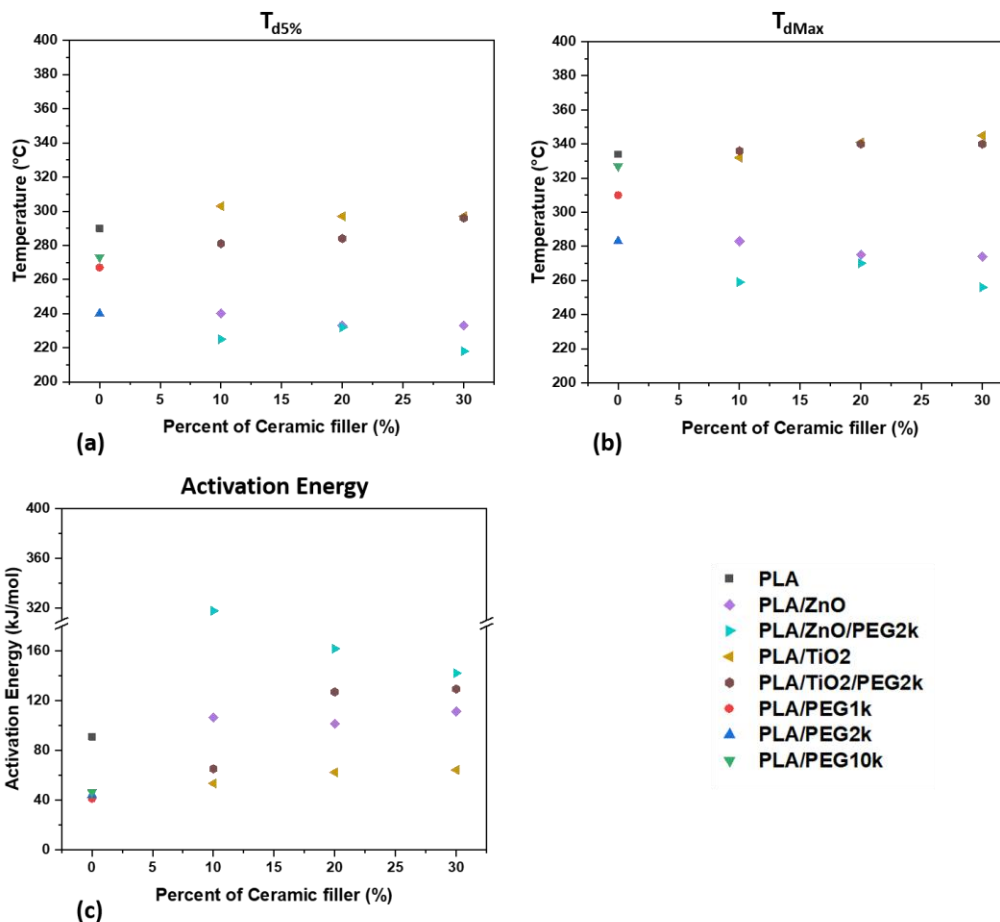


Figure 4.7: The thermal properties of the composite filaments: (a) the onset of thermal degradation ($T_{d5\%}$); (b) the decomposition temperature (T_{dMax}); and (c) the activation energy.

Table 4.6: Thermal stability of the composite filaments (decomposition values take from 5°C/min and thermal kinetic parameters taken from 15°C/min).

Sample	$T_{d5\%}$ (°C)	T_{dMax} (°C)	E_a (kJ/mol)	A (min^{-1})
PLA	290	334	91.0604	$3.51 \cdot 10^5$
PLA/ZnO 90/10	240	283	106.4672	$4.81 \cdot 10^7$
PLA/ZnO 80/20	233	275	101.5866	$2.34 \cdot 10^8$
PLA/ZnO 70/30	233	274	111.3312	$1.82 \cdot 10^9$
PLA/TiO2 90/10	303	332	53.44145	$7.26 \cdot 10^{11}$
PLA/TiO2 80/20	297	341	62.36291	$1.32 \cdot 10^{13}$

PLA/TiO ₂ 70/30	297	345	64.21288	2.27*10 ³
PLA/PEG1k 90/10	267	310	41.02541	4.05*10 ⁻¹
PLA/PEG2k 90/10	240	283	44.06685	2.42*10 ⁰
PLA/PEG10k 90/10	273	327	46.33837	1.20*10 ¹
PLA/ZnO/PEG2k 80/10/10	225	259	317.722	6.04*10 ²⁸
PLA/ZnO/PEG2k 70/20/10	232	270	161.9581	7.74*10 ¹³
PLA/ZnO/PEG2k 60/30/10	218	256	142.2528	9.74*10 ¹¹
PLA/TiO ₂ /PEG2k 80/10/10	281	336	65.18235	2.52*10 ³
PLA/TiO ₂ /PEG2k 70/20/10	284	340	127.1121	1.40*10 ⁹
PLA/TiO ₂ /PEG2k 60/30/10	296	340	129.4734	1.78*10 ⁹

4.3.4 Mechanical Characterization

Through tensile testing the composite filaments, three values were measured: the engineering stress, engineering strain, and the Young's modulus. For relevant understanding of mechanical properties, the averaged maximum values for stress and strain were tabulated. Maximum stress values occurred after the initial linear viscoelastic region, which is useful in understanding capacity and loads that could be withstood. After the linear region, a necking phenomenon occurred and stress values undulated as strain kept monotonically increasing. The maximum strain occurred at the moment of filament breakage, which is useful in understanding the physical mechanical limits of the material. The Young's modulus is the slope of the linear viscoelastic region and is a measure of whether a material exhibits flexibility or brittleness. All three measured mechanical properties for the composite filaments are shown in Figure 4.8 and Table 4.7. For the processed PLA filament, the averaged maximum engineering stress and strain and Young's modulus were 49 MPa \pm 7 MPa, and 6% \pm 2%, and 2314 MPa \pm 300 MPa, respectively.

When ceramics were incorporated into the PLA network, the mechanical properties of the filaments became measurably different. A small decrease in maximum stress is observed upon addition of either ZnO or TiO₂, which is mostly a constant step drop for

each of the filler additions; however, a large decrease in maximum stress occurred in the PLA/TiO₂ 70/30 sample. The addition of 10 wt% ceramic filler did not alter the maximum strain of the PLA filament, but increasing the ceramic content to 20 or 30 wt% decreased the maximum strain noticeably. At similar wt%, ZnO and TiO₂ composites exhibited comparable maximum strain values. It has been reported that adding ceramics to polymers makes the overall material more brittle, and thus increases the Young's modulus [35]. Yet embedding ZnO in PLA increased the Young's modulus only slightly, with the greatest change of 15% occurring in the PLA/ZnO 70/30 composite. Interestingly, all samples containing TiO₂ exhibited a decrease in the Young's modulus, with no relationship between the wt% added and the magnitude of the decrease. This can be explained from the crystallinity view point; previous research showing incorporating TiO₂ increased the brittleness also showed an increase in crystallinity [33]. Because the composite filaments with TiO₂ exhibited a lower crystallinity, the strength decreases accordingly.

It is worth pointing out that the maximum stress is reduced when incorporating 10 wt% PEG, with the effect inversely proportional to the molecular weight of the PEG added. While the maximum stress decreased upon addition of PEG, the maximum strain was significantly increased by its incorporation. It should be noted that while PLA/PEG1k exhibited a 741% increase in strain when compared with PLA, PLA/PEG10k exhibited a 1129% increase, and PLA/PEG2k exhibited a 1661% increase. PEG is known for rendering PLA and other polymers more pliable [36], which is similarly demonstrated here for filaments. Incorporating PEG into the PLA matrix caused a reduction in the Young's modulus, with higher molecular weight PEGs yielding lesser effects. It should be noted that in this vein, PLA/PEG1k and PLA/PEG2k composites exhibited approximately three-

fold lower Young's-modulus values than PLA filaments, whereas the value for the PLA/PEG10k composite was only slightly lower (13.5%) than that of PLA comparatively.

The mechanical properties of the composites with ceramic fillers and PEG are shown in Figure 4.8. It was observed that 10 wt% PEG2k reduced the maximum stress of all samples with ZnO and TiO₂. Additionally, while altering the amount of ceramic filler altered the maximum stress, inclusion of 10 wt% PEG2k exhibited similar values for each sample tested, regardless of filler content. The reverse was observed with regards to maximum strain; adding PEG2k increased the elongation of the samples, with the sole exception of PLA/ZnO/PEG2k 70/20/10, which was lower than PLA/ZnO 80/20. The largest change was observed in PLA/TiO₂/PEG2k 80/10/10, which demonstrated a 938% increase compared to PLA/TiO₂ 90/10. Similar to maximum stress, adding PEG2k to the composite resulted in a reduction in the Young's modulus for all the samples and like the maximum stress of the samples, altering the amount of ceramic filler does not significantly change the Young's modulus in the filaments with PEG2k incorporated, with the only exception being PLA/ZnO/PEG2k 70/20/10. This sample showed minor differences compared to PLA/ZnO 80/20, suggesting that the stiffness does not change drastically.

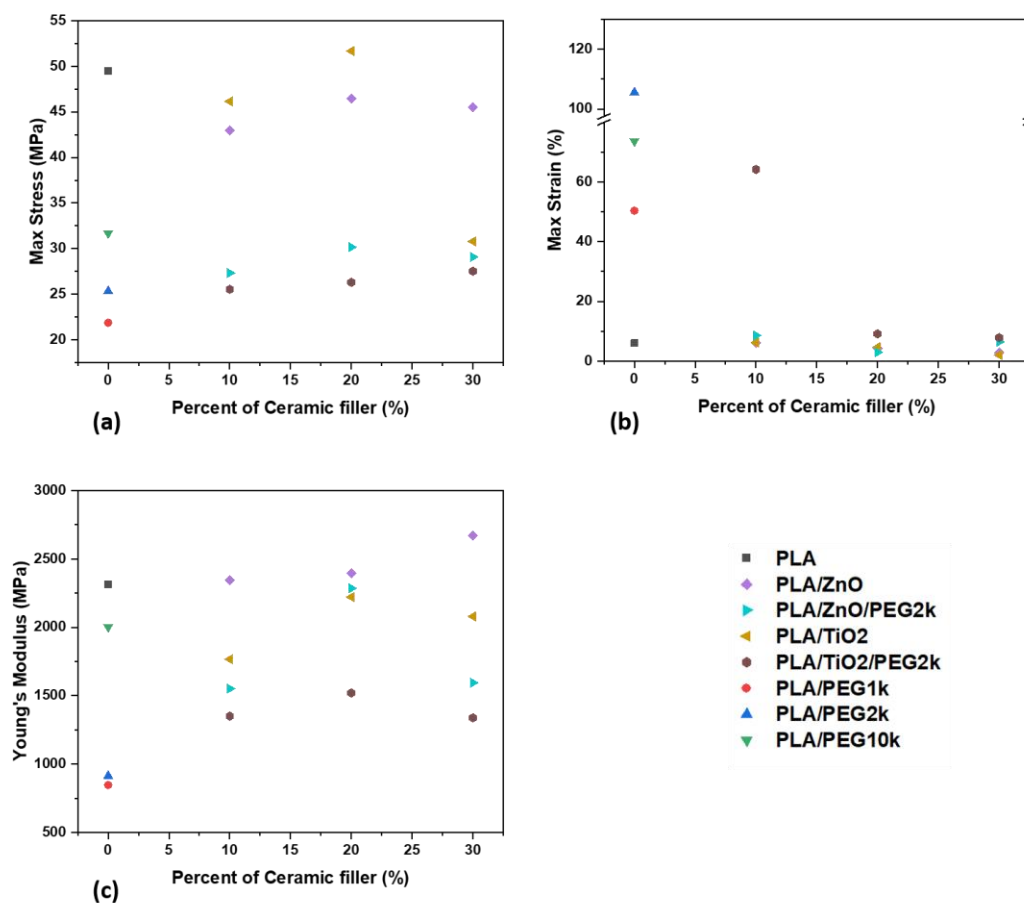


Figure 4.8: The mechanical properties of the composite filaments: (a) max stress; (b) max strain; and (c) Young's modulus.

Table 4.7: Mechanical properties of the composite filaments.

Sample	Max Stress (MPa)	Max Strain (%)	Young's Modulus (MPa)
PLA	49.5	6.00	2314
PLA/ZnO 90/10	43.0	6.18	2345
PLA/ZnO 80/20	46.5	4.30	2397
PLA/ZnO 70/30	45.5	2.78	2671
PLA/TiO2 90/10	46.2	6.19	1767
PLA/TiO2 80/20	51.7	4.67	2221
PLA/TiO2 70/30	30.8	2.01	2080
PLA/PEG1k 90/10	21.9	50.40	846
PLA/PEG2k 90/10	25.3	105.53	912
PLA/PEG10k 90/10	31.7	73.65	2002
PLA/ZnO/PEG2k 80/10/10	27.3	8.62	1551

PLA/ZnO/PEG2k 70/20/10	30.2	2.95	2286
PLA/ZnO/PEG2k 60/30/10	29.1	6.40	1595
PLA/TiO ₂ /PEG2k 80/10/10	25.5	64.24	1351
PLA/TiO ₂ /PEG2k 70/20/10	26.3	9.15	1520
PLA/TiO ₂ /PEG2k 60/30/10	27.5	7.88	1338

4.3.5 Antimicrobial Efficacy

Microbial activity (alteration of the filament surface) was most prominent on pure PLA filaments, where abundant colonial and filamentous growth patterns were observed. Interestingly, the surface of the PLA filament incubated in soil exhibited areas where relatively large “flakes” (50–100 microns in diameter) had sloughed from the surface (e.g., Figure 4.9 (a)). These regions of “flaking” were typically associated with robust microbial colonization. Inclusion of TiO₂ and, especially, ZnO ceramics into the PLA filaments reduced the amount of visible microbial colonization and surface alteration (Figure 4.9 (a) vs. Figures 4.9 (b) and (c)). The addition of PEG did not affect these properties; thus, it can be used purely to tune the physical material properties of the filaments without affecting the biodegradability of the polymers. The addition of 10 wt% gelatin to the soils did not have a noticeable effect on microbial colonization patterns or pitting/flaking on the filament surfaces (data not shown).

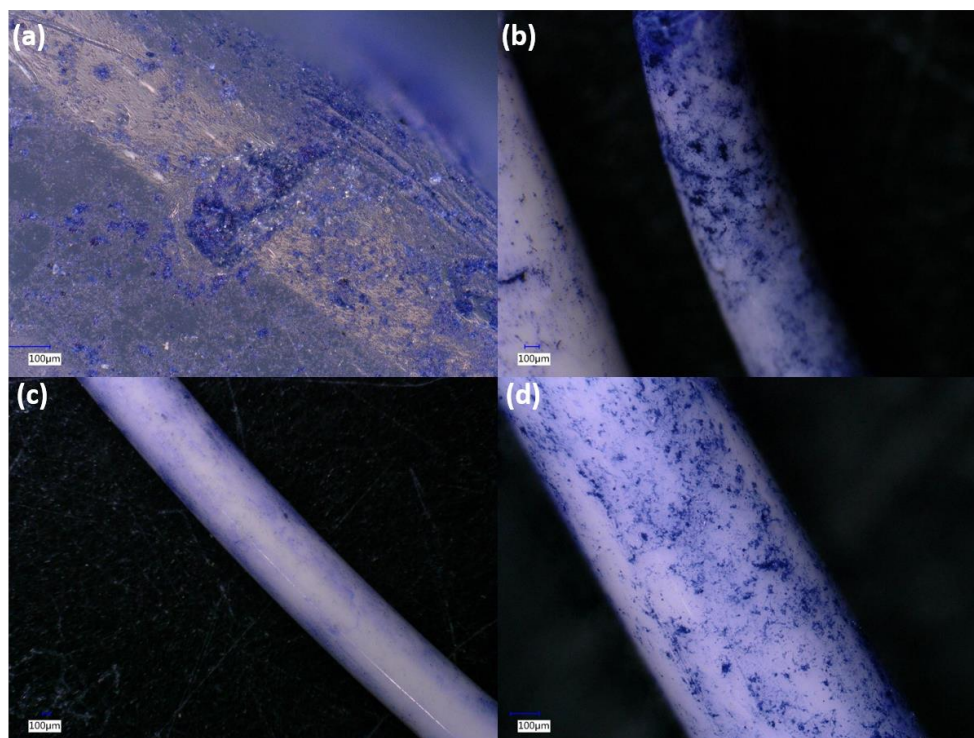


Figure 4.9: Microscopy images of stained composite filaments that were incubated in soil for a month: (a) PLA; (b) PLA/TiO₂ 90/10 with gelatin; (c) PLA/ZnO 90/10; and (d) PLA/ZnO 90/10 with gelatin.

The PLA, PLA/TiO₂ 90/10, and PLA/ZnO 90/10 filaments were analyzed to find the regions with the greatest amount of pitting so that the degradation could be measured on a per area basis. Pitting is a removal of the surface layer, so a quantitative determination could be performed by finding the ratio of area removed against the surface area measured. In the most damaged area, pits covered 1.30% of the PLA filament surface, compared to 0.40% and 0.34% of the PLA/TiO₂ 90/10 and PLA/ZnO 90/10 filament surfaces, respectively. Additionally, the largest pits found measured approximately 20,000 µm² for PLA, compared to 7000 µm² and 2000 µm² for the PLA/TiO₂ 90/10 and PLA/ZnO 90/10, respectively. Thus, adding the ceramics not only reduced the amount of visible microbial

colonization and surface alteration, but also had a measured order of magnitude less microbial degradation as well.

4.4 Conclusions

Antimicrobial composites have been heavily researched and successfully transitioned into commercial products, yet the question of whether their mechanical properties can be tuned while engineering additional multifunctionality had not been addressed for 3D-printing applications before this study. We demonstrate that by using a solvent treatment method for filament feedstock fabrication, homogenous composites can be developed for 3D-printing applications. High weight percent loading (10–30 wt%) of TiO₂ and ZnO ceramic fillers into PLA filaments was achieved to imbue antimicrobial characteristics, and PEG was added to control the mechanical properties as well as allow pathways for further biological modifications.

By fabricating the filaments using the process described in this study, homogeneous materials were created that can be used for FFF. Thermal phase behavior and stability demonstrated that the composite filaments will soften during the 3D-printing process and survive at elevated temperature regimes. Indeed, all the composite filaments are stable up to 200 °C, which is suitable for FFF regimes. Furthermore, the filaments with TiO₂ resulted in being more thermally stable than those with ZnO, where a 60 °C difference was observed. Additionally, the mechanical behaviors can be tuned based on ceramic filler loading and types and via the inclusion of PEG. This is demonstrated by the inclusion of 10 wt% PEG generally reducing the maximum stress of a by 35–50%, while dramatically increasing and decreasing the maximum elongation and Young's modulus, respectively, in some cases. Finally, incorporating ceramic fillers significantly reduced pitting and

degradation on PLA filament surfaces due to microbial activity. PEG did not affect the antimicrobial properties of the ceramic/PLA composites, so it can be added solely to alter the physical material properties. Our study thus expands the range of functional materials for FFF and advanced manufacturing.

References

1. Royte, E. Corn plastic to the rescue. *Smithson. Mag.* 2006, 37, 84–88.
2. Avinc, O.; Khoddami, A. Overview of Poly(lactic acid) (PLA) Fibre. *Fibre Chem.* 2009, 41, 391–401, doi:10.1007/s10692-010-9213-z.
3. Sawyer, D.J. Bioprocessing—No longer a field of dreams. In *Macromolecular Symposia*; Wiley Online Library: Hoboken, NJ, USA, 2003.
4. Nofar, M.; Sacligil, D.; Carreau, P.J.; Kamal, M.R.; Heuzey, M.-C. Poly (lactic acid) blends: Processing, properties and applications. *Int. J. Biol. Macromol.* 2019, 125, 307–360, doi:10.1016/j.ijbiomac.2018.12.002.
5. Scaffaro, R.; Lopresti, F.; Marino, A.; Nostro, A. Antimicrobial additives for poly(lactic acid) materials and their applications: Current state and perspectives. *Appl. Microbiol. Biotechnol.* 2018, 102, 7739–7756, doi:10.1007/s00253-018-9220-1.
6. Wang, L.; Gramlich, W.M.; Gardner, D.J. Improving the impact strength of Poly(lactic acid) (PLA) in fused layer modeling (FLM). *Polymer* 2017, 114, 242–248, doi:10.1016/j.polymer.2017.03.011.
7. Thanki, P.N.; Dellacherie, E.; Six, J. Surface characteristic of PLA and PLGA films. *Appl. Surf. Sci.* **2006**, 253, 2758–2764.

8. Karamanlioglu, M.; Preziosi, R.; Robson, G.D. Abiotic and biotic environmental degradation of the bioplastic polymer poly(lactic acid): A review. *Polym. Degrad. Stab.* 2017, *137*, 122–130, doi:10.1016/j.polymdegradstab.2017.01.009.
9. Liu, J.; Sun, L.; Xu, W.; Wang, Q.; Yu, S.; Sun, J. Current advances and future perspectives of 3D printing natural-derived biopolymers. *Carbohydr. Polym.* 2019, *207*, 297–316, doi:10.1016/j.carbpol.2018.11.077.
10. Thompson, M.K.; Moroni, G.; Vaneker, T.; Fadel, G.; Campbell, R.I.; Gibson, I.; Bernard, A.; Schulz, J.; Graf, P.; Ahuja, B.; et al. Design for Additive Manufacturing: Trends, opportunities, considerations, and constraints. *CIRP Ann.* 2016, *65*, 737–760, doi:10.1016/j.cirp.2016.05.004.
11. Levy, G.N.; Schindel, R.; Kruth, J. Rapid manufacturing and rapid tooling with layer manufacturing (LM) technologies, state of the art and future perspectives. *CIRP Ann.* 2003, *52*, 589–609, doi:10.1016/s0007-8506(07)60206-6.
12. Bayer, I.S. Thermomechanical Properties of Polylactic Acid-Graphene Composites: A State-of-the-Art Review for Biomedical Applications. *Materials* 2017, *10*, 748, doi:10.3390/ma10070748.
13. Wang, H.; Qiu, Z. Crystallization kinetics and morphology of biodegradable poly (l-lactic acid)/graphene oxide nano-composites: Influences of graphene oxide loading and crystallization temperature. *Thermochim. Acta* 2012, *527*, 40–46.
14. Kim, I.-H.; Jeong, Y.G. Polylactide/exfoliated graphite nanocomposites with enhanced thermal stability, mechanical modulus, and electrical conductivity. *J. Polym. Sci. Part B Polym. Phys.* 2010, *48*, 850–858, doi:10.1002/polb.21956.

15. Hassouna, F.; Raquez, J.-M.; Addiego, F.; Dubois, P.; Toniazzo, V.; Ruch, D. New approach on the development of plasticized polylactide (PLA): Grafting of poly(ethylene glycol)(PEG) via reactive extrusion. *Eur. Polym. J.* 2011, *47*, 2134–2144.
16. You, Y.; Lee, S.W.; Youk, J.H.; Min, B.-M.; Lee, S.J.; Park, W.H. In vitro degradation behaviour of non-porous ultra-fine poly(glycolic acid)/poly(L-lactic acid) fibres and porous ultra-fine poly(glycolic acid) fibres. *Polym. Degrad. Stab.* 2005, *90*, 441–448, doi:10.1016/j.polymdegradstab.2005.04.015.
17. Li, H.-Z.; Chen, S.-C.; Wang, Y.-Z. Thermoplastic PVA/PLA Blends with Improved Processability and Hydrophobicity. *Ind. Eng. Chem. Res.* 2014, *53*, 17355–17361, doi:10.1021/ie502531w.
18. Grande, R.; Pessan, L.A.; Carvalho, A.J. Ternary melt blends of poly(lactic acid)/poly(vinyl alcohol)-chitosan. *Ind. Crop. Prod.* 2015, *72*, 159–165, doi:10.1016/j.indcrop.2014.12.041.
19. Bartczak, Z.; Galeski, A.; Kowalczyk, M.; Sobota, M.; Malinowski, R. Tough blends of poly(lactide) and amorphous poly([R, S]-3-hydroxy butyrate)—morphology and properties. *Eur. Polym. J.* 2013, *49*, 3630–3641.
20. Dong, W.; Ma, P.; Wang, S.; Chen, M.; Cai, X.; Zhang, Y. Effect of partial crosslinking on morphology and properties of the poly(β -hydroxybutyrate)/poly(D,L-lactic acid) blends. *Polym. Degrad. Stab.* 2013, *98*, 1549–1555, doi:10.1016/j.polymdegradstab.2013.06.033.

21. Sedlarik, V.; Saha, N.; Sedlarikova, J.; Sába, P. Biodegradation of Blown Films Based on Poly(lactic acid) under Natural Conditions. *Macromol. Symp.* 2008, 272, 100–103, doi:10.1002/masy.200851214.
22. Mallick, S.; Ahmad, Z.; Touati, F.; Bhadra, J.; Shakoor, R.A.; Al-Thani, N.J. PLA-TiO₂ nanocomposites: Thermal, morphological, structural, and humidity sensing properties. *Ceram. Int.* 2018, 44, 16507–16513.
23. Man, C.; Zhang, C.; Liu, Y.; Wang, W.; Ren, W.; Jiang, L.; Reisdorffer, F.; Nguyen, T.P.; Dan, Y. Poly (lactic acid)/titanium dioxide composites: Preparation and performance under ultraviolet irradiation. *Polym. Degrad. Stab.* 2012, 97, 856–862, doi:10.1016/j.polymdegradstab.2012.03.039.
24. Segura González, E.A.; Olmos, D.; Lorente, M.Á.; Vélaz, I.; González-Benito, J. Preparation and characterization of polymer composite materials based on PLA/TiO₂ for an-tibacterial packaging. *Polymers* 2018, 10, 1365.
25. Marra, A.; Silvestre, C.; Duraccio, D.; Cimmino, S. Polylactic acid/zinc oxide biocomposite films for food packaging application. *Int. J. Biol. Macromol.* 2016, 88, 254–262, doi:10.1016/j.ijbiomac.2016.03.039.
26. Doumbia, A.S.; Vezin, H.; Ferreira, M.; Campagne, C.; Devaux, E. Studies of polylactide/zinc oxide nanocomposites: Influence of surface treatment on zinc oxide anti-bacterial activities in textile nanocomposites. *J. Appl. Polym. Sci.* 2015, 132, doi:10.1002/app.41776.
27. Ponnamma, D.; Cabibihan, J.-J.; Rajan, M.; Pethaiah, S.S.; Deshmukh, K.; Gogoi, J.P.; Pasha, S.K.; Ahamed, M.B.; Krishnegowda, J.; Chandrashekar, B.; et al. Synthesis,

- optimization and applications of ZnO/polymer nanocomposites. *Mater. Sci. Eng. C* 2019, 98, 1210–1240, doi:10.1016/j.msec.2019.01.081.
28. Marra, A.; Cimmino, S.; Silvestre, C. Effect of TiO₂ and ZnO on PLA degradation in various media. *Adv. Mater. Sci.* 2017, 2, 1–8, doi:10.15761/AMS.1000122.
29. Buerki-Thurnherr, T.; Xiao, L.; Diener, L.; Arslan, O.; Hirsch, C.; Maeder-Althaus, X.; Grieder, K.; Wampfler, B.; Mathur, S.; Wick, P.; et al. In vitro mechanistic study towards a better understanding of ZnO nanoparticle toxicity. *Nanotoxicology* 2013, 7, 402–416.
30. Pandurangan, M.; Kim, D.H. In vitro toxicity of zinc oxide nanoparticles: A review. *J. Nanoparticle Res.* 2015, 17, 1–8, doi:10.1007/s11051-015-2958-9.
31. Zhu, X.; Chang, Y.; Chen, Y. Toxicity and bioaccumulation of TiO₂ nanoparticle aggregates in *Daphnia magna*. *Chemosphere* 2010, 78, 209–215, doi:10.1016/j.chemosphere.2009.11.013.
32. Menard, A.; Drobne, D.; Jemec, A. Ecotoxicity of nanosized TiO₂. Review of in vivo data. *Environ. Pollut.* 2011, 159, 677–684, doi:10.1016/j.envpol.2010.11.027.
33. Buzarovska, A. PLA Nanocomposites with Functionalized TiO₂Nanoparticles. *Polym. Technol. Eng.* 2013, 52, 280–286, doi:10.1080/03602559.2012.751411.
34. Wang, X.-J.; Huang, Z.; Wei, M.-Y.; Lu, T.; Nong, D.-D.; Zhao, J.-X.; Gao, X.-Y.; Teng, L.-J. Catalytic effect of nanosized ZnO and TiO₂ on thermal degradation of poly(lactic acid) and isoconversional kinetic analysis. *Thermochim. Acta* 2019, 672, 14–24, doi:10.1016/j.tca.2018.12.008.

35. Temenoff, J.S.; Mikos, A.G. *Biomaterials: The Intersection of Biology and Materials Science*; Pearson/Prentice Hall: Upper Saddle River, NJ, USA, 2008; Volume 1.
36. Bijarimi, M.; Ahmad, S.; Rasid, R.; Khushairi, M.A.; Zakir, M. Poly (lactic acid)/Poly (ethylene glycol) blends: Mechanical, thermal and morphological properties. In *AIP Conference Proceedings*; AIP Publishing LLC: Melville, NY, USA, 2016.
37. Phan, Q.T.; Le, M.H.; Le, T.T.H.; Tran, T.H.H.; Xuan, P.N.; Ha, P.T. Characteristics and cytotoxicity of folate-modified curcumin-loaded PLA-PEG micellar nano systems with various PLA:PEG ratios. *Int. J. Pharm.* 2016, 507, 32–40, doi:10.1016/j.ijpharm.2016.05.003.
38. Kumar, A.; Rao, T.V.; Chowdhury, S.R.; Reddy, S.R. Compatibility confirmation and refinement of thermal and mechanical properties of poly (lactic acid)/poly (ethylene-co -glycidyl methacrylate) blend reinforced by hexagonal boron nitride. *React. Funct. Polym.* 2017, 117, 1–9, doi:10.1016/j.reactfunctpolym.2017.05.005.
39. Jia, S.; Yu, D.; Zhu, Y.; Wang, Z.; Chen, L.; Fu, L. Morphology, Crystallization and Thermal Behaviors of PLA-Based Composites: Wonderful Effects of Hybrid GO/PEG via Dynamic Impregnating. *Polymers* 2017, 9, 528, doi:10.3390/polym9100528.
40. Toncheva, A.; Mincheva, R.; Kancheva, M.; Manolova, N.; Rashkov, I.; Dubois, P.; Markova, N. Antibacterial PLA/PEG electrospun fibers: Comparative study between grafting and blending PEG. *Eur. Polym. J.* 2016, 75, 223–233, doi:10.1016/j.eurpolymj.2015.12.019.
41. Greenwald, R. PEG drugs: An overview. *J. Control. Release* 2001, 74, 159–171, doi:10.1016/s0168-3659(01)00331-5.

42. Brounstein, Z.; Talley, S.; Dumont, J.H.; Zhao, J.; Lee, K.-S.; Labouriau, A. Fused filament fabrication of polymer composites for extreme environments. *J. Mater. Res.* 2020, *35*, 1493–1503, doi:10.1557/jmr.2020.118.
43. Fischer, E.W.; Sterzel, H.J.; Wegner, G. Investigation of the structure of solution grown crystals of lactide copolymers by means of chemical reactions. *Kolloid-Z. Z. Polym.* 1973, *251*, 980–990, doi:10.1007/bf01498927.
44. Coats, A.W.; Redfern, J.P. Kinetic Parameters from Thermogravimetric Data. *Nat. Cell Biol.* 1964, *201*, 68–69, doi:10.1038/201068a0.
45. Ebrahimi-Kahrizsangi, R.; Abbasi, M. Evaluation of reliability of Coats-Redfern method for kinetic analysis of non-isothermal TGA. *Trans. Nonferrous Met. Soc. China* 2008, *18*, 217–221, doi:10.1016/s1003-6326(08)60039-4.
46. Brems, A.; Baeyens, J.; Beerlandt, J.; Dewil, R. Thermogravimetric pyrolysis of waste polyethylene-terephthalate and polystyrene: A critical assessment of kinetics modelling. *Resour. Conserv. Recycl.* 2011, *55*, 772–781, doi:10.1016/j.resconrec.2011.03.003.
47. Gao, W.; Chen, K.; Xiang, Z.; Yang, F.; Zeng, J.; Li, J.; Yang, R.; Rao, G.; Tao, H. Kinetic study on pyrolysis of tobacco residues from the cigarette industry. *Ind. Crop. Prod.* 2013, *44*, 152–157, doi:10.1016/j.indcrop.2012.10.032.
48. Butbunchu, N.; Pathom-Aree, W. Actinobacteria as Promising Candidate for Polylactic Acid Type Bioplastic Degradation. *Front. Microbiol.* 2019, *10*, 2834, doi:10.3389/fmicb.2019.02834.

49. Popelka, Š.; Machová, L.; Rypáček, F. Adsorption of poly(ethylene oxide)–block–polylactide copolymers on polylactide as studied by ATR-FTIR spectroscopy. *J. Colloid Interface Sci.* 2007, *308*, 291–299, doi:10.1016/j.jcis.2006.12.022.
50. Chieng, B.W.; Ibrahim, N.A.B.; Yunus, W.M.Z.W.; Hussein, M.Z. Poly(lactic acid)/Poly(ethylene glycol) Polymer Nanocomposites: Effects of Graphene Nanoplatelets. *Polymers* 2013, *6*, 93–104, doi:10.3390/polym6010093.
51. Jayaramudu, J.; Das, K.; Sonakshi, M.; Reddy, G.S.M.; Aderibigbe, B.; Sadiku, R.; Ray, S.S. Structure and properties of highly toughened biodegradable polylactide/ZnO biocomposite films. *Int. J. Biol. Macromol.* 2014, *64*, 428–434, doi:10.1016/j.ijbiomac.2013.12.034.
52. Yuniarto, K.; Purwanto, Y.A.; Purwanto, S.; Welt, B.A.; Purwadaria, H.K.; Sunarti, T.C. Infrared and Raman studies on polylactide acid and polyethylene glycol-400 blend. In *AIP Conference Proceedings*; AIP Publishing LLC: Melville, NY, USA, 2016.
53. Saeidlou, S.; Huneault, M.A.; Li, H.; Park, C.B. Poly (lactic acid) crystallization. *Prog. Polym. Sci.* 2012, *37*, 1657–1677.
54. Murariu, M.; Paint, Y.; Murariu, O.; Raquez, J.-M.; Bonnaud, L.; Dubois, P. Current progress in the production of PLA-ZnO nanocomposites: Beneficial effects of chain extender addition on key properties. *J. Appl. Polym. Sci.* 2015, *132*, doi:10.1002/app.42480.

55. Lizundia, E.; Pérez-Álvarez, L.; Sáenz-Pérez, M.; Patrocinio, D.; Vilas, J.L.; León, L.M. Physical aging and mechanical performance of poly(l-lactide)/ZnO nanocomposites. *J. Appl. Polym. Sci.* 2016, *133*, doi:10.1002/app.43619.
56. Nonato, R.; Mei, L.; Bonse, B.; Chinaglia, E.; Morales, A. Nanocomposites of PLA containing ZnO nanofibers made by solvent cast 3D printing: Production and characterization. *Eur. Polym. J.* 2019, *114*, 271–278, doi:10.1016/j.eurpolymj.2019.02.026.
57. Carrion, F.; Sanes, J.; Bermúdez, M.-D. Influence of ZnO nanoparticle filler on the properties and wear resistance of pol-ycarbonate. *Wear* 2007, *262*, 1504–1510.
58. Pantani, R.; Gorrasi, G.; Vigliotta, G.; Murariu, M.; Dubois, P. PLA-ZnO nanocomposite films: Water vapor barrier properties and specific end-use characteristics. *Eur. Polym. J.* 2013, *49*, 3471–3482.
59. Brems, A.; Baeyens, J.; Vandecasteele, C.; Dewil, R. Polymeric Cracking of Waste Polyethylene Terephthalate to Chemicals and Energy. *J. Air Waste Manag. Assoc.* 2011, *61*, 721–731, doi:10.3155/1047-3289.61.7.721.
60. Mohapatra, A.K.; Mohanty, S.P.; Nayak, S.K. Effect of PEG on PLA/PEG blend and its nanocomposites: A study of thermo-mechanical and morphological characterization. *Polym. Compos.* 2013, *35*, 283–293, doi:10.1002/pc.22660.
61. Abe, H.; Takahashi, N.; Kim, K.J.; Mochizuki, M.; Doi, Y. Thermal Degradation Processes of End-Capped Poly(l-lactide)s in the Presence and Absence of Residual Zinc Catalyst. *Biomacromolecules* 2004, *5*, 1606–1614, doi:10.1021/bm0497872.

Chapter 5 Tuning the Thermomechanical Properties of 3D Printed Radiation

Shields

5.1 Introduction

As the world advances in additive manufacturing and materials science, many forms of 3D printing are being researched with regard to materials development and macroscopic part fabrication. Indeed, major progress in vat polymerization [1,2], selective laser melting [3,4], and direct ink writing (DIW) [5–7] has demonstrated the variety of means in which advanced composites can be used to construct geometries and structures that traditional manufacturing techniques have difficulty fabricating. DIW 3D printing, a technology under the ISO/ASTM 52900:2015 category of material extrusion, includes ink jet printing [8–10], micropen writing [11,12], fused filament fabrication (FFF) [13–15], hot-melt extrusion [16,17], and robocasting [18,19] and is especially useful because of the wide array of material selection available and the continued development which increases the capabilities of these techniques. DIW, in particular, is especially suitable for advanced materials capabilities due to its range of ink formulations and versatility in part extrusion and curing. Customarily, DIW refers to the 3D printing technique where a shear-thinning fluid, ink, or paste is extruded through a nozzle and possesses a high enough storage modulus to build a part layer by layer. Additionally, these extrusion methods also allow for numerous hardening regimes such as UV curing, elevated temperature curing, freeze drying, and other means, which increases the possible range of new materials that can be 3D printed. Examples include aerogels and foams developed from ceramics and carbonaceous materials [20–23], synthetic bone and osteoinduction scaffolds [24–27], smart magneto-responsive devices [28–30], and more. Thus, DIW lends itself to immense

materials development exploration and can result in a variety of specialty parts for many applications.

One area that would benefit from the advances in manufacturing science that DIW offers is that of radiation shielding. Since commercial nuclear power has become more widespread, ionizing radiation in the form of gamma rays and neutrons has been attenuated with large blocks of concrete, lead, or boron [31–33]. Additionally, some high-Z elements such as gadolinium and tungsten were and are still used for gamma radiation shielding [34,35]. Recently, more precise radiation shielding materials have been developed such as glasses and amorphous alloys for use in other nuclear technologies such as radiation protection and medicine [36–38]. The advancement in this area of materials development has also occurred with 3D printing technology, where filaments for FFF and inks for DIW have been created in contemporary research [14,39–44]. Indeed, the merging of the two fields of nuclear technology and advanced manufacturing proves especially prolific and rewarding due to the unique part fabrication that 3D printing offers, where commercial entities have begun selling radiation shielding material specifically for additive manufacturing technologies. Although at the nascent stage where much materials research and development needs to occur, this nevertheless represents a growing endeavor due to the continued and increasing interest in nuclear energy, nuclear medicine, nuclear waste storage, high-energy physics, and space exploration [35,45–48].

With regard to 3D printing, there are two large factors that imbue a final product with its material properties. These are the basic characteristics of the constituent components and the auxiliary characteristics of the macroscopic structure, which provide the essential and specialty qualities of a material, respectively. The former factor is shared

with traditional manufacturing techniques, but the latter is given by how the material is printed with whichever 3D printing technology is used. Thus, besides the rapid prototyping and part development that are manufacturing advantages, 3D printing technologies offer hierarchical structural properties. Examples of these can be geometries that are impossible or near impossible to fabricate with traditional manufacturing techniques, where shape, hollowness, and porosity combine to allow parts with precise customized material properties [49–54]. By controlling the shape, hollowness, and porosity of an additively manufactured product, transport properties such as diffusion, thermal conductivity, and mechanical response can be governed [55,56].

In this work, various ink formulations were developed for DIW 3D printing that behave as radiation shields and possess tunable thermomechanical properties. Using a base formulation with two siloxane copolymers and a platinum catalyst that enables a curing reaction based on elevated temperatures, fillers such as fumed silica, tungsten, tungsten (VI) oxide, gadolinium (III) oxide, and boron were incorporated into 3D printable inks. Rheological properties of a representative sample of the inks were evaluated, and an empirical relationship was developed that provides a model for the upper limit on the spacing ratio, a lattice parameter, during 3D printing. Compressive strain and thermal conductivity measurements of the printed structure demonstrated that there is a correlation between porosity and thermomechanical properties. Additionally, thermal stability experiments showed that the radiation shielding ink formulations can be used in environments at much higher temperatures than a regular ink which controls for just rheology. Neutron radiography experiments provided evidence that the printed formulations attenuate ionizing radiation. Finally, heterogeneous printed parts were

produced using two different ink formulations to demonstrate that the capabilities offered by this technology allow for greater materials development precision than traditional manufacturing.

5.2 Experimental

5.2.1 Materials

The siloxanes that composed the polymer network included vinyl-terminated (4–6% diphenylsiloxane)-dimethylsiloxane copolymer (PDV–541) and trimethylsiloxy-terminated methylhydrosiloxane-dimethylsiloxane copolymer (HMS 301), both from Gelest (Gelest, Inc., Morrisville, PA, USA). A cure inhibitor in the form of 1-ethynyl-1-cyclohexanol was used (Sigma Aldrich, 99%) (Millipore Sigma, St. Louis, MO, USA), and crosslinking was induced with a high-temperature platinum catalyst (platinum carbonyl cyclovinylmethylsiloxane complex; 1.85–2.1% Pt in cyclomethyl vinyl siloxanes) (Gelest, SIP6829.2). An OH-functionalized fumed silica (Evonik Aerosil 300) (Evonik Industries AG, Essen, Germany) and PDMS-functionalized fumed silica (CAB-O-SIL TS-720) (Cabot Corporation, Boston, MA, USA) were incorporated into the polymer matrix. Boron, tungsten, tungsten (VI) oxide, and gadolinium (III) oxide powders, supplied by American Elements (American Elements, Los Angeles, CA, USA), were used as fillers in the formulation. Isotopically enriched B10 was supplied by 3M (3M Company, Saint Paul, MN, USA). Isopropanol (IPA) was supplied by Thermo Fisher Scientific (Thermo Fisher Scientific, Waltham, MA, USA). Ultra-high purity nitrogen was supplied by Airgas (Airgas, Padnor, PA, USA).

5.2.2 Formulation Development and 3D Printing

Stable and 3D-printable inks depend on the formulation exhibiting specific rheological properties. In particular, the ink needs to exhibit shear thinning; it must flow when a force is applied and remain stiff otherwise. This is especially the case once the ink is printed into a part where it must support its own weight and not collapse. This specific non-Newtonian rheological characteristic was imparted to the polymer matrix by incorporating fumed silicas, whereby varying the amount of fumed silicas allowed the rheological properties to be tuned. PDMS-functionalized fumed silica, referred to in this study as TS720, acted as an inert filler which solely provided shear thinning characteristics. OH-functionalized silica, referred to in this study as A300, behaved as a filler that could form hydrogen bonds, thus providing both shear thinning characteristics and increasing the amount of physical crosslinks in the network. The vinyl-terminated copolymer, referred to in this study as PDV, was always added in a 9:1 w/w ratio with the trimethylsiloxy copolymer, referred to in this study as HMS, which was found in previous work to attenuate radiolysis and prevent crystallization [39,57]. Metal and ceramic fillers were sieved (Gilson Company, Inc., Lewis Center, OH, USA) so the particle size distributions had an upper limit of 53 μm .

To begin producing formulations, an ink containing only silica as a filler was first developed and studied. Increasing the weight percent of silica resulted in a more viscous ink. Due to the nature of DIW 3D printing, a requirement of the formulation is that it remains stiff and rigid while under the force of gravity, but when a sufficiently high force is applied, it becomes liquid-like and flows. It was found that when the OH-functionalized fumed silica (A300) content was under 10 wt%, the DIW formulation flowed even without

an applied force, thus making it unusable for printing. At 10 wt%, the ink was viscous enough and could be printed successfully. Rheological experiments were performed on this recipe to determine its equilibrium storage modulus, yield stress, and flow point. After this formulation was characterized, other fillers were incorporated to develop new recipes. Using amounts of 50 wt% non-SiO₂ filler, the fumed silica content was modified to obtain similar rheological properties to the 10 wt% silica recipe.

Although the PDMS-functionalized silica (TS720) increased the rheological properties of the ink enough to where printing was possible, the printed layers of the final part had an excessive amount of slumping and thickness deviations. Additionally, larger amounts of TS720 were required to achieve adequate rheology for printing, which led to fewer amounts of other fillers added and to the inks being too dry to adhere onto the glass plates where printing occurred. This was remedied with IPA, where, by adding 10–20 wt%, the solvent swelled the polymer matrix and allowed for high amounts of filler to be incorporated and produce an adequate print. Unfortunately, during the high-temperature curing process at 150°C, cracks were formed in the final part, and it appeared that while varying the amounts of all the components led to more or less defects, flaws were always present in the end. This is inferred to be due to the IPA evaporating and leaving mesoscale pores of non-uniform size and morphology within the struts, which was confirmed when viewed under a confocal digital microscope. While this hierarchical porous architecture is an area of further research, and continued pursuit could be beneficial towards other applications, this study wanted to focus on denser printed pads for radiation shielding. As such, TS720, with its lack of hydrogen bonding, was not used further in this study. Moving forward, A300 was the silica of choice, which did not require the use of IPA.

Once the resins were formulated and mixed for DIW printing, they were transferred into a metal syringe (EMO-XT printer head, Hyrel 3D) (Hyrel 3D, Atlanta, GA, USA) and then centrifuged at 2000 rpm for 1–2 min to remove any air bubbles. A MATLAB script was created to generate a Gcode with varying amounts of spacing and geometries. Repetrel software (Hyrel 3D) was used to control the printer and ran at a travel rate at 2250 mm/min, with the material flow rate at 150 pulses/ μ L onto a glass substrate from the build stage. The geometries of the 3D parts were disks possessing a diameter of 5 cm and consisted of eight layers with each layer organized in a faced-centered tetragonal (FCT) structure. Four different spacings between the printed struts (500 μ m, 750 μ m, 1000 μ m, and 1500 μ m) were used for tuning the thermomechanical properties and were cured in an oven at 150°C for 2 hours.

5.2.3 Material Characterization Techniques

Rheological experiments on a representative sample of ink formulations were conducted on a TA Discovery Series Hybrid Rheometer DHR-3 (TA Instruments, New Castle, DE, USA) using a 25 mm cross-hatched parallel plate fixture geometry. Strain sweeps were performed from 0.001% to 10% strain at an angular frequency of 10 rad/s to determine the extent of the linear viscoelastic region of the samples. The sample containing boron and gadolinium (III) oxide (B/Gd₂O₃) was run from 0.00025% to 0.5% at an angular frequency of 1 rad/s. Stress sweeps were performed from 10 to 10,000 Pa at an angular frequency of 10 rad/s. The equilibrium storage moduli G'_{eq} for the samples were determined from the plateau of the stress sweeps in the linear viscoelastic region. The yield stress σ_y was determined from the intersection of lines formed from the storage moduli of the linear viscoelastic region and the beginning of the nonlinear viscoelastic region. The

flow point is the stress at which the storage and loss moduli cross or intersect. Based on calibration testing from the manufacturer and comparative measurements, the error associated with this instrument and the resulting values are less than 1%.

Uniaxial compression tests were performed using an INSTRON[®] 3343 Low-Force Testing System (Instron, Norwood, MA, USA) with the BlueHill Universal software. Each printed sample was compressed for 4 cycles at a rate of 0.05 mm/sec through the stress range from 0 to 0.4 MPa. The cyclic stress–strain curve and the Young’s modulus were reported from the fourth cycle to minimize the Mullins effects. Based on calibration testing from the manufacturer and comparative measurements, the error associated with this instrument and the resulting values are less than 1%.

Thermal conductivity was performed by a TA Fox 50 Heat Flow Meter (TA Instruments, New Castle, DE, USA). Compressed air flowed to the instrument at 60 psi in order to pneumatically compress the samples between two thermally responsive plates. The protocol included nine temperature regimes where the upper and lower plates had a temperature difference of 10 °C, starting with the plates equilibrating to 20 °C and 10 °C, and ending with the plates equilibrating to 100 °C and 90 °C. Based on calibration testing from the manufacturer and comparative measurements, the error associated with this instrument and the resulting values are less than 3%.

Thermogravimetric analysis (TGA) was performed on a TA Q Discovery 2000 series TGA instrument (TA Instruments, New Castle, DE, USA). The protocol included ramping the surrounding temperature of a sample weighing approximately 5 mg from 25 to 750 °C at a heating rate of 10 °C/min. Ultra-high purity nitrogen flowed across the sample at a rate of 40 mL/min. The onset of thermal degradation $T_{d5\%}$ was taken as the

temperature at which a sample lost 5% of its mass (or possessed 95% of its mass remaining). The decomposition temperatures T_{dMax} are those temperatures at which the derivative TGA curves (DTGA) are at a local maximum. The final mass m_f is the residual mass of the sample after the temperature protocol has been executed. Based on calibration testing from the manufacturer and comparative measurements, the error associated with this instrument and the resulting values are less than 1%.

The magnified and cross-section views of the sample images were taken from a confocal digital microscope (Keyence VHX-6000) (Keyence Corporation, Osaka, Japan) and micro X-ray fluorescence (MXRF) (Bruker M4 Tornado) (Bruker Corporation, Billerica, MA, USA). Magnifications of 20x, 30x, and 100x were used to investigate the network of the resulting 3D-printed pads. Measurements of the printed struts were obtained from the Keyence analysis software. Elemental color maps were generated from MXRF images using the instrument software. The acquisition parameters included an X-ray tube operating at 50 kV and 200 μ A, a spectrometer operating at 40 keV and 130 kcps, a spot size of 20 μ m, a dwell time of 5 ms per pixel, and a step size of 10 (cross-section) by 20 μ m (top down).

Advanced neutron radiography was performed at the Los Alamos Neutron Science Center (LANSCE) via energy-resolved neutron imaging (ERNI). Neutrons in the energy range from 0.001 to 100 eV (epi-thermal to thermal) pulsed at 20 Hz at printed samples, which were in front of an ultra-fast MCP-Timpix neutron imaging detector. Details can be found in our previous work [39]. In the resulting radiographs, lighter images correspond to more neutrons hitting the detector, whereas darker images correspond to less neutrons hitting the detector, providing a qualitative measure of the neutron attenuation abilities of

the printed radiation shields. It should be noted that the neutron background at thermal energies was not well characterized during the ERNI experiments. Without proper background characterization, quantitative comparisons are more difficult to perform. That stated, the qualitative assessment using this technique provides ample evidence of successful neutron attenuation.

5.3 Results and Discussion

5.3.1 Rheology

When developing ink formulations with A300, incorporating a single metal or ceramic filler that was denser than boron (tungsten, tungsten (VI) oxide, and gadolinium (III) oxide) at 50 wt% was printable with 4.5 wt% fumed silica. To confirm that these formulations matched the 10 wt% silica formulation, rheological experiments were performed on the tungsten and tungsten (VI) oxide recipes. These strain and stress sweep experiments validated that the amount of silica and other fillers demonstrated similar rheological properties to the 10 wt% silica formulation. As boron is less dense than the other metals and ceramics, a recipe containing 50 wt% boron will correspond to a greater volume percent than the others. Thus, the silica content needed to be further reduced. It was found that incorporating 1.5 wt% A300 with boron led to the desired rheological properties. Following the success of developing and 3D printing the boron formulations, combinations of the metals and ceramics were made into recipes. Specifically, B/Gd₂O₃ and B/Gd₂O₃/WO₃ formulations were created with a combined 70 wt% non-SiO₂ filler content. A similar silica content was found to result in successful recipes, and rheological experiments were performed on the 40/30 wt% B/Gd₂O₃ formulation. The equilibrium storage modulus was found to be greater than the others; however, the linear viscoelastic

region, yield stress, and flow point were in similar ranges, and the ink could be successfully 3D printed. The formulations developed for this study, along with their filler weight and volume percent, and density, are presented in Table 5.1. The densities of the inks ρ_{ink} were determined from the weight fractions of the constituent components w_i and their individual densities ρ_i using Equation 5.1.

$$\rho_{ink} = \frac{1}{\sum_i \frac{w_i}{\rho_i}} \quad \text{Equation 5.1}$$

Table 5.1: The formulations developed and their densities along with the weight and volume percent of each filler component.

	Weight Percent (w/w)/Volume Percent (v/v)					Density (g/cm ³)
	SiO ₂	W	WO ₃	Gd ₂ O ₃	B	
SiO₂	10/4.3	0/0	0/0	0/0	0/0	1.064
W	4.5/3.6	50/5.2	0/0	0/0	0/0	2.004
WO₃	4.5/3.3	0/0	50/12.9	0/0	0/0	1.842
Gd₂O₃	4.5/3.3	0/0	0/0	50/12.4	0/0	1.850
B	1.5/0.9	0/0	0/0	0/0	50/30	1.424
B/Gd₂O₃	1.5/1.2	0/0	0/0	30/8.1	40/33.7	1.998
B/Gd₂O₃/WO₃	1.5/1.2	0/0	20/5.6	10/2.7	40/33.7	1.995

Strain and stress sweep rheological experiments were performed to determine when the ink formulations cross from the linear viscoelastic region to the nonlinear viscoelastic region. The storage moduli, taken during the stress sweep experiments, of the inks are shown in Figures 5.1 (a) and (b), which present the storage and loss moduli of the W formulation taken from the stress sweep experiment, where the flow point, which is the stress at which the storage and loss moduli cross or intersect, can be observed. Storage and loss moduli curves are shown for the all ink formulations that underwent rheology experiments are presented in the Appendix as Figure A.2. The equilibrium storage

modulus, yield stress, and flow point values for the ink formulations tested in rheology experiments are presented in Table 5.2. The values demonstrate similar rheological properties and an ability of the inks to be successfully 3D printed with the motor capabilities of the DIW printer used.

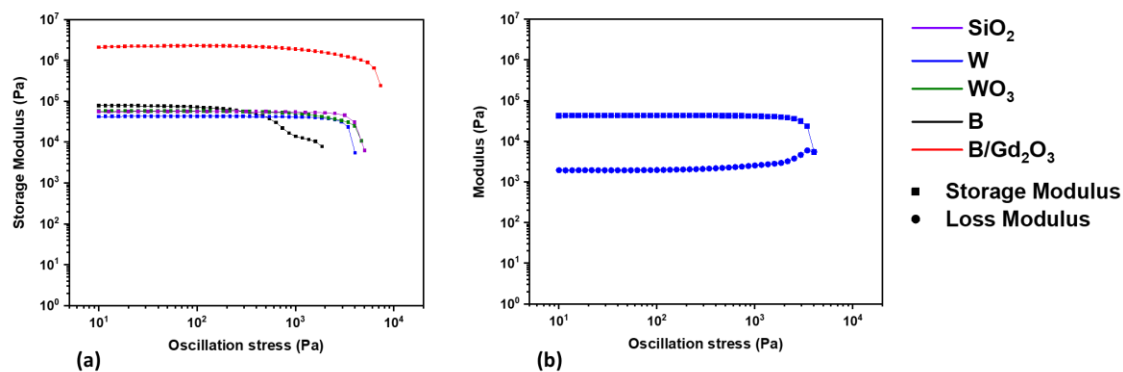


Figure 5.1: Rheological experiments showing (a) the storage modulus of the linear viscoelastic region and beginning of the nonlinear viscoelastic region of a representative sample of ink formulations, and (b) the loss and storage moduli of the W formulation until the flow point.

Table 5.2: Rheological properties of a representative sample of ink formulations.

Formulation	Equilibrium Storage Modulus (G'_{eq}) (Pa)	Yield Stress (σ_y) (Pa)	Flow Point (Pa)
SiO ₂	55470	3650	4610
W	42600	3390	3900
WO ₃	57400	2940	4480
B	78720	400	2270
B/Gd ₂ O ₃	2277190	5330	11050

5.3.2 3D Printing

Using the ink formulations, cylinders in the form of disks were 3D printed with increasing amounts of introduced porosity. Figure 5.2 shows 3D printed cylinders of the formulations detailed in this study. Printing with well-defined porosity was accomplished

by varying the spacing ratio $\eta = L/d$, which is the ratio of the center-to-center distance between adjacent struts L to the diameter of the printed struts d . Cylinders were printed with spacing ratios of 2, 3, 4, and 6. As the printing nozzle measured 250 μm in diameter, which corresponds to the diameter of the struts, the spacing ratio corresponds to center-to-center distances between adjacent struts of 500, 750, 1000, and 1500 μm .

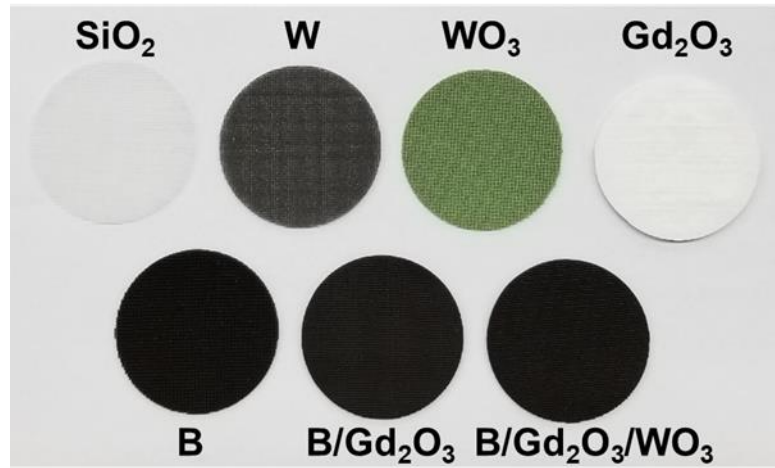


Figure 5.2: 3D-printed cylinders of the ink formulations detailed in this study.

Considering the theoretical model relating the porosity of a structure with an *FCT* geometry to the spacing ratio (presented in the Appendix), taking the limit yields a theoretical porosity as a function of the spacing ratio, which is presented as Equation 5.2. Using the calculated densities of the ink and measuring the densities of the 3D printed cylinders structured with *FCT* geometries $\rho_{structure}$, the actual porosities of the cylinders were calculated using Equation 5.3. A graph of the porosity of the printed parts plotted against their spacing ratio is presented in Figure 5.3 along with the theoretical porosity.

$$\varphi_{FCT}^{\infty} = \lim_{n \rightarrow \infty} \varphi_{FCT} = 1 - \frac{\pi d}{4L} = 1 - \frac{\pi}{4\eta} \quad \text{Equation 5.2}$$

$$\varphi_{FCT} = \varphi_{structure} = 1 - \frac{\rho_{structure}}{\rho_{ink}}$$

Equation 5.3

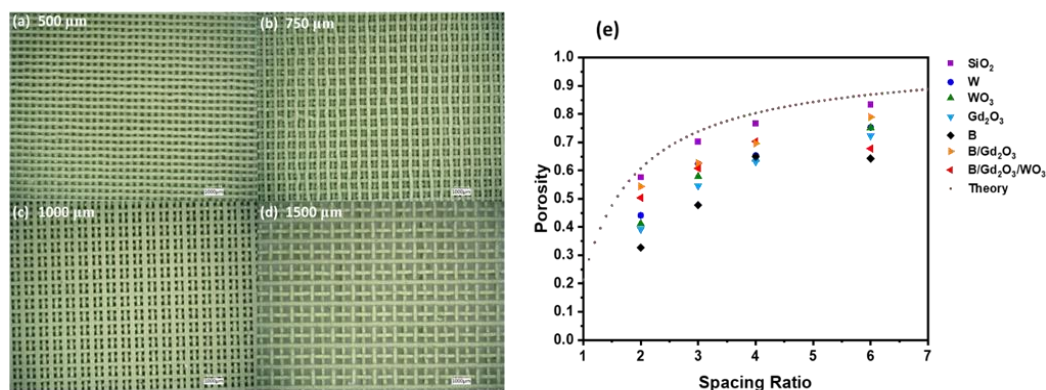


Figure 5.3: Porosities of the printed formulations at varying spacing ratios, with microscopy images of WO₃ at (a) 500 μm or η = 2; (b) 750 μm or η = 3; (c) 1000 μm or η = 4; and (d) 1500 μm or η = 6; and (e) comparing the porosities of the printed samples along with the theoretical 3D-printed porosities.

5.3.3 Relating Rheology to Printing

It is worth pointing out that all the cylinders exhibit porosities less than the theoretical porosity, thus demonstrating that Equation 5.2 is an upper limit. This can be observed more distinctly when comparing the side views of some of the printed cylinders. An example is Figure 5.4, which shows side views of printed SiO₂ and WO₃ samples. Notice in Figure 5.4 (a) that the SiO₂ lattice structure is aligned such that there do not appear to be deviations, while in Figure 5.4 (b), the WO₃ lattice has some bending or deflections in the printed struts.

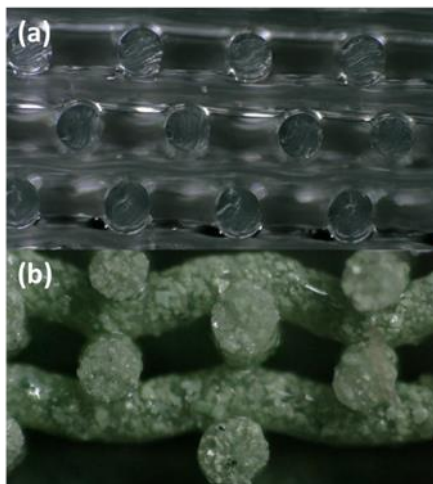


Figure 5.4: Side views comparing deviations in printed (a) SiO_2 and (b) WO_3 samples.

Previous researchers have attempted to capture this phenomenon with a variety of theoretical, phenomenological, and empirical models, where the properties of the ink formulation relate to the printed lattice structure. Smay et al. correlated deflection in a strut with the distance between struts across a variety of ink formulations at different pH values and provided a criterion for the storage modulus [50]. The relevant values for the ink formulations in this study were placed in this criterion, which was not found to accurately predict the printing behavior. M'Barki et al. also developed a model that incorporated other variables such as the yield stress, print height, and capillary forces; however, it did not relate these to the spacing ratio of the lattice structure [58]. Chan et al. tested the rheology of some inks against their printability and came to the same conclusion [49] for the two models studied. To move the discussion forward, Chan et al. proposed an empirical relation between the equilibrium storage modulus, recovery of the storage modulus after shearing, and the yield stress. A constant derived from a linear discriminant function was able to separate the ink formulations into those that slumped upon printing and those that printed

well; however, this model does not correlate the ink rheology with the printability of a lattice structure based on the spacing ratio. Therefore, the ink formulations in this study were used to inform another model that can relate rheology and printability.

To understand the deflection behavior observed in Figure 5.4, an appropriate model can be constructed by considering the simplified scenario of a beam with supports on either end. This is a standard problem in civil engineering, where it can be assumed that a beam is supported by the two orthogonally printed struts below it, and there are no layers printed above. Thus, the length of the strut is the center-to-center distance between the struts below $L = \eta d$, and the only acting force F is gravitational. The deflection δ that the beam experiences is a function of the force, beam length, Young's modulus of the ink E , and the moment of inertia I of a cylinder rotated about its axial direction, which is shown in Equation 5.4. Considering the deflection as a percentage of the beam diameter $\delta = \alpha d$ and rearranging all the numerical constants on one side and all the variables on the other side result in Equation 5.5.

$$\delta = \frac{FL^3}{48EI} = \frac{\rho g \frac{\pi}{4} d^2 L^4}{48E \frac{\pi}{64} d^4} \quad \text{Equation 5.4}$$

$$3\alpha = \frac{\rho g \eta^4 d}{E} = (E^{-1} \rho g)(\eta^4 d) \quad \text{Equation 5.5}$$

This model demonstrates which material properties are important towards understanding beam deflection with supports on either side. Building up this model to describe an entire printed lattice can be conducted in a phenomenological way by utilizing similar variables to those in Equation 5.5; however, instead of evaluating the deflection of a single beam, the relationship between the ink properties and overall lattice structure can

be investigated. As Young's modulus is a measure of an elastic material and the ink is viscoelastic, conceptually equivalent material properties that describe the system should be used instead. Young's modulus is the stiffness of a material in the linear viscoelastic region, meaning a commensurate property to determine the stiffness of the inks would be the equilibrium storage modulus. Indeed, others have shown that the storage modulus and yield stress are correlated with the layer shape retention of deposited layers [44,51]. Conceptually, this makes sense, where the lattice structure and its deviations should be able to be represented by the ink's equilibrium storage modulus and yield stress, which describe how an ink prints and whether it can support itself. Using these, a variable referred to as the ink parameter was defined, $K_{ink} = G'_{eq} \sigma_y^{-2} \rho_{ink} g$. To incorporate the printed structure itself, a variable called the lattice parameter was defined, $\Psi_{lattice} = \eta^4 d$. The product of these two variables is a dimensionless quantity called the structure parameter in this study, which is given as Equation 5.6. This product, being dimensionless and of similar form to Equation 5.5, can provide an empirical determination on how the spacing ratio in a lattice and general printing properties can be related to the ink formulation attributes.

$$K_{ink} \Psi_{lattice} = (G'_{eq} \sigma_y^{-2} \rho_{ink} g)(\eta^4 d) \quad \text{Equation 5.6}$$

Notice from Figure 5.3 that the SiO₂-formulated cylinders are closest to the theoretical limit. Thus, the height of the printed SiO₂ cylinders was used as an ideal for comparison purposes. Defining the thickness deviation of a printed cylinder $t' = 1 - \frac{h_{ink,\eta}}{h_{SiO_2,\eta}}$ in terms of the SiO₂ print with the same spacing ratio, all the inks that had their rheological properties tested can be compared. Figure 5.5 (a) presents a graph plotting the thickness deviations against the logarithm of the structure parameters. The horizontal

straight line represents a thickness deviation at one standard deviation. Thus, all the points below the horizontal line represent printed samples that have heights within one standard deviation of the ideal height, which is represented by the SiO₂ prints. Likewise, all the points above the horizontal line represent printed samples that have heights less than one standard deviation of the ideal height. Thickness deviations above this line mean that the print failed and that the ink does not have the rheological properties to support the spacing ratio. Linear extrapolations were conducted for each formulation to relate the thickness deviation to the structure parameters. Finding each ink's linear relationship led to the determination of the maximum spacing ratio η_{max} , which is the spacing ratio that produces a print with the thickness deviation equal to one standard deviation. Each formulation thus had a set of coordinates $(\eta_{max}, K_{ink} \Psi_{lattice})$ that were plotted, and a logarithmic curve was fitted to the data. The resulting empirical relationship is given as Equation (7), where the structure parameters must be in the region between that of SiO₂ and the fitted model. Hence, this relationship demonstrates that based on the rheological properties of an ink, it can be determined how much spacing can be introduced during 3D printing for an FCT structure. Figure 5.5 (b) presents $K_{ink} \Psi_{lattice}$ against the spacing ratio for the five formulations in which rheology was performed.

From these data, a printability profile was developed which shows regions of poor and good printability (Figure 5.6). Equation 5.7 defines the boundary of these regions, where good printability means that for a 250 μm nozzle printing an FCT part with a certain ink formulation, the resulting thickness will be within one standard deviation. A poor printability in this context means that the ink formulation will slump and have thickness deviations greater than one standard deviation. Using Equation 5.7, the ink parameter and

maximum spacing ratio are provided for the rheological-tested ink formulations in Table 5.3.

$$K_{ink}\Psi_{lattice} \leq 2.7686e^{0.323\eta} + 5.056 \quad \text{Equation 5.7}$$

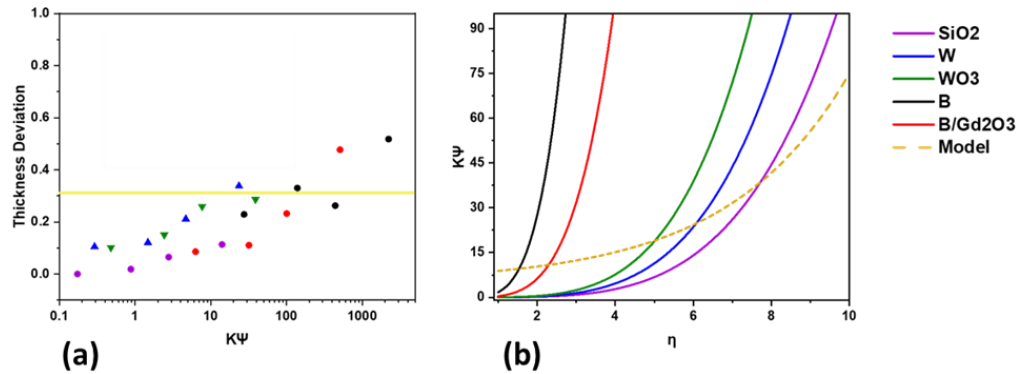


Figure 5.5: Determining how the structure parameters are related to spacing ratios, where (a) the thickness deviation is plotted against $K_{ink}\Psi_{lattice}$, with a yellow line at the one standard deviation mark denoting whether a print was acceptable, and (b) $K_{ink}\Psi_{lattice}$ plotted against the spacing ratio along with the model presenting the upper bound for the structure parameters.

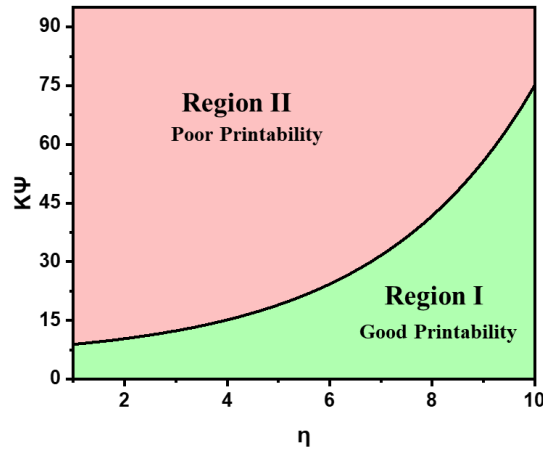


Figure 5.6: Using a 250 μm nozzle and an FCT geometry, rheology-tested ink formulations were assessed based on their material properties and thickness deviations to determine Equation (7), which provides a regime for printability. Values below the upper limit in Equation (7) are in Region I (Good Printability), which is defined as minimal slumping and within one standard deviation. Values above the upper limit are in Region II (Poor Printability), which is defined as thickness deviations above one standard deviation.

Table 5.3: Ink parameters for the rheological-tested ink formulations and their maximum spacing ratios according to Equation 5.7.

Formulation	$K_{\text{ink}} \text{ (m}^{-1}\text{)}$	η_{max} (From Equation (7))
SiO₂	4.345×10^1	7.7
W	7.286×10^1	6.0
WO₃	1.200×10^2	5.0
B	6.874×10^3	1.5
B/Gd₂O₃	1.571×10^3	2.2

5.3.4 Thermomechanical Properties

Each of the printed cylinders underwent compressive strain testing, where the protocol utilized four compression and decompression cycles reaching a maximum load of 0.4 MPa. Taking the last cycle for data analysis, maximum compressive strains were determined and each sample's Young's modulus in the linear viscoelastic region was evaluated. Figures 5.7 (a) and (b) show these material characteristics plotted against the porosities of the measured samples, respectively. From Figure 5.7 (a), it appears that the maximum compressive strains are bound within a region and increase in proportion to the porosity. This phenomenon is intuitive, where greater porosity in a viscoelastic material means that during compressions, more void spaces are filled in with material. This phenomenon is similar to what can explain Figure 5.7 (b), where Young's modulus can describe how stiff or flexible a material is before it deforms. When all the samples are plotted together, the graph appears sigmoidal, where above a critical porosity, there is a dramatic decrease in the stiffness. This point seems to be approximately $\varphi_c = 0.55$, where every formulation except for SiO₂ had at least one sample below this amount. Notice that samples with porosities less than the critical porosity exhibited a Young modulus between

0.45 and 0.7 MPa, while those samples with porosities greater than the critical porosity exhibited a Young modulus between near 0 and 0.25 MPa. As the maximum load during the compression cycles was 0.4 MPa, this means that samples with porosities above the critical porosity were maximally compressed.

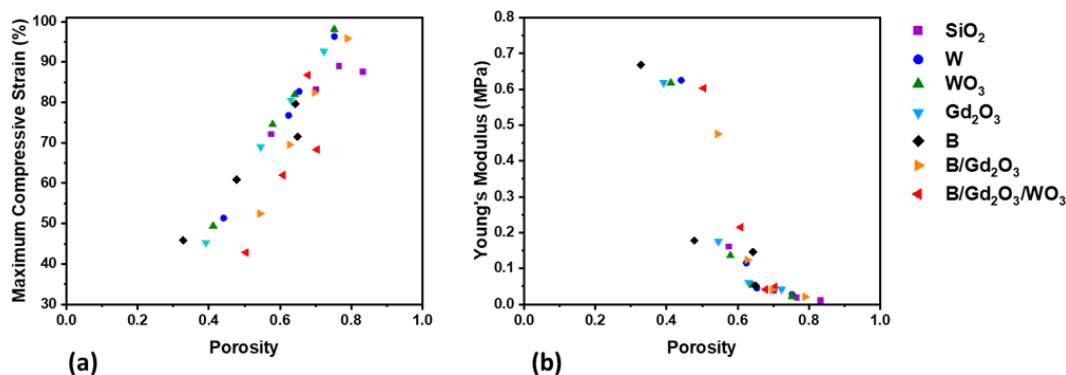


Figure 5.7: Mechanical properties from compression testing as functions of sample porosity: (a) maximum compressive strain, and (b) Young's modulus.

Thermal conductivity was explored in the formulations with 50 wt% metal or ceramic fillers, which include 3D-printed cylinders of B, W, WO₃, and Gd₂O₃. Figures 5.8 (a) and (b) present graphs of thermal conductivity against porosity and maximum compressive strain, respectively. The first observation from these figures is that thermal conductivity increases with porosity. As the maximum compressive strain and porosity are positively correlated, this means that thermal conductivity and maximum compressive strain should be positively correlated as well, which is demonstrated in Figure 5.8 (b). Additionally, the instrument that measures thermal conductivity applies a pressure of 60 psi \approx 0.4 MPa and thus maximally compresses the samples with porosity greater than 55%. Therefore, greater contact is made between the printed layers, and heat can flow with fewer obstructions due to air voids. Another interesting point to take note of is how the thermal

conductivities in Figure 5.8 are clustered together. Notice that B cylinders exhibit greater thermal conductivity than the others. This is due to the volume percent of the B ink; although all the formulations possess 50 wt% metal or ceramic filler, boron is less dense than the other fillers, and thus its volume fraction is much greater. This contributes towards a greater percolation of boron particles, where at 30 volume%, the heat flow has a less obstructed path due to the siloxane matrix and silica filler. On the other side, tungsten has a much greater density than tungsten (VI) oxide or gadolinium (III) oxide; thus, the volume percent of the filler in the W formulation (5.2%) is less than that of the WO_3 (12.9%) and Gd_2O_3 (12.4%) formulations. This is overcome by the fact that metals, in general, have much greater thermal conductivities than ceramics, and this is indeed true when comparing tungsten ($170 \text{ Wm}^{-1}\text{K}^{-1}$) to tungsten (VI) oxide ($4.5 \text{ Wm}^{-1}\text{K}^{-1}$) or gadolinium (III) oxide ($27 \text{ Wm}^{-1}\text{K}^{-1}$). Thus, despite the lower volume percent of the filler in W, the thermal conductivity is balanced out, and the W, WO_3 , and Gd_2O_3 printed cylinders exhibit similar thermal conductivity values.

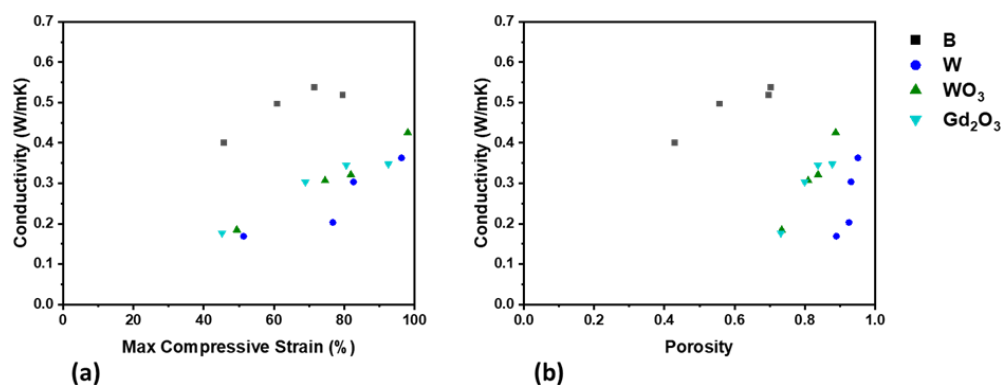


Figure 5.8: Thermal conductivity of 50 wt% metal- and ceramic-filled printed cylinders plotted against (a) porosity and (b) maximum compressive strain.

One aspect of this work that must be pointed out is the blatant difference between many types of porosities. Throughout the literature, it is well documented that as porosity increases, many transport properties such as thermal and electrical conductivity decrease. Thus, a distinction must be made for micropores, which are voids within the material formulation itself, either by initial or process design, and structural voids, which are voids not in the ink but in the overall lattice structure. Although both types of pores would contribute towards increasing the compressive strain and thus increasing thermal conductivity, 3D printing offers a way to directly tune the porosity due to structural voids and therefore control the thermomechanical properties.

To understand the thermal limits of the printed parts, thermogravimetric analysis (TGA) was performed. Both the TGA and derivative TGA (DTGA) curves are shown for the printed parts in Figure 5.9. Data concerning the onset of thermal degradation, temperature of thermal decomposition, and residual mass for the printed parts are presented in Table 5.4. The formulations that do not incorporate boron are presented in Figures 5.9 (a) and (b), where two distinct degradation peaks occur. One interesting aspect is that the onset of thermal degradation $T_{d5\%}$ of the SiO_2 formulation occurs at a lower temperature than the others. Indeed, there is a 40°C increase once the other fillers are added. Additionally, the residual mass of the parts with 4.5 wt% silica increases by 10 wt% when compared to the SiO_2 formulation. Thus, the fillers increase the thermal stability of the ink. The first DTGA peak for all these printed formulations occurs around the same temperature, indicating the main pathway for thermal decomposition is unaltered. The TGA and DTGA curves for the samples containing boron are presented in Figures 5.9 (c) and (d). The B printed formulation demonstrates a 60°C increase in $T_{d5\%}$ compared to the

SiO₂ printed formulation, and this value increases further when multiple fillers are added. The printed formulation that has the highest $T_{d5\%}$ is the B/Gd₂O₃/WO₃ ink, which is 15°C higher than the B/Gd₂O₃ ink and 130°C higher than the SiO₂ ink. Interestingly, the boron-containing printed parts exhibit only one main thermal decomposition peak, and it is shifted by an increase of 170°C. As this is only observed in the ink formulations with boron, this indicates that boron affects the pathway of thermal decomposition. Indeed, a similar phenomenon has been observed before, where Rallini et al. reported that a polymeric matrix incorporating boron carbide resulted in a substantial shift in thermal stability towards higher temperatures [59]. It was proposed that this behavior resulted from the conversion to boron oxide and the subsequent inhibition of oxidation of the polymer matrix. In addition to the shift in thermal stability, a decrease in residual mass was observed when comparing the B and SiO₂ formulations. The B printed parts exhibit a decrease in the residual mass, thus indicating that char products differ by way of B modifying the thermal decomposition chemistry. Overall, whenever fillers other than SiO₂ were used, an increase in thermal stability was observed. Additionally, boron-containing inks, especially the ink that incorporates neutron and gamma shielding components, demonstrate the highest thermal stability of all the formulations.

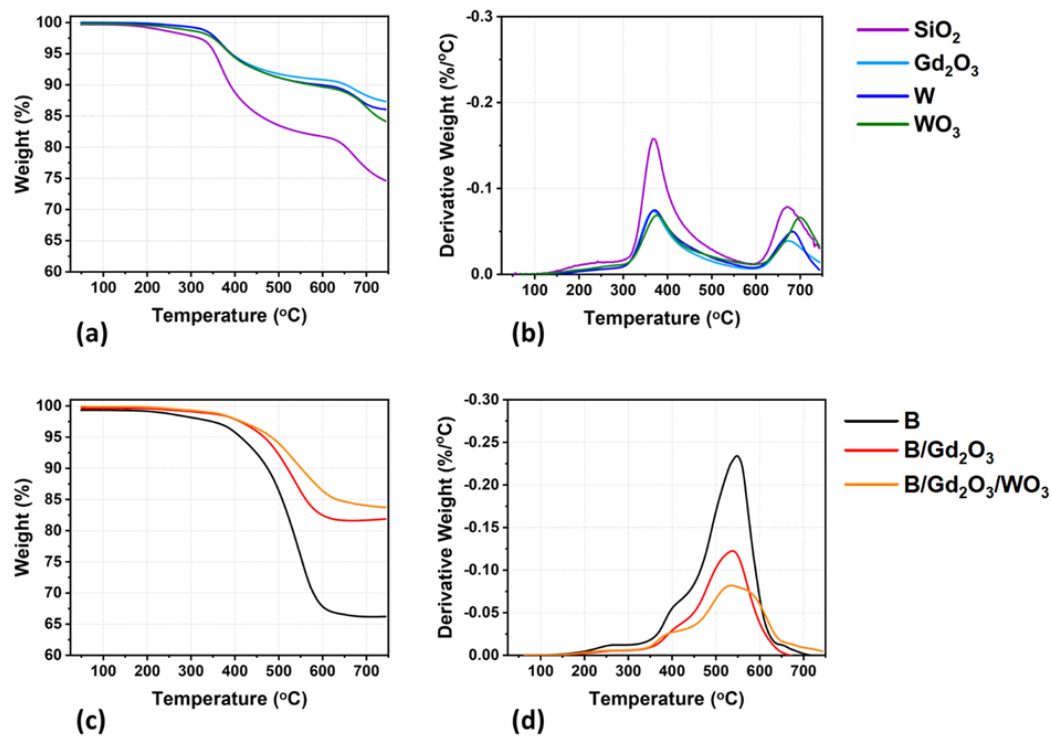


Figure 5.9: TGA curves for the 3D-printed cylinders: (a) weight percent for samples without boron; (b) derivative weight percent for samples without boron; (c) weight percent for samples with boron; and (d) derivative weight percent for samples with boron.

Table 5.4: Thermal stability properties of the 3D-printed formulations.

Formulation	T _{d5%} (°C)	T _{dMax} (°C)	m _f (%)
SiO ₂	355	371	75
W	392	373	86
WO ₃	390	377	84
Gd ₂ O ₃	392	369	87
B	413	548	66
B/Gd ₂ O ₃	467	536	82
B/Gd ₂ O ₃ /WO ₃	483	537	84

5.3.5 Attenuation of Ionizing Radiation

Neutron radiography was performed on some printed samples to obtain a qualitative assessment of their ability to behave as radiation shields. Five ink formulations were used to print cylinders for this experiment: B^N ; Gd_2O_3 ; B^N/Gd_2O_3 ; B^{10}/Gd_2O_3 ; and SiO_2 . B^N in the formulations refers to natural abundance boron, which contains approximately 20% B^{10} and 80% B^{11} . B^{10} in the formulations refers to isotopically enriched boron, which is nearly 100% B^{10} . Besides the SiO_2 , all the formulations had 50 wt% non-silica filler. The B^N/Gd_2O_3 and B^{10}/Gd_2O_3 formulations contained 40 wt% boron and 10 wt% gadolinium (III) oxide. The qualitative results of the 2D radiography experiments are shown in Figure 5.10. The amount of light corresponds to the amount of neutrons that passed through the detector, which was being blocked by the printed cylinders. Thus, a lighter image corresponds to more neutrons passing through, while a darker image corresponds to less neutrons passing through. Therefore, the darker the image, the greater the printed cylinder behaved as a radiation shield. As it can be observed in the figure, the SiO_2 cylinder did not attenuate much at all, while the other printed samples attenuated a significant amount of incoming neutrons. As expected, due to B^{10} being the isotope that absorbs neutrons, the B^{10}/Gd_2O_3 sample provided the greatest shielding.

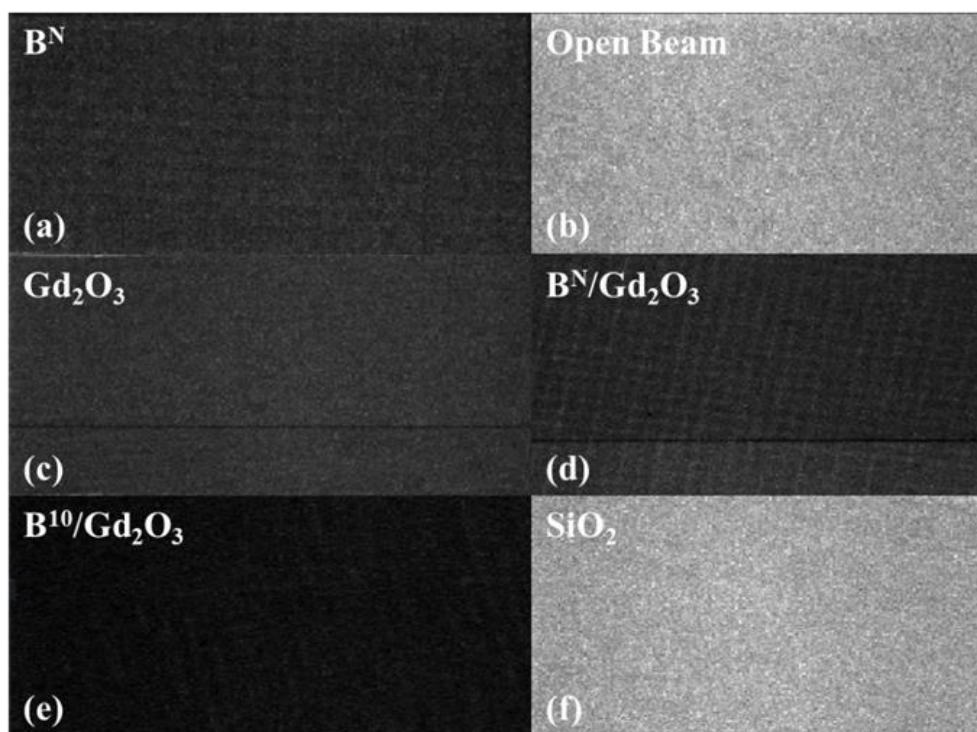


Figure 5.10: 2D radiographs, summed over all neutron energies from 0.001 to 100 eV, of printed samples. For the formulations besides SiO₂, the total filler content was 50 wt%. Lighter images correspond to more neutrons passing into the detector, while darker images correspond to a greater attenuation of incoming neutrons: (a) 50 wt% B^N; (b) open beam (no sample); (c) 50 wt% Gd₂O₃; (d) 40/10 wt% B^N/Gd₂O₃; (e) 40/10 wt% B¹⁰/Gd₂O₃; and (f) 10 wt% SiO₂. All neutron-exposed pads were 3D printed using 500 μm spacing.

After the neutron radiography experiments proved that the ink formulations performed successfully as shields, more carefully designed printed structures were developed to incorporate additional functionality. This was conducted by 3D printing multi-material heterogeneous cylinders using Gd₂O₃ and WO₃ inks. As a comparison, homogeneous parts were also fabricated. For the homogeneous parts, Gd₂O₃ and WO₃ were incorporated into the same ink formulation as already described and printed. Using X-ray fluorescence (XRF), a color map was generated, shown as Figure 5.11 (a), where the green coloration represents WO₃, and the white coloration represents Gd₂O₃. Observe that both colorations are superimposed, and thus the fillers exist in a homogeneous distribution

within the printed part. This is in contrast to Figure 5.11 (b), where separate formulations of Gd_2O_3 and WO_3 were used to print a single part where they did not exist in the same space, thus exhibiting a heterogeneous distribution. Although multi-material 3D-printed structures have been explored [19], this further demonstrates that a single printed part for radiation shielding can be constructed from a variety of ink formulations to possess multifunctional characteristics.

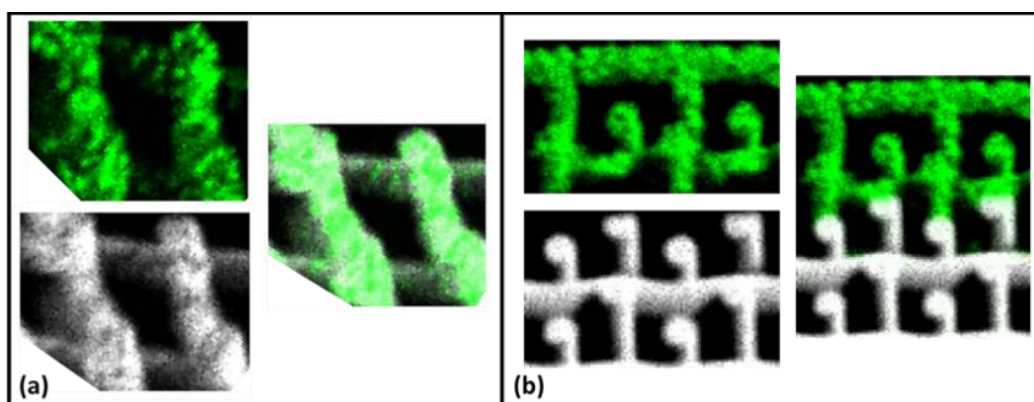


Figure 5.11: 3D printing with formulations of WO_3 and Gd_2O_3 (a) in one ink to create a homogeneous part and (b) as separate inks to produce a heterogeneous part.

5.4 Conclusions

Radiation shielding DIW 3D printing formulations were developed, optimized, characterized, and used for 3D printing. Varying spacing ratios, which are the ratios of the center-to-center distance between adjacent struts to the diameter of the printed struts, were used when printing face-centered tetragonal (FCT) lattice structures. A height deviation was observed in the final printed cylinders when compared to the theoretical design, which was a result of the ink rheological properties. Previous models that correlate rheology and printability were found to not accurately predict the observations in this study, and as such, a new model was needed. Using beam deflection as a starting point for a model, an

empirical relationship was created that correlated the maximum printable spacing ratio with the structure parameter, which is defined as the product of the ink and lattice parameters. Thus, using this empirical model allows for the refinement of new ink formulations in the future by way of relating the rheological properties of an ink to the quality of its final printed structure.

By varying the spacing ratio of the printed cylinders, the thermomechanical properties of printed parts were able to be altered and thus characterized. Increasing the spacing ratio led to an increase in porosity, which results in an increase in the maximum compressive strain, a decrease in Young's modulus, and an increase in thermal conductivity while compressed. Furthermore, the thermal stability of the samples was assessed, and it was found that incorporating fillers in addition to silica increased the thermal stability of the printed cylinders. When boron was used as a filler, the pathway of thermal decomposition was altered as well, leading to formulations that possessed much greater thermal stability than the other printed formulations.

Neutron radiography proved that the parts behaved successfully as radiation shields, and thus further developments and refinements can be made to the ink formulations for specific applications. Furthermore, heterogeneity in printing these radiation shields was tested, where an ink formulation combining WO_3 and Gd_2O_3 was used to print a homogeneous cylinder, and two different ink formulations, one containing WO_3 and the other containing Gd_2O_3 , were used to print a heterogeneous cylinder. Using X-ray fluorescence (XRF), a color map of the elements was generated and demonstrated that the printed cylinders were indeed homogeneous and heterogeneous. Thus, this work provides

a foundation for further research into developing greater tunable DIW inks that can be used for multi-ink-specific heterogeneous 3D printing for a variety of specialty applications.

References

1. Davoudinejad, A.; Diaz-Perez, L. C.; Quagliotti, D.; Pedersen, D. B.; Albajez-García, J. A.; Yagüe-Fabra, J. A.; Tosello, G. Additive manufacturing with vat polymerization method for precision polymer micro components production. *Procedia CIRP* 2018, 75, 98–102.
2. Ng, W. L.; Lee, J. M.; Zhou, M.; Chen, Y.-W.; Lee, K.-X. A.; Yeong, W. Y.; Shen, Y.-F. Vat polymerization-based bioprinting—Process, materials, applications and regulatory challenges. *Biofabrication* 2020, 12, 022001.
3. Kruth, J.P.; Mercelis, P.; Van Vaerenbergh, J.; Froyen, L.; Rombouts, M. Binding mechanisms in selective laser sintering and selective laser melting. *Rapid Prototyp. J.* 2005 11.
4. Yap, C.Y.; Chua, C. K.; Dong, Z. L.; Liu, Z. H.; Zhang, D. Q.; Loh, L. E.; Sing, S. L. Review of selective laser melting: Materials and applications. *Appl. Phys. Rev.* 2015, 2, 041101.
5. Lewis, J.A.; Smay, J. E.; Stuecker, J.; Cesarano, J. Direct ink writing of three-dimensional ceramic structures. *J. Am. Ceram. Soc.* 2006, 89, 3599–3609.
6. Franchin, G.; Scanferla, P.; Zeffiro, L.; Elsayed, H.; Baliello, A.; Giacomello, G.; Pasetto, M.; Colombo, P. Direct ink writing of geopolymeric inks. *J. Eur. Ceram. Soc.* 2017, 37, 2481–2489.

7. Tagliaferri, S., A. Panagiotopoulos, and C. Mattevi, Direct ink writing of energy materials. *Mater. Adv.* 2021, 2, 540–563.
8. Calvert, P. Inkjet printing for materials and devices. *Chem. Mater.* 2001, 13, 3299–3305.
9. Minemawari, H.; Yamada, T.; Matsui, H.; Tsutsumi, J. y.; Haas, S.; Chiba, R.; Kumai, R.; Hasegawa, T. Inkjet printing of single-crystal films. *Nature* 2011, 475, 364–367.
10. Li, Z.; Li, P.; Chen, G.; Cheng, Y.; Pi, X.; Yu, X.; Yang, D.; Han, L.; Zhang, Y.; Song, Y. Ink engineering of inkjet printing perovskite. *ACS Appl. Mater. Interfaces* 2020, 12, 39082–39091.
11. Kong, S.; Liao, D.-j.; Jia, Y.-m.; An, C.-w.; Li, C.-y.; Ye, B.-y.; Wu, B.-d.; Wang, J.-y.; Guo, H.; Hong, Z.-w. Performances and direct writing of CL-20 based ultraviolet curing explosive ink. *Def. Technol.* 2020 in press
12. Dimitriou; E; Michailidis, N.S. Printable conductive inks used for the fabrication of electronics: An overview. *Nanotechnology* 2021, doi:10.1088/1361-6528/abefff
13. Rodzeń, K.; Sharma, P. K.; McIlhagger, A.; Mokhtari, M.; Dave, F.; Tormey, D.; Sherlock, R.; Meenan, B. J.; Boyd, A. The Direct 3D Printing of Functional PEEK/Hydroxyapatite Composites via a Fused Filament Fabrication Approach. *Polymers* 2021, 13, 545.
14. Brounstein, Z.; Talley, S.; Dumont, J. H.; Zhao, J.; Lee, K.-S.; Labouriau, A. Fused filament fabrication of polymer composites for extreme environments. *J. Mater. Res.* 2020, 35, 1493–1503.

15. Brounstein, Z., C.M. Yeager, and A. Labouriau, Development of Antimicrobial PLA Composites for Fused Filament Fabrication. *Polymers* 2021, 13, 580.
16. Zhang, J.; Feng, X.; Patil, H.; Tiwari, R. V.; Repka, M. A. Coupling 3D printing with hot-melt extrusion to produce controlled-release tablets. *Int. J. Pharm.* 2017, 519, 186–197.
17. Musazzi, U.M.; Selmin, F.; Ortenzi, M. A.; Mohammed, G. K.; Franzé, S.; Minghetti, P.; Cilurzo, F. Personalized orodispersible films by hot melt ram extrusion 3D printing. *Int. J. Pharm.* 2018, 551, 52–59.
18. Tabard, L.; Garnier, V.; Prud'Homme, E.; Courtial, E.-J.; Meille, S.; Adrien, J.; Jorand, Y.; Gremillard, L. Robocasting of highly porous ceramics scaffolds with hierarchized porosity. *Addit. Manuf.* 2021, 38, 101776.
19. Zhang, D.; Jonhson, W.; Heng, T. S.; Ang, Y. Q.; Yang, L.; Tan, S. C.; Peng, E.; He, H.; Ding, J. A 3D-printing method of fabrication for metals, ceramics, and multi-materials using a universal self-curable technique for robocasting. *Mater. Horiz.* 2020, 7, 1083–1090.
20. Liu, D.; Chen, C.; Zhou, Y.; Bao, Y.; Wang, R.; Liu, Y.; He, S.; Huang, H.; Zhang, C.; Foster, B. 3D-Printed, High-Porosity, High-Strength Graphite Aerogel. *Small Methods* 2021, 2001188.
21. Chandrasekaran, S.; Yao, B.; Liu, T.; Xiao, W.; Song, Y.; Qian, F.; Zhu, C.; Duoss, E. B.; Spadaccini, C. M.; Li, Y. Direct ink writing of organic and carbon aerogels. *Mater. Horiz.* 2018, 5, 1166–1175.

22. Li, V.C.-F.; Dunn, C. K.; Zhang, Z.; Deng, Y.; Qi, H. J. Direct ink write (DIW) 3D printed cellulose nanocrystal aerogel structures. *Sci. Rep.* 2017, 7, 1–8.
23. Minas, C.; Carnelli, D.; Tervoort, E.; Studart, A. R. 3D printing of emulsions and foams into hierarchical porous ceramics. *Adv. Mater.* 2016, 28, 9993–9999.
24. Chen, Y.; Han, P.; Vandi, L.-J.; Dehghan-Manshadi, A.; Humphry, J.; Kent, D.; Stefani, I.; Lee, P.; Heitzmann, M.; Cooper-White, J. A biocompatible thermoset polymer binder for Direct Ink Writing of porous titanium scaffolds for bone tissue engineering. *Mater. Sci. Eng. C* 2019, 95, 160–165.
25. Koons, L. G.; Diba, M.; Mikos, A.G. Materials design for bone-tissue engineering. *Nat. Rev. Mater.* 2020, 5, 584–603.
26. Coffigniez, M.; Gremillard, L.; Balvay, S.; Lachambre, J.; Adrien, J.; Boulnat, X. Direct-ink writing of strong and biocompatible titanium scaffolds with bimodal interconnected porosity. *Addit. Manuf.* 2021, 39, 101859.
27. Yan, Y.; Chen, H.; Zhang, H.; Guo, C.; Yang, K.; Chen, K.; Cheng, R.; Qian, N.; Sandler, N.; Zhang, Y. S. Vascularized 3D printed scaffolds for promoting bone regeneration. *Biomaterials* 2019, 190, 97–110.
28. Compton, B.G.; Kemp, J. W.; Novikov, T. V.; Pack, R. C.; Nlebedim, C. I.; Duty, C. E.; Rios, O.; Paranthaman, M. P. Direct-write 3D printing of NdFeB bonded magnets. *Mater. Manuf. Process.* 2018, 33, 109–113.
29. Erkoc, P.; Odeh, Y. N.; Alrifai, N.; Zirhli, O.; Gunduz Akdogan, N.; Yildiz, B.; Misirlioglu, I. B.; Akdogan, O. Photocurable pentaerythritol triacrylate/lithium phenyl-

- 2, 4, 6-trimethylbenzoylphosphinate-based ink for extrusion-based 3D printing of magneto-responsive materials. *J. Appl. Polym. Sci.* 2020, *137*, 49043.
30. Bastola, A; Paudel, M.; Li, L. Development of hybrid magnetorheological elastomers by 3D printing. *Polymer* 2018, *149*, 213–228.
31. Kharita, M; Yousef, S.; AlNassar, M. Review on the addition of boron compounds to radiation shielding concrete. *Prog. Nucl. Energy* 2011, *53*, 207–211.
32. Tyagi, G.; Singhal, A.; Routroy, S.; Bhunia, D.; Lahoti, M. A review on sustainable utilization of industrial wastes in radiation shielding concrete. *Mater. Today Proc.* 2020, *32*, 746–751.
33. McCaffrey, J.; Shen, H.; Downton, B.; Mainegra-Hing, E. Radiation attenuation by lead and nonlead materials used in radiation shielding garments. *Med. Phys.* 2007, *34*, 530–537.
34. Chang, L.; Zhang, Y.; Liu, Y.; Fang, J.; Luan, W.; Yang, X.; Zhang, W. Preparation and characterization of tungsten/epoxy composites for γ -rays radiation shielding. *Nucl. Instrum. Methods Phys. Res. Sect. B: Beam Interact. Mater. At.* 2015, *356*, 88–93.
35. Li, R.; Gu, Y.; Wang, Y.; Yang, Z.; Li, M.; Zhang, Z. Effect of particle size on gamma radiation shielding property of gadolinium oxide dispersed epoxy resin matrix composite. *Mater. Res. Express* 2017, *4*, 035035.
36. Kaky, K.M.; Sayyed, M.; Laariedh, F.; Abdalsalam, A. H.; Tekin, H.; Baki, S. Structural, optical and radiation shielding properties of zinc boro-tellurite alumina glasses. *Appl. Phys. A* 2019, *125*, 1–12.

37. Alshahrani, B.; Olarinoye, I.; Mutuwong, C.; Sriwunkum, C.; Yakout, H.; Tekin, H.; Al-Buriahi, M. Amorphous alloys with high Fe content for radiation shielding applications. *Radiat. Phys. Chem.* 2021, *183*, 109386.
38. Kilic, G.; El Agawany, F.; Ilik, B. O.; Mahmoud, K.; Ilik, E.; Rammah, Y. Ta₂O₅ reinforced Bi₂O₃–TeO₂–ZnO glasses: Fabrication, physical, structural characterization, and radiation shielding efficacy. *Opt. Mater.* 2021, *112*, 110757.
39. Talley, S.J.; Robison, T.; Long, A. M.; Lee, S. Y.; Brounstein, Z.; Lee, K.-S.; Geller, D.; Lum, E.; Labouriau, A. Flexible 3D Printed Silicones for Gamma and Neutron Radiation Shielding. *Radiation Physics and Chemistry*, 2021, *188*, 109616.
40. Ceh, J.; Youd, T.; Mastrovich, Z.; Peterson, C.; Khan, S.; Sasser, T. A.; Sander, I. M.; Doney, J.; Turner, C.; Leevy, W. M. Bismuth Infusion of ABS Enables Additive Manufacturing of Complex Radiological Phantoms and Shielding Equipment. *Sensors* 2017, *17*, 459.
41. Woosley, S.; Galehdari, N. A.; Kelkar, A.; Aravamudhan, S. Fused deposition modeling 3D printing of boron nitride composites for neutron radiation shielding. *J. Mater. Res.* 2018, *33*, 3657–3664.
42. Szentmiklosi, L.; Maroti, B.; Kis, Z.; Janik, J.; Horvath, L. Z. Use of 3D mesh geometries and additive manufacturing in neutron beam experiments. *J. Radioanal. Nucl. Chem.* 2019, *320*, 451–457.
43. Chandrasekaran, S.; Lu, R.; Landingham, R.; Cahill, J. T.; Thornley, L.; Du Frane, W.; Worsley, M. A.; Kuntz, J. D. Additive manufacturing of graded B₄C–Al cermet with complex shapes. *Mater. Des.* 2020, *188*, 108516.

44. Costakis, W.J., Jr.; Rueschhoff, L. M.; Diaz-Cano, A. I.; Youngblood, J. P.; Trice, R. W. Additive manufacturing of boron carbide via continuous filament direct ink writing of aqueous ceramic suspensions. *J. Eur. Ceram. Soc.* 2016, *36*, 3249–3256.
45. Al-Hadeethi, Y; Sayyed, M.; Al-Buriahi, M. Bioactive glasses doped with TiO₂ and their potential use in radiation shielding applications. *Ceram. Int.* 2020, *46*, 14721–14732.
46. Mirji, R; Lobo, B. 24. Radiation shielding materials: A brief review on methods, scope and significance. In Proceedings of the National Conference on ‘Advances in VLSI and Microelectronics. PC Jabin Science College, Huballi, India, 27 January 2017.
47. Levchenko, I.; Bazaka, K.; Belmonte, T.; Keidar, M.; Xu, S. Advanced Materials for Next-Generation Spacecraft. *Adv. Mater.* 2018, *30*, 1802201.
48. Al-Ghamdi, H.; Dong, M.; Sayyed, M. I.; Wang, C.; Almuqrin, A. H.; Almasoud, F. I. The Vital Role of La²O³ on the La²O³-CaO-B²O³-SiO² Glass System for Shielding Some Common Gamma Ray Radioactive Sources. *Materials* 2021, *14*, 4776.
49. Chan, S, S.; Sesso, M.L.; Franks, G.V. Direct ink writing of hierarchical porous alumina-stabilized emulsions: Rheology and printability. *J. Am. Ceram. Soc.* 2020, *103*, 5554–5566.
50. Smay, E, J.; Cesarano, J.; Lewis, J.A. Colloidal inks for directed assembly of 3-D periodic structures. *Langmuir* 2002, *18*, 5429–5437.
51. Talley, S.J.; Branch, B.; Welch, C. F.; Park, C. H.; Watt, J.; Kuettner, L.; Patterson, B.; Dattelbaum, D. M.; Lee, K.-S. Impact of filler composition on mechanical and dynamic

- response of 3-D printed silicone-based nanocomposite elastomers. *Compos. Sci. Technol.* 2020, *198*, 108258.
52. Smay, J.E.; Gratson, G. M.; Shepherd, R. F.; Cesarano III, J.; Lewis, J. A. Directed colloidal assembly of 3D periodic structures. *Adv. Mater.* 2002, *14*, 1279–1283.
53. Duoss, E.B.; Weisgraber, T. H.; Hearon, K.; Zhu, C.; Small IV, W.; Metz, T. R.; Vericella, J. J.; Barth, H. D.; Kuntz, J. D.; Maxwell, R. S. Three-dimensional printing of elastomeric, cellular architectures with negative stiffness. *Adv. Funct. Mater.* 2014, *24*, 4905–4913.
54. Mora, A; Verma, P.; Kumar, S. Electrical conductivity of CNT/polymer composites: 3D printing, measurements and modeling. *Compos. Part B Eng.* 2020, *183*, 107600.
55. Song, R.; Wang, Y.; Ishutov, S.; Zambrano-Narvaez, G.; Hodder, K. J.; Chalaturnyk, R. J.; Sun, S.; Liu, J.; Gamage, R. P. A comprehensive experimental study on mechanical behavior, microstructure and transport properties of 3D-printed rock analogs. *Rock Mech. Rock Eng.* 2020, *53*, 5745–5765.
56. Karande, S.T.; Ong, J.L.; Agrawal, C.M. Diffusion in musculoskeletal tissue engineering scaffolds: design issues related to porosity, permeability, architecture, and nutrient mixing. *Ann. Biomed. Eng.* 2004, *32*, 1728–1743.
57. Zlatanic, A.; Radojicic, D.; Wan, X.; Messman, J. M.; Dvornic, P. R. Suppression of crystallization in polydimethylsiloxanes and chain branching in their phenyl-containing copolymers. *Macromolecules* 2017, *50*, 3532–3543.

58. M'barki, A; Bocquet, L.; Stevenson, A. Linking rheology and printability for dense and strong ceramics by direct ink writing. *Sci. Rep.* 2017, 7, 1–10.
59. Rallini, M.; Torre, L.; Kenny, J. M.; Natali, M. Effect of boron carbide nanoparticles on the thermal stability of carbon/phenolic composites. *Polym. Compos.* 2017, 38, 1819–1827.

Chapter 6 3D Printed Chromophoric Sensors

6.1 Introduction

As an engineered and high-performance silicone material, Sylgard 184 is used for many specialized applications such as micro-separations and diffusion[1-5], triboelectric nanogenerators (TENG)[6-9], tissue engineering[10-13], shape-memory and self-healing materials[14-17], and more. Many of the properties exhibited by Sylgard 184 (which may be referred to in literature as poly (dimethyl siloxane) (PDMS)) are due to the Si-O-Si bond, which gives flexibility to silicones, and to the ease of controlling the functional groups and side chains of siloxanes. Additionally, many new and enhanced characteristics can be imbued to Sylgard 184 by incorporating fillers and other polymers to create composite materials. Indeed, the facile ability to combine metals, ceramics, glasses, functionalized particles, and/or biomolecules into Sylgard 184 and develop distinct layers which can contain heterogeneous fillers makes it an incredibly versatile and popular polymeric system. Our team has previously worked on aspects of this, where composites were made using different types of Sylgard and fillers to alter the surface adhesion and thermomechanical properties[18, 19].

One class of composites that has been studied and heavily developed is that of Sylgard 184 sensors. Indeed, Sylgard 184 is an ideal candidate for sensing applications because of its selective permeability to gases, optical transparency, chemical inertness, and ease of patterning via soft lithography, casting, and other techniques. As such, quite a bit of research has explored Sylgard 184 in active and passive sensors such as lab-on-a-chip devices for biosensing[20-22], mechanoresponsive devices, e.g. capacitive pressure (or

tactile) sensors[23, 24] and strain sensors[25, 26], and environmental sensors that can detect changes in temperature[27, 28], pH[29-31], relative humidity[32, 33], and certain gas species[34, 35]. In high-hazard occupations or areas where workers may be exposed to hazardous conditions, a device that produces an easy to see change can alert workers if a dangerous threat is immediately present. Such a sensor would need to have a long lifespan, function continuously and passively, and demonstrate an irreversible visual cue in order to protect people in situations with inherent risk.

Three hazards that could be present in high risk occupational areas include elevated temperatures, acidic chemical species, or basic chemical species. If a visual cue was available, such as a color change in a sensor, this could help alert workers if one of these hazards is immediately present. Compounds exist that do exhibit halochromic and thermochromic effects. Some of these include pure indicators such as thymol blue, bromothymol blue, phenolphthalein, methyl red, and methyl yellow as well as commercially available indicating paints. The pure indicators exhibit their halochromic effects through similar mechanisms, where protonation and deprotonation cause a macroscopic color change [36-38]. Thymol blue has been encapsulated in a siloxane matrix, where its surface area effects and sensitivity to pH was investigated [39]. Thymol blue has also been used to detect CO₂ via pH in a europium polymer composite film [40, 41]. Bromothymol blue has been used with high density polyethylene (HDPE), ethylene vinyl acetate (EVA), and silica to detect spoiled milk via pH changes [42] and combined with carbon nanotubes to detect epinephrine [43]. The well-known pH indicator phenolphthalein has been functionalized with formaldehyde and immobilized in diacetylcellulose to create an optical sensor [44] as well as electrospun with

poly(acrylonitrile-co-vinyl acetate) (PAN) in N, N-dimethylformamide (DMF) to develop halochromic nanosensors [45]. Besides being halochromic, methyl red exhibits excellent humidity sensing capabilities and research groups have inkjet printed composites of methyl red with graphene in-between inter-digital transducer (IDT) electrodes to develop highly sensitive devices [46, 47]. Additionally, the transesterification reaction of trisopropanolamine and methyl red-amidopropyltrimethoxysilane (MR-APTMS) results in a colorimetric sensor that can detect Hg²⁺ in the micromolar levels [48]. Methyl yellow has found many uses in various sensors and devices, where one notable application is in the detection of formaldehyde via pH changes [49-51]. These compounds, along with some commercial indicating paints, could be used in the facile fabrication of passive environmental sensors that can alert workers if certain hazards are immediately present.

In this work, Sylgard 184 was used as the encapsulating network for halochromic and thermochromic indicators. Passive environmental chromophoric sensors were created and their performance was assessed via high temperature and liquid and vapor phase exposure to acidic and basic chemical species. Additionally, the composite sensors were enhanced by developing 3D printed Direct Ink Writing (DIW) formulations and subsequently printing devices with increased surface areas and porosity in order to create a better visual cue of any color change. Material properties of the sensors were investigated via solvent swelling, Shore A Hardness, and thermogravimetric analysis experiments.

6.2 Experimental

6.2.1 Materials

Dow SYLGARD™ 184 Silicone Elastomer was formulated from a base agent and curing agent, both of which were supplied by Ellsworth. Acid Detecting Paint and Base

Detecting Paint, referred to in this study as acid paint and base paint, respectively, were both purchased from RAMCO Manufacturing Company. Non-Reversible Single-Change Indicating Thermal Paint 155°C/311°F, referred to in this study as thermal paint, was purchased from TIPTEMP. Thymol blue, bromothymol blue, phenolphthalein, methyl red, and methyl yellow were purchased from ACROS Organics. TS-720 CAB-O-SIL fumed silica was purchased from Cabot Corporation. The liquids such as HPLC grade toluene, 1-propanol, hydrochloric acid, nitric acid, ammonium hydroxide, and sodium hydroxide were supplied by Thermo Fisher Scientific. Ultra-high purity nitrogen was supplied by Airgas. All chemicals were used as received.

6.2.2 Formulation Development

Eight chromophoric indicators were investigated in this study. Three indicators were in paint form: acid detecting paint; base detecting paint; and non-reversible single-change indicating thermal paint 155°C. Throughout this study, these will be referred to as acid paint, base paint, and thermal paint, respectively. Acid paint changes color from yellow to red when its pH drops below 3. Base paint changes color from white to blue when its pH rises above 10. Thermal paint changes color from turquoise to green-gray when it is exposed to temperatures above 155°C for ten continuous minutes. Five indicators were in pure powder form: thymol blue; bromothymol blue; phenolphthalein; methyl red; and methyl yellow. The powders range in colors and can change acidic and basic solutions to varying hues depending on the pH of the solution, which are listed in Table 6.1.

Table 6.1: Solution pH and colors associated with the powder indicators in this study.

Indicator	Solution pH, Color	Solution pH, Color
Thymol blue [36]	< 8, yellow	> 9, blue
Bromothymol blue [38]	< 6, yellow	> 7, blue

Phenolphthalein [52]		> 8, pink
Methyl red [52, 53]	< 4, red	> 6, yellow
Methyl yellow [53]	< 3, red	> 4, yellow

A ratio of 10:1 w/w of base agent to curing agent was used to make Sylgard 184. Using a THINKY ARV-310 planetary mixer, the indicator and base agent were mixed for two minutes at 2,000 rpm at a vacuum of 0.2 psi and then the curing agent was added using the same mixing settings. This resulting solution was then poured in molds and cured at 25°C for one week. Although Sylgard 184 cures and can be used within two days, full mechanical properties are not reached until one week after mixing. When making the 3D printing formulations, PDMS-functionalized fumed silica was incorporated into the base/indicator slurry to create a non-Newtonian shear-thinning fluid that was suitable for DIW 3D printing. The proportions of the 3D printing formulations included 15 wt% fumed silica.

Four different weight percents of the indicators were tested (0.5, 1, 5, and 10 wt%) and almost all exhibited the property of being successful as a sensor at all proportions. Table 6.2 lists the notation for the passive environmental sensors used in this study along with their components.

Table 6.2: Notation of the passive environmental chromophoric sensors used in this study and their components.

Sample	Components
tpS184	Sylgard 184 + thermal paint
bpS184	Sylgard 184 + base paint
apS184	Sylgard 184 + acid paint
tbS184	Sylgard 184 + thymol blue
bbS184	Sylgard 184 + bromothymol blue
ppS184	Sylgard 184 + phenolphthalein
mrS184	Sylgard 184 + methyl red
myS184	Sylgard 184 + methyl yellow

6.2.3 Material Characterization Techniques

While the chemistry of curing PDMS via the hydrosilylation reaction is well-known, if any of the bonds or functional groups of the indicators changed while in the Syglard 184 composite, then the sensor may not function as designed. To ensure that the composites had their components intact, Fourier transform infrared (FTIR) spectroscopy was performed on the samples. A Thermoscientific Nicolet iS50 FT-IR instrument was used in Attenuated Total Reflection (ATR) mode with a diamond crystal reference and an average of 32 scans at a resolution of 4 cm^{-1} between $4000\text{-}525\text{ cm}^{-1}$. The stage was cleaned and a background spectrum was taken before each measurement.

Acid and base exposure experiments were performed as vapor and liquid phase tests. For the liquid phase tests, a single drop of each acid (hydrochloric acid and nitric acid, both at a pH of 0) or base (ammonium hydroxide at a pH of 12 and sodium hydroxide at a pH of 14) was placed on the surface of the samples. For the vapor phase tests, hydrochloric acid or ammonium hydroxide were placed in small open vials within a closed glass chamber along with a pH strip on the sidewalls of the chamber and a composite halochromic sensor located in the middle. The acids and bases were tested with pH strips for the liquid and vapor phase tests to ensure that the experiments did not yield false negatives or false positives for the sensors. Changes in color for the liquid and vapor phase tests were documented with respect to time using a stopwatch. Elevated temperature exposure experiments were performed for the tpS184 samples in an oven at 160°C . Enough tpS184 samples were placed in the oven so that they could be removed in 30 minute intervals.

Chromophoric behavior was assessed by performing ultraviolet-visible (UV-Vis) spectrophotometry on pristine and exposed samples. UV-Vis spectrophotometry experiments were conducted on an AvaSpec-ULS2048CL-EVO detector and a grating of 300 lines/mm, which has a range spanning 200-1100 nm. Natural light was used as a light source and spectra were obtained with measurements using the same darkness reference.

Solvent swelling experiments were used to evaluate the crosslinking of the polymer network in each sample. The composite passive environmental sensors were swollen to equilibrium in toluene for 24 hours at 25°C. After being swollen, the samples were gently patted dry to remove residual toluene before recording the swollen mass. The samples were subsequently dried at 25°C for 24 hours and then at 70°C for 48 hours under vacuum. Percent loss from the solvent is reported as the difference between the initial mass and the vacuum dried mass. The network swelling is reported as the difference between the fully swollen mass and vacuum dried mass. Densities were evaluated by measuring the initial masses and volumes. Each sample was run in triplicate and standard deviation is reported as the error.

By using the density and solvent swelling data, crosslink density values for the polymer composites can be determined. The Flory-Rehner equation for a phantom network was applied because it models the PDMS and toluene system well[54, 55]. The specific crosslink density ν_x , in units of moles of crosslinks per gram of material, is the reciprocal of the average molecular weight of the polymer between crosslinks M_C , which was derived in previous work[56]. It is a function of the polymer volume fraction ϕ_p , the Flory-Huggins polymer-solvent interaction parameter χ , the polymer density ρ_p (which is taken as the density of the composite), and the molar volume of the solvent $\nu_{m,s}$ (for toluene, this value

is 106.2 mL/mol) (Equation 6.1). The polymer volume fraction was calculated from the network swelling S and the densities of the polymer and solvent (Equation 6.2). Many groups have studied the interaction between PDMS and toluene and proposed that the Flory-Huggins polymer-solvent interaction parameter can be modeled from the polymer volume fraction (Equation 6.3)[57].

$$p_x = \frac{1}{M_c} = \frac{\ln(1-\varphi_p) + \varphi_p + \chi\varphi_p^2}{-\frac{1}{2}v_{m,s}\rho_p\varphi_p^{1/3}} \quad \text{Equation 6.1}$$

$$\varphi_p = \left(1 + S \frac{\rho_p}{\rho_s}\right)^{-1} \quad \text{Equation 6.2}$$

$$\chi = 0.459 + 0.134\varphi_p + 0.590\varphi_p^2 \quad \text{Equation 6.3}$$

Each composite's resistance to indentation, or hardness, was assessed with a benchtop HPE II Zwick Roell Shore A durometer. Cylinders measuring 12 mm in height and 26 mm in diameter were used as durometry test samples. Each composite had three samples and two trials were conducted on each cylinder in different locations. Shore A Hardness values were averaged from these trials and the standard deviations are reported as the error.

To evaluate the thermal stability and decomposition of the composites, Thermogravimetric analysis (TGA) experiments were conducted using a TA Instrument TGA 550, Discovery Series. Samples weighing approximately 10 mg were subjected to a heating ramp of 10°C/min until they reached 750°C while in an inert nitrogen atmosphere flowing at 20 mL/min. The onset of thermal degradation, $T_{d5\%}$, is the temperature at which the residual mass is 95%. The decomposition temperature, T_{dMax} , is the temperature at which the

derivative curve (DTGA) is a maximum. The final residual mass, m_f , is the mass percent that remains after the TGA experiment has ended.

Chromophoric composite sensors for 3D printing were formulated for DIW. 3D printing was performed using a Hyrel 30M printer and EMO-25 printer head along with the Repetrel software (all Hyrel products). A 250 μm nozzle was used with a travel rate of 2250 mm/min to extrude the material, which was programmed to have a flow rate of 150 pulses/ μL . Finished printed parts were 5 cm diameter disks comprising eight layers of a staggered face-centered tetragonal (FCT) geometry with a 500 μm spacing between the centers of two struts. The parts were cured at 25°C for two days or at 150°C for two hours.

Magnified top and cross-section views of the samples were taken using a confocal digital microscope (Keyence VHX-6000). Magnifications of 20x – 150x were used to investigate the network of the resulting 3D printed pads. Measurement of the beams was obtained from the Keyence analysis software.

6.3 Results and Discussion

6.3.1 Sensor Performance

A top view of all the composite chromophoric sensors in this study is shown in Figure 6.1. The lowest and highest proportions of indicators (0.5 wt% and 10 wt%) were used in the figure to observe how the intensity of the initial colors could be distinguished.

Passive Environmental Chromophoric Sensors

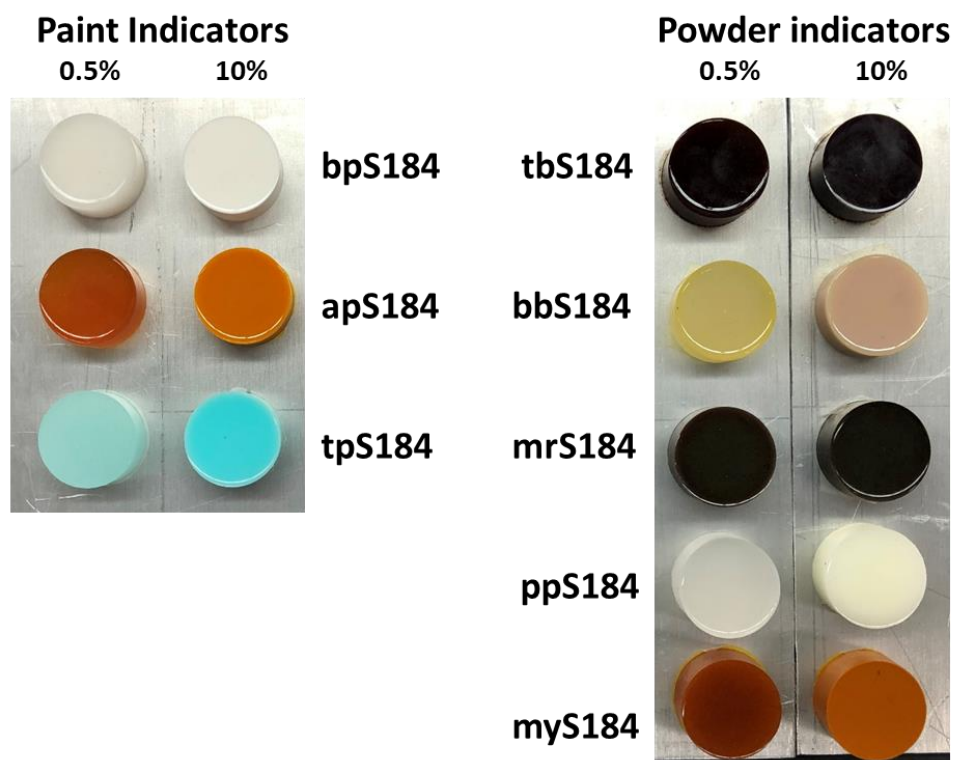


Figure 6.1: Pristine composite passive environmental chromophoric sensors separated by indicator weight percent (0.5 wt% on the left and 10 wt% on the right of each photo) and by the initial indicator form (paint-based on the left and powder-based on the right).

Using the four different proportions of indicators (0.5%, 1%, 5%, and 10% by mass), liquid and vapor phase tests were conducted on all the samples except for tpS184, in which case elevated temperature experiments were performed. Generally, cylinders measuring 12 mm in height and 26 mm in diameter were used, but flat films measuring between 1 to 2 mm in thickness were also investigated. It was found that if a sensor worked for the vapor phase tests, then they successfully worked in the liquid phase tests.

While the liquid phase tests produced a more obvious change, vapor exposure represents a more difficult hazard to identify and mitigate in occupational scenarios,

therefore vapor phase tests were considered a better standard with which to compare the samples. Pristine specimens were placed in a container with a vial of a volatile acidic or basic solution for three minutes. The associated color changes of the 0.5 wt% sensors are shown in Figure 6.2 along with tpS184, which was subjected to 160°C for 45 minutes. Within a few seconds, apS184 began changing from orange to red. After three minutes, tbS184 changed from dark green to reddish violet. Although the color change is obvious when in certain light, the pristine and exposed tbS184 are both dark and it can be difficult to distinguish between the two in low-light conditions. Going from beige-yellow to a mossy green, bbS184 began visibly changing first at the rim after two minutes then slowly spread to the rest of the sample. Another interesting phenomenon occurred to bbS184 samples a day after both liquid and vapor exposure, where the specimen changed from mossy green to bright yellow and red. This has been observed in multiple samples across varying proportions. Therefore, a temporal color change phenomenon is exhibited in bbS184, where immediate basic species exposure results in a change to a green hue and in the days after exposure results in a yellow and red hue (see Figure 6.3). Like the apS184 samples, within a few seconds the myS184 specimen began changing color, however the color change was to a much darker red. After 45 minutes in an 160°C oven, the tpS184 samples changed from turquoise to greenish gray. Films with less than 5 wt% thermal paint and that were 1 mm thick did not exhibit a blueish hue and thus the color changing properties were not discernable. Films with 5 wt% thermal paint and between 1 and 2 mm thick showed a color change after 30 minutes. Therefore, thicker samples require more time for the thermal paint composite sensors to change color while also needing less indicator to be thermochromic. It should be noted that films made with the other indicators exhibited

enough of a color change to be distinguishable from regular Sylgard 184 for all indicator concentrations and thus could be used as sensors. Another important observation was that the exposed samples remained in their altered colored state without any signs of reversing to their pristine condition, even after a year following exposure. Additionally, the sensors were able to perform as intended after a storage period after a year, where the pristine samples changed color once exposed. Thus, these composite sensors demonstrate an irreversibility and long lifespan that aids in their passive behavior.

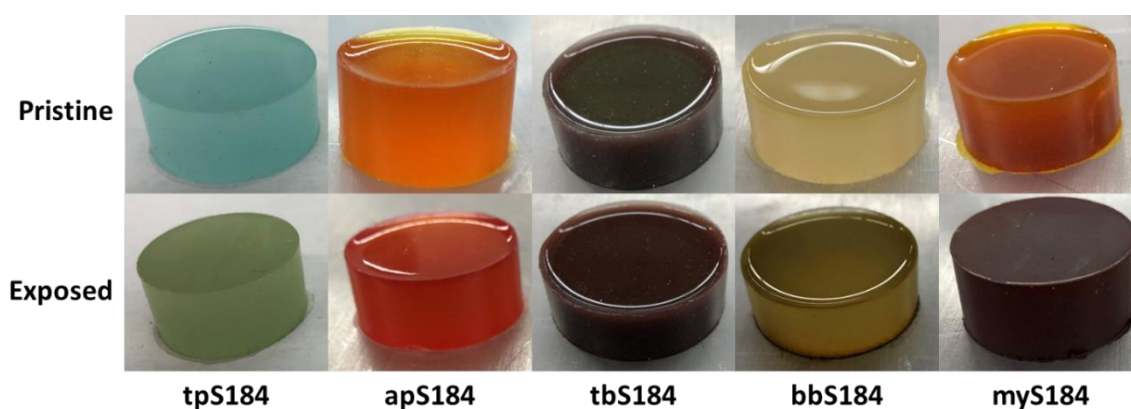


Figure 6.2: Comparison of the color changes between pristine and exposed composite chromophoric sensors (0.5 wt%).

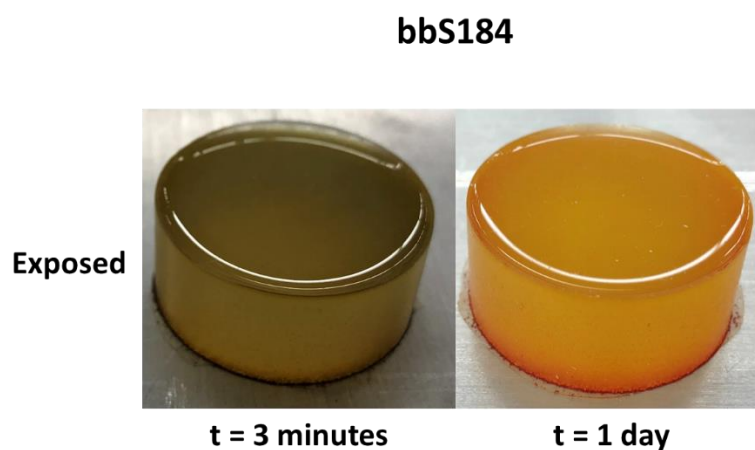


Figure 6.3: The temporal change of bbS184 one day after exposure.

Three composites did not work for the vapor phase tests: bpS184; mrS184; and ppS184. Subjecting strong bases in the form of liquid droplets to the bpS184 samples also did not produce a color change. This indicates that bpS184 would not be applicable as a sensor for any of the concentrations. While mrS184 did not produce an observable color change during the vapor phase tests, an issue with the composite is that for all proportions made, mrS184 was too dark in hue to make accurate color comparisons. A similar phenomenon occurred with ppS184, except that the pristine coloring was light enough to discern that no color change transpired with vapor and liquid phase tests. To assess the color changes, ultraviolet-visible (UV-Vis) spectrophotometry was performed on the tpS184, apS184, tbS184, bbS184, myS184, and mrS184 samples. With a range spanning 200 – 1100 nm, UV-Vis spectroscopy provides a better determination on how the sensors exhibited their chromophoric behavior. Comparing the pristine and exposed samples demonstrated obvious changes for each sensing device (see Figure 4) by way of shifting, adding, or subtracting peaks in a spectrum. Furthermore, the spectroscopy data validated that some samples may be difficult to distinguish between pristine and exposed states. This includes tbS184 and mrS184, where the biggest peaks show a slight shifting towards larger wavelengths (approximately 700 nm) and a subtraction of the peaks shorter than 640 nm, which is not as drastic a change as the other sensors. Thus, while all of these specimen exhibit some chromophoric property, making the tbS184 and mrS184 sensors as a solid device does not prove to be feasible for detecting a color change with the unaided eye.

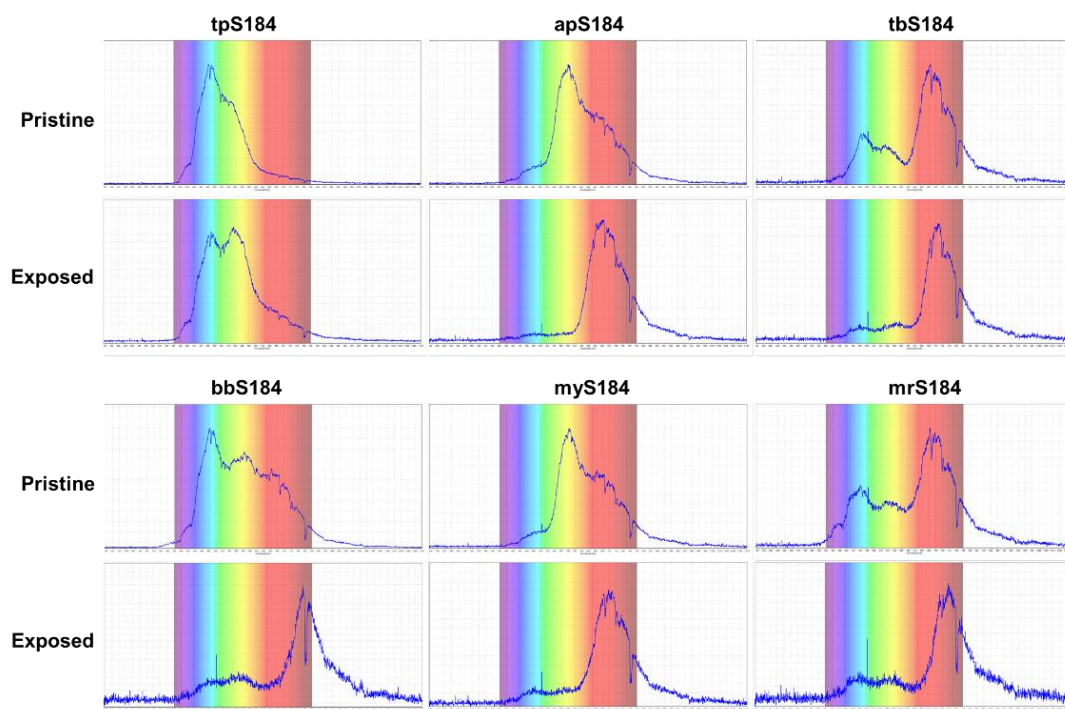


Figure 6.4: UV-Vis spectrophotometry data demonstrating the chromophoric behavior of the sensing devices.

Indeed, vapor and liquid phase tests did not change the color of mrS184 samples dramatically enough to be able to distinguish the exposed from the pristine specimen. However, applying acidic solutions as droplets to the samples did reveal surface effects. The droplets were clear solutions when applied to mrS184 samples and quickly turned a dark yellow-orange hue. When the acidic solutions were wiped away, no visible markings were left on the samples, but the wipes retained a yellow-orange residue. This occurred with all proportions of mrS184. A similar phenomenon occurred with ppS184, except that the pristine coloring was light enough to discern that no color change transpired with vapor and liquid phase tests. When a basic droplet was applied to ppS184 samples, the liquid changed from clear to bright pink (see Figure 6.4). And similar to mrS184, wiping away

the liquid left no markings on the sample but a visible residue (bright pink) on the wipe. Thus, bpS184 exhibits no sensing properties while mrS184 and ppS184 exhibit only surface sensing when in contact with liquid drops of acidic and basic species, respectively.

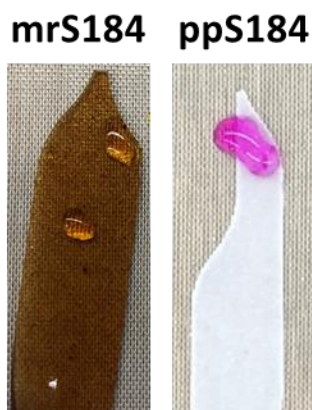


Figure 6.5: Surface sensing properties of mrS184 and ppS184. Observe that the sensors themselves did not change color but the clear liquid that was applied did.

When liquid phase tests were performed, color-changing droplets were observed in a similar fashion to mrS184 and ppS184 samples. Droplets on tbS184 changed from clear to dark blue, those on bbS184 became light blue, and those on apS184 and myS184 became red. Therefore, all of these composites demonstrate surface sensing properties as well.

6.3.2 Sensor Material Characterization

FTIR spectra for the composites revealed that the signal from Sylgard 184 overshadows the peaks from the indicators. This makes sense considering that the composites are between 90% and 99.5% Sylgard 184, meaning that the vibrational modes of the indicators barely contribute to the overall spectra. That stated, no new peaks were observed, demonstrating that no chemical interactions occurred between the indicators and Sylgard 184 and thus the FTIR spectra reveal that the sensors are true composites.

In addition to the sensing properties the indicators imbue to the composites, other characteristics and material properties of Sylgard 184 were affected as well. Because the lowest mass fraction of indicators (0.5 wt%) worked well as composite sensors, the material properties were tested using these samples. As a starting point, the actual polymer network was investigated via solvent swelling in toluene. This allows for the evaluation of the network swelling and specific crosslink density using Equation 6.1. The densities of the 0.5 wt% samples were approximately 1.06 g/cm^3 . As noted in previous literature, some mechanical properties correlate with the structure of the polymer network and its degree of crosslinking[56, 58, 59], thus the Shore A Hardness values for the samples are presented along with the network swelling values and specific crosslink densities for the sensors in Table 6.3. In general, solvent swelling is inversely related to the density of crosslinks in a network, so lower swelling values indicate that the crosslink density is greater. Reviewing Table 6.3, the values correspond to this relationship, where the largest network swelling values are from bpS184, apS184, mrS184, and myS184 (all above the network swelling value of 147% for Sylgard 184), which also exhibit the lowest specific crosslink density (all below $2.60 \times 10^{-4} \text{ mol crosslink / g material}$). Additionally, the least network swelling occurs in tbS184 (106%), which has the greatest specific crosslink density (almost $4 \times 10^{-4} \text{ mol crosslink / g material}$). Furthermore, a positively-correlated relationship between a material's specific crosslink density and resistance to indentation (Shore A Hardness) is observed in Table 6.3. Based on how the indicators affect the material properties, the hardest composites, ppS184, tpS184, tbS184, and bbS184 (all above 40 ShA and above $3 \times 10^{-4} \text{ mol crosslink / g material}$), can be classified as reinforcing fillers and the softest

composites, myS184, bpS184, apS184, and mrS184 (all below 33 ShA), can be classified as plasticizers[60, 61]. Relevant data for regular Sylgard 184 is also included in Table 6.3.

Table 6.3: Solvent swelling properties and Shore A Hardness of the 0.5 wt% composite chromophoric sensors compared to Syglard 184.

Sample	Network Swelling (%)	Specific Crosslink Density (mol crosslink / g material)	Shore A Hardness
tpS184	115 ± 3	3.60×10 ⁻⁴	42.6 ± 0.4
bpS184	151 ± 2	2.52×10 ⁻⁴	31.2 ± 1.0
apS184	149 ± 7	2.57×10 ⁻⁴	31.2 ± 1.4
tbS184	106 ± 0	3.94×10 ⁻⁴	42.9 ± 0.2
bbS184	122 ± 2	3.35×10 ⁻⁴	41.0 ± 1.1
ppS184	127 ± 2	3.27×10 ⁻⁴	43.0 ± 0.4
mrS184	159 ± 3	2.44×10 ⁻⁴	32.2 ± 0.6
myS184	149 ± 2	2.48×10 ⁻⁴	30.4 ± 0.2
Sylgard 184	147 ± 1	3.16×10 ⁻⁴	37.3 ± 0.3

Due to the polymer network being similar for all the composites, swelling data can be used to compare the polymer-indicator interactions. If an indicator interacts well with the polymer chains, there would be additional bonding, which could lead to an increase in specific crosslink density. Thus, indicators that behave as reinforcing fillers interact with the polymer network. Otherwise, the indicators do not interact well within the polymer network, leading to a plasticizing effect. This can aid in understanding the resulting structure and mechanical properties, especially when comparing the composites to regular Sylgard 184. Thus, for similar indicator concentrations, the composites with the greatest specific crosslink densities (tbS184, tpS184, bbS184, and ppS184) exhibit the best interactions with Sylgard 184. Swelling experiments support this argument, especially when evaluating the mass loss percent, which assesses the extracts. Although at 0.5 wt%

concentration the composites had similar losses of 4%, the extracts of composites with low specific crosslink densities (plasticizers) turned toluene from clear to a translucent but deep coloration. Indeed, apS184 and myS184 turned toluene yellow-orange and mrS184 turned toluene red. The only composite with a low specific crosslink density that did not change the color of toluene was bpS184, which did not exhibit any sensing properties. This phenomenon of toluene changing color did not occur with the composites exhibiting a higher specific crosslink density (reinforcing fillers). Furthermore, when solvent swelling experiments were performed on 10 wt% sensors, the loss percent of the composites with good interactions remained at 4% while the composites with no interactions increased to 10%.

Understanding the applicable range of the sensors requires a knowledge of their thermal stability. Three measures of thermal stability allow for a broad understanding of their use, and they are the onset of thermal degradation $T_{d5\%}$, temperature of thermal decomposition T_{dMax} , and residual mass m_f . These thermal stability properties are given in Table 6.4. The composites fall within a 26°C range for $T_{d5\%}$ (400°C-426°C), which shows an improvement of at least 30°C compared to regular Sylgard 184 (a $T_{d5\%}$ of 370°C is demonstrated in our own laboratory results in and literature[56, 62, 63]). The T_{dMax} of the composites is more varied, where the range spans 266°C (499°C-665°C). These temperatures correspond to the breaking of the main PDMS chain backbone, which occurs from 400°C-650°C[64-66]. In Sylgard 184 the largest thermal decomposition peak occurs around 540°C in a nitrogen atmosphere, which resides within the range of PDMS backbone decomposition. The thermal decomposition of the sensors, like Sylgard 184, exhibit multiple decomposition peaks within the described range, and despite their maximal peaks

varying with temperature they all fall within these bounds. Residual masses are lower than Sylgard 184, which exhibits a final mass percent between 40-50%. Thus, thermal decomposition releases more volatiles from the sensors than Sylgard 184.

Table 6.4: Thermal properties of the 0.5 wt% composite chromophoric sensors compared to Sylgard 184.

Sample	T_{d5%} (°C)	T_{dMax} (°C)	m_r (%)
tpS184	409	544	33
bpS184	424	616	46
apS184	400	508	31
tbS184	426	579	47
bbS184	415	665	31
ppS184	409	499	35
mrS184	423	527	20
myS184	408	527	28
Sylgard 184	370	540	45

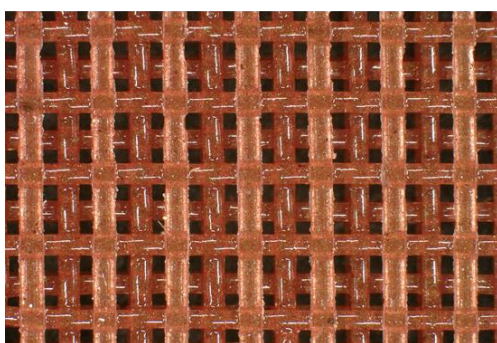
6.3.3 3D Printing

Pads with FCT structure described in previous work[62] were successfully 3D printed using the formulation described in Section 2.2 (15 wt% fumed silica) with low (0.5 and 1 wt%) amounts of indicator (see Figure 6.5). A 3D printed FCT pad was also printed with 10 wt% thermal paint to make the color change more discernable. Like the casted cylindrical samples, the 3D printed sensors were cured at 25°C for two days. Additionally, some FCT pads were cured at 150°C for two hours to investigate how accelerated curing would affect the composites. Interestingly, the only visible difference between these two curing procedures was with tbS184 and bbS184, both of which exhibited a color change. While the room temperature cured tbS184 FCT pad was dark green like the casted cylinder, the sample cured at an elevated temperature was a deep violet color. For the bbS184, the

difference was a light pink hue when cured at an elevated temperature instead of a yellow-beige color when cured at room temperature. Although the bbS184 FCT pads had a low amount of indicator, the light pink hue was similar to a high weight percent loading bromothymol blue (which is a pink powder) as a casted cylinder (see Figure 6.1).

Face-Centered Tetragonal Structure

Top view



Side view

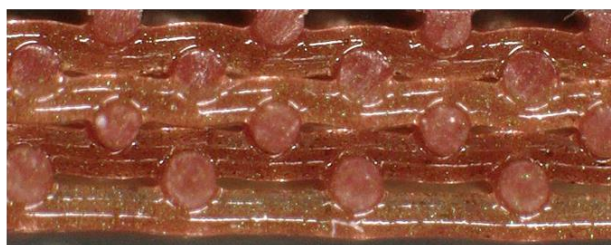


Figure 6.6: A 3D printed sensor with an FCT structure.

Further interesting observations were made concerning the tbS184, bbS184, and mrS184 FCT pads. The first is that despite the varying curing regimes producing different colored tbS184 and bbS184 parts, they still exhibited a halochromic sensing property, as seen in Figure 6.6. The second observation is that the mrS184 parts were able to be distinguishable when exposed to acidic species. Indeed, by having some porosity an observable color change occurred, where the 3D printed sensor transitioned from dark red to dark violet after exposure to either hydrochloric acid or nitric acid. Similarly, 3D printed tbS184 was more readily distinguishable once exposed to basic species than its casted counterpart. The other 3D printed sensors also behaved well as chromophoric devices. The

increase in efficacy (being able to distinguish pristine and exposed tbS184 and mrS184) for the 3D printed sensors over the casted samples can be explained with an increase in surface area and porosity, which allows a greater amount of active sites and better visibility in any color change. Thus, 3D printed DIW chromophoric sensors allow for a broader range of materials to be used where traditionally manufactured composites are difficult to be applicable in less than ideal situations such a low-light scenarios.

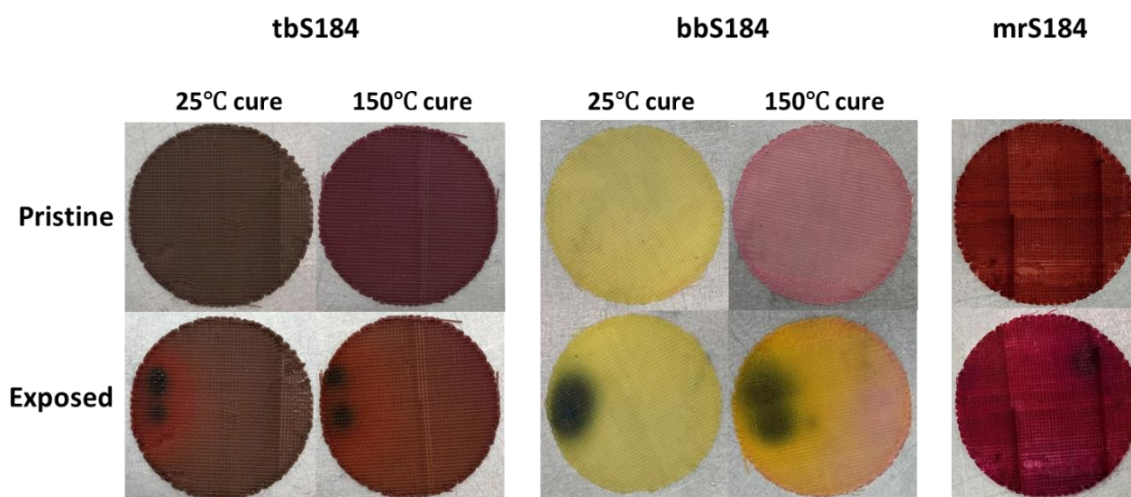


Figure 6.7: Comparison of the color changes in some of the 3D printed sensors – The sensors tb184 and bbS184 exhibited a color change when cured at an elevated temperature but it did not disrupt their sensing ability. Additionally, the porosity in the 3D printed sensors aided in providing a better visual cue for when tbS184 and mrS184 were exposed to basic or acidic chemical species, respectively.

6.4 Conclusions

Chromophoric sensors were developed as composite materials using Sylgard 184 and various indicators. Paint-based indicators were acid detecting paint, base detecting paint, and non-reversible single-change indicating thermal paint 155°C. Powder-based indicators were thymol blue, bromothymol blue, phenolphthalein, methyl red, and methyl yellow. The sensors were fabricated using four different indicator proportions (0.5, 1, 5,

and 10 wt%) and it was found that if sensing properties were observable at all, they were observable for any of the four ratios investigated. . Because of this ability for the sensors to successfully perform and change colors in the presence of stimuli, only 0.5 wt% indicator is necessary for applications investigated in this work. For actual sensing properties, bpS184 did not exhibit any halochromic behavior, ppS184 exhibited only surface sensing halochromic behavior via vapor exposure, and all the other composites demonstrated not only surface sensing behavior, but could respond to vapor and liquid phase exposures. Although the tbS184 and mrS184 composites did change color once exposed, as evidenced by the UV-Vis experiments, the sensors fabricated using the traditional manufacturing technique were difficult to detect with the unaided eye. Once the sensing devices exhibited a color change, they remained in the exposed state without reverting. Additionally, the samples could be stored for at least a year and still perform as intended. Therefore, these composite chromophoric sensors are passive and irreversible, allowing them to be demonstrate that a change in the immediate environment had occurred.

Probing the chemical structure of the composites revealed that no new chemical bonds were formed; therefore, the materials displayed additional properties to Sylgard 184. Additionally, solvent swelling experiments investigated the polymer network and demonstrated that tbS184, tpS184, bbS184, and ppS184 interacted well with Sylgard 184, forming additional crosslinks and increasing the mechanical properties while myS184, bpS184, apS184, and mrS184 did not interact with the polymer network. Thermal properties of the composites were evaluated as well, which demonstrated that the thermal stability and applicability of the sensors were similar.

The chromophoric sensors with 15 wt% fumed silica were 3D printed using DIW and were cured at 25°C for two days or 150°C for two hours. Varying the temperatures demonstrated that the materials were able to perform as sensors at these two curing regimes. Additionally, composites that were difficult to distinguish between pristine and exposed via a traditional casting method (tbS184 and mrS184) were easier to discern as printed sensors because of porosity. Thus, these passive environmental chromophoric sensors can be engineered into flexible and long-lasting customized shapes, which easily scale up and are cost-efficient to do so.

References

1. Jung, B.-J.; Kim, J.; Kim, J.-a.; Jang, H.; Seo, S.; Lee, W., PDMS-parylene hybrid, flexible microfluidics for real-time modulation of 3D helical inertial microfluidics. *Micromachines* **2018**, *9* (6), 255.
2. Warkiani, M. E.; Khoo, B. L.; Tan, D. S.-W.; Bhagat, A. A. S.; Lim, W.-T.; Yap, Y. S.; Lee, S. C.; Soo, R. A.; Han, J.; Lim, C. T., An ultra-high-throughput spiral microfluidic biochip for the enrichment of circulating tumor cells. *Analyst* **2014**, *139* (13), 3245-3255.
3. Bhagat, A. A. S.; Hou, H. W.; Li, L. D.; Lim, C. T.; Han, J., Pinched flow coupled shear-modulated inertial microfluidics for high-throughput rare blood cell separation. *Lab on a Chip* **2011**, *11* (11), 1870-1878.
4. Warkiani, M. E.; Bhagat, A. A. S.; Khoo, B. L.; Han, J.; Lim, C. T.; Gong, H. Q.; Fane, A. G., Isoporous Micro/Nanoengineered Membranes. *ACS Nano* **2013**, *7* (3), 1882-1904.

5. Nam, J.; Jang, W. S.; Lim, C. S., Viscoelastic separation and concentration of fungi from blood for highly sensitive molecular diagnostics. *Scientific reports* **2019**, *9* (1), 1-12.
6. Chun, J.; Kim, J. W.; Jung, W.-s.; Kang, C.-Y.; Kim, S.-W.; Wang, Z. L.; Baik, J. M., Mesoporous pores impregnated with Au nanoparticles as effective dielectrics for enhancing triboelectric nanogenerator performance in harsh environments. *Energy & Environmental Science* **2015**, *8* (10), 3006-3012.
7. Shahriar, M.; Vo, C. P.; Ahn, K. K., Self-powered flexible PDMS channel assisted discrete liquid column motion based triboelectric nanogenerator (DLC-TENG) as mechanical transducer. *International Journal of Precision Engineering and Manufacturing-Green Technology* **2019**, *6* (5), 907-917.
8. Zhu, G.; Yang, W. Q.; Zhang, T.; Jing, Q.; Chen, J.; Zhou, Y. S.; Bai, P.; Wang, Z. L., Self-powered, ultrasensitive, flexible tactile sensors based on contact electrification. *Nano letters* **2014**, *14* (6), 3208-3213.
9. Shin, S. Y.; Saravanakumar, B.; Ramadoss, A.; Kim, S. J., Fabrication of PDMS-based triboelectric nanogenerator for self-sustained power source application. *International Journal of Energy Research* **2016**, *40* (3), 288-297.
10. Borenstein, J. T.; Terai, H.; King, K. R.; Weinberg, E.; Kaazempur-Mofrad, M.; Vacanti, J., Microfabrication technology for vascularized tissue engineering. *Biomedical microdevices* **2002**, *4* (3), 167-175.
11. Leclerc, E.; Sakai, Y.; Fujii, T. In *A multi-layer PDMS microfluidic device for tissue engineering applications*, The Sixteenth Annual International Conference on Micro Electro Mechanical Systems, 2003. MEMS-03 Kyoto. IEEE, IEEE: 2003; pp 415-418.

12. Mata, A.; Fleischman, A. J.; Roy, S., Characterization of polydimethylsiloxane (PDMS) properties for biomedical micro/nanosystems. *Biomedical microdevices* **2005**, *7* (4), 281-293.
13. Li, J.; Liu, X.; Crook, J. M.; Wallace, G. G., Development of a porous 3D graphene-PDMS scaffold for improved osseointegration. *Colloids and Surfaces B: Biointerfaces* **2017**, *159*, 386-393.
14. Wang, C.; Ding, Z.; Purnawali, H.; Huang, W.; Fan, H.; Sun, L., Repeated instant self-healing shape memory composites. *Journal of materials engineering and performance* **2012**, *21* (12), 2663-2669.
15. Orellana, J.; Moreno-Villoslada, I.; Bose, R. K.; Picchioni, F.; Flores, M. E.; Araya-Hermosilla, R., Self-healing polymer nanocomposite materials by Joule effect. *Polymers* **2021**, *13* (4), 649.
16. Sun, L.; Huang, W. M.; Ding, Z.; Zhao, Y.; Wang, C. C.; Purnawali, H.; Tang, C., Stimulus-responsive shape memory materials: a review. *Mater Design* **2012**, *33*, 577-640.
17. Cui, H.; Song, C.; Huang, W.; Wang, C.; Zhao, Y., Rubber-like electrically conductive polymeric materials with shape memory. *Smart materials and structures* **2013**, *22* (5), 055024.
18. Murphy, E. C.; Dumont, J. H.; Park, C. H.; Kestell, G.; Lee, K. S.; Labouriau, A., Tailoring properties and processing of Sylgard 184: Curing time, adhesion, and water affinity. *Journal of Applied Polymer Science* **2020**, *137* (14), 48530.
19. Gupta, N. S.; Lee, K.-S.; Labouriau, A., Tuning Thermal and Mechanical Properties of Polydimethylsiloxane with Carbon Fibers. *Polymers* **2021**, *13* (7), 1141.

20. Ibarlucea, B.; Fernández-Sánchez, C.; Demming, S.; Büttgenbach, S.; Llobera, A., Selective functionalisation of PDMS-based photonic lab on a chip for biosensing. *Analyst* **2011**, *136* (17), 3496-3502.
21. Ghasemi, M.; Roostaei, N.; Sohrabi, F.; Hamidi, S.; Choudhury, P., Biosensing applications of all-dielectric SiO₂-PDMS meta-stadium grating nanocombs. *Optical Materials Express* **2020**, *10* (4), 1018-1033.
22. Dang, B. V.; Hassanzadeh-Barforoushi, A.; Syed, M. S.; Yang, D.; Kim, S.-J.; Taylor, R. A.; Liu, G.-J.; Liu, G.; Barber, T., Microfluidic Actuation via 3D-Printed Molds toward Multiplex Biosensing of Cell Apoptosis. *ACS sensors* **2019**, *4* (8), 2181-2189.
23. Su, L.; Jiang, Z.; Tian, Z.; Wang, H.; Wang, H.; Zi, Y., Self-powered, ultrasensitive, and high-resolution visualized flexible pressure sensor based on color-tunable triboelectrification-induced electroluminescence. *Nano Energy* **2021**, *79*, 105431.
24. Lei, K. F.; Lee, K.-F.; Lee, M.-Y., Development of a flexible PDMS capacitive pressure sensor for plantar pressure measurement. *Microelectronic Engineering* **2012**, *99*, 1-5.
25. Gong, X. X.; Fei, G. T.; Fu, W. B.; Fang, M.; Gao, X. D.; Zhong, B. N.; Zhang, L. D., Flexible strain sensor with high performance based on PANI/PDMS films. *Organic Electronics* **2017**, *47*, 51-56.
26. Wu, S.; Ladani, R. B.; Zhang, J.; Ghorbani, K.; Zhang, X.; Mouritz, A. P.; Kinloch, A. J.; Wang, C. H., Strain sensors with adjustable sensitivity by tailoring the microstructure of graphene aerogel/PDMS nanocomposites. *ACS applied materials & interfaces* **2016**, *8* (37), 24853-24861.

27. Yang, J.; Wei, D.; Tang, L.; Song, X.; Luo, W.; Chu, J.; Gao, T.; Shi, H.; Du, C., Wearable temperature sensor based on graphene nanowalls. *RSC Advances* **2015**, *5* (32), 25609-25615.
28. Wu, L.; Qian, J.; Peng, J.; Wang, K.; Liu, Z.; Ma, T.; Zhou, Y.; Wang, G.; Ye, S., Screen-printed flexible temperature sensor based on FG/CNT/PDMS composite with constant TCR. *Journal of Materials Science: Materials in Electronics* **2019**, *30* (10), 9593-9601.
29. Dang, W.; Manjakkal, L.; Lorenzelli, L.; Vinciguerra, V.; Dahiya, R. In *Stretchable pH sensing patch in a hybrid package*, 2017 IEEE SENSORS, 29 Oct.-1 Nov. 2017; 2017; pp 1-3.
30. Sousa, R. P. C. L.; Ferreira, B.; Azenha, M.; Costa, S. P. G.; Silva, C. J. R.; Figueira, R. B., PDMS Based Hybrid Sol-Gel Materials for Sensing Applications in Alkaline Environments: Synthesis and Characterization. *Polymers* **2020**, *12* (2), 371.
31. Mani, G. K.; Nimura, Y.; Tsuchiya, K., Advanced Artificial Electronic Skin Based pH Sensing System for Heatstroke Detection. *ACS Sensors* **2020**, *5* (4), 911-916.
32. Komazaki, Y.; Uemura, S., Stretchable, printable, and tunable PDMS-CaCl₂ microcomposite for capacitive humidity sensors on textiles. *Sensors and Actuators B: Chemical* **2019**, *297*, 126711.
33. Tripathy, A.; Sharma, P.; Sahoo, N.; Pramanik, S.; Osman, N. A., Moisture sensitive inimitable Armalcolite/PDMS flexible sensor: a new entry. *Sensors and Actuators B: Chemical* **2018**, *262*, 211-220.

34. Hwang, I.-S.; Kim, Y.-S.; Kim, S.-J.; Ju, B.-K.; Lee, J.-H., A facile fabrication of semiconductor nanowires gas sensor using PDMS patterning and solution deposition. *Sensors and Actuators B: Chemical* **2009**, *136* (1), 224-229.
35. Nam, Y.-S.; Yoo, I.; Yarimaga, O.; Park, I. S.; Park, D.-H.; Song, S.; Kim, J.-M.; Lee, C. W., Photochromic spiropyran-embedded PDMS for highly sensitive and tunable optochemical gas sensing. *Chemical Communications* **2014**, *50* (32), 4251-4254.
36. H. Zhang, R. Byrne, Spectrophotometric pH measurements of surface seawater at in-situ conditions: absorbance and proto-nation behavior of thymol blue, *Marine Chemistry* *52*(1) (1996) 17-25.
37. H. Yamazaki, R.P. Sperline, H. Freiser, Spectrophotometric determination of the dissociation constant (pKa) of arsenous acid, *Analytica Chimica Acta* *284*(2) (1993) 379-384.
38. P. Balderas-Hernández, M. Ramírez-Silva, M. Romero-Romo, M. Palomar-Pardavé, G. Roa-Morales, C. Barrera-Diaz, A. Ro-jas-Hernández, Experimental correlation between the pKa value of sulfonphthaleins with the nature of the substituents groups, *Spectrochimica Acta Part A: Molecular and Biomolecular Spectroscopy* *69*(4) (2008) 1235-1245.
39. F.R. Zaggout, I.M. El-Nahhal, A.E.-F.A. Qaraman, N. Al Dahoudi, Behavior of thymol blue analytical pH-indicator entrapped into sol-gel matrix, *Materials Letters* *60*(29) (2006) 3463-3467.
40. N. Nakamura, Y. Amao, An optical sensor for CO₂ using thymol blue and europium(III) complex composite film, *Sensors and Actuators B: Chemical* *92*(1) (2003) 98-101.

41. N. Nakamura, Y. Amao, Optical sensor for carbon dioxide combining colorimetric change of a pH indicator and a reference luminescent dye, *Analytical and Bioanalytical Chemistry* 376(5) (2003) 642-646.
42. M.K. Stocker, M.L. Sanson, A.A. Bernardes, A.M. Netto, R. Brambilla, Acid–base sensor based on sol–gel encapsulation of bromothymol blue in silica: application for milk spoilage detection, *Journal of Sol-Gel Science and Technology* 98(3) (2021) 568-579.
43. P. Pradhan, R.J. Mascarenhas, T. Thomas, I.N. Namboothiri, O.J. D’Souza, Z. Mekhalif, Electropolymerization of bromothymol blue on carbon paste electrode bulk modified with oxidized multiwall carbon nanotubes and its application in amperometric sensing of epinephrine in pharmaceutical and biological samples, *Journal of Electroanalytical Chemistry* 732 (2014) 30-37.
44. Z. Liu, F. Luo, T. Chen, Phenolphthalein immobilized membrane for an optical pH sensor, *Analytica chimica acta* 510(2) (2004) 189-194.
45. A.N. Sharifabad, S.H. Bahrami, Halochromic chemosensor from poly (acrylonitrile)/phenolphthalein nanofibers as pH sensor, *IEEE Sensors Journal* 16(4) (2015) 873-880.
46. S. Ali, A. Hassan, G. Hassan, J. Bae, C.H. Lee, All-printed humidity sensor based on graphene/methyl-red composite with high sensitivity, *Carbon* 105 (2016) 23-32.
47. G. Hassan, M. Sajid, C. Choi, Highly sensitive and full range detectable humidity sensor using PEDOT: PSS, methyl red and graphene oxide materials, *Scientific reports* 9(1) (2019) 1-10.

48. G. Singh, S. Girdhar, A. Singh, A. Saroa, J.S. Lakhi, S. Khullar, S.K. Mandal, Selective mercury ion recognition using a methyl red (MR) based silatrane sensor, *New Journal of Chemistry* 42(8) (2018) 6315-6321.
49. N. Nakano, M. ISHIKAWA, Y. KOBAYASHI, K. NAGASHIMA, Development of a monitoring tape for formaldehyde using hydroxylamine sulfate and methyl yellow, *Analytical sciences* 10(4) (1994) 641-645.
50. X. Wang, Y. Si, J. Wang, B. Ding, J. Yu, S.S. Al-Deyab, A facile and highly sensitive colorimetric sensor for the detection of formaldehyde based on electro-spinning/netting nano-fiber/nets, *Sensors and Actuators B: Chemical* 163(1) (2012) 186-193.
51. D.L. Cruickshank, C.H. Hendon, M.J. Verbeek, A. Walsh, C.C. Wilson, Polymorphism of the azobenzene dye compound methyl yellow, *CrystEngComm* 18(19) (2016) 3456-3461.
52. G. Patterson, A Simplified Method for Finding the pKa of an Acid-Base Indicator by Spectrophotometry, *Journal of Chemical Education* 76(3) (1999) 395.
53. A. Shokrollahi, F. Zarghampour, S. Akbari, A. Salehi, Solution scanometry, a new method for determination of acidity constants of indicators, *Analytical Methods* 7 (2015) 3551-3558.
54. W. Chasse, M. Lang, J.-U. Sommer, K. Saalwachter, Cross-link density estimation of PDMS networks with precise consideration of networks defects, *Macromolecules* 45(2) (2012) 899-912.
55. M.S. Dimitriyev, Y.-W. Chang, P.M. Goldbart, A. Fernández-Nieves, Swelling thermodynamics and phase transitions of polymer gels, *Nano Futures* 3(4) (2019) 042001.

56. Z. Brounstein, J. Zhao, D. Geller, N. Gupta, A. Labouriau, Long-Term Thermal Aging of Modified Sylgard 184 Formulations, *Polymers* 13(18) (2021) 3125.
57. W. Chassé, M. Lang, J.-U. Sommer, K. Saalwächter, Correction to cross-link density estimation of PDMS networks with pre-cise consideration of networks defects, *Macromolecules* 48(4) (2015) 1267-1268.
58. M. Krumova, D. Lopez, R. Benavente, C. Mijangos, J. Perena, Effect of crosslinking on the mechanical and thermal properties of poly (vinyl alcohol), *Polymer* 41(26) (2000) 9265-9272.
59. D.L. Safranski, K. Gall, Effect of chemical structure and crosslinking density on the thermo-mechanical properties and toughness of (meth) acrylate shape memory polymer networks, *Polymer* 49(20) (2008) 4446-4455.
60. J.H. Dumont, E. Murphy, D. Geller, K.-S. Lee, A. Labouriau, Effects of thermal aging and ionizing radiation on sPVC and aromatic polyether urethane used to store nuclear materials, *Polym Test* 78 (2019) 105960.
61. M. Titow, *PVC technology*, Springer Science & Business Media 2012.
62. J. Engel, J. Chen, D. Bullen, C. Liu, Polyurethane rubber as a MEMS material: characterization and demonstration of an all-polymer two-axis artificial hair cell flow sensor, 18th IEEE International Conference on Micro Electro Mechanical Systems, 2005. MEMS 2005., IEEE, 2005, pp. 279-282.
63. S. Zulfiqar, S. Ahmad, Thermal degradation of blends of PVAC with polysiloxane—II, *Polym Degrad Stabil* 71(2) (2001) 299-304.
64. M. Olima, *Mechanical Characterization of Polydimethylsiloxane*, (2017).

65. T.H. Thomas, T. Kendrick, Thermal analysis of polydimethylsiloxanes. I. Thermal degradation in controlled atmospheres, *Journal of Polymer Science Part A-2: Polymer Physics* 7(3) (1969) 537-549.
66. A. Örn, Degradation studies on polydimethylsiloxane, (2019).

Chapter 7 Long-Term Thermal Aging of Modified Sylgard 184 Formulations

7.1 Introduction

Sylgard 184 is commercial high-performance silicone elastomer comprised of poly(dimethyl siloxane) (PDMS) and other silicon-based compounds originally developed by Dow Corning Corporation. Due to its optical transparency[1], thermal stability[2], mechanical advantages[3], and resistance to oxidation and hydrolysis[4], Sylgard 184 has been used as a potting material in numerous applications, spanning microelectromechanical systems (MEMS)[5, 6], electronic devices, and aerospace adhesives[7]. It is fabricated by mixing a prepolymer base (Part A), also referred to as the elastomer resin, and curing agent (Part B), also referred to as the hardener[8]. What separates Sylgard 184 from PDMS is that there are additional components other than the siloxane units in parts A and B. Besides siloxane units, the prepolymer base comprises a vinylated and methylated surface-modified silica filler component and vinyl-terminated and branched siloxane components[9]. The curing agent also contains linear and cyclosiloxanes, the modified silica filler, and platinum to catalyze the hydrosilylation reaction mechanism responsible for forming the crosslinked PDMS network. The hydrosilylation reaction entails Si-H groups interacting with vinyl moieties in the presence of a catalyst[10-12] to form new bonds between the two chemical groups. Once both parts A and B are mixed together, the polymer undergoes crosslinking and cures in 48 hours with full mechanical properties being demonstrated after a week[13]. Although the standard mixing ratio of 10:1 resin to hardener produces a material that exhibits hyperelasticity, high surface adhesion, and low Young's modulus, these properties can be altered for a variety of applications by increasing or decreasing the mixing ratio[13, 14]. In

addition to altering the mixing ratio, many complementary products exist to change the viscosity and curing time[15]. Accelerating the curing time is routinely performed by curing at higher temperatures[16-18], however for many applications this approach is not feasible because the components surrounding Sylgard 184 could be heat-sensitive. One available commercial product, DOWSIL 3-6559 Cure Accelerator, which includes a platinum catalyst and oligomeric, vinyl-terminated PDMS, can accelerate the room-temperature curing of silicone rubbers. Although this commercial product exists, it is desirable to tune the kinetics of the hydrosilylation reaction with controlled additions of either well-defined vinyl or silane moieties to accelerate room-temperature curing.

In addition to understanding and altering the rate at which Sylgard 184 cures, evaluating the material performance over its lifetime is necessary for its safe and predictable use. Because of its ubiquity and wide range of applications, Sylgard 184, often referred to in literature as PDMS, has been extensively studied with regards to its material properties, including how its behavior changes when combined with fillers and other polymers to make composites. These span many cutting edge materials such as shape memory elastomers [19-24] and wearable electronics[25, 26]. Despite the plethora of research conducted on PDMS and PDMS composites, there has been much less focus on investigating how the performance of Sylgard 184 changes over time. Some work examining how aged Sylgard changes includes thermally aging chemically modified Sylgard 184[27], UV aging PDMS insulation[28], thermally aging resin-filled PDMS elastomers[29], humidity aging siloxane foams[30, 31], and gamma irradiation aging silicones[32]. Natural and induced aging can lead to device or application failure and could potentially introduce new hazards. One prevalent example involves volatile products from

siloxane compounds. Although it is well-known and documented within the literature and industry that hydrogen generation from silicon compounds could pose serious direct and indirect hazards[17, 33, 34], there have been no long-term studies quantitatively measuring hydrogen generation from PDMS. Furthermore, studies have not evaluated whether other volatiles are generated in the aging of PDMS. Instead, studies that probe volatile product generation of silicone compounds focus on induced thermal decomposition[35-41]. Additionally, while volatile gas evolution may pose a serious problem, of prime concern is how the material itself changes over its lifetime; yet there is much more literature on the short-term behavioral and property changes. Thus, volatile product generation taken together with long-term behavior of PDMS represents a significant gap in knowledge and literature.

The present study is an investigation aiming to solve the three problems that have been previously described. First, Sylgard 184 was modified with well-known compounds to accelerate the curing reaction at room temperature. Our team had previously worked on room-temperature curing of Sylgard 184, which resulted in finding that incorporating 0.1-0.3 wt% Ashby-Karstedt catalyst accelerated the curing time and improved the mechanical properties[13]. Additionally, we found that the incorporation of tetrakis (dimethylsiloxy) silane (TDS) (a siloxane-based silane crosslinking agent) was able to reduce the curing time significantly. Four different formulations of Sylgard 184, comprising a control and combinations of the Ashby-Karstedt catalyst and TDS, were studied for their curing time and other initial properties. Second, thermal accelerated aging was performed on the formulations in isothermal conditions from 25°C to 90°C for up to twelve months. Long-term material performance was evaluated and modeled to predict behavior based on this

data. Third, headspace analysis was conducted on two of the formulations to determine which volatile components were being generated during aging. Inert and oxygen-rich atmospheres were used to probe how the surrounding environment might affect the materials' properties. Chemical, mechanical, and thermal properties were investigated to produce a thorough assessment of the lifetime performance of Sylgard 184. Thus, this study is a novel investigation into the comprehensive, long-term aging behavior of Sylgard 184 and its fast-curing formulations.

7.2 Materials and Methods

7.2.1 Materials

Dow SYLGARD™ 184 Silicone Elastomer was formulated from a base agent and curing agent, both of which were supplied by Ellsworth. Ashby-Karstedt catalyst (platinum-cyclovinylmethyl-siloxane complex; 2% Pt(0) in cyclomethylvinylsiloxanes) was supplied by Gelest. Tetrakis (dimethylsiloxy) silane (TDS) was supplied by Gelest. Ultra-high purity nitrogen was supplied by Airgas. HPLC-grade chloroform and toluene were supplied by Thermo Fisher Scientific.

7.2.2 Sylgard 184 Formulations

A ratio of 10:1 w/w was used for the base agent and curing agent, respectively, to make the standard Sylgard 184 framework. All the samples were made from the same batch. It should be noted that the formulations must be made in a specific order. The TDS crosslinker and Ashby-Karstedt catalyst, when used in the formulations, are added to the elastomer base and curing agent, respectively. This is because of what they resemble in Parts A and B; TDS is chemically similar to the branched silane found in Part A while the Ashby-Karstedt catalyst is chemically similar to the cyclosiloxane and Pt found in Part B.

Incorporating the additional compounds into the unlike part will result in the hydrosilylation reaction occurring before the prepolymer base and curing agent are added, yielding a non-uniform elastomer matrix. The TDS and Ashby-Karstedt catalyst compounds were always added in proportion to the total mass of the standard Sylgard 184 framework. For the samples made in this study, the order (if the component was present) went: (1) TDS; (2) Elastomer base; (3) Curing Agent; and (4) Ashby-Karstedt catalyst. This present study investigates the material properties regarding four different formulations of Sylgard 184 that are listed in Table 1. Once all the constituents were added together, the mixture was placed in a THINKY ARV-310 planetary mixer for two minutes at 2,000 rpm at a vacuum of 0.2 psi. After pouring the resulting blend into the desired mold, the polymer solution was cured in a 25°C oven for one week.

Table 7.1: The formulations of Sylgard 184 used in this study.

Formulation Name	wt% TDS	wt% Asbhy-Karstedt Catalyst
Control	0	0
Opt2	0	0.2
1pt1	1	0.1
1pt2	1	0.2

7.2.3 Thermal Accelerated Aging

Determining long-term material performance and behavior of polymers has been investigated using the concept and methodology of thermal accelerated aging[42-48]. After samples had reached their gel point and fully cured, which was determined by rheology and the technical data sheet, respectively, in a 25°C oven, they were grouped to be

thermally aged. Six ovens were kept isothermal at 25°C, 50°C, 60°C, 70°C, 80°C, and 90°C. Samples that did not have TDS added (Control and Opt2 formulations) were placed in sealed canisters. Each non-TDS formulation was placed in an individual canister per oven above 25°C, which made up ten canisters. Samples were placed such that they did not have contact with the metal canisters. After they were securely sealed and fastened, the canisters had their air evacuated, creating a vacuum around 10^{-3} torr, and filled with ultra-high purity nitrogen to around 600 torr. An additional Control canister and Opt2 canister went through the same process as described above with the exception that these two canisters were kept in air at atmospheric pressure and placed in the 90°C oven. Enough specimens were placed in the ovens that could be removed after aging for two, five, and twelve months. As an experimental note, two sample canisters for the 12-month aging Control (60°C and 70°C), leaked on their way to be analyzed and no mass spectrometry data could be recovered. Plots for the Control omit these two data points.

7.2.4 Chemical Characterization Techniques

Rheological measurements were taken with a TA Instruments Discover HR-2 Rheometer. For the gel point determination, a 25 mm parallel plate attachment was used with a gap height of 1000 μm . With a strain rate of 4% and a frequency of 10 rad/s, the system was kept isothermal at 25°C and the storage and loss moduli were measured as a function of time. The gel point, or working time, of the formulations was determined as the time elapsed from the beginning of the experiment until a crossover of the moduli was observed, where the loss modulus fell below the storage modulus.

Fourier transform infrared (FTIR) spectroscopy was used to determine the functional groups of the materials. FTIR was performed using a Thermoscientific Nicolet

iS50 FTIR with an average of 32 scans at a resolution of 4 cm^{-1} between $4000\text{-}525\text{ cm}^{-1}$. The measurements were performed in Attenuated Total Reflection (ATR) mode with a diamond crystal reference. A background spectrum was taken before each measurement.

Contact angle measurements were used to determine how hydrophobicity changed over time. It has been shown that low molecular weight PDMS chains migrate to the surface, which has quickly rendered an altered hydrophilic surface into a hydrophobic one[49]. Static contact angle measurements were performed using a Drop Shape Analyzer (DSA30) from Krüss. An automated drop dispenser and deposition system was used to perform the measurements. A drop of $2\text{ }\mu\text{L}$ deionized (DI) water was dropped on the material surface and the static contact angle was then determined by the computer software. A minimum of four trials were performed on different parts of the sample surface and two samples from each formulation were tested, giving eight pairs of contact angles for each material. The reported values of static contact angle are an average and standard deviation of the measurements.

Solvent swelling and gel permeation chromatography (GPC) experiments were used to evaluate the crosslinking density and molecular weight of the non-bound extracts, respectively. Solvent swelling and GPC were performed using toluene and chloroform, respectively, which are good solvents for PDMS[6, 50-52]. For GPC, $5.5 \pm 5\text{ g}$ of each sample was swollen in 20 g of chloroform for 24 hours at 25°C . After swelling, the excess solvent that was not absorbed by the polymer was filtered using a $0.22\text{ }\mu\text{m}$ PTFE filter and then analyzed using an Agilent Infinity II instrument, with a Shodex (K-805L) column, and Wyatt Technology detectors: Dawn multi-angle light scattering (MALS, 25°C) and Optilab refractive index (RI, 30°C). The instrument used $75\text{ }\mu\text{L}$ of each sample per experiment and

ran the material through the column at a rate of 1.0 mL/min. Data was analyzed using Astra Software. Values for the number average molar mass, M_n , weight average molar mass, M_w , and polydispersity, \mathcal{D} , were obtained using the Debye model for light scattering and a refractive index increment $dn/dc = -0.0646$. For solvent swelling, Sylgard 184 and its modifications were swollen to equilibrium in toluene for 24 hours at 25°C[6]. Additional experiments were run to ensure swelling equilibrium would be attained. Control samples were swollen in toluene for 1, 2, 3, 6, and 7 days and subsequently vacuum dried. All the samples had the same relative swollen mass and relative dried mass, thus confirming that swelling equilibrium is reached after one day. After being swollen, the samples were gently patted dry to remove residual toluene before recording the swollen mass. The samples were then dried at 25°C for 96 hours under vacuum.

Percent swelling from the solvent is reported as the difference between the fully swollen mass and initial mass. Percent loss from the solvent is reported as the difference between the initial mass and the vacuum dried mass. The network swelling is reported as the difference between the fully swollen mass and vacuum dried mass. Each sample was run in triplicate and standard deviation is reported as the error. Sample dimensions were 11.1 mm in diameter and 0.98 ± 0.1 mm in thickness.

The polymer volume fraction φ_p was determined using the respective partial volumes of the polymer V_p and solvent V_s . Because these values are not easily measured, the densities of the polymer ρ_p and solvent ρ_s were used along with the network swelling, S , to obtain the volume fraction, which is shown as Equation 7.1. This was used to evaluate the Flory-Huggins polymer-solvent interaction parameter χ between PDMS and toluene, where many equations have been developed to describe the interaction parameter from

theory and experimental methods[52-57]. Searching through literature regarding swelling PDMS with toluene, the equation that best describes the systems in this study is a finite Taylor series as a function of the polymer volume fraction with values shown in Equation 7.2[58].

$$\varphi_p = \frac{V_p}{V_p + V_s} = \left(1 + S \frac{\rho_p}{\rho_s}\right)^{-1} \quad \text{Equation 7.1}$$

$$\chi = \chi_0 + \chi_1 \varphi_p + \chi_2 \varphi_p^2 = 0.459 + 0.134 \varphi_p + 0.590 \varphi_p^2 \quad \text{Equation 7.2}$$

Using the interaction parameter along with the polymer volume fraction and molar volume of the solvent $v_{m,s}$ the average molecular weight of the polymer between crosslinks M_c can be evaluated using a modified version of the Flory-Rehner equation. The standard Flory-Rehner equation is derived from thermodynamic interactions and treats the swollen polymer as a perfect network, where the numerator and denominator correspond to the elastic and mixing contributions, respectively[52, 59-62]. Groups working with both theoretical and experimental methods regarding polymer swelling behavior have shown that a phantom network models a swollen polymer with better precision and as such is used in this study as Equation 7.3[52, 59]. The same Flory-Rehner equation can also relate the effective number of chains in the network ν_e to the average molecular weight of the polymer between crosslinks and Avogadro's number N_A shown as Equation 7.4. Rearranging the terms in Equation 7.4 produces the specific crosslink density ρ_x of the polymer, shown as Equation 7.5, which describes the moles of crosslinks per mass of polymer.

$$M_c = \frac{-\frac{1}{2}v_{m,s}\rho_p\varphi_p^{1/3}}{\ln(1-\varphi_p)+\varphi_p+\chi\varphi_p^2} \quad \text{Equation 7.3}$$

$$v_e = \frac{\rho_p N_A}{M_c} \quad \text{Equation 7.4}$$

$$\frac{v_e}{\rho_p N_A} = \frac{1}{M_c} = \rho_x \quad \text{Equation 7.5}$$

Mass spectrometry was performed on the headspace of each sealed canister using a Finnigan MAT 271 magnetic-sector mass spectrometer. In addition to the standard Faraday-cup detector, this closed-source, electron-ionization (EI) gas mass spectrometer is equipped with a secondary electron multiplier for detection of trace species. The two detectors were calibrated against standards for several permanent gases. For other gases and vapors, estimates were made from the sensitivities based on the electric dipole polarizabilities of the molecules relative to those of the calibration gases[63]. Species were identified by comparison of the measured spectra against the National Institute of Standards and Technology (NIST) electron ionization catalog and the EI fragmentation patterns are used to subtract the contributions by ions of higher-mass molecules from lower-mass peaks. Raw data was in the form of parts per million (ppm) and was converted to moles using the ideal gas law and the measured pressure of the canisters.

7.2.5 Mechanical Characterization Techniques

Shore A Hardness (ShA) testing was performed on a benchtop HPE II Zwick Roell Shore A hardness tester using discs with a diameter of 29 mm and a thickness between 10 and 13 mm because samples with a thickness greater than 6 mm reduce the error associated with the test[13]. Values were taken at equilibrium when the hardness reading had stopped

changing. Hardness values were averaged using three samples that were each tested in at least three different locations. Standard deviation is reported as the error.

Tensile strength was measured using an ADMET eXpert 7601 testing system. All samples were cut into dumbbell shapes, referred to as dogbones, using a type-A specimen die following ASTM D412 standards. The samples were loaded into the uniaxial grips and then pulled to reach a break point at the speed of 3.84 mm/sec. Three trials were performed for each sample and the engineering stress, strain, and Young's modulus are reported as averages and corresponding standard deviations.

7.2.6 Thermal Characterization Techniques

Thermogravimetric analysis (TGA) experiments were conducted to evaluate the thermal stability of the samples. TGA was performed using a TA Instrument TGA 550, Discovery Series. Samples weighing $10 \text{ mg} \pm 1 \text{ mg}$ were heated at a temperature ramping of $5^\circ\text{C}/\text{min}$ to 750°C under nitrogen passing through the furnace at $40 \text{ mL}/\text{min}$. The onset of thermal degradation $T_{d5\%}$ is a measure of thermal stability and applicability, which is determined from the temperature at which the residual mass is 95% of the total. The temperature of thermal decomposition is that temperature at which the derivative graph (DTGA) is a maximum. Differential Scanning Calorimetry (DSC) experiments were conducted to determine the glass transition temperature T_g along with any phase transitions. DSC experiments were performed using a TA Instrument, DSC Q20a, Q Series. The samples, weighing between 5 and 10 mg, were cooled down at $10^\circ\text{C}/\text{min}$ to -150°C , ramped at $5^\circ\text{C}/\text{min}$ to -100°C , and then ramped at $10^\circ\text{C}/\text{min}$ to 30°C . The reported glass transition temperatures are those found along the heating curve. Coefficient of linear thermal expansion (CTE) experiments were conducted using the dilatometer TA

Instrument DIL 802. Cylindrical samples measuring approximately 19.00 mm in length and 4.5 mm in diameter were placed next to a fused silica standard and heated under nitrogen at a rate of 5°C/min until the furnace reached 150°C. The CTE value α evaluated using Equation 7.6, was provided by the instrument's software based on the change in length ΔL change in temperature ΔT and original length L_0 . Average values and standard deviations are reported from CTE values after they reached a stable number, typically after the sample reached above 40°C.

$$\alpha = \frac{1}{L_0} \frac{\Delta L}{\Delta T} \quad \text{Equation 7.6}$$

7.3 Results and Discussion

7.3.1 Material Properties of Pristine Samples

Rheology performed on the four formulations (Control, 0pt2, 1pt1, and 1pt2) shows that the gel point, which is when the polymer forms a 3D network and can be used as a comparison for the curing time, decreased significantly from the Control to any of the formulations with the Ashby-Karstedt catalyst. The reduction in the time for the gel point to appear was even more significant with samples containing TDS. The rheology results, shown in Figure 1, demonstrate that a small addition to the formulation can speed up the curing of the thermoset elastomer. Compared to the unmodified Control, the 0pt2, 1pt1, and 1pt2 formulations had a reduction in the gel point time by 86%, 94%, and 98%, respectively. From this, it is inferred that a greater amount of Pt and vinyl groups within the Ashby-Karstedt catalyst contribute towards the crosslinking of the prepolymer and resin. This has also been seen when the standard 10:1 ratio of base to hardener is lowered so that there is more platinum that can react with the prepolymer, which leads to a faster

curing time[64, 65]. Studies that demonstrate this fact also demonstrate that Sylgard 184 prepared with the lowered ratio comes with varying mechanical properties. Additionally from the rheology, it can be inferred that the TDS acts as a bridge between separately formed PDMS chains that would have otherwise either not joined the network or taken much longer to do so. Thus, incorporating both the Ashby-Karstedt catalyst and TDS allows for more reaction sites and vinyl groups to participate in the crosslinking reaction and make a more connected network.

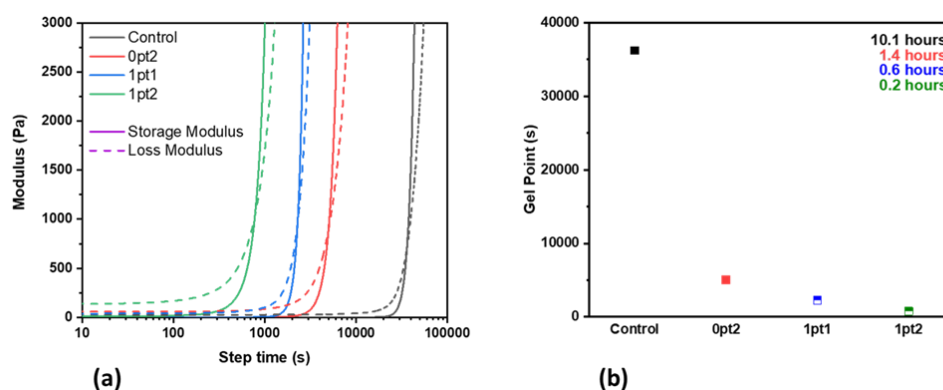


Figure 7.1: Rheology of the four formulations – (a) Storage and Loss Moduli and (b) Gel Point.

The FTIR spectra for Sylgard 184 is shown in Appendix as Figure A.3 along with five IR peak assignments. Comparing the FTIR spectra for all four formulations reveals distinct regions in similar locations with similar intensities. Thus, the modified formulations do not appear to differ from the Control with respect to the chemical functional groups. GPC experiments, which evaluated the molecular weights and distributions of the extractable material in the formulations, showed three peaks for the samples that occurred around two, four, and ten minutes, which correspond to weights of 10^7 , 10^6 , and 10^3 g/mol, respectively. All the formulations exhibited these peaks and the

cumulative molar mass distributions for the samples, shown in the Appendix as Figure A.4, exhibited similar results for each formulation.

With regards to surface characteristics, Sylgard 184 is naturally hydrophobic due to the methyl end groups on the polymer chain, however it can easily be chemically and physically altered to exhibit other surface characteristics[66]. The Control samples demonstrated a static contact angle with water of $110^\circ \pm 9^\circ$, which agrees with literature values reporting measurements of 109° . Measured static contact angles for the modifications are $110^\circ \pm 11^\circ$ for 0pt2, $110^\circ \pm 4^\circ$ for 1pt1, and $114^\circ \pm 13^\circ$ for 1pt2, thus showing that hydrophobicity is invariant across the formulations.

Swelling experiments of the pristine specimen showed that while all the samples absorbed enough toluene to nearly double their mass, the Control formulation clearly absorbed the most solvent. Indeed, the Control formulation absorbed enough solvent to increase its mass by over 125% while the modified samples were under 100%. The mass losses after drying were all similar across the samples, which measured around 4%. Comparisons of swelling between the samples are shown in Figure 2(a). The measured density of the samples averaged to 0.98 g/cm^3 and is used throughout this study. While the manufacturer reports a density of 1.03 g/cm^3 , others such as Olima have reported 1.18 g/cm^3 [3]. Equation 5 provides the specific crosslink densities of the pristine samples, which are shown in Figure 2(b). A decrease in swelling corresponds to an increase in the crosslink density, thus Figures 2(a) and 2(b) both describe a similar phenomenon, where the modified samples have a greater specific crosslink density than the Control.

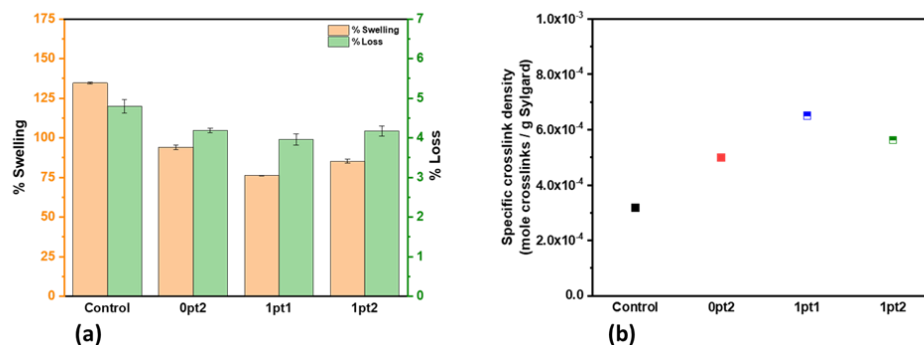


Figure 7.2: Solvent swelling experiments of the pristine samples in toluene – (a) Swelling and Loss percent for the formulations and (b) Specific crosslinking density ρ_x for the formulations

The mechanical data shows the first recognizable distinction between the four formulations; the modified samples became harder and less flexible on a qualitative basis compared to the Control. Tension tests performed on the dogbone samples confirmed this quantitatively. The results of the tension and hardness tests, shown in Figure 3, demonstrate that all the modified samples become stiffer and less flexible by measure of the maximum elongation and stress and Young's modulus. Hardness measurements, by way of Shore A Hardness durometry, also quantitatively prove that the modified pristine samples are more resistant to indentation than the Control. These results correlate with Figure 7.2, where an increase in the specific crosslink density is associated with an increase in hardness and Young's modulus.

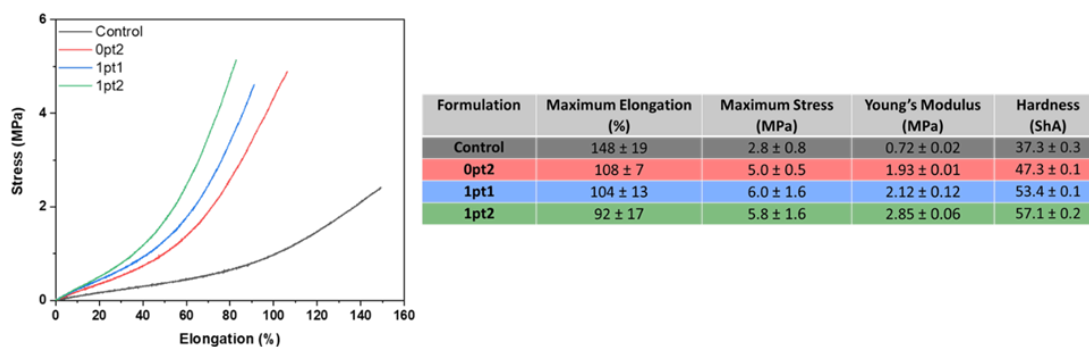


Figure 7.3: Mechanical properties of the pristine samples.

All four formulations exhibit thermal degradation at similar temperatures, as observed in the TGA and DTGA curves in Figure 4. Figure 4(b) shows all the DTGA curves magnified four times so that the peaks are more readily observed. The differences in the thermal stability between the modified and unmodified Sylgard 184 samples were compared using the onset of thermal degradation $T_{d5\%}$ which is the temperature at which the materials lose 5% of their initial mass. While the Control sample exhibited an onset degradation temperature at 370°C, all the $T_{d5\%}$ for the modified samples were similar with values of 355°C for 0pt2, 352°C for 1pt1, and 355°C for 1pt2, a 15°C decrease. Additionally, the modified formulations had similar thermal degradation mechanisms, where residual masses were comparable (Figure 7.4 (a)) and thermal decomposition peaks were located at the same temperatures (Figure 7.4 (b)), while the Control sample sharply deviated after the first thermal degradation mechanism. Furthermore, the Control sample had a 30 wt% lower residual mass than the modified formulations, indicating that more volatile products were formed due to thermal decomposition. The high residual mass exhibited in Figure 7.4 (a) has also been observed in literature for Sylgard 184 and some silicone polymers[3, 67-69]. The greatest difference in the degradation profiles was with

the quality of the peaks. In the DTGA curves for the modified samples, three peaks are observed, with the greatest relative peak being the first one, which occurs around 360°C and is comparable to literature values for PDMS decomposition[36, 37, 70]. Additionally, all three peaks occur in similar temperature regions for the modified samples. This is in contrast to the Control, where the second peak is so pronounced that it obscures the others in the pristine sample. The decomposition peaks from DTGA curves correspond to approximately 360°C, 470°C, and 650°C in nitrogen. These have been observed before and have been attributed to the depolymerization process of the chain backbone[3, 41, 71]. Figure 7.4 demonstrates that the pristine Control samples are initially more thermally stable and the chain backbone can withstand greater thermal excitations than the modified samples, however once the depolymerization process begins to occur, the Control samples rapidly decompose and form volatile products while the modified formulations decompose less readily.

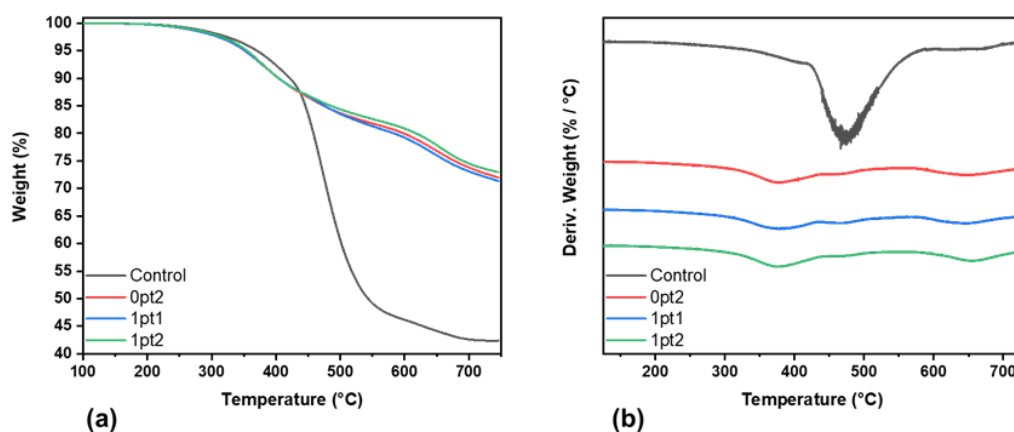


Figure 7.4: Thermal stability of the pristine samples – (a) TGA curves and (b) DTGA curves magnified.

CTE values were 266 ppm K⁻¹ for the Control, 250 ppm K⁻¹ for Opt2, 203 ppm K⁻¹ for 1pt1, and 207 ppm K⁻¹ for 1pt2. Along with the original manufacturer of Sylgard 184 claiming that it has a coefficient of linear thermal expansion of 340 ppm K⁻¹[8], Liu et al reports 300 ppm K⁻¹[72], Müller et al reports 310 ppm K⁻¹[73], and Kong et al reports 362 ppm K⁻¹[74]. The measured CTE values show an improved performance with the modified samples compared to the Control for applications using Sylgard 184, such as micromechanical devices and optical instruments. This is because the polymer is frequently in contact with metals or materials that conduct heat and exhibit low thermal expansion coefficients. Equipment and tools such as these frequently fail due to thermal expansion mismatch, which is why methods that reduce the thermal expansion coefficient are thought to improve performance. The range of CTE values measured for the four formulations and found from literature demonstrates that while the CTE of Sylgard 184 is significantly higher than most polymers, metals, and other materials, there is a large variability in this property, likely due to fluctuations in different batches.

The glass transition temperature for all the formulations are similarly at -120°C. No crystallization or melting peaks were observed in any heating or cooling cycles, even when the range was extended from -150°C to 200°C. This agrees with previous results where Sylgard 184 has a T_g around -125°C and exhibits no crystallization peaks, making the material a fully amorphous polymer[3].

7.3.2 Mechanisms for Aging under Nitrogen

The Control and Opt2 samples underwent thermal accelerated aging under a nitrogen atmosphere. Swelling data for the aged Control and Opt2 samples is shown in Figures 7.5 (a) and (b), respectively. An immediate observation from Figure 7.5 is that both

formulations undergo a post-curing reaction, where the swelling at room and elevated temperatures indicates that the crosslink density increases. A second observation is that after two months of thermal accelerated aging, the swelling of both the Control and Opt2 samples reaches a plateau, revealing that the majority of the hydrosilylation reaction has run to completion. The third observation, which highlights the difference between the Control and Opt2 samples, is that the Opt2 samples experience a less overall change in swelling than the Control and it occurs more rapidly. A final observation is from the samples aged in air at 90°C, which are colored yellow and offset in Figure 5 at 92°C solely for legibility. Notice that the samples aged in air at 90°C exhibit similar swelling behavior to those samples aged in nitrogen at 90°C.

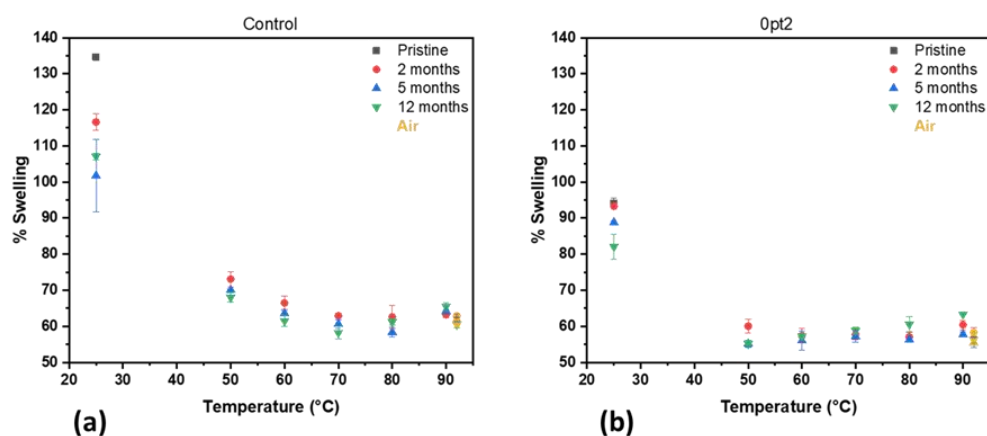


Figure 7.5: Swelling of the thermally aged samples – (a) Control and (b) Opt2.

The hydrosilylation reaction responsible for the curing of Sylgard 184 creates crosslinks but does not generate volatile products. Analysis of the headspace of the sealed canisters via mass spectrometry allows for an evaluation of the volatile products and can assist in proposing mechanisms responsible for the reactions. The most common evolved

products were hydrogen, methane, and ethane, with the former two making up the vast majority of volatiles detected. These can be produced from a proposed reaction mechanism involving water interacting with Si-H groups. Although the hydrosilylation reaction is an addition reaction between Si-H and vinyl groups in the presence of a catalyst, notably Pt, water can also attack Si-H to form Si-OH in the presence of the same catalyst [17, 34]. Additionally, siloxanols can be created from the hydrolysis of PDMS, where a water molecule attacks a siloxane chain, resulting in a chain scission and two hydroxyl-terminated chains[75-77]. If a siloxanol encounters a silane, a new crosslink will form between the two moieties and H₂ gas will be produced. If, however, a siloxanol encounters a Si-CH₃ group instead, a new crosslink will form between the two moieties and CH₄ gas will be produced[78, 79]. Ethane is produced in a similar manner, except with a Si-C₂H₅ group encountering a siloxanol.

The cumulative amount of hydrogen and methane in the Control and Opt2 samples are shown in Figure 7.6. Furthermore, samples that were aged at 90°C in air are included as before: yellow and offset in Figure 7.6 to be 92°C solely for legibility. Two initial observations stand out, which are that as time progresses and as temperature increases, the cumulative amount of volatiles becomes greater. Additional interesting observations can be made when comparing volatile product generation between the two formulations. One would be that there is more hydrogen generation for the Control than Opt2 samples. The other would be the case for methane generation, where Opt2 generated much more methane than Control samples.

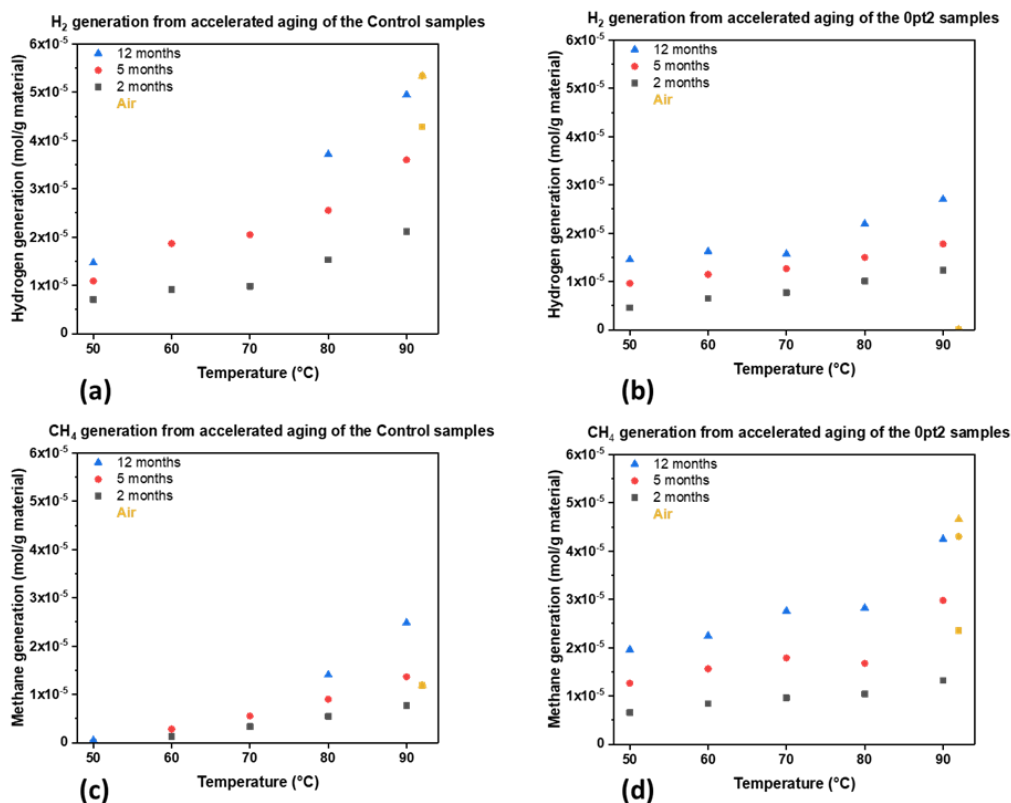


Figure 7.6: Measuring the volatile products that evolved while undergoing thermal accelerated aging on a per mass of Sylgard basis: (a) hydrogen generation from the control; (b) hydrogen generation from Opt2; (c) methane generation from the control; and (d) methane generation from Opt2.

The proposed mechanism, which depends on trace water, should be able to be indirectly observed via Si-OH bonds. Based on FTIR data, there are peaks around 845 cm⁻¹ and 865 cm⁻¹ (shown in the Appendix as Figure A.5), which correspond to Si-O stretching in Si-OH[66]. Additionally, mass spectrometry revealed small amounts of trace water (in ppm levels) in the headspace. Although the FTIR data was not quantitatively analyzed, reviewing the spectra and mass spectrometry of the samples lends credence towards this proposed mechanism. The addition of the 2% Pt Ashby-Karstedt catalyst, which introduces more vinyl groups and thus promotes crosslinking, leaves fewer available Si-H groups for

H₂ generation. Thus, the Opt2 samples should be expected to generate less H₂ gas than the Control samples but generate more CH₄. Additionally, observe how the volatile gas production in Figure 6 increases with temperature. Greater thermal energy leads to more chain mobility and thus more interactions between siloxanes, silanes, and siloxanols. Thus, the proposed mechanism provides an explanation for the observed data.

It is possible to draw conclusions about the specific crosslink density using Equation 7.5. Based on the proposed mechanisms, all the crosslinks in the polymer network are assumed to be from the hydrosilylation (cure and post-cure) and trace water-promoted reactions. Treating the specific crosslink density as separable with regards to reactions that generate crosslinks, it can be thought of as the sum of the specific crosslink density due to hydrosilylation $p_x^{hydrosilylation}$ and water reactions p_x^{water} as shown in Equation 7.7. Because the hydrosilylation reaction does not generate volatile gas, each molecule of volatile gas is produced as a result of a crosslink formed from a trace water reaction. Thus, summing the moles of hydrogen, methane, and ethane measured via mass spectrometry yields the amount of crosslinks formed due to trace water. Additionally, Equation 7.7 can be used to define the fraction of specific crosslink density due to trace water η_{water} as shown in Equation 7.8.

$$p_x = p_x^{hydrosilylation} + p_x^{water} \quad \text{Equation 7.7}$$

$$\eta_{water} = \frac{p_x^{water}}{p_x^{hydrosilylation} + p_x^{water}} \quad \text{Equation 7.8}$$

Equation 7.8 can now be used to observe how changes in the specific crosslink density for the aged formulations (shown in the Appendix as Figure A.6) are due to various reactions. Using the mass spectrometry data along with the swelling data allows for an

understanding of the crosslinking behavior due to the cure, post-cure, and trace water reactions, which is shown in Figure 7.7. The specific crosslink density due to the hydrosilylation reaction for Control and Opt2 (Figures 7.7 (a) (b)) show that the amount of crosslinks per mass of Sylgard does not change significantly, which mimics the swelling data. Indeed, both the Control and Opt2 samples seem to level off between 0.7-0.8 mmol of crosslinks due to curing and post-curing per gram of Sylgard. Additionally, Opt2 samples converge to the plateau at a much earlier time than the Control, where after two months the Opt2 samples do not exhibit any significant change in specific crosslink density. Furthermore, the fraction of specific crosslink density due to trace water reactions (Figures 7.7 (c) (d)) increases over time and temperature. Thus, while the post-curing reaction ceases after two months and stops contributing to the specific crosslink density, the trace water reactions continue to promote crosslinking and gas evolution.

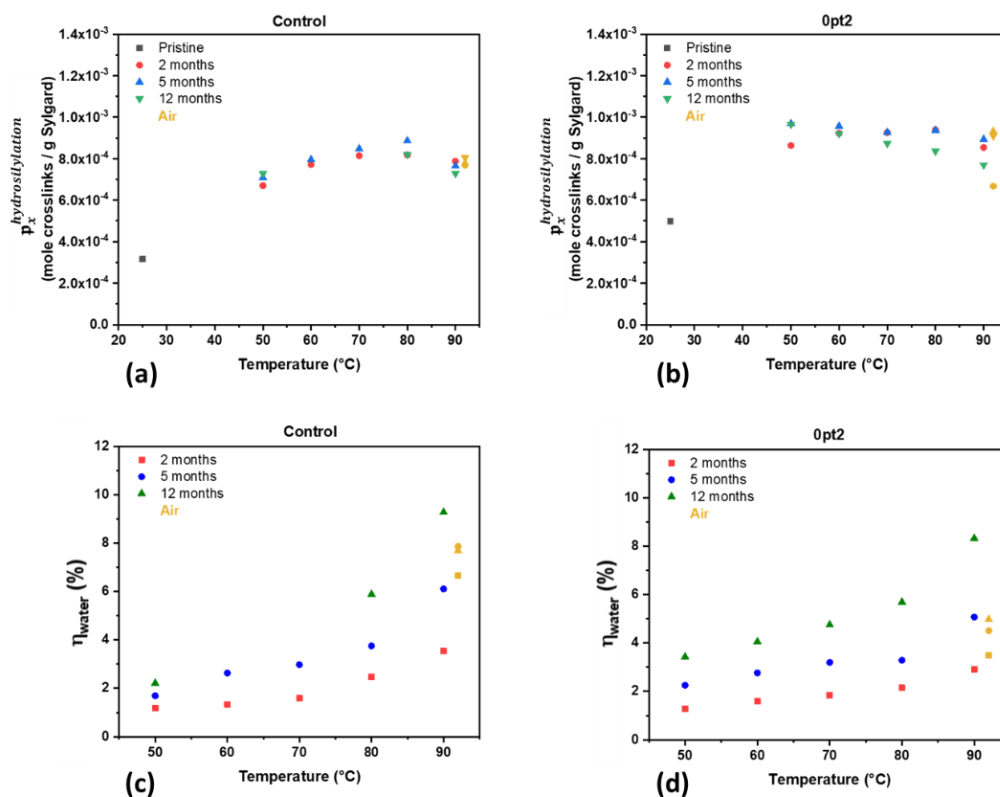


Figure 7.7: Specific crosslink density – (a) Crosslinks due to hydrosilylation for Control; (b) Crosslinks due to hydrosilylation for Opt2; (c) Water fraction for Control; and (d) Water fraction for Opt2.

Traditionally, time-temperature superposition (TTS) is performed in relation to stress, creep, or dynamic loading, but in essence, material properties need to be measured and compared to a reference for the principle to be applicable. Because the aging temperatures used in this study are well below that of any thermal decomposition and well above any thermal phase transition, mass spectrometry can be used according to TTS and a master curve can be created as a function of shift time. The lowest temperature used for mass spectrometry, 50°C, was the reference temperature T_0 . After two months, the shift factor a_T was defined in terms of the moles of gas produced n , shown in Equation 7.9,

which allowed for a new axis of shift time $a_T t$ to be used where all the data can be superimposed. For specific degradation or reaction mechanisms, if Arrhenius behavior was followed, the apparent activation energy E can be defined in terms of the universal gas constant R , the shift factor, and the differences in reciprocal temperatures in Kelvin, as shown in Equation 7.10. Performing TTS with mass spectrometry data can be validated with these equations if there is a linear relationship between $\ln(a_T t)$ and $1/T$, which is shown as Figure A.7.

$$a_T = \frac{n_{species}(T)}{n_{species}(T_0)} \quad \text{Equation 7.9}$$

$$E = \frac{R \ln(a_T)}{\frac{1}{T_0} - \frac{1}{T}} \quad \text{Equation 7.10}$$

Plotting all the evolved gases (hydrogen, methane, and ethane) for the Control and Opt2 samples against shift time, a trend can be observed. Using statistical regression, the superposition data was modeled with a power function. These are shown in Figure 7.8 along with the coefficient of determination R^2 . Although Figure 7.6 shows that the Control samples generate more hydrogen than Opt2, enough methane and ethane were generated by Opt2 to have its model appear greater for overall volatile gas production. Power functions were used in the superposition model because there were few volatiles evolved at the beginning of aging but gradually increased as more time went on. The average activation energy for the Control and Opt2 samples was 38.2 kJ/mol and 15.5 kJ/mol, respectively, which is not surprising given that the shifted time values are much closer together for Opt2 than the Control.

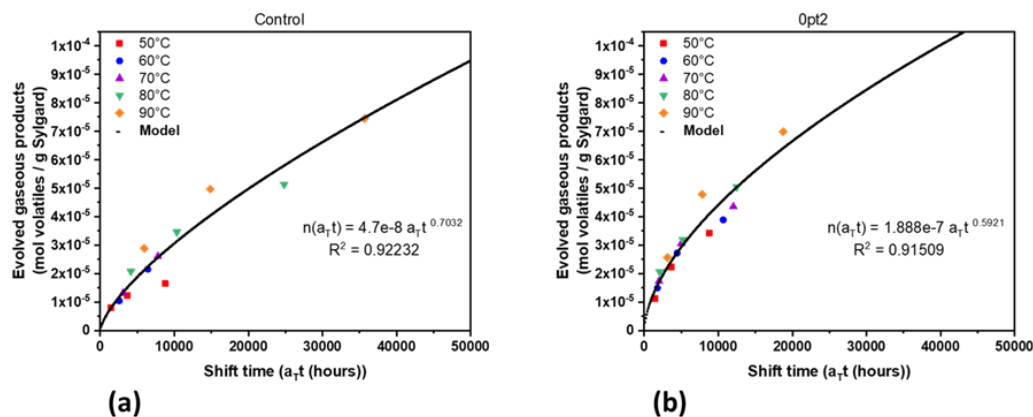


Figure 7.8: Time-temperature superposition master curve models of the three major evolved gaseous products – (a) Control and (b) Opt2.

Because hydrogen generation is a major known cause of hazards when dealing with siloxanes and silicon-based polymers in general, models were also developed for the Control and Opt2 samples regarding hydrogen evolution. Using the same procedure as detailed above for all major volatiles, the power law models were derived. For the Control, the coefficient and exponent in shift time are 4.22×10^{-8} and 0.7257, respectively. For the Opt2, the coefficient and exponent in shift time are 1.2×10^{-7} and 0.5391, respectively. Plots of these models are shown together in the Appendix as Figure A6. The average apparent activation energy for the Control and Opt2 samples was 33.4 kJ/mol and 14.4 kJ/mol, respectively.

It is apparent from Figure 7.6 that the Control samples generated more hydrogen than Opt2 samples while Opt2 samples generated more methane than Control samples. Interestingly, an oxygen-rich environment (air) causes more hydrogen to be produced with the Control than in nitrogen while almost no hydrogen is present for two, five, and twelve months of thermal accelerated aging of the Opt2 samples. Additionally, an oxygen-rich

environment causes more methane generation in the Opt2 samples than an inert environment while methane ceases to generate in an oxygen-rich environment after two months of aging for the Control. Indeed, an initial amount of methane was produced after two months at 90°C in air, but afterwards the cumulative amount barely increases.

Therefore, the presence of oxygen also has an influence on the volatile products. It appears that whichever gas species is more prominent (hydrogen or methane), oxygen increases its production while it sequesters the other evolved gas (methane or hydrogen). These observations can be seen when comparing Figure 7.6(a) with 7.6(d) and Figure 7.6(b) with 7.6(c). These novel data and results suggest that a preference can be chosen for both the formulation of Syglard 184 as well as the atmosphere it is stored in to selectively generate or suppress certain evolved permanent gases.

7.3.3 Material Properties of Aged Samples

Figure 7.9 shows the four formulations after twelve months of thermal accelerated aging. There is a general trend, where aging at higher temperatures lead to a greater amount of discoloration. This is exhibited in every formulation and throughout the interior of the samples, although the extent of discoloration is more pronounced in the modified specimen. The clear-to-yellow discoloration phenomenon of silicones is known to be caused from the platinum complex interactions and does not affect material performance[80-83]. Interestingly, all samples produce an obvious yellowing at 80°C if they haven't already been discolored. The greater discoloration of the modified samples can be explained due to the addition of the Asbhy-Karstedt catalyst, which introduces more platinum to complex. Furthermore, the addition of TDS prevents discoloration up to 70°C when comparing 1pt1 and 1pt2 samples to Opt2. The Control samples, which have no

additional platinum added, exhibit the least discoloration. Comparing aging nitrogen versus air, while the Opt2 samples were all yellow, the samples aged in air were the deepest brown color and the Control sample aged in air did not experience a yellowing effect at all.

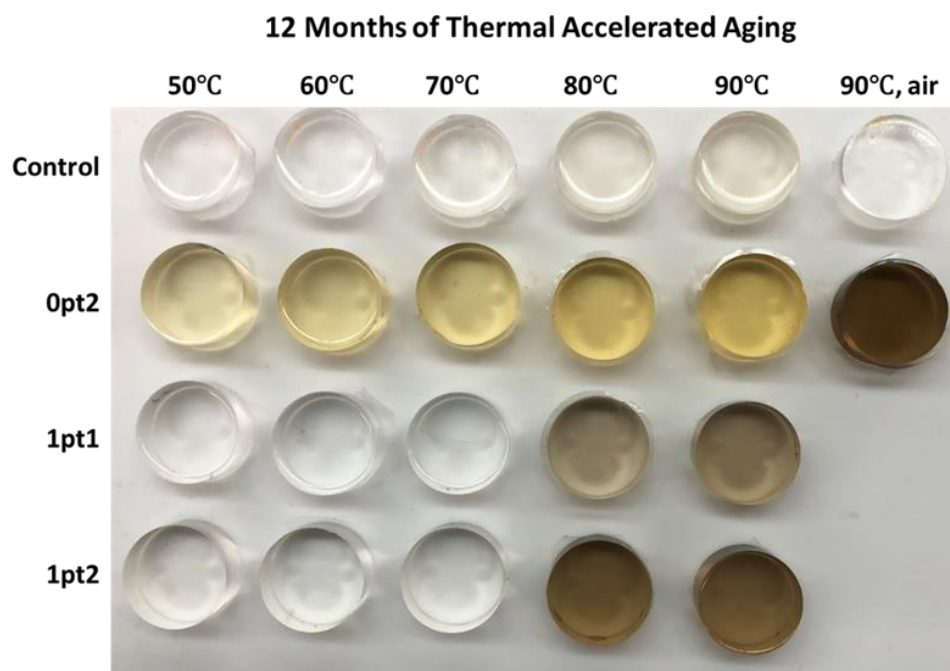


Figure 7.9: Discoloration of the four formulations after 12 months of thermal accelerated aging.

From a chemical structure perspective, the FTIR data shows that the peaks for all formulations make a near perfect superposition when comparing aging time and temperature. Additionally, no new peaks have formed. Thus, any chemical changes within the material are the product of rearrangement of bonds due to furthering the hydrosilylation reaction and other crosslinks due to trace water. Over time, all the aged formulations still exhibited contact angles above 90°, thus they continued to demonstrate hydrophobicity. No significant changes to hydrophobicity were observed during the aging process.

The 1pt1 and 1pt2 formulations exhibited a decrease in the solvent swelling similar to the others shown in Figure 7.5, where there was an increase in the specific crosslink density for all the formulations over their aging conditions. It should be noted that during swelling experiments, the mass of the extracts for all the samples changed little from the pristine, exhibiting values around 3.5%. For swelling, there is significantly less change after two months of aging, where considerable overlap occurs between five and twelve months. The final swelling values, taken from samples aged at 90°C for 12 months in air, were 60%, 56%, 58%, and 56% for the Control, 0pt2, 1pt1, and 1pt2 samples, respectively. For the same samples, the final specific crosslink densities were 8.7×10^{-4} , 9.6×10^{-4} , 9.3×10^{-4} , and 1.0×10^{-3} mole crosslinks/gram Sylgard for the Control, 0pt2, 1pt1, and 1pt2 samples, respectively. Evaluating the relative changes for the swelling and specific crosslink density demonstrated that the Control formulation experienced a greater overall change compared to the modified samples for both quantities.

Similar trends were observed for the mechanical properties. Like the swelling data, there were no statistically significant differences between the samples aged at 90°C in nitrogen or air; the atmosphere did not affect the final values of the mechanical properties. Obtaining values from the samples aged at 90°C for 12 months in air, the final mechanical properties are displayed in Table 7.2. Similar to the swelling behavior, the Control samples exhibited the greatest percent change overall, which can be seen when comparing the values from Table 7.2 with Figure 7.3. In general, all the formulations became harder and stiffer over time, along with the materials not being able to be stretched as much as they originally could without breaking. As an example, the Control, 0pt2, 1pt1, and 1pt2 samples increased in Shore A Hardness after thermal aging by 72%, 40%, 26%, and 20%,

respectively. Thus, final values for maximum elongation decreased while Shore A Hardness, maximum stress, and Young's modulus increased.

Table 7.2: Final mechanical properties of the four Sylgard 184 formulations.

Formulation	Maximum Elongation (%)	Maximum Stress (MPa)	Young's Modulus (MPa)	Shore A Hardness (ShA)
Control	74 ± 3	10.4 ± 0.7	5.74 ± 0.27	64.3 ± 0.3
0pt2	65 ± 5	8.8 ± 1.4	6.23 ± 0.32	66.4 ± 0.5
1pt1	70 ± 3	10.8 ± 1.1	6.86 ± 0.23	67.3 ± 0.8
1pt2	63 ± 3	9.3 ± 1.2	6.91 ± 0.40	68.4 ± 0.7

Shore A Hardness values were used for making TTS predictive master curves, which are shown in Figure 7.10. The reference temperature used in the procedure was 50°C. Because the hardness is generally monotonic and reaches a limit (Figure A.9 in the Appendix), a logistic curve was used to fit the shift time data using Equation A.1. The parameters of each logistic curve are given in the Appendix Table A.1. An interesting observation from performing this procedure is that the apparent activation energy at a given temperature is about 20% more than the activation energy for the samples aged 10°C higher. For the highest temperature, 90°C, the apparent activation energies were 9.0 kJ/mol, 5.0 kJ/mol, 1.9 kJ/mol, and 1.4 kJ/mol for the Control, 0pt2, 1pt1, and 1pt2 formulations, respectively. Similar to the mass spectrometry data, a plot to validate using TTS models for hardness data is shown in Figure A.10. From the TTS master curve model, aging at an elevated temperature of 50°C would take 82 days, 39 days, 38 days, and 35 days for the Control, 0pt2, 1pt1, and 1pt2 samples, respectively, to reach 95% of their final hardness values.

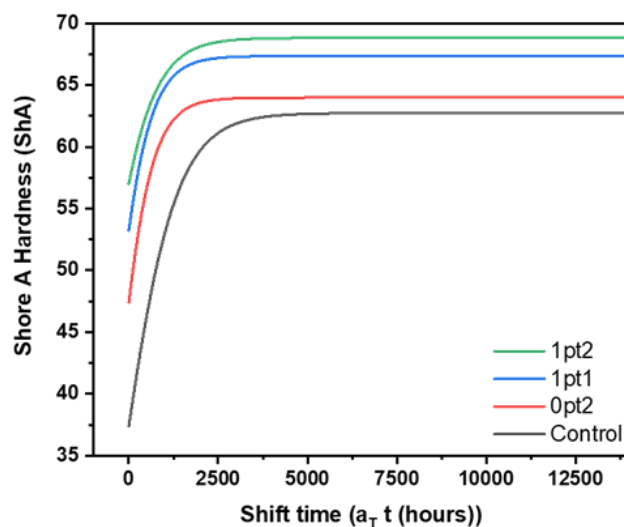


Figure 7.10: Time-temperature superposition master curve models of Shore A Hardness for the four thermal accelerated aged Sylgard 184 formulations.

The onset of thermal degradation, $T_{d5\%}$, for the formulations changed throughout the aging process. To better visualize the trends due to accelerated aging, linear regression was performed on the data. This linear regression found the best fit line for $T_{d5\%}$ against aging temperature and aging time and is displayed for the four formulations in Figure 7.11. Additionally, the listed slopes in the figure provide insight into how the thermal stability of the formulations will change over their lifespan. From Figure 7.11, all the modified formulations become more thermally stable for increasing aging temperatures while the Control remains steady. The largest changes came from the TDS-modified samples, which experienced a 10% (40°C) increase in thermal stability. Control samples aged in air had similar thermal stability as those aged in nitrogen and the 0p2 samples aged in air had an increase in thermal stability when compared against those aged in nitrogen.

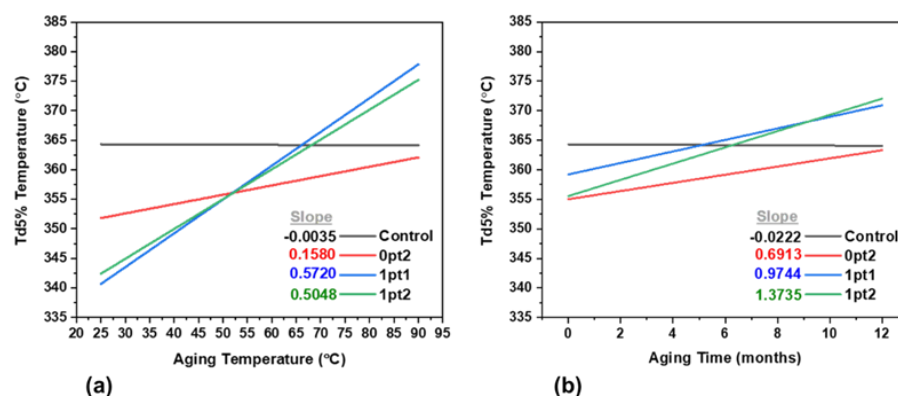


Figure 7.11: Linear regression of the thermally aged sampled – (a) as a function of aging temperature and (b) as a function of aging time.

The glass transition temperature for all the formulations remained at -120°C , which was expected, as the aging process occurs well above the glass transition. A similar linear regression treatment was performed for the coefficient of thermal expansion of the aged samples, however no clear trend existed. At the end of the 12 months of aging, all the samples fell within a range of 200-260 ppm K^{-1} .

7.4 Conclusions

This work examined how small chemical changes to Sylgard 184 affected its curing behavior at room temperature. Modified formulations were created using small amounts of the Ashby-Karstedt catalyst, a complex of 2% Pt(0) in cyclomethylvinylsiloxanes, and TDS, tetrakis (dimethylsiloxy) silane, both of which bolster the hydrosilylation reaction that provides the curing in the Sylgard framework. The Ashby-Karstedt catalyst introduces more vinyl groups and platinum while TDS introduces more silane reactive groups. It was found that all the modified formulations exhibited a dramatic reduction in the working time

by over 85% (less than 1.5 hours) at room temperature and that they had a greater degree of crosslinking than the Control.

Thermal accelerated aging was performed on the four formulations (Control, Opt2, 1pt1, and 1pt2) in isothermal conditions at 25°C, 50°C, 60°C, 70°C, 80°C, and 90°C and spanned time periods of two, five, and twelve months. Additionally, the Control and Opt2 samples were aged under controlled nitrogen and air atmospheres so that the evolving gases could be probed. Mass spectrometry data showed that hydrogen, methane, and ethane were the major volatile components of Sylgard 184. Two mechanisms were proposed to be responsible for aging. The hydrosilylation reaction is most responsible for the post-cure and thus changes to solvent swelling and mechanical behavior, while trace water present throughout the polymer network explained the volatile products. The Flory-Rehner equation along with the solvent swelling and mechanical data demonstrate that post-curing ceases after two months of thermal aging. Additionally, using shift factors from the time-temperature superposition principle, master curves were developed for volatile evolution and Shore A Hardness, which can be used to predict lifetime material performance. Mechanical tests demonstrated that all the formulations converge to specific limiting values, where all the samples became stiffer and harder over time and with the Control exhibited the greatest change overall. Indeed, the Control, Opt2, 1pt1, and 1pt2 samples increased in Shore A Hardness after thermal aging by 72%, 40%, 26%, and 20%, respectively. Thermal stability tests showed that the modified samples had an increase in their onset of thermal degradation over aging times and that the Control samples did not change significantly. The largest increase in thermal stability was observed in the TDS samples, which had a 10% (40°C) increase in thermal stability, from 350°C to 390°C.

Comparing the four formulations from an initial and aging standpoint, it is clear that the modified samples experience less aging. Indeed, the Control samples demonstrated a greater percent change in solvent swelling and every mechanical property examined (Shore A Hardness, maximum elongation, maximum stress, and Young's modulus), thus illustrating that the material properties of the modified samples are more consistent throughout their lifespan. Additionally, because the material properties vary, Sylgard 184 can be altered to fit specific applications. This extends to volatile gas production, where the formulation and aging atmosphere had an effect on which gases evolved and in varying quantities. In essence, Sylgard 184 can be tailored with small amounts of well-known compounds to optimize material properties and lifetime performance.

References

1. Harley, S.J., E.A. Glascoe, and R.S. Maxwell, Thermodynamic study on dynamic water vapor sorption in Sylgard-184. *The Journal of Physical Chemistry B*, 2012. 116(48): p. 14183-14190.
2. Kendrick, T., B. Parbhoo, and J. White, Appendix to 'Siloxane polymers and copolymers'. *The Silicon-Heteroatom Bond* (1991), 1991: p. 141-150.
3. Olima, M., *Mechanical Characterization of Polydimethylsiloxane*. 2017.
4. Owen, M.J., *Siloxane surface activity*. 1990, ACS Publications.
5. Schneider, F., et al., Process and material properties of polydimethylsiloxane (PDMS) for Optical MEMS. *Sensors and Actuators A: Physical*, 2009. 151(2): p. 95-99.
6. Lee, J.N., C. Park, and G.M. Whitesides, Solvent compatibility of poly(dimethylsiloxane)-based microfluidic devices. *Analytical chemistry*, 2003. 75(23): p. 6544-6554.

7. Henrey, M., et al. Sticking in space: manufacturing dry adhesives and testing their performance in space environments. in 12th Symp. on Adv. Space Technologies in Robotics and Automation. 2013.
8. Dow, SYLGARD™184 Silicone Elastomer Technical Data Sheet. 2017.
9. Ortiz-Acosta, D., Sylgard® Cure Inhibition Characterization. 2012, Los Alamos National Lab.(LANL), Los Alamos, NM (United States).
10. Marciniak, B., Comprehensive handbook on hydrosilylation. 2013: Elsevier.
11. Hammouch, S.O., G. Beinert, and J. Herz, Contribution to a better knowledge of the crosslinking reaction of polydimethylsiloxane (PDMS) by end-linking: the formation of star-branched PDMS by the hydrosilylation reaction. *Polymer*, 1996. 37(15): p. 3353-3360.
12. Marciniak, B., Hydrosilylation: a comprehensive review on recent advances. 2008.
13. Murphy, E.C., et al., Tailoring properties and processing of Sylgard 184: Curing time, adhesion, and water affinity. *Journal of Applied Polymer Science*, 2020. 137(14): p. 48530.
14. Gao, J., et al., Material characterization and transfer of large-area ultra-thin polydimethylsiloxane membranes. *Journal of Microelectromechanical Systems*, 2015. 24(6): p. 2170-2177.
15. Bello, M., et al., Sylgard® Mixing Study. 2014, ; Los Alamos National Lab. (LANL), Los Alamos, NM (United States). p. Medium: ED.
16. Eddington, D.T., W.C. Crone, and D.J. Beebe. Development of process protocols to fine tune polydimethylsiloxane material properties. in 7th International Conference on Miniaturized Chemical and Biochemical Analysis Systems. 2003.

17. Barnes, S., S. Riley, and S. Wolfe, Hydrogen evolution from silicone resins for primary coating applications. *IEE Proceedings J-Optoelectronics*, 1985. 132(3): p. 169-171.
18. Liu, M., J. Sun, and Q. Chen, Influences of heating temperature on mechanical properties of polydimethylsiloxane. *Sensors and Actuators A: Physical*, 2009. 151(1): p. 42-45.
19. Luo, X. and P.T. Mather, Preparation and characterization of shape memory elastomeric composites. *Macromolecules*, 2009. 42(19): p. 7251-7253.
20. Ko, Y.-I., et al., Silicone-coated elastomeric polylactide nanofiber filaments: mechanical properties and shape memory behavior. *RSC Advances*, 2013. 3(43): p. 20091-20098.
21. Robertson, J.M., et al., Mechanically programmed shape change in laminated elastomeric composites. *Soft Matter*, 2015. 11(28): p. 5754-5764.
22. Wang, C., et al., Repeated instant self-healing shape memory composites. *Journal of materials engineering and performance*, 2012. 21(12): p. 2663-2669.
23. Orellana, J., et al., Self-healing polymer nanocomposite materials by Joule effect. *Polymers*, 2021. 13(4): p. 649.
24. Cui, H., et al., Rubber-like electrically conductive polymeric materials with shape memory. *Smart materials and structures*, 2013. 22(5): p. 055024.
25. Hong, S., et al., Highly stretchable and transparent metal nanowire heater for wearable electronics applications. *Advanced materials*, 2015. 27(32): p. 4744-4751.
26. Gong, S., et al., Highly Stretchy Black Gold E-Skin Nanopatches as Highly Sensitive Wearable Biomedical Sensors. *Advanced Electronic Materials*, 2015. 1(4): p. 1400063.

27. Lay, M., et al., Crosslink network and phenyl content on the optical, hardness, and thermal aging of PDMS LED encapsulant. *Journal of Applied Polymer Science*, 2019. 136(34): p. 47895.
28. Ghosh, D. and D. Khastgir, Degradation and stability of polymeric high-voltage insulators and prediction of their service life through environmental and accelerated aging processes. *ACS omega*, 2018. 3(9): p. 11317-11330.
29. Yeh, C.J., et al., Fracture and thermal aging of resin-filled silicone elastomers. *Journal of Polymer Science Part B: Polymer Physics*, 2016. 54(2): p. 263-273.
30. Labouriau, A., et al., Aging mechanisms in RTV polysiloxane foams. *Polymer Degradation and Stability*, 2015. 121: p. 60-68.
31. Labouriau, A., et al., Mössbauer, NMR and ATR-FTIR spectroscopic investigation of degradation in RTV siloxane foams. *Polymer degradation and stability*, 2007. 92(3): p. 414-424.
32. Labouriau, A., et al., Gamma irradiation and oxidative degradation of a silica-filled silicone elastomer. *Polymer Degradation and Stability*, 2015. 116: p. 62-74.
33. Barnes, S., S. Riley, and S. Wolfe, Hydrogen evolution behaviour of silicone-coated optical fibres. *Electronics Letters*, 1985. 21(16): p. 712-713.
34. *Materials Handling Guide: Hydrogen-Bonded Silicon Compounds*. August 2007, Operating Safety Committee of the Silicones Environmental, Health and Safety Council of North America.
35. Manders, W. and J. Bellama, Multiphoton infrared laser-induced degradation of polydimethylsiloxane and hexamethyldisiloxane. *Journal of Polymer Science: Polymer Chemistry Edition*, 1985. 23(2): p. 351-357.

36. Grassie, N. and I. Macfarlane, The thermal degradation of polysiloxanes—I. Poly (dimethylsiloxane). *European polymer journal*, 1978. 14(11): p. 875-884.
37. Camino, G., S. Lomakin, and M. Lazzari, Polydimethylsiloxane thermal degradation Part 1. Kinetic aspects. *Polymer*, 2001. 42(6): p. 2395-2402.
38. Thomas, T.H. and T. Kendrick, Thermal analysis of polysiloxanes. II. Thermal vacuum degradation of polysiloxanes with different substituents on silicon and in the main siloxane chain. *Journal of Polymer Science Part A-2: Polymer Physics*, 1970. 8(10): p. 1823-1830.
39. Camino, G., S. Lomakin, and M. Lagueard, Thermal polydimethylsiloxane degradation. Part 2. The degradation mechanisms. *Polymer*, 2002. 43(7): p. 2011-2015.
40. Belot, V., et al., Thermal redistribution reactions in crosslinked polysiloxanes. *Journal of Polymer Science Part A: Polymer Chemistry*, 1992. 30(4): p. 613-623.
41. Thomas, T.H. and T. Kendrick, Thermal analysis of polydimethylsiloxanes. I. Thermal degradation in controlled atmospheres. *Journal of Polymer Science Part A-2: Polymer Physics*, 1969. 7(3): p. 537-549.
42. Hukins, D., A. Mahomed, and S. Kukureka, Accelerated aging for testing polymeric biomaterials and medical devices. *Medical engineering & physics*, 2008. 30(10): p. 1270-1274.
43. Goliszek, M., et al., Investigation of accelerated aging of lignin-containing polymer materials. *International journal of biological macromolecules*, 2019. 123: p. 910-922.
44. Celina, M., K.T. Gillen, and R. Assink, Accelerated aging and lifetime prediction: review of non-Arrhenius behaviour due to two competing processes. *Polymer Degradation and Stability*, 2005. 90(3): p. 395-404.

45. Celina, M., et al., Overview of accelerated aging and polymer degradation kinetics for combined radiation-thermal environments. *Polymer Degradation and Stability*, 2019. 166: p. 353-378.
46. Celina, M.C., Review of polymer oxidation and its relationship with materials performance and lifetime prediction. *Polymer Degradation and Stability*, 2013. 98(12): p. 2419-2429.
47. Zheng, Z., et al., Theoretical Model of Time–Temperature Superposition Principle of the Self-Healing Kinetics of Supramolecular Polymer Nanocomposites. *Macromolecular rapid communications*, 2018. 39(20): p. 1800382.
48. Li, R., Time-temperature superposition method for glass transition temperature of plastic materials. *Materials Science and Engineering: A*, 2000. 278(1-2): p. 36-45.
49. Galliano, A., S. Bistac, and J. Schultz, Adhesion and friction of PDMS networks: molecular weight effects. *Journal of colloid and interface science*, 2003. 265(2): p. 372-379.
50. Büyüktanir, E.A.n. and Z. Küçükyavuz, Solution properties of poly (dimethyl siloxane). *Journal of Polymer Science Part B: Polymer Physics*, 2000. 38(20): p. 2678-2686.
51. Morariu, S., et al., The Behavior of Poly (dimethylsiloxane-co-diphenylsiloxane) s in Good and Theta Solvents. *Journal of Chemical & Engineering Data*, 2011. 56(4): p. 1468-1475.
52. Chasse, W., et al., Cross-link density estimation of PDMS networks with precise consideration of networks defects. *Macromolecules*, 2012. 45(2): p. 899-912.

53. Valentín, J., et al., Uncertainties in the determination of cross-link density by equilibrium swelling experiments in natural rubber. *Macromolecules*, 2008. 41(13): p. 4717-4729.
54. Muramoto, A., Studies on the Interaction Parameter in Polysiloxane Solutions. *Polymer Journal*, 1970. 1(4): p. 450-456.
55. Horkay, F., A.M. Hecht, and E. Geissler, Thermodynamic interaction parameters in polymer solutions and gels. *Journal of Polymer Science Part B: Polymer Physics*, 1995. 33(11): p. 1641-1646.
56. Bueche, A., Interaction of polydimethylsiloxanes with swelling agents. *Journal of Polymer Science*, 1955. 15(79): p. 97-103.
57. Favre, E., Swelling of crosslinked polydimethylsiloxane networks by pure solvents: influence of temperature. *European polymer journal*, 1996. 32(10): p. 1183-1188.
58. Chassé, W., et al., Correction to cross-link density estimation of PDMS networks with precise consideration of networks defects. *Macromolecules*, 2015. 48(4): p. 1267-1268.
59. Dimitriyev, M.S., et al., Swelling thermodynamics and phase transitions of polymer gels. *Nano Futures*, 2019. 3(4): p. 042001.
60. Pacios, I.E., et al., Correlation of swelling and crosslinking density with the composition of the reacting mixture employed in radical crosslinking copolymerization. *Journal of applied polymer science*, 2007. 103(1): p. 263-269.
61. Oh, K.S., et al., Effect of cross-linking density on swelling behavior of NIPA gel particles. *Macromolecules*, 1998. 31(21): p. 7328-7335.
62. Gwaily, S., et al., Influence of thermal aging on crosslinking density of boron carbide/natural rubber composites. *Polymer testing*, 2003. 22(1): p. 3-7.

63. Lampe, F., J. Franklin, and F. Field, Cross sections for ionization by electrons. *Journal of the American Chemical Society*, 1957. 79(23): p. 6129-6132.
64. Prabowo, F., A.L. Wing-Keung, and H.H. Shen. Effect of curing temperature and cross-linker to pre-polymer ratio on the viscoelastic properties of a PDMS elastomer. in *Advanced Materials Research*. 2015. Trans Tech Publ.
65. Johnston, I., et al., Mechanical characterization of bulk Sylgard 184 for microfluidics and microengineering. *Journal of Micromechanics and Microengineering*, 2014. 24(3): p. 035017.
66. Efimenko, K., W.E. Wallace, and J. Genzer, Surface modification of Sylgard-184 poly (dimethyl siloxane) networks by ultraviolet and ultraviolet/ozone treatment. *Journal of colloid and interface science*, 2002. 254(2): p. 306-315.
67. Hanu, L.G., G.P. Simon, and Y.-B. Cheng, Thermal stability and flammability of silicone polymer composites. *Polymer degradation and stability*, 2006. 91(6): p. 1373-1379.
68. Johnson Jr, R., R. Biefeld, and J. Sayre, High-temperature electrical conductivity and thermal decomposition of Sylgard® 184 and mixtures containing hollow microspherical fillers. *Polymer Engineering & Science*, 1984. 24(6): p. 435-441.
69. Rucigaj, A., M. Krajnc, and U. Sebenik, Kinetic study of thermal degradation of polydimethylsiloxane: The effect of molecular weight on thermal stability in inert atmosphere. *Polym. Sci*, 2017. 3(9).
70. Planes, M., et al., Polydimethylsiloxane/additive systems for thermal and ultraviolet stability in geostationary environment. *Journal of Spacecraft and Rockets*, 2016. 53(6): p. 1128-1133.

71. Örm, A., Degradation studies on polydimethylsiloxane. 2019.
72. Liu, J., et al., Effects of fumed and mesoporous silica nanoparticles on the properties of sylgard 184 polydimethylsiloxane. *Micromachines*, 2015. 6(7): p. 855-864.
73. Müller, A., M.C. Wapler, and U. Wallrabe, A quick and accurate method to determine the Poisson's ratio and the coefficient of thermal expansion of PDMS. *Soft matter*, 2019. 15(4): p. 779-784.
74. Kong, K., et al., Enhanced conductivity behavior of polydimethylsiloxane (PDMS) hybrid composites containing exfoliated graphite nanoplatelets and carbon nanotubes. *Composites Part B: Engineering*, 2014. 58: p. 457-462.
75. Rücker, C. and K. Kümmerer, Environmental chemistry of organosiloxanes. *Chemical Reviews*, 2015. 115(1): p. 466-524.
76. Ducom, G., et al., Hydrolysis of polydimethylsiloxane fluids in controlled aqueous solutions. *Water science and technology*, 2013. 68(4): p. 813-820.
77. West, J.K., Theoretical analysis of hydrolysis of polydimethylsiloxane (PDMS). *Journal of Biomedical Materials Research: An Official Journal of The Society for Biomaterials and The Japanese Society for Biomaterials*, 1997. 35(4): p. 505-511.
78. Venkatachalam, S. and D. Hourlier, Heat treatment of commercial Polydimethylsiloxane PDMS precursors: Part I. Towards conversion of patternable soft gels into hard ceramics. *Ceramics International*, 2019. 45(5): p. 6255-6262.
79. Bahloul-Hourlier, D., J. Latournerie, and P. Dempsey, Reaction pathways during the thermal conversion of polysiloxane precursors into oxycarbide ceramics. *Journal of the European Ceramic Society*, 2005. 25(7): p. 979-985.

80. Antosik, A.K., P. Bednarczyk, and Z. Czech, Aging of silicone pressure-sensitive adhesives. *Polymer Bulletin*, 2018. 75(3): p. 1141-1147.
81. McIntosh, K.R., et al., The effect of accelerated aging tests on the optical properties of silicone and EVA encapsulants. 24th EUPVSEC, Hamburg, 2009: p. 3475.
82. Cifter, E.D., et al., In vitro study of effects of aging and processing conditions on colour change in maxillofacial silicone elastomers. *BMC oral health*, 2019. 19(1): p. 1-10.
83. Gary, J.J. and C.T. Smith, Pigments and their application in maxillofacial elastomers: a literature review. *The Journal of prosthetic dentistry*, 1998. 80(2): p. 204-208.

Chapter 8 Conclusions and Future Work

Building off the work described in the previous chapters, further experiments are going to be conducted to elucidate the behavior and material properties of other polymeric systems. These further experiments involve more 3D printing and accelerated aging studies. For the 3D printing work, composites for FFF will be made that incorporate tungsten (W) and polyethylene glycol (PEG) into either ABS or PLA. Similar to the DIW radiation shielding investigation, once these composites are developed, 3D printed parts will have varying porosities and resulting thermomechanical and radiation shielding characteristics will be assessed. For the future accelerated aging studies, two systems will be investigated: a boron/polyethylene (B/PE) composite and Sylgard 186. Like the Sylgard 184 aging treatment, modified Sylgard 186 formulations will be aged in elevated temperatures in varying atmospheric conditions, however the B/PE will be aged in a nuclear reactor. Once aging of each system is complete, a battery of characterization tests will be performed to determine how the polymer networks changed and how the behavior of the overall materials have shifted from their pristine properties.

As observed in the antimicrobial FFF work, PEG behaves as a plasticizer in PLA and as such composites that incorporated PEG becomes less stiff by way of a decreased Young's Modulus and had a dramatic increase in the maximum elongation. Because the ceramic fillers caused the opposite effects, the mechanical properties of the filaments were able to be tuned. In a similar effort, tungsten will be incorporated into PLA and ABS networks to create radiation shielding composites. Once the amount of tungsten reaches above a threshold (determined by the volume percent in the composite and denoted as the

percolation threshold), the thermal and electrical properties should increase drastically. In order to avoid the composite thus possessing undesirable mechanical properties due to likely high amount of tungsten filler needed to cross the percolation threshold (tungsten has a density of about 20 g/cm^3), PEG will be added as a plasticizer. Once this is performed, filaments will be created and parts will be 3D printed. Additionally, the 3D parts will be similar in geometry but possess varying amounts of controlled porosity so that the macroscopic material properties will be tunable. Because tungsten can shield gamma rays, the resulting parts will be exposed to a high-energy Cs^{137} source (0.6 MeV) and the attenuation will be characterized.

In the same class as Sylgard 184, Sylgard 186 is created using similar components and chemistry. The way these two siloxanes differ is the proportion of their individual components. Sylgard 186 is a more viscous formulation, has different thermal and electrical properties, and is semi-crystalline, whereas Sylgard 184 is purely amorphous. That stated, the two are comparable with regards to how they are combined (mix parts A and B) and used (as an encapsulant and adhesive). To expand on the aging work performed on modified Sylgard 184 formulations, the ashby-karstedt catalyst and tetrakis (dimethylsiloxy) silane (TDS) will be used to make modified Sylgard 186 formulations. Additionally, a thermal aging treatment will be conducted similarly to that previously described and mass spectrometry will be used to probe the volatile products that are generated. The time-temperature superposition (TTS) principle will be employed to convert time data into shift time and master curves will be created in order to make predictions about long-term performance and behavior of modified Sylgard 186 formulations.

B/PE composites will be made using isotopically enriched B¹⁰ and ultra-high molecular weight polyethylene (UHMWPE). The polymer network will be assessed as a pristine composite and then multiple parts will be exposed to rods in a nuclear reactor. These parts will be exposed in the same run at the same time so as to create a statistically significant data set of aged B/PE composites. Once the exposed samples can be recovered and safely handled, the polymer network will be explored to determine whether any changes occurred. After this is performed, mechanisms will be evaluated to discern how the system ages under nuclear reactor conditions. Additionally, computational models will be used to verify the understanding of the governing physics and chemistry, which can be validated using experimental results. This work will help benefit and steer future materials science endeavors to develop novel and refine existing materials for nuclear applications.

Appendix

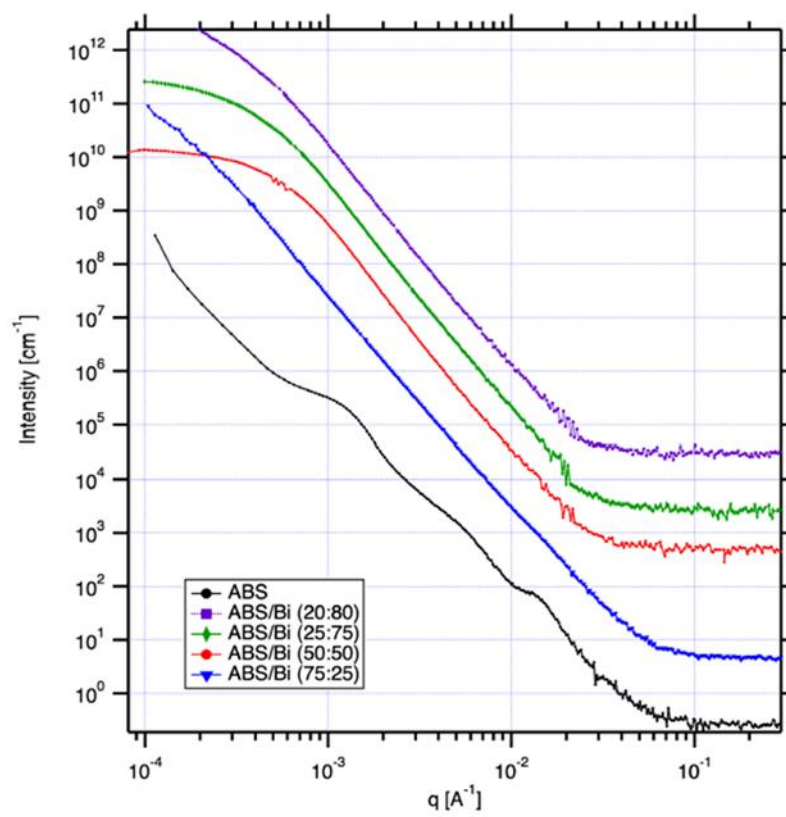


Figure A.1: USAXS and SAXS profiles of pure ABS and ABS/Bi composites.

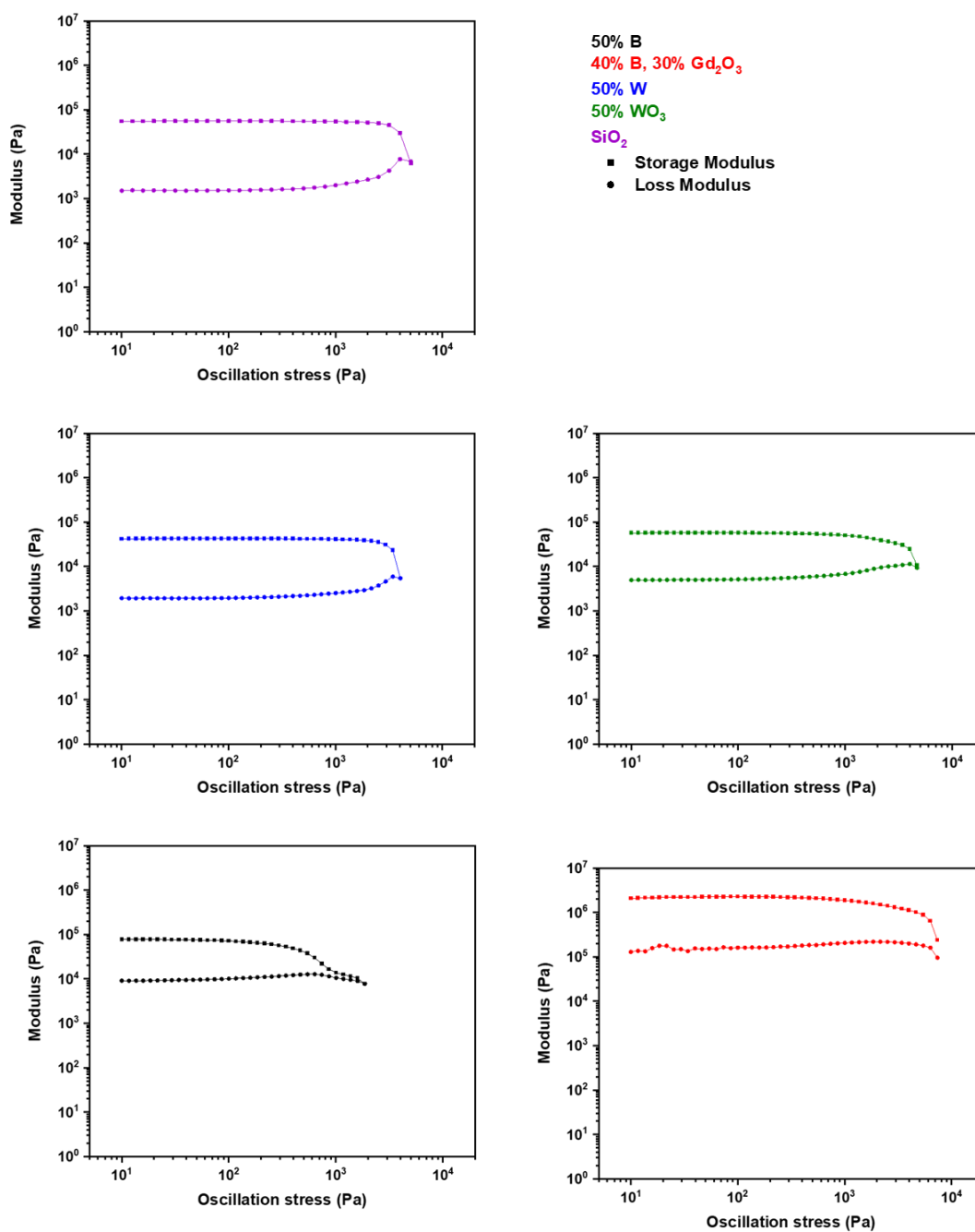
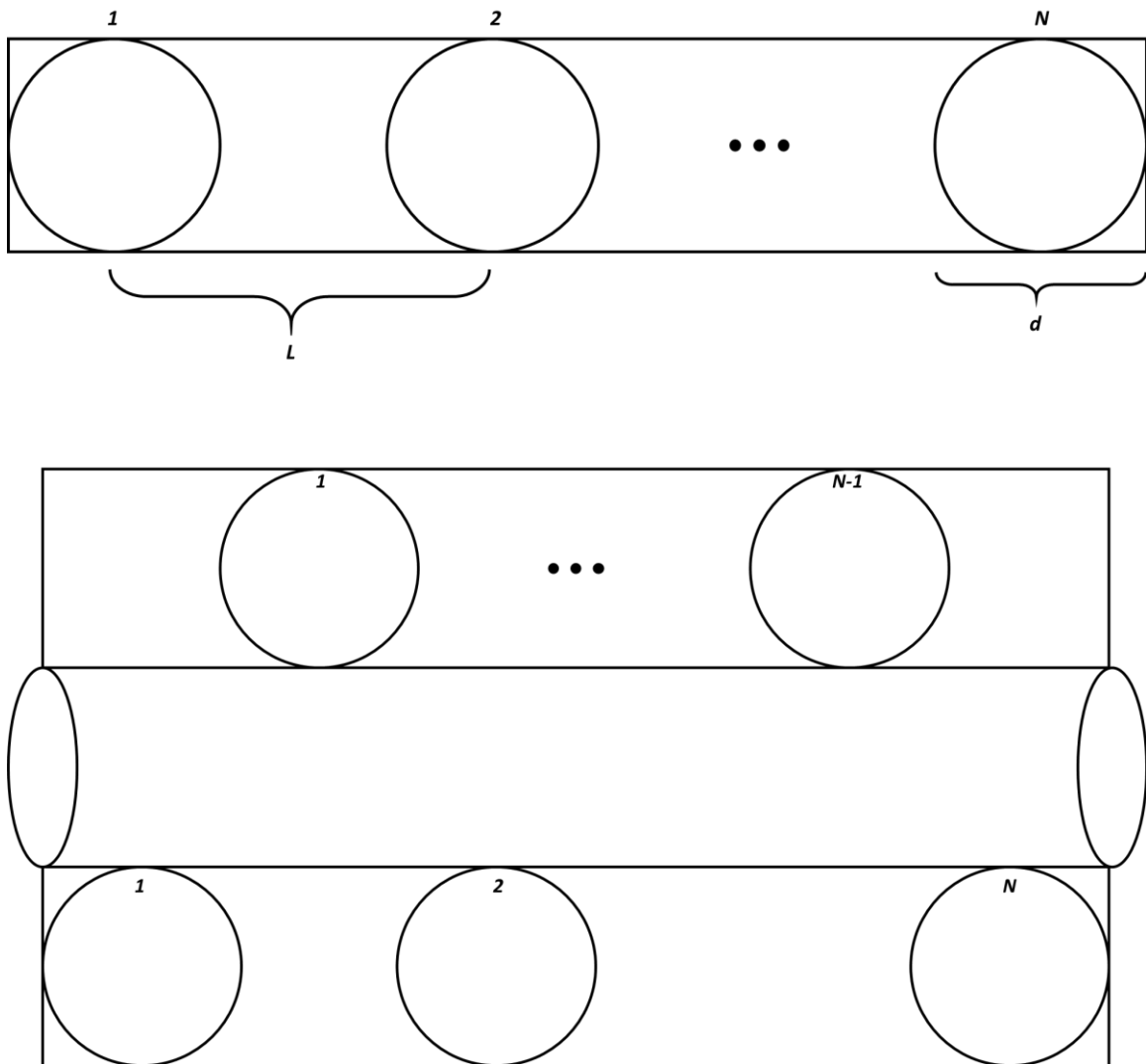


Figure A.2: Storage and loss moduli of the rheology-tested ink formulations during the stress sweeps.

FCT geometry theoretical porosity calculation:

Consider a rectangular prism constructed of layers of 3D printed struts. The struts have a diameter d and the center-to-center distance between the struts is L . The first layer comprises N printed struts oriented in the same direction and each layer is oriented orthogonal to the layers printed directly above and below. Furthermore, every other layer is staggered, where the printed struts are in-between those from two layers above and below. The figures below demonstrate this construction.



Thus, the height, width, and length of each layer is d , $(n-1)L+d$, and $(n-1)L+d$, respectively. Due to the staggered nature of the lattice, every four layers repeats. Therefore, only considering four layers, where the first two have N struts and the last two have $N-1$ struts, the porosity can be evaluated by comparing the volumes of the struts against the total

control volume. The volume of a printed strut is that of a cylinder $V_{strut} = \frac{\pi}{4}d^2((N-1)L+d)$, whereas the volume of a layer is that of a rectangular prism $V_{layer} = d((n-1)L+d)^2$.

Because the porosity is the empty space, $\varphi_{FCT} = 1 - \frac{(2n+2(n-1))V_{strut}}{4V_{layer}} = 1 - \frac{(2n-1)\pi d}{8((n-1)L+d)}$, the idealized porosity of the FCT geometry can be assessed by taking the limit as the number of struts in a layer goes to infinity $\varphi_{FCT}^{\infty} = \lim_{n \rightarrow \infty} \varphi_{FCT} = 1 - \frac{\pi d}{4L} = 1 - \frac{\pi}{4\eta}$, where $\eta = L/d$ is the spacing ratio for the lattice structure.

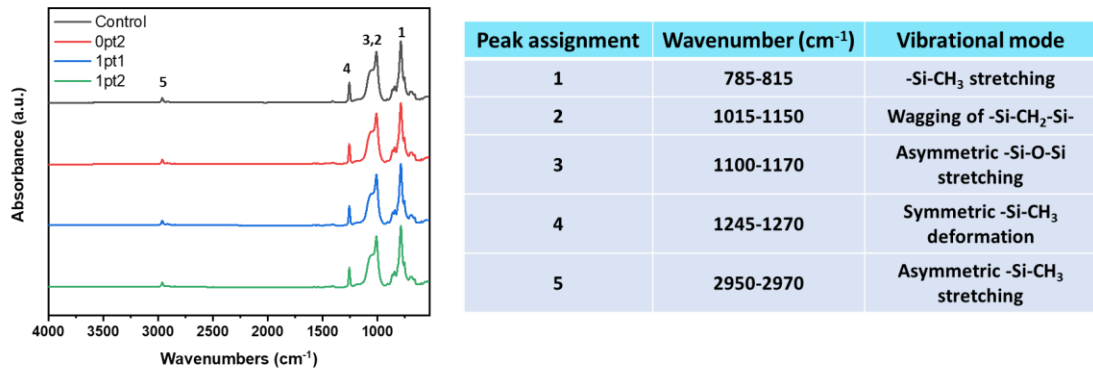


Figure A.3: FTIR spectra of formulations along with their peak assignments.

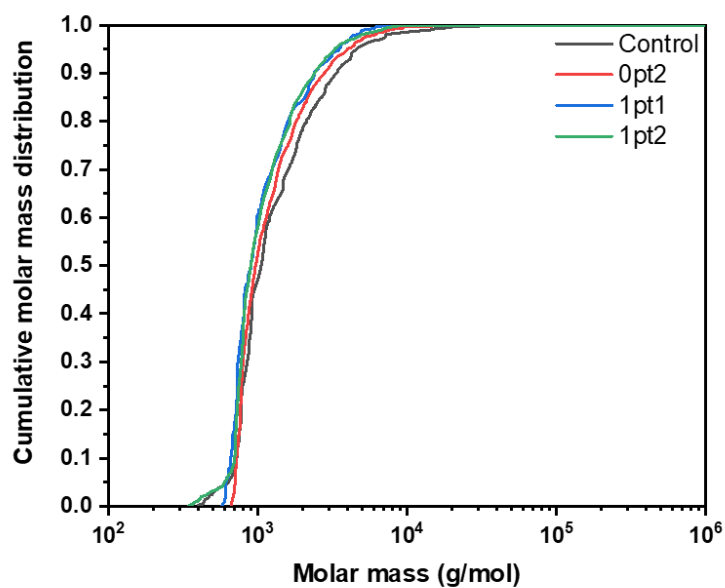


Figure A.4: Cumulative molar mass distribution of the extracts from pristine samples.

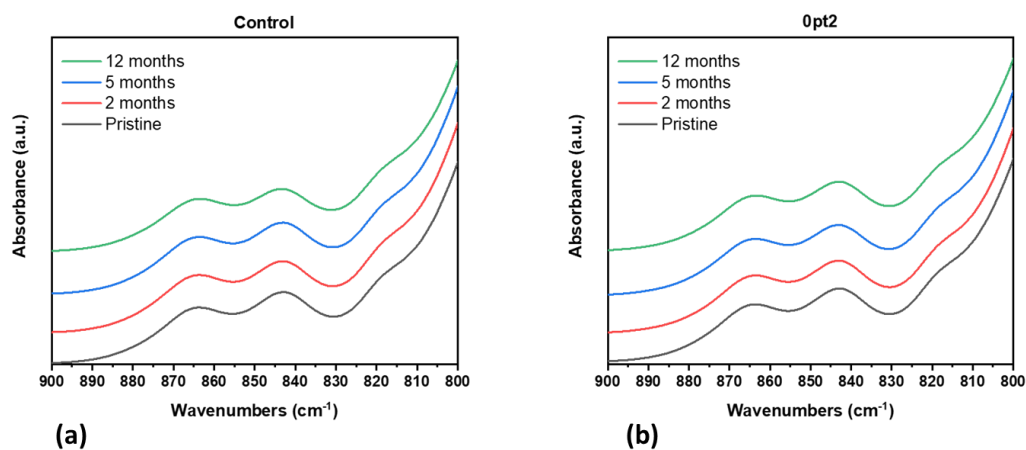


Figure A.5: FTIR absorbance spectra of pristine and 50°C aged samples showing peaks at 845 cm^{-1} and 865 cm^{-1} which correspond to siloxanol groups (Si-OH) – (a) Control and (b) Opt2.

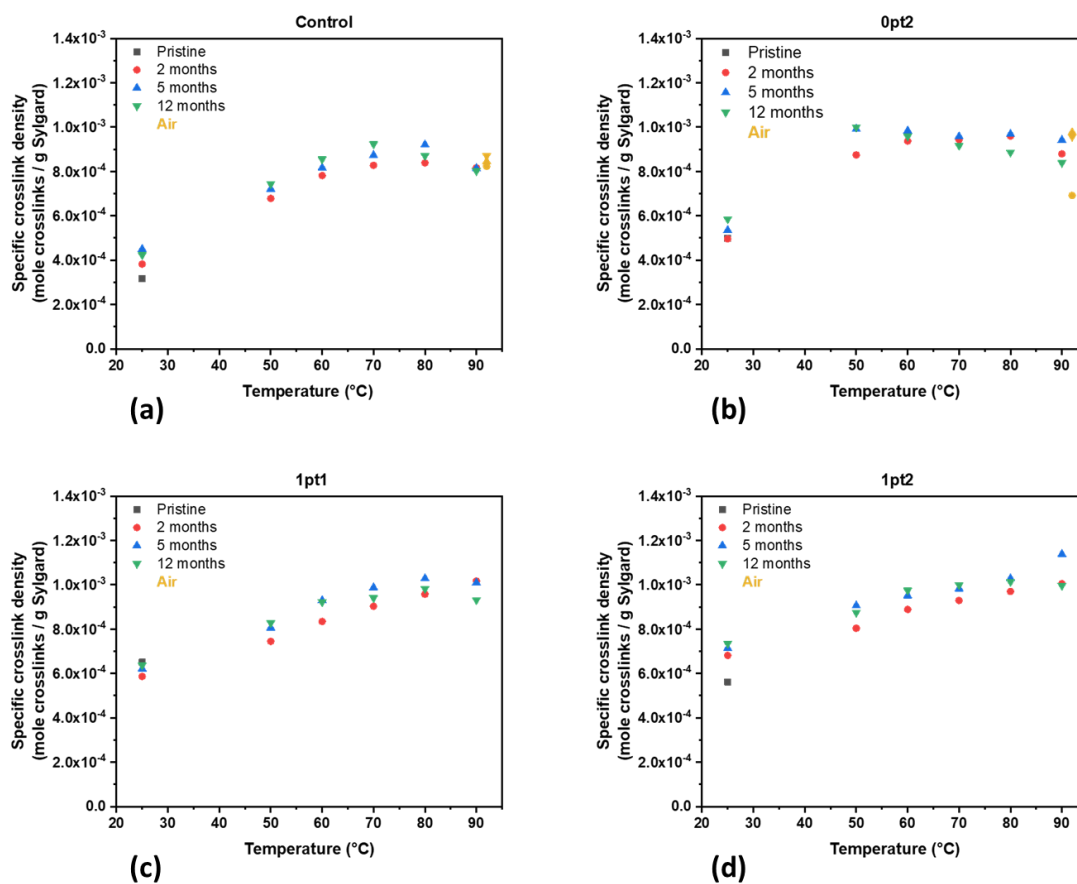


Figure A.6: Specific crosslink density of the thermally aged samples – (a) Control; (b) Opt2; (c) 1pt1; and (d) 1pt2.

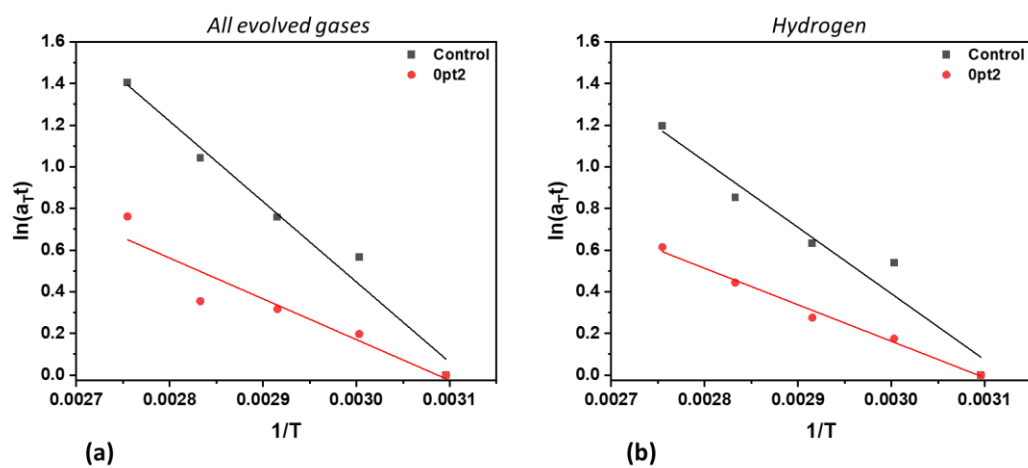


Figure A.7: Validity of the TTS model for mass spectrometry data, where $\ln(a_T t)$ and $1/T$ display a linear relationship for (a) all evolved gases and (b) hydrogen.

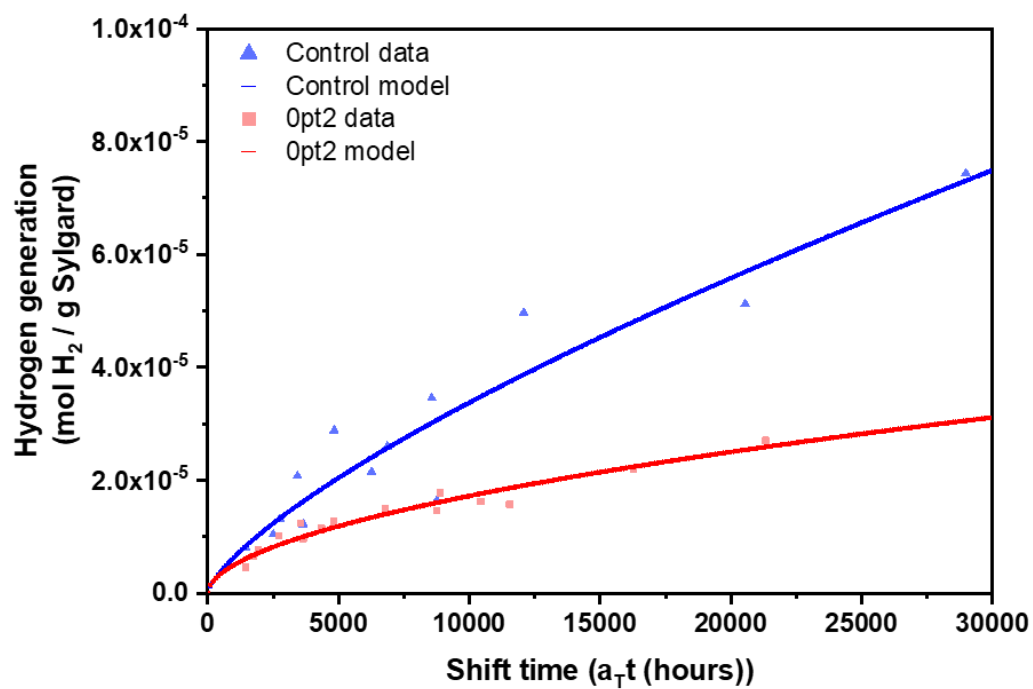


Figure A.8: Hydrogen generation for the Control and Opt2 formulations. Included is the shifted data and the model. For the Control, the equation is $n(a_T t) = 4.22 \times 10^{-8} a_T t^{0.7257}$ and for the Opt2, the equation is $n(a_T t) = 1.20 \times 10^{-7} a_T t^{0.5391}$.

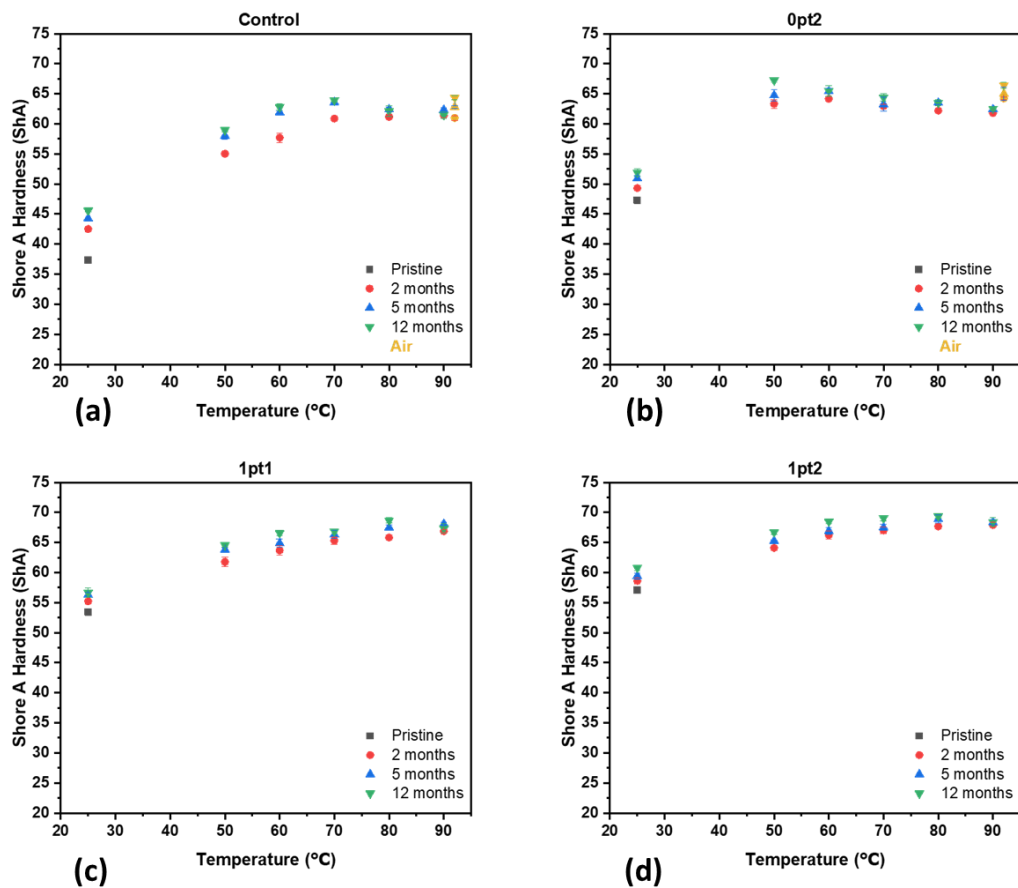


Figure A.9: Shore A Hardness of the thermally aged samples– (a) Control; (b) 0pt2; (c) 1pt1; and (d) 1pt2.

$$ShA(a_T t) = \frac{ShA^\infty}{1 + e^{-k(a_T t - a_T t_{1/2})}} \text{ Equation A1}$$

Table A.1: Time-temperature superposition Shore A Hardness master curve model parameters.

Formulation	Final Hardness (ShA^∞)	Steepness (k)	Midpoint ($a_T t_{1/2}$)
Control	62.73	0.0013	-300
0pt2	63.98	0.0020	-525
1pt1	67.34	0.0019	-700
1pt2	68.82	0.0015	-1050

Final hardness, ShA^∞ , values were averaged over every measurement that ended up being associated with a shift time of over 9,000 hours. The values presented in the table maximize R^2 .

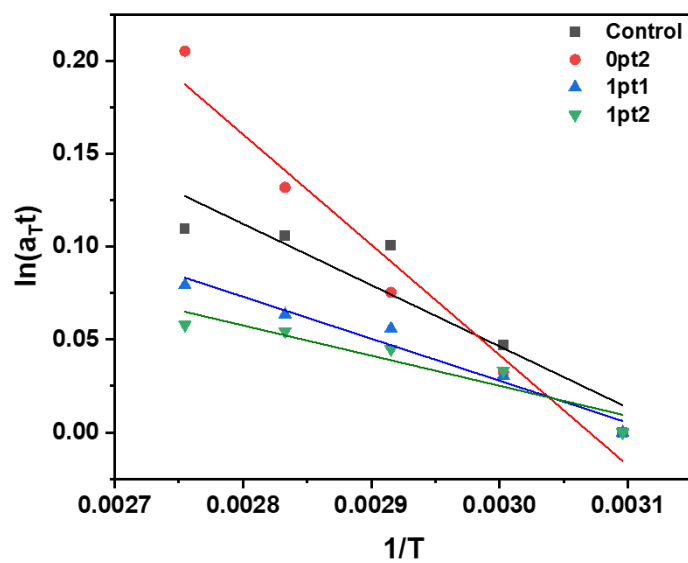


Figure A.10: Validity of the TTS model for Shore A Hardness data, where $\ln(a_T t)$ and $1/T$ display a linear relationship for all the modifications